MOCVD growth and characterisation of III-nitride semiconductors, heterostructures and devices

Stepanov, Sergei

Award date:
2003

Awarding institution:
University of Bath

MOCVD GROWTH AND CHARACTERISATION OF III-NITRIDE SEMICONDUCTORS, HETEROSTRUCTURES AND DEVICES

submitted by Sergei Stepanov Stepanov

for the degree of PhD

of the University of Bath

2003

ProQuest LLC
789 East Eisenhower Parkway
P.O. Box 1346
Ann Arbor, MI 48106-1346

Abstract

This thesis focuses on several important aspects of growth, characterisation and physics of III-nitride semiconductors. The first chapter contains a brief review of physical properties of III-Nitrides. The second chapter covers the principles of the metal organic chemical vapour deposition process and its application for the epitaxial growth of III-Nitrides. Following chapters focus on the nucleation process of GaN on sapphire (chapter 3), the p-type doping of GaN (chapter 5), the growth of AlGaN and InGaN alloys (chapters 6 and 7). In chapter 4 we discuss the use of x-ray diffraction for characterisation of III-nitride epitaxial films and suggest a new method to extract structural parameters of epilayers from x-ray diffraction scans. In chapter 8 we analyse current spreading in III-nitride based light emitting diodes. It is shown that efficient current spreading is limited by the resistance of the n-type layer. Chapter 9 covers the growth and properties of Si doped AlGaN/GaN superlattices. Due to formation of two dimensional electron gas, these superlattices have high mobility of electrons and can be used as current spreading layers in III-nitride based devices. Chapter 10 describes the growth of strained Mg-doped AlGaN/GaN superlattices to improve p-dopant activation. The growth of InGaN/GaN quantum wells is discussed in chapter 11. Chapter 12 reports on successful fabrication of InGaN light emitting diodes. Chapter 13 presents the results on optical pumping of III-nitride based laser structures.

Table of contents

Introduction

The Group-III nitride-based compounds have been considered as promising semiconductor materials. The most sought after property of III-Nitride semiconductors is their wide direct bandgap, permitting the fabrication of highly efficient optoelectronic devices operating in the blue and ultraviolet part of the spectrum. The wurtzite polytypes of GaN, AlN and InN form a continuous alloy system whose direct bandgap ranges from 1.9 eV to 6.4 eV. Because of their wide band gap, they can be used in violet, blue and green light emitting devices, covering a part of the electromagnetic spectrum that is not covered by conventional semiconductor technology. Traditional III-V semiconductor technology covers the spectrum from infrared to green.

The first studies of III-nitrides began in early 1970's. However, the development of III-nitride based semiconductor devices was slow, mostly due to poor material quality and miscellaneous technological problems. The material quality has been steadily improving, and this improvement opened up new opportunities for rapid progress in III-Nitride related devices in the early 1990's. The major breakthroughs were the development of a low-temperature nucleation layer, which allowed the growth of device-quality GaN on sapphire substrates, and the successful growth of the p-type GaN using Mg dopant. First commercial high-brightness LEDs operating in blue and green regions of the visible spectrum were produced in Japan in 1995. This has led to a revolution in LED technology and opened up enormous new markets that were not accessible before. Full-colour displays, for example, require at least three primary colours, usually red, green and blue, to produce any visible colour. Bright red-emitting LEDs had been already commercialised by that time, and the emergence of blue and green light emitters allowed to cover the whole colour range, including white light. First full-colour display based on III-nitride LEDs was demonstrated in 1996 in Japan.

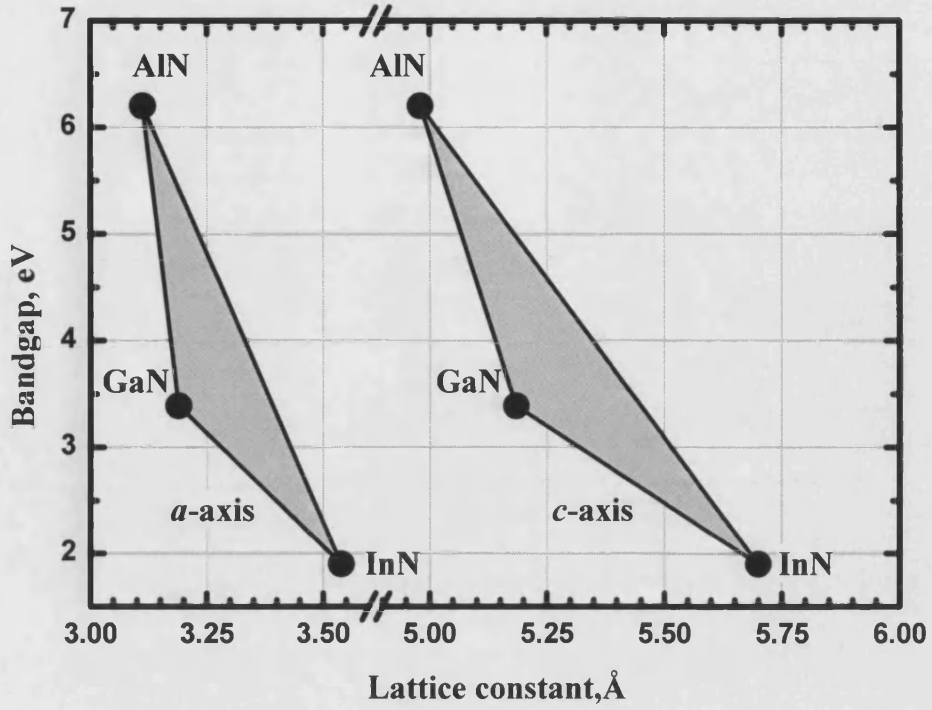

Figure 1.1 Bandgap energy of wurtzite GaN, AlN and InN versus lattice constants *a* and *c*.

Solid-state lighting is another large niche for nitride-based light emitting diodes. White light can be obtained by mixing monochromatic light from two or more LEDs (e.g. red, green and blue LEDs). Another approach utilises conversion of short-wave radiation (blue or UV) from III-Nitride LED into longer wavelength using a phosphor. Such all-solid-state white-light-emitting devices would be more durable with less power consumption than conventional incandescent bulbs or fluorescent lamps.

Blue-violet laser diodes are in high demand for optical storage applications. The shorter the wavelength of laser emission, the smaller is the focused spot, which means higher information density. Current DVD disk technology relies on red aluminium indium gallium phosphide (AlInGaP) semiconductor lasers and have a data capacity of about 4.7 gigabytes, compared with 0.65 gigabytes for CDs, which use infrared aluminium gallium arsenide (AlGaAs) laser diodes. By moving to violet wavelengths through the use of nitride-based laser diodes the capacity of optical disks can be increased up to 20 gigabytes.

Portable cost-effective nitride lasers can replace bulky and expensive gas lasers in applications like underwater communication systems, detectors for chemical and biological compounds, scientific equipment and many others.

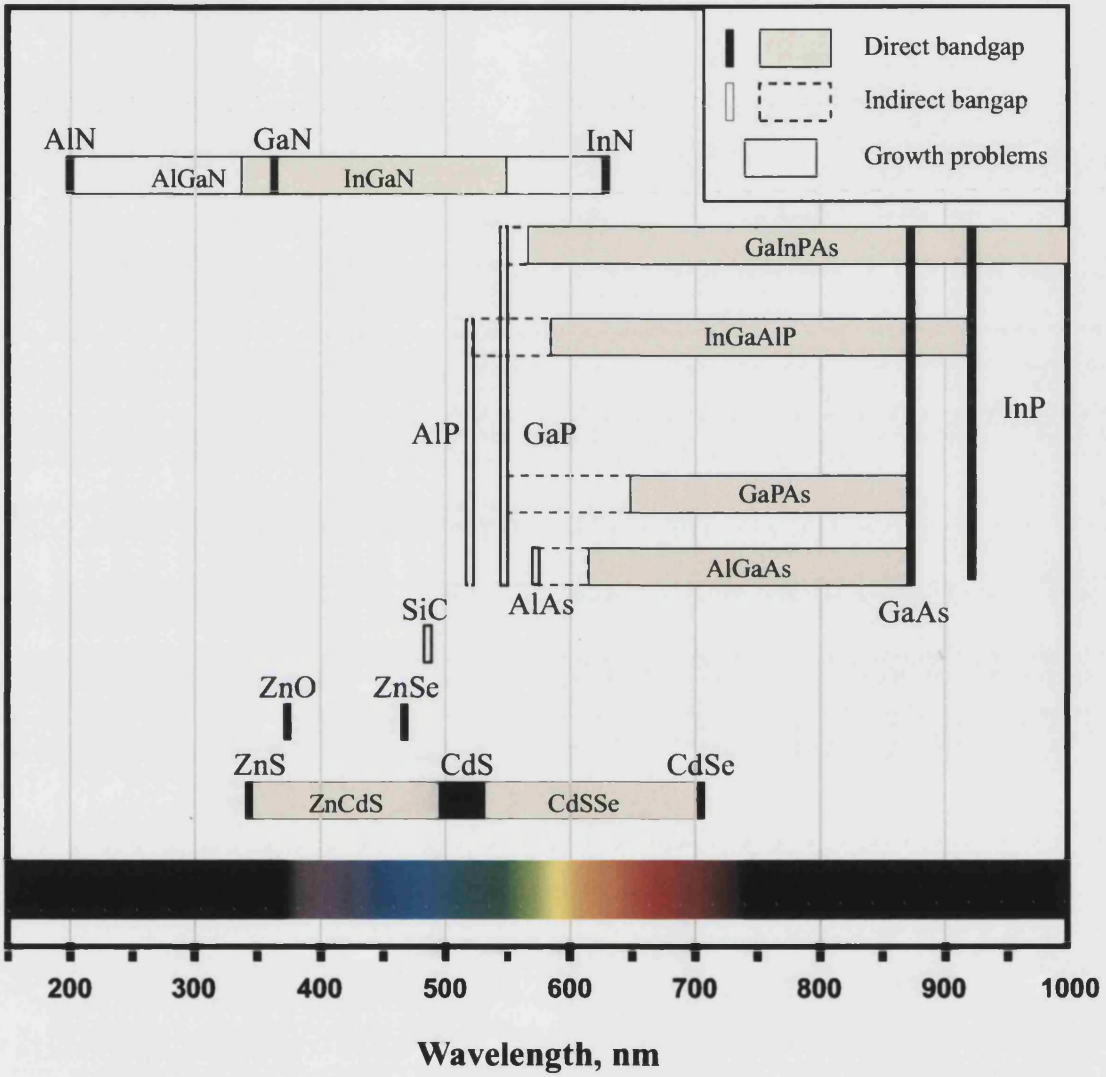

Figure 1.2 Spectral range coverage of various semiconductor materials

S. Nakamura and co-workers have laid the first milestone in nitride laser diode research. In 1996 they demonstrated pulse-mode nitride blue-violet laser. The following year the same group of researchers demonstrated a continuous wave operation of a nitride laser diode. Recently, these results were repeated and improved by a number of research groups in Japan, USA and Europe. Nitride lasers with lifetimes in excess of 10,000 hours have been reported.

Despite quick commercial success, many issues still remain to be solved. This work is focused on the growth and characterisation of III-nitrides and III-nitride based heterostructures and devices.

1. Physical properties of GaN, AlN, InN and their alloys

Despite the relatively short history of III-Nitrides, they are fairly well reviewed in scientific literature. A number of conference proceedings, authored and edited books have been published on these semiconductors. Very informative reviews on various properties of Group III nitride semiconductors have been written by Ambacher [1], Jain *et al* [2], Morkoc *et al* [3,4,5]. An informative review of dopant characteristics of III-nitrides has been published by Sheu *et al* [6]. Another comprehensive source of physical properties of III-nitrides and related materials is the book [7] by Levinshtein and co-authors. Also, we shall mention here the online database on Physical Properties of Semiconductors [8] maintained by the Ioffe Institute. Since the detailed information on III-nitrides can be readily found in the above-mentioned references, in this chapter we will give only a brief summary of the most essential facts and properties of GaN, AlN, InN and their alloys.

1.1. Structural properties

In contrast to conventional III-V semiconductors like GaAs, which form the zincblende (cubic) structure, III-Nitrides can crystallize in wurtzite (hexagonal) or zincblende polytypes. At high pressures, a cubic high-pressure modification with NaCl structure has also been observed. For practical device applications wurtzite and zincblende structures are the most important. The wurtzite structure is more common, as it is the only thermodynamically stable phase of all III-nitrides. The zincblende phase is metastable under normal conditions. Nevertheless zincblende III-Nitrides can be grown under special growth conditions on cubic substrates like Si, GaAs and MgO. Besides, coexistence of wurtzite and zincblende phases is possible in epitaxial layers, for example due to stacking faults. So far, hexagonal nitrides are normally used for device applications and are much better studied. On the other hand, owning to their higher crystallographic symmetry, cubic

nitrides are expected to have several advantages such as higher mobility and better doping efficiency.

Crystallographically, the zincblende structure and wurtzite structure are very closely related. Both structures have the tetrahedron arrangement of chemical bonds. They only differ in stacking sequence of nitrogen and metal atoms. For wurtzite GaN the sequence in [0001] direction is $Ga_AN_aGa_BN_bGa_AN_aGa_BN_b$..., or AB AB AB. For zincblende GaN the stacking sequence in [0001] direction is $Ga_AN_aGa_BN_bGa_CN_cGa_AN_aGa_BN_bGa_CN_c$ ..., or ABC ABC ABC. In other words, the coordination of the nearest neighbours is the same for both structures (tetrahedral). But the coordination of next-nearest neighbours is different (cuboctahedral for zincblende and anti-cuboctahedral for wurtzite).

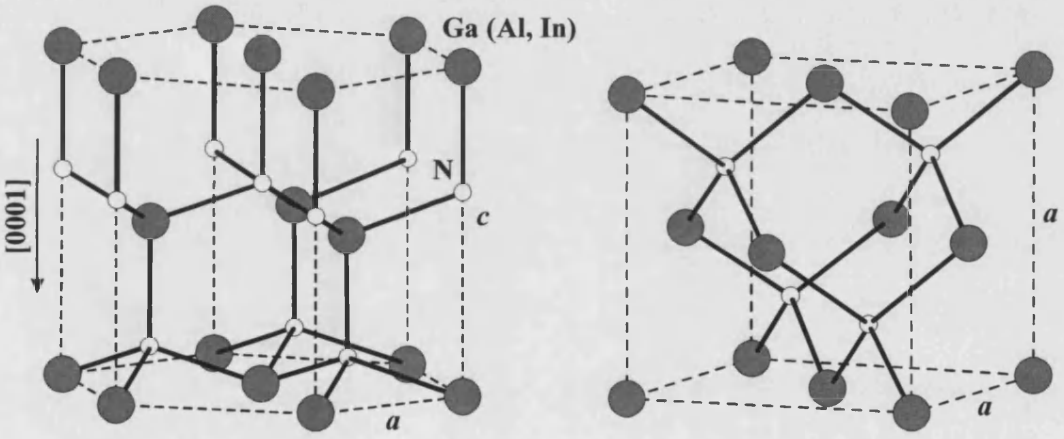

Wurtzite **Zincblende**

Figure 1.1. Wurtzite and Zincblende structures of Group III nitrides.

A schematic diagram of atom arrangement for the wurtzite and zincblende structures is shown in Figure 1.1.

Wurtzite has hexagonal crystalline structure which is described by two lattice parameters *a* and *c*. The *a* lattice parameter measures the length of the basal hexagon, the *c* lattice parameter is the height of the hexagon prism. Commonly, crystallographic directions and planes in hexagonal crystals are described ether in three- or four-index notation. In case of three-index notation the basis is formed by axes a_1, a_2 and *c*. However,

in three-index notation, equivalent planes or directions do not have similar indices. For that reason many researchers prefer to use four indices, based on four axes a_1, a_2, a_3 and c. Since all three a axes are equivalent, the equivalent planes are obtained simply by permutations of the first three indices. The first three indices for the plane $(hkil)$ are always related by the equation

$$i = -(h+k) \tag{1.1}$$

Since the third index is completely determined by the first two an abbreviated style $(hk \cdot l)$ may be used where the third index is replaced by a dot.

A direction in four-index notation may be specified by the four vector components $[uvtw]$ of the vector $\bar{r} = u\bar{a}_1 + v\bar{a}_2 + t\bar{a}_3 + w\bar{c}$. Again, the first three indices are interdependent and related by the equation

$$t = -(u+v) \tag{1.1}$$

The transformation of the indices of the planes from three-index notation (hkl) to four-index notation $(hkil)$ is quite easy. The third index i is always given by the equation

$$i = -(h+k) \tag{1.2}$$

The transformation back from four to three requires dropping the third index i.

Transformational equations for directions are more complicated. If the same vector is written as $[UVW]$ in three-index notation and as $[uvtw]$ in four-index notation, the following equations hold

$$U = u - t \qquad V = v - t \qquad W = w \tag{1.2}$$

$$u = \tfrac{1}{3}(2U - V) \qquad v = \tfrac{1}{3}(2V - U) \qquad t = -(u+v) \qquad w = W$$

Four index notation in triangular brackets $\langle uvtw \rangle$ denote a system of equivalent directions. The individual vectors are obtained using equation (1.2) and by permutations of the first

three indices. For example, $\frac{1}{3}\langle 11\bar{2}0\rangle$ denotes all directions along one of the sides of the basal hexagon.

For ideal wurtzite structure, the ratio of lattice parameters is fixed $c/a=(8/3)^{1/2}\approx 1.633$. In real crystals, the c/a ratio is slightly smaller. In this sense, real crystals can be considered as an ideal wurtzite structure compressed along [0001] direction.

Table 1. Lattice constants for AlN, GaN and InN.

	GaN (WZ)	GaN (ZB)	AlN (WZ)	InN (WZ)
a, Å	3.189	4.52	3.112	3.533
c, Å	5.186	-	4.982	5.693
c/a	1.6259	-	1.6010	1.6114

Both wurtzite and zincblende structures have polar axes (lack of inversion symmetry). In the wurtzite structure, the bonds in ⟨0001⟩ direction are all faced by cations in one direction and anions in the opposite direction. As a result, directions [0001] and $[000\bar{1}]$ are not equivalent. By convention, the [0001] direction is given by a vector pointing from a metal atom to a nearest-neighbour N atom. As we mentioned before, in the wurtzite structure atoms are arranged in cation and anion layers stacked along ⟨0001⟩ direction. Therefore, the basal plane of hexagonal should be either metal or nitrogen faced. Both bulk and surface properties can depend significantly on whether the surface is faced by nitrogen or metal atoms. For example, it has been reported that the smooth side of GaN bulk crystals corresponds to the Ga-face (0001) whereas the N-face $(000\bar{1})$ is much rougher. Hexagonal GaN epitaxial layers grown by MOCVD on c-plane sapphire have [0001] axis directed from the substrate to the surface of the film. Consequently, MOCVD-grown GaN layers are Ga-faced. On the contrary, MBE growth commonly occurs in the $[000\bar{1}]$ direction yielding an N-faced film.

1.2. Piezoelectric properties

Wurtzite III-nitrides have two components of polarisation. The first component is the so-called spontaneous polarisation along $[000\bar{1}]$ direction related to the low symmetry of the wurtzite structure. The spontaneous polarisation is strain-independent and is present even in unstrained material. The increasing nonideality of the crystal structure going from GaN to InN to AlN (c/a decreases) corresponds to an increase in spontaneous polarisation. The second component is strain-dependent. It is referred as piezoelectric polarisation. In the absence of electric fields, the total polarisation is given as a sum of spontaneous polarisation in the equilibrium lattice and the strain-induced piezoelectric polarisation.

Knowledge of polarisation properties is very important for devices, as internal electric field modifies the shape of the band edges and the carrier distribution inside heterostructures. Further discussion on polarisation properties of III-Nitride semiconductors, as well as experimental demonstration of polarisation-related effects can be found in Chapters 9,10,11.

1.3. Electronic Band Structure

Hexagonal polytypes of GaN, AlN and InN have direct bandgaps of 3.4 eV, 6.2 eV and 1.9 eV[a], respectively. In cubic form, GaN and InN have direct bandgaps, while AlN is indirect. The band structure of zincblende GaN is similar to that of GaAs (see Figure 1.2). The valence band at $k = 0$ consists of three subbands, referred as *A*, *B*, and *C*, bands. The *C* band is split off due to spin-orbit coupling, and is referred as a split-off band. Bands *A* and *B* form a multiplet; the degeneracy can be removed by shear component of the biaxial

[a] According to recent publications InN has much narrower bandgap of 0.7-1 eV. See Chapter 7 and references there

strain. Holes in the *A* band have smaller effective mass than the holes in the *B* band. The two hole bands are known as the light hole band and heavy hole band.

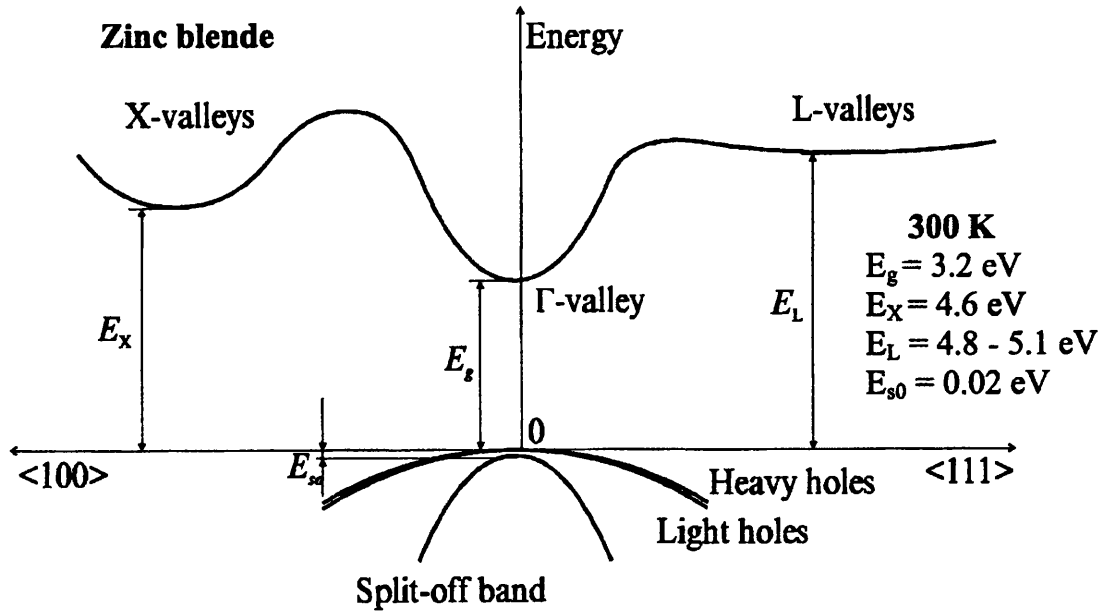

Figure 1.2. Band structure of zincblende (cubic) GaN (From Suzuki *et al* [9])

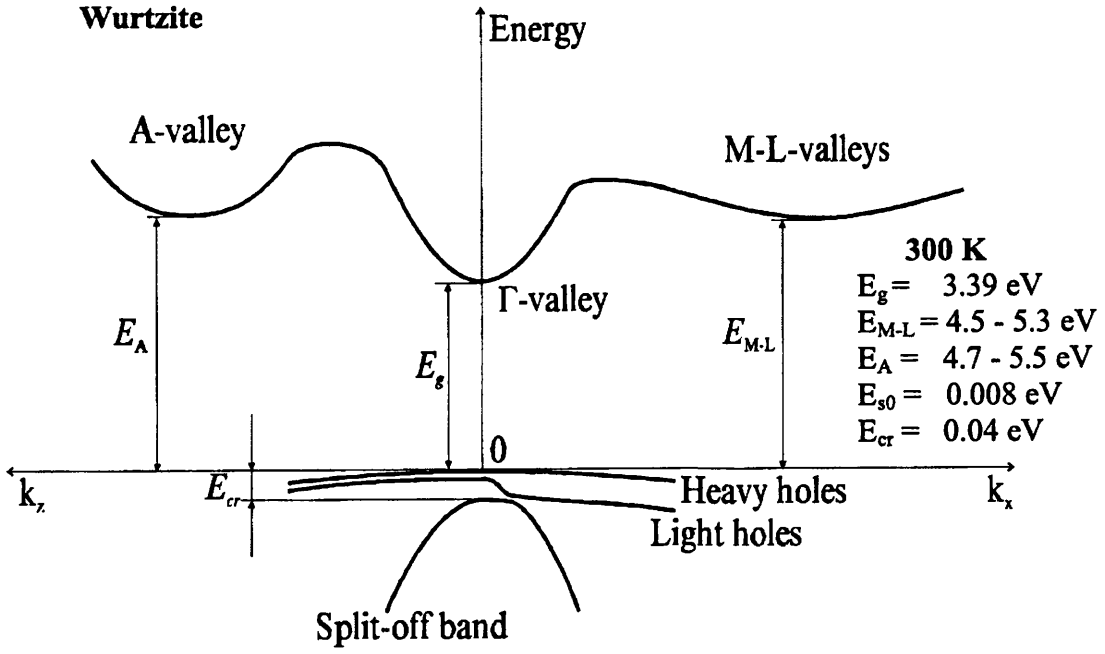

Figure 1.3. Band structure of wurtzite (hexagonal) GaN (From Suzuki *et al* [9])

The bandgap of wurtzite nitrides is higher than that of zincblende nitrides. The key difference between the zincblende and wurtzite band structures is the splitting of the valence band degeneracy due to the presence of the crystal field (see Figure 1.3).

Consequently, there are three bandgap excitons, usually labelled A-, B-, and C-exiton. In this sense, the wurtzite structure acts like a "pre-strained" cubic crystal. Therefore, for wurtzite III-Nitrides, the effects of strain on the valence band dispersion are much less dramatic than in GaAs and related III-V materials [10]

The effective masses of holes and electrons near Γ valley are given in Table 2. However, it should be noted that the effective mass approximation has very limited use for III-nitride valence bands, since valence bands are highly non-parabolic.

Table 2. Effective masses in GaN, AlN and InN

Zincblende, 300K		**GaN**	**InN**	**AlN**
Effective electron mass	m_e	$0.13m_0$ [11]	-	-
Effective heavy hole mass	m_{hh}	$1.3m_0$ [12]	-	-
	$m_{[100]}$	$0.8m_0$ [12]		
	$m_{[111]}$	$1.6m_0$ [12]		
Effective light hole mass	m_{lh}	$0.19m_0$ [12]	-	-
	$m_{[100]}$	$0.21m_0$ [12]		
	$m_{[111]}$	$0.18m_0$ [12]		
Wurtzite, 300K		**GaN**	**InN**	**AlN**
Effective electron mass	m_e	$0.20m_0$ [11]	$0.11m_0$ [13]	$0.4m_0$ [14]
Effective heavy hole mass	m_{hh}	$1.4m_0$ [12]	$1.63m_0$ [14]	-
	m_{hhz}	$1.1m_0$ [12]	-	$3.53m_0$ [15]
	$m_{hh\perp}$	$1.6m_0$ [12]	-	$10.42m_0$ [15]
Effective light hole mass	m_{lh}	$0.3m_0$ [12]	$0.27m_0$ [14]	-
	m_{hhz}	$1.1m_0$ [12]	-	$3.53m_0$ [15]
	$m_{hh\perp}$	$0.15m_0$ [12]	-	$0.24m_0$ [15]

1.4. Band offsets

Knowledge of band discontinuities between nitride materials in heterojunctions is important for designing electronic and optoelectronic devices. The band splitting parameters and the band offsets for III-nitride system has been experimentally and theoretically determined in several studies; there is, however, significant disparity between results. Band discontinuities depend on the strain state of the epilayer and, strictly speaking, on the interface order. For example, the band offsets for InN/GaN

heterojunctions are different from the offsets for GaN/InN heterojunctions. Approximate band offsets are given in Figure 1.4; for more detailed discussion on band offsets we refer the reader to Refs [1,2,16].

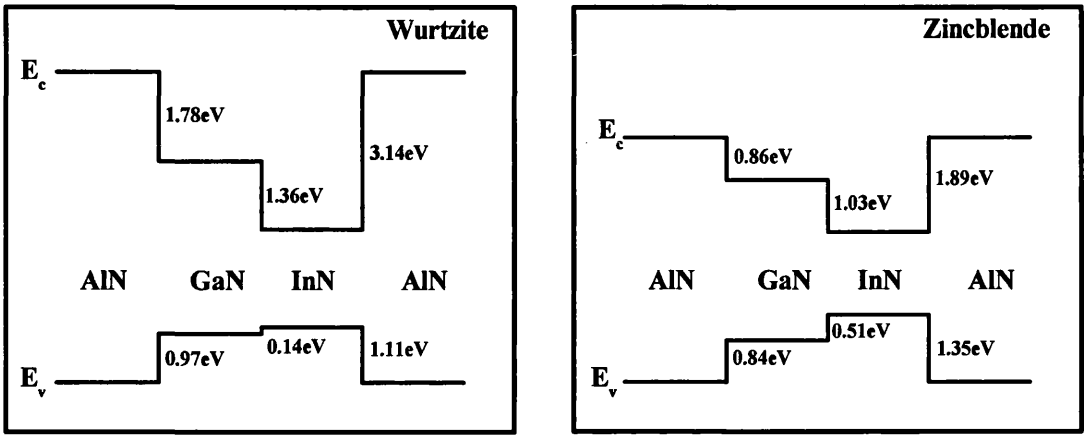

Figure 1.4. The approximate band offsets for wurtzite and zincblende Group III-Nitrides at room temperature. Polarization effects are ignored. (from Ambacher [1])

1.5. Doping of III-Nitrides

Undoped GaN films exhibit n-type conductivity. Typically, the background electron concentration in nominally undoped GaN is about 10^{16}–10^{17} cm^{-3}, depending on the growth technique. Commonly, this background conductivity is explained by the presence of defect-related donor levels like nitrogen vacancies. Unintentionally doped InN and InGaN films are heavily n-type (10^{18}–10^{20} cm^{-3}), regardless of the growth technique [6], and this is usually ascribed to the presence of indium vacancies. Impurities like oxygen and carbon can be also responsible for the strongly n-type conductivity in InN. As grown AlN always has a large concentration of C, O, and H impurities. However, because of very wide bandgap, these impurities form deep levels in the forbidden gap. Therefore, undoped AlN is generally semi-insulating. Intentional doping of AlN is also quite difficult due to high donor (acceptor) activation energy.

As it is generally known, group IV elements like Si, Ge and Sn can act as a donor or acceptor in III-V semiconductors depending, on which site it is substituted (a group III or group V element). As a rule, group IV element incorporates at group III element site and act as a donor. Under specific growth conditions, it can be incorporated as an acceptor; for example, in liquid-phase epitaxial growth.

In GaN, Si is usually used to produce n-type material. Electron concentrations up to 2×10^{19} cm^{-3} have been demonstrated by Nakamura [10]. The doping characteristics of Ge in GaN are similar to those for Si and have been demonstrated by Nakamura *et al* [17,10]. The carrier concentration up to 1×10^{19} cm^{-3} has been achieved. However, GeH_4 is ten times less efficient compared to SiH_4. Some experiments have demonstrated that alternative n-type dopants, such as Se and O, are also possible. Nevertheless, these dopants are more of academic interest as the doping efficiency is much lower compared to that of Si.

For p-type doping, the acceptor level of GaN is deeper than the GaAs acceptor level due to its larger hole mass. This leads to the difficulty in p-type doping and very low activation of dopants at room temperature for GaN. The most commonly used dopant for p-type GaN is magnesium. No other impurity has been so successful in producing p-type conductivity in GaN. However, activation energy of Mg is ~150 meV, which is quite large, compared to kT at room temperature. Therefore, only a few per cent of the Mg atoms are ionised at room temperature. Very high doping levels of 10^{19}–10^{20} cm^{-3} must be used to achieve hole concentrations in the middle of 10^{17} cm^{-3} region. Further improvement of the hole concentration is quite a challenging task, the determining factor being the solubility of Mg in GaN and various self-compensating mechanisms. In AlGaN, the activation energy of Mg increases rapidly with increasing Al content. On the contrary, in InGaN the activation energy of Mg is smaller than that in GaN. In spite of this, p-type doping of InGaN is still difficult due to higher background electron concentration.

Zn doping of GaN has been intensively investigated by many researchers worldwide. Although Zn doping produces a deep acceptor level with high activation energy, it has some practical applications. For example, Zn-Si co-doping was used in early nitride-based light emitting diodes to create donor-acceptor recombination centres [10]. Also, Zn doping can be used to produce highly insulating GaN layers [18] required in certain device applications.

More specific details of the doping process of III-nitrides are covered in the following chapters of the present work. In the Chapter 5 we will address various aspects of efficient p-type doping of GaN and related materials. Chapters 9 and 10 present the experimental results and theoretical analysis on doped p- and n-type superlattice structures.

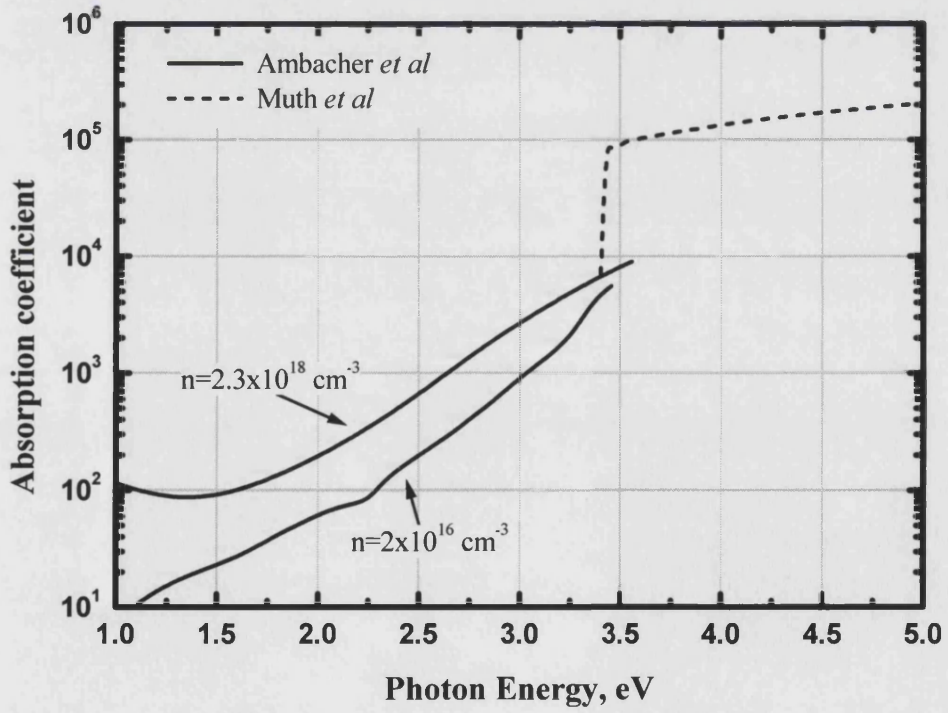

Figure 1.5. Room temperature absorption coefficient of wurtzite GaN versus photon energy. (from Ambacher *et al* [19] and Muth et al [20])

1.6. Optical Properties

Extensive work on the luminescence of III-nitrides has been done and several reviews have been published (see e.g. [2] and references there). For information on optical transitions in III-nitrides one should refer to above-mentioned sources.

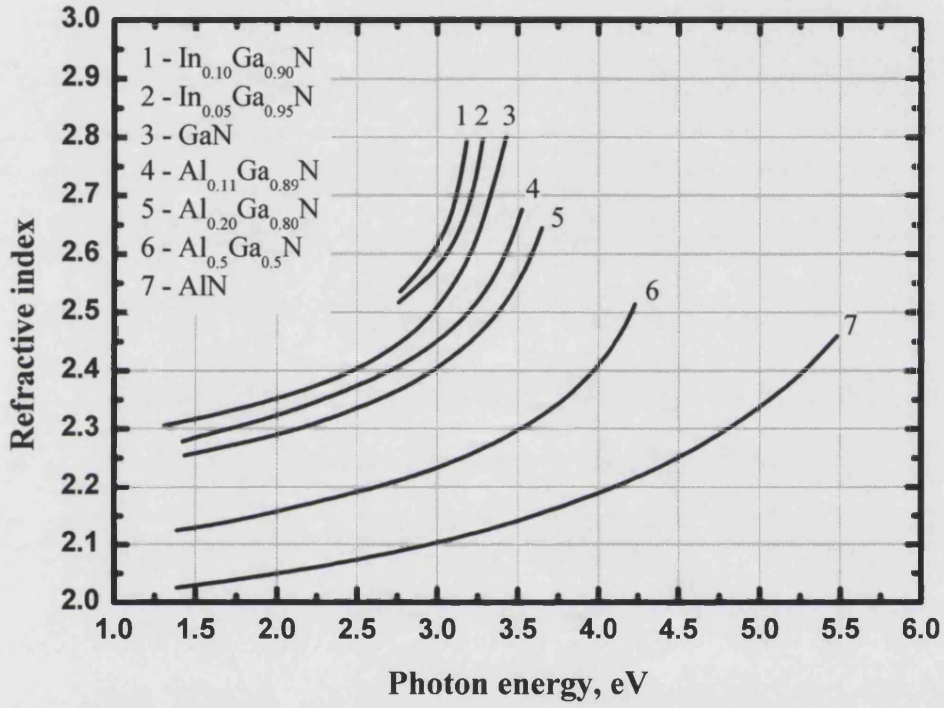

Figure 1.6. Refraction index of different AlGaN and InGaN films versus photon energy at room temperature (from Brunner *et al* [21] and Bougrov *et al* [22]).

For example, in GaN the refractive index changes from 2.3 for infrared radiation to ~2.8 for the photons with bandgap energy. The refractive index of III-nitrides has more pronounced dispersion than that of traditional III-V semiconductors. The dispersions curves for different III-nitride materials are presented in Figure 1.6.

Here we will discuss briefly light absorption and refractive properties of III-nitrides as these parameters are of key importance for optoelectronic devices such as lasers or light emitting diodes.

In contrast to conventional III-V semiconductors, III-nitrides have pronounced low-energy absorption tails. For example, for lasing photon energy of a GaAs/AlGaAs laser with a GaAs active region (corresponds to 40 meV redshift from the band-gap energy) absorption of light in AlGaAs cladding layers is less than 10 cm^{-1} even for very small mole fractions of AlAs. But in nitride materials, absorption coefficients at lasing wavelength are expected to be about 10^3 cm^{-1}. The dependence of the absorption coefficient on the photon energy is presented in Figure 1.5.The infrared refractive indices of the wurtzite GaN, AlN and InN are 2.3, 2.0, 2.9–3.1, respectively. As usual, the refractive index is increasing as the photon energy approaches the bandgap.

1.7. References

1. O.Ambacher, J. Phys. D: Appl. Phys. 31, 2653 (1998)
2. S.C. Jain, M. Willander, J. Narayan, R. Van Overstraeten, J. Appl. Phys 87, 965 (2000)
3. W.Kim, O. Aktas, A.E. Botchkarev, A. Salvador, S.N. Mohammad, H. Morkoc, J. Appl. Phys. 79, 7657 (1996)
4. H.Morkoc, S. Strite, G.B. Gao, M.E. Lin, B. Sverdlov, M. Burns, J. Appl. Phys. 76, 1363 (1994)
5. S.Strite, H. Morkoc, J. Vac. Sci. Technol. B 10, 1237 (1992)
6. J.K. Sheu, G.C. Chi, J. Phys.: Condens. Matter 14 R657–R702 (2002)
7. Properties of Advanced Semiconductor Materials GaN, AlN, InN, BN, SiC, SiGe . Eds. Levinshtein M.E., Rumyantsev S.L., Shur M.S., John Wiley & Sons, Inc., New York, 2001
8. New Semiconductor Materials. Characteristics and Properties, http://www.ioffe.ru/SVA/NSM/Semicond/index.html
9. Suzuki, M, T. Uenoyama, A. Yanase, Phys. Rev. B 52, 11, 8132-8139 (1995).
10. S. Nakamura, G. Fasol, "The blue laser diode", Spinger, 1997
11. Bougrov V., Levinshtein M.E., Rumyantsev S.L., Zubrilov A., in Properties of Advanced Semiconductor Materials GaN, AlN, InN, BN, SiC, SiGe . Eds. Levinshtein M.E., Rumyantsev S.L., Shur M.S., John Wiley & Sons, Inc., New York, 2001, 1-30.
12. Leszczynski, M., H. Teisseyre, T. Suski, I. Grzegory, M. Bockowski, J. Jun, S. Porowski, K. Pakula, J.M. Baranowski, C.T. Foxon, T.S. Cheng, Appl. Phys. Lett. 69(1) (1996), 73-75.
13. Lambrecht, W.R., Segall B., Phys. Rev. B 47, 9289-9296, (1993)
14. Xu, Y.N, Ching W.Y., Phys Rev. B 48, 7, 4335-4351, (1993).

15. Suzuki, M., Uenoyama T., J. Appl. Phys. 80, 12, 6868-6874, (1996).

16. H. Ünlü, A. Asenov, J. Phys. D: Appl. Phys. 35, 591, (2002)

17. Nakamura S, Mukai T and Senoh M Japan. J. Appl. Phys. 31 2883 (1992)

18. N. I. Kuznetsov, A. E. Nikolaev, A. S. Zubrilov, Yu.V. Melnik, V.A. Dmitriev, Appl. Phys. Lett., Vol. 75, 3138 (1999)

19. O. Ambacher, W. Rieger, P. Ansmann, H. Angerer, T.D. Moustakas, M. Stutzman, Sol. State Commun. 97(5), 365-370 (1996).

20. J.F Muth , J.H. Lee, I.K. Shmagin, R.M. Kolbas, H.C. Casey, Jr., B.P. Keller, U.K. Mishra, S.P. DenBaars, Appl. Phys. Lett. 71(18), 2572-2574 (1997)

21. D. Brunner, H. Angerer, E. Bustarret, F. Freudenberg, R. Hopler, R. Dimitrov,O.Ambacher, M. Stutzmann, J. Appl. Phys. 82 (10), 5090 (1997)

22. V. E. Bougrov and A. S. Zubrilov, J. Appl. Phys. 81,2952 (1997)

2. MOCVD growth of III-nitrides

2.1. Introduction

Metalorganic chemical vapour deposition (MOCVD), also referred to as metalorganic vapour phase epitaxy (MOVPE), is used in both the research and manufacturing areas of the semiconductor industry. MOCVD has become a very popular technique for growing thin, high purity epitaxial films with applications in electronics and optics. The ability of the process to produce complex multi-layered structures has stimulated the usage of MOCVD for the growth of modern semiconductor devices such as light emitting diodes, lasers, photodiodes, solar cells, heterojunction bipolar transistors and field effect transistors.

MOCVD is distinguished from other vapour phase epitaxy (VPE) techniques by the chemical nature of the precursor gases. As the name implies, metalorganic compounds of group II or III elements are employed. They are reacted with group V or VI hydrides (or other compounds), and during pyrolysis the semiconductor compound forms. The great advantage of using metalorganic compounds is that they are volatile at moderately low temperatures; therefore, they can be easily transported to the reactor by the carrier gas flow.

The development of the MOCVD technique started in late 1960s with the pioneering work of Manasevit *et al* [1]. Nowadays, MOCVD is the dominant technique for the production of compound semiconductors. In case of group III-nitride materials, MOCVD is the only technique which has gained commercial success.

2.2. Overview of the MOCVD process

Although the MOCVD growth of III-nitrides is a complex process, the underlying idea is quite simple. The film is deposited through a chemical reaction occurring between

metalorganic precursors and nitrogen compounds. The growth process entails the transport of precursors in a carrier gas flow towards the heated substrate on which they pyrolyse and react with each other to produce an epitaxial film.

2.2.1. Source molecules

Usually, the choice of metalorganic precursors is limited to methyl or ethyl compounds of Al, Ga, and In. Ammonia (NH_3) is typically used as a nitrogen precursor. However, the use of alternative nitrogen precursors like hydrazine (N_2H_4), tetra-butylamine (t-$BuNH_2$), isopropylamine (i-$PrNH_2$), trimethylsilylazide (Me_3SiN_3)[a] has been reported [2].

Table 3. Properties of common metalorganic precursors used for the growth of III-nitrides.

Abbreviation	TMGa	TEGa	TMAl	TEAl	TMIn	TEIn
Chemical formula	$Ga(CH_3)_3$	$Ga(C_2H_5)_3$	$Al(CH_3)_3$	$Al(C_2H_5)_3$	$In(CH_3)_3$	$Al(C_2H_5)_3$
Formula weight	114.82	156.91	72.09	114.17	159.93	202.01
Melting point, °C	-15.8	-82.3	15.4	-52.5	88.4	-32
Boiling point, °C	55.7	143	127	194	133.8	184
Density, g/cm^3	1.151	1.06	0.752	0.835	1.3	1.260
V.P. @20°C, mm Hg	182	5	8.7	0.02	1.7	

These compounds have lower thermal stability compared to ammonia, therefore allowing the use of lower substrate temperatures and reduced V/III ratios. We shall also mention so-called single source precursors, which already contain nitrogen and group III elements. These include $[Al(NR_2)_3]_2$, $[HAl(NR_2)_2]_2$, $(Me_2AlNH_2)_3$, $(Et_2AlN_3)_3$, and $(Me_2AlNH_2)_3$. The so-called azide precursors, $[R_2Ga(\mu^2\text{-}N_3)]$, $[(R_2N)_2Ga(\eta^1\text{-}N_3)]$ and

[a] Hereafter Me, Et, and Bu denote methyl (CH_3), ethyl (C_2H_5) and butyl (C_3H_9) radicals, respectively. R denotes either methyl or ethyl radical.

$(N_3)_2Ga[(CH_2)_3NMe_2]$, also have gained some attention because they are less toxic and pyrophoric than conventional precursors.Although many chemical compounds can be considered as precursors for nitride epitaxy, methyl and ethyl metalorganic compounds and ammonia remain to be the industry standard for MOCVD growth of III-Nitrides. They are produced commercially in large quantities and purities required in semiconductor technology. The physical properties of conventional metalorganic precursors are listed in the Table 3.

The methyl sources are more often used due to their higher vapour pressure and greater thermal stability. The ethyl sources have lower vapour pressure, which may be an advantage for the growth of thin layers, quantum wells and superlattices. Another important characteristic of ethyl sources is that they pyrolyse through a β-hydride elimination mechanism without producing highly reactive CH_3 radicals which are believed to be the main source of carbon in the epitaxial layers [3]. TEIn is the least stable compound and has been observed to decompose spontaneously during storage. The pyrolysis of TEIn begins at <100°C and is complete at 400°C. Because of reduced bond strength, TEIn has been known to improve the efficiency of indium incorporation relative to TMIn. The use of TEIn is generally limited due to its propensity to participate in parasitic gas phase reactions resulting in indium droplets. This adversely affects the growth rate. The most important advantage of TEIn precursor for III-nitride epitaxy is low melting point. In contrast to TMIn which is solid at room temperature, TEIn is liquid. The use of solid TMIn precursor can limit the transport rate. Also, the surface area of TMIn crystals can change with time, due to recrystallisation by vapour transport, resulting in an effective vapour pressure that decreases with time during storage and use. Recently, Epichem has developed an efficient method to deliver TMIn via a novel precursor system. In this system, solid TMIn is suspended in an extremely low VP adduct solution. The evaporated TMIn is continuously replenished by dissolution during usage.

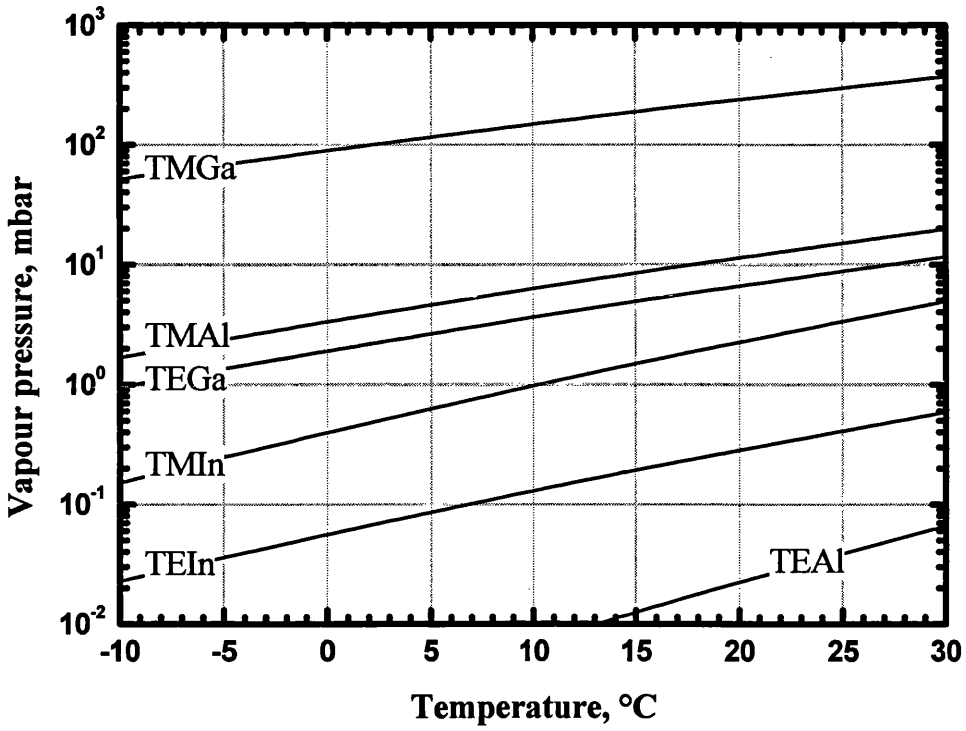

Figure 2.1. Temperature dependence of vapour pressure for common group III metalorganic precursors

2.2.2. Dopant precursors

The most important dopant impurities for III-nitrides are magnesium (Mg), which acts as an acceptor producing p-type material, and silicon (Si), which is a shallow donor producing n-type material. Doping by zinc (Zn) is also used in III-nitride technology to produce semi-insulating material, or to create recombination centres.

The most commonly used magnesium precursor is bis(cyclopentadienyl)magnesium $Mg(C_5H_5)_2$ (Cp_2Mg). It has been demonstrated to be useful as as a p-type dopant of III-V alloys. In traditional compound semiconductors like GaAs and InP p-type doping with Cp2Mg is a well established process. Now, its use as a dopant in nitride based systems is also included in the standard process for blue ultra-high brightness LEDs. A potential problem with Cp_2Mg is that it is a solid at room temperature. The efficiency of a solid metalorganic source is less stable compared to that of a liquid source and can degrade with time.

Alternatively, bis(methylcyclopentadienyl)magnesium $Mg(C_6H_7)_2$ ($(MeCp)_2Mg$) can be used as magnesium precursor. It has a lower melting point (29°C), therefore can be used as a liquid source avoiding problems peculiar to sublimation sources. However, p-type doping of III-V semiconductors using $(MeCp_2)Mg$ is a less well established process. Also, $(MeCp)_2Mg$ is reported to be more reactive than Cp_2Mg and more susceptible to parasitic reactions which reduce doping efficiency. Recently, Epichem developed an efficient magnesium precursor system, which combines the advantages of well-established Cp_2Mg doping process with the reliability of liquid precursor. In this system, solid Cp_2Mg is suspended in an extremely low vapour pressure hydrocarbon liquid. The solvent forms a liquid layer over the solid Cp_2Mg and it is assumed that the Cp_2Mg is vaporized directly from the solution.

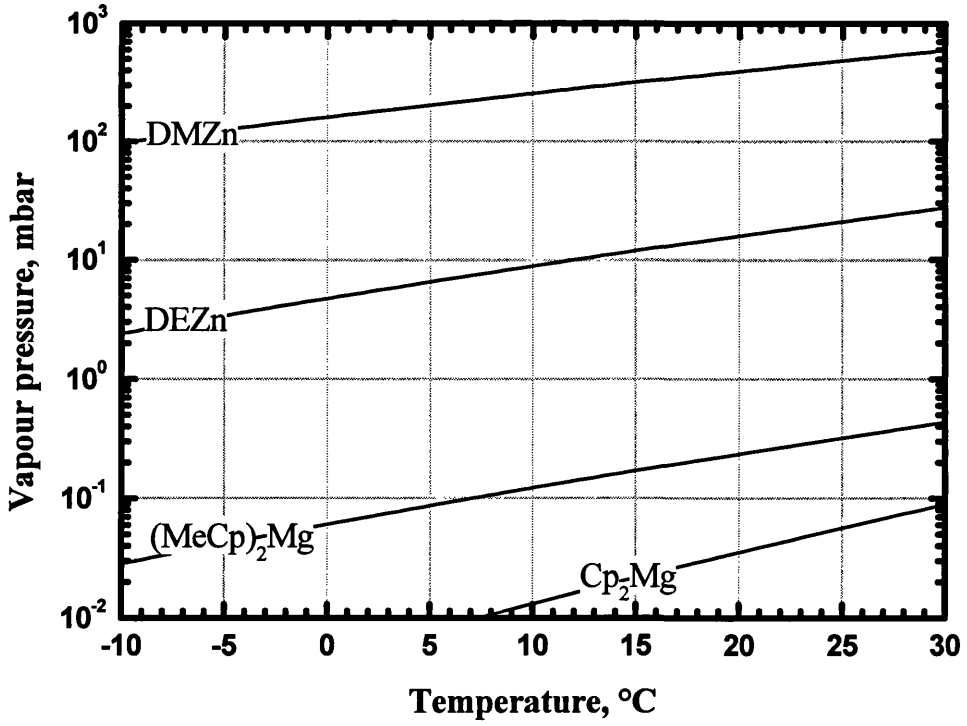

Figure 2.2 Temperature dependence of vapour pressure for dopant precursors

Ethyl and methyl zinc metalorganic compounds have been demonstrated to be useful as a p-type dopant of III-V alloys. Dimethylzinc $Zn(CH_3)_2$ (DMZn) is a less common doping source because of its high vapour pressure. Cooling of the source is required to

access the useful range of concentrations. Diethylzinc $Zn(C_2H_5)_2$ (DEZn) has lower vapour pressure and, therefore, is more compatible with the doping process.

Silicon can be used either in hydride form (monosilane SiH_4, disilane Si_2H_6) or silicon organic compound form (tetramethylsilane $Si(CH_3)_4$, tetraethylsilane $Si(C_2H_5)_4$). Gaseous monosilane and disilane are more widely used for n-type doping because they do not require temperature-stabilised bubbler. Typically hydride dopants are diluted with hydrogen at 200 ppm. Successful growth of n-type GaN using tetraethylsilane precursor has been also reported by a number of authors.

2.2.3. Chemistry of the MOCVD process

The basic MOCVD reaction describing the GaN deposition process can be described by the following reaction:

$$Ga(CH_3)_3 + NH_3 \rightarrow GaN + 3CH_4 \qquad (2.1)$$

However this equation simply balances the input and output reagents and does not reflect actual reaction path and intermediate compounds involved. The more likely mechanism involves pyrolysis of metalorganic precursors and ammonia leading to the formation of highly reactive radicals, which in turn produce III-nitride epitaxial film. The high thermal stability of NH_3 is one reason for the use of high substrate temperatures, typically more than 550°C for InN and above 900°C for GaN and AlN. For this reason very high V/III ratios are typically used in nitride epitaxy. Even at high temperatures, the decomposition of ammonia is quite slow in the absence of suitable catalyst. Ammonia is thought to decompose heterogeneously on the GaN surface or reactor walls to yield atomic nitrogen or a nitrogen containing radical at high growth temperatures. The pyrolysis of ammonia can be described by the following reaction

$$NH_3 \rightarrow NH_{3-x} + xH \qquad (2.2)$$

Metalorganic compounds are much less stable compared to ammonia and decompose at lower temperatures (see Figure 2.3). Therefore, the decomposition rate of metalorganic

precursors is not the limiting factor in the nitride epitaxy. Metalorganic precursors can pyrolyse through different reactions mechanisms, depending on the type of metalorganic compound and gas ambient. In nitrogen or inert gas atmosphere, methyl compounds decompose via homolytic fission.

$$\begin{aligned} Ga(CH_3)_3 &\rightarrow Ga(CH_3)_2 + CH_3 \\ Ga(CH_3)_2 &\rightarrow Ga(CH_3) + CH_3 \\ Ga(CH_3) &\rightarrow Ga + CH_3 \end{aligned} \qquad (2.3)$$

In the presence of hydrogen the decomposition process follows the hydrolysis mechanism

$$Ga(CH_3)_3 + 1\frac{1}{2}H_2 \rightarrow Ga + CH_4 \qquad (2.4)$$

In contrast, ethyl metalorganic compounds decompose via β-elimination process.

$$(CH_2{-}CH_3){-}Ga{-}R \rightarrow CH_2{=}CH_2 + H{-}Ga{-}R \qquad (2.5)$$

Since no radicals or other external reaction partners are needed, the β-elimination is not sensitive to the carrier gas and occurs both in N_2 and H_2. The important characteristic of β-elimination mechanism is that it does not involve the formation of highly reactive methyl radicals, which are assumed to be the main source of carbon contamination in III-V epitaxial films.

Figure 2.3 presents experimental data on percent of pyrolysis versus temperature for various metalorganic compounds. As one can see, ethyl compounds decompose at lower temperature than methyl compounds. This can be attributed to weaker bond strength and lower activation energy for β-elimination reaction. The influence of carrier gas is much stronger for methyl compounds, as addition of hydrogen gas changes the decomposition mechanism and reduces the decomposition temperature. In the case of ethyl compounds the decomposition mechanism remains the same for hydrogen and inert gas ambients; therefore, the dependence of decomposition temperature on carrier gas composition is weaker.

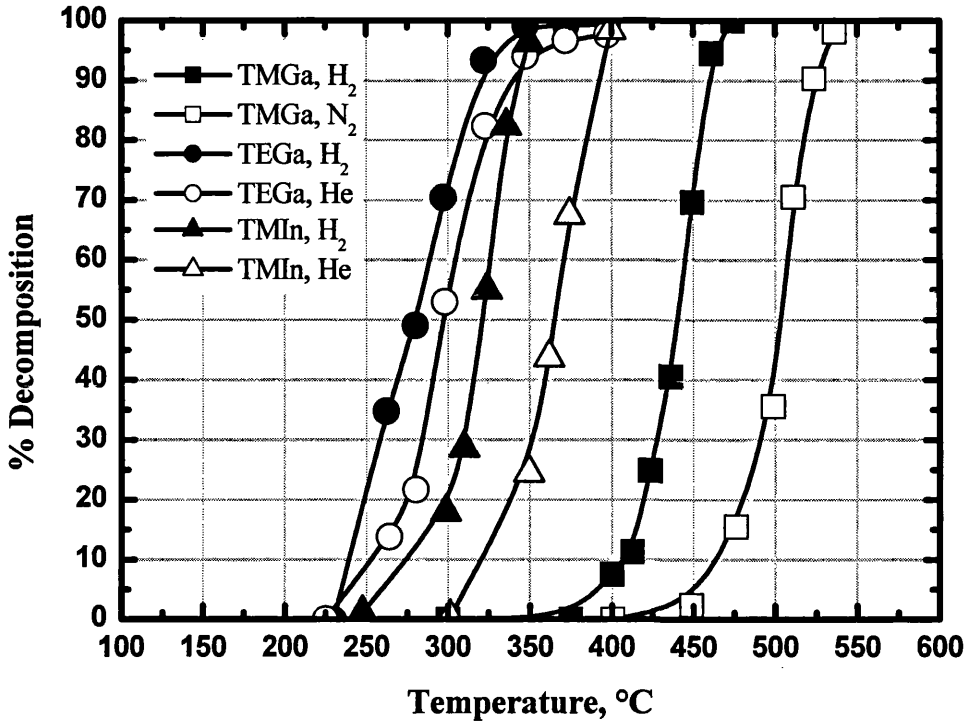

Figure 2.3. Percent pyrolysis versus temperature for TMGa, TEGa, TMIn in several ambients (from Stringfellow [3])

One possible growth mechanism of GaN involves the heterogeneous reaction at the solid gas interface of $Ga(CH_3)_x$ or GaH_x radicals with NH_x radicals. Alternatively, metalorganic compounds can react with ammonia in the gas phase to form the adducts of the kind $[R_3MNH_3]$ and $[R_3MNH_2R']$. These adducts eliminate radicals on heating to form $[R_2MNH_2]_n$, $[R_2MNHR']_n$ and $M(NH)_2M$ compounds, where n=2 or 3. These species finally eliminate H_2 and CH_4 to form III-nitride film at the substrate surface [2]. Very high V/III ratios typically used in the epitaxy of III-nitrides favour the predeposition reaction of metalorganic precursors with ammonia. Very often, the pre-reaction of precursors in the gas phase reduces the growth rate and the efficiency of the reaction due to low adduct volatility. Formation of gas-phase adducts is especially important for the growth of AlN and AlGaN. On the contrary, the GaN deposition process is less sensitive to adduct formation. R_3Ga compounds are weaker electron acceptors than the corresponding R_3Al

compounds, and thus the scarcity of any such adducts with NH_3, could be expected due to redissociation in the hot zone of the reactor [2].

2.3. MOCVD system and reactor design issues

Now, we would like to review the technical aspects of the MOCVD growth. As we mentioned before, the MOCVD epitaxy is a complex process governed by a large number of factors, including mass transfer, gas flow dynamics, homo- and heterogeneous chemical reactions etc. The precise control of all these factors is achieved by careful engineering of the growth apparatus. Successful MOCVD system design must meet the following criteria:

- Uniformity of layer thickness
- Uniformity of alloy composition
- Abruptness of interfaces
- Ability to create desired doping profiles
- Reproducibility from run to run
- Wide process window

For mass production MOCVD systems, factors of high throughoutput, maintenance and operation cost, source usage, etc are also very important.

A typical MOCVD system comprises a reactor chamber, a gas distribution system, a temperature controller, an exhaust system and control electronics. A schematic block diagram of a MOCVD system is presented in Figure 2.4. In this chapter, we will discuss the design issues of the two most critical parts of the MOCVD setup: the gas distribution system and the reactor.

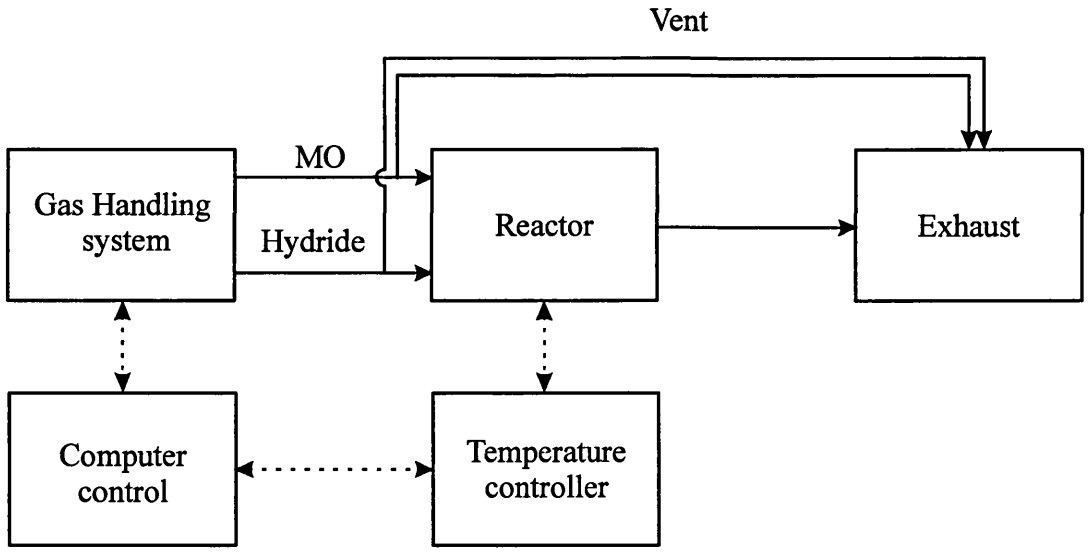

Figure 2.4 Schematic block diagram of MOCVD system

2.3.1. Gas distribution system

The purpose of the gas handling system is to deliver metered amounts of reagents into the reactor and to provide fast switching between reagents. Nowadays this is a mature technology and most of the manufactures use standard engineering solutions. Nevertheless, the gas distribution system is one of key elements of a MOCVD setup therefore worth giving it due attention.

Metalorganic compounds are liquids or volatile solids under normal conditions. The most convenient containers for metalorganic compounds are bubblers, made from stainless steel. For a constant vapour pressure, the bubblers are immersed in temperature-controlled baths. The total pressure in the bubbler is stabilised by the pressure controller. Metered amounts of a carrier gas are passed through the bubbler. There carrier gas is saturated with metalorganic vapour. The amount of metalorganic compound transported to the reactor is controlled using the bubbler temperature, the mass flow of the carrier gas, which goes through the bubbler, and the bubbler pressure.

The standard MO source (see Figure 2.5) incorporates a source mass flow controller (MFC), controlling the quantity of carrier gas going through the bubbler. The pressure in the bubbler is set using the pressure controller. Optionally, the gas after the bubbler is

mixed with pusher flow. This additional flow serves two purposes. First, it accelerates the MO flow and reduces the switching time between different metalorganic sources. Secondly, it facilitates the optimum flow adaptation through the pressure controller.

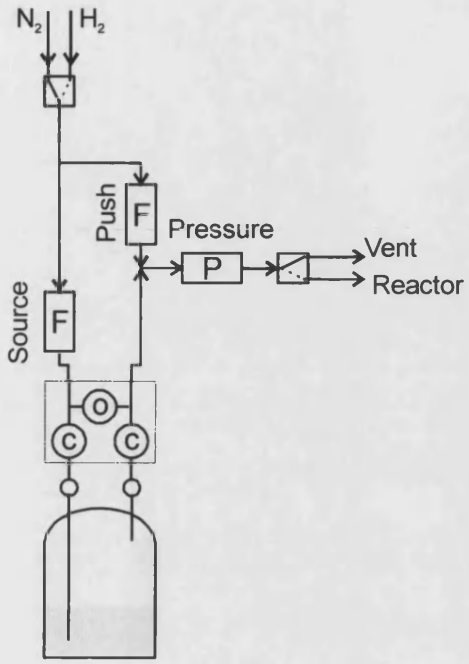

Standard MO source

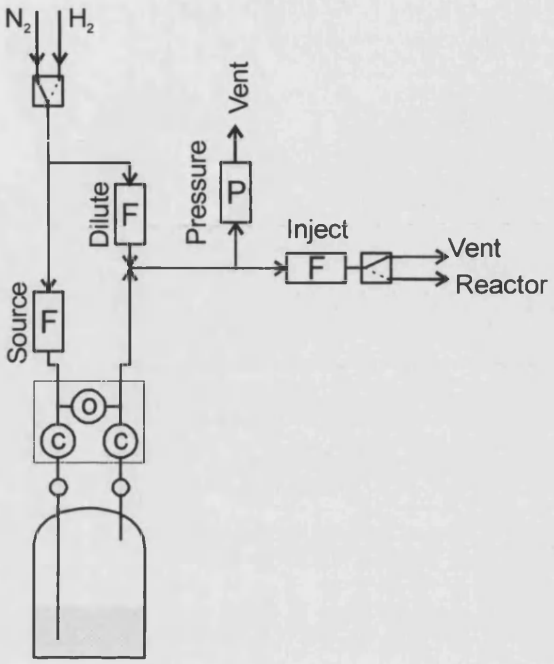

MO source with dilution

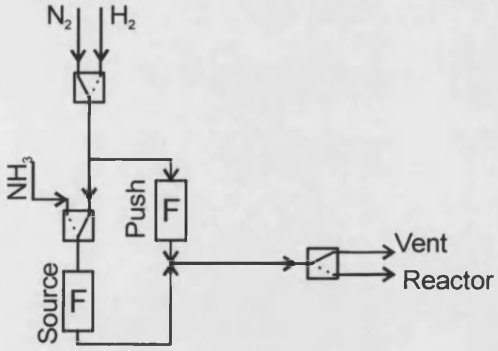

Standard hydride source

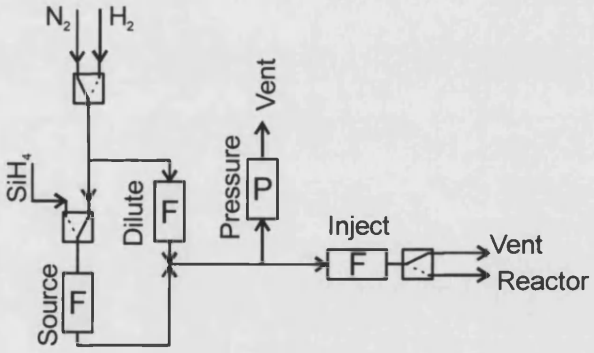

Hydride source with dilution

Figure 2.5 Typical design of metalorganic and hydride sources

For handling of small amounts of metalorganic compounds, e.g. for doping or for the growth of quantum size structures, a metalorganic source with dilution is used. In the dilution source the flow after the bubbler is mixed with dilution flow. A small percentage

of the gas mixture is passed into the reactor through the injection mass flow controller, and the excess gas mixture is conducted to the vent line through the pressure controller.

Hydride precursors are stored in special gas cabinets outside the system, filled in cylinders under high pressure, diluted or highly concentrated. They are delivered to the system in the gaseous form; therefore, hydride sources are simpler than MO sources, as they do not comprise bubblers and temperature-stabilised baths. Standard hydride source includes one source MFC and optional push MFC. Hydride sources with dilution are typically used for dopant precursors like silane. The principle of operation is similar to that used in MO sources with dilution. The source flow is mixed with dilute flow and fed to the reactor via injection MFC. The pressure controller sets the operating pressure of the injection MFC and leads the excess gas to the vent line.

All sources are connected to the reactor via special source-switching manifold. Its construction is very important, as the physical switch of precursor chemicals is the first factor in controlling the interface abruptness. The manifold should provide fast switching of the reagents without producing pressure fluctuations. Normally, a gas handling system has two separate manifold lines, one for metalorganics, and another one for hydrides. Some systems have additional injection lines for dopant sources. Typically, a run-vent manifold is used for process gas switching. This configuration includes the run line, which leads to the reactor, and the vent line, which leads directly to the exhaust. The sources can be switched between the reactor and the vent line. The carrier gas continuously flows through the run and vent lines for purging and for adjusting the flow speed through the reactor. Run-vent manifold design allows purging and stabilising the source before connecting it to the reactor. Some MOCVD systems have a differential pressure controlled run-vent manifold. This ensures equal pressure in run and vent lines and prevents fluctuations of pressure and flows during switches. When large gas volumes are being switched, an additional flow of carrier gas is switched in opposition, to replace the switched gas volume

during switches and minimise the pressure fluctuation in the injector block. However, the physical switch of different precursors in gas phases is much more complicated than a simple volume replacement, because the density and the viscosity of each gas is different.

2.3.2. Reactor

After the run-vent manifold the reagents are delivered to the reactor. The geometry of the reactor chamber is very important as it must provide a stable gas phase at all growth temperatures, pressures and flows that are used in the process. In the case of the MOCVD growth of III-nitrides, it is important to overcome problems presented by high growth temperature and adduct formation in the gas phase. As we mentioned above, ammonia tends to pre-react with the group III metalorganic compounds to form non-volatile adducts. When mixed at room temperature, the adduct formation between TMGa or TMAl and ammonia is completed in less than 0.2 s. Such parasitic reactions in the gas phase could cause adverse effects like defect formation on the substrate surface and growth suffocation. Therefore, to avoid the unwanted pre-reaction the reactants must be allowed to interact with one another only in the vicinity of the substrate.

Several types of reactor geometries have been developed for the MOCVD growth of III-nitride based materials and devices. Both atmospheric pressure and low-pressure systems are being produced by the major MOCVD equipment manufacturer as Aixtron GmbH, Emcore Corp., Nippon Sanso, and Thomas Swan, Ltd. (now an Aixtron subsidiary). In addition, a number of GaN-based device manufacturers like Nichia Chemicals and Toyoda Gosei use in-house built MOCVD reactors. It is not our intent to judge which reactor design is superior as all systems are producing high quality GaN and device structures. The benefits of each approach will be specific to the ultimate device and materials being grown.

Atmospheric pressure reactors offer the advantage of higher nitrogen partial pressures. Low-pressure reactors have better control of convectional flows and pre-

reactions in the gas phase. All MOCVD reactors incorporate laminar flow and feature separate inlets for group III precursors and ammonia. A rotating susceptor is widely used to enhance the uniformity of the deposited films.

A classical horizontal configuration of the reactor is widely used for MOCVD growth of III-nitrides, particularly for small, research-scale reactors (e.g Aixtron 200 series). In the horizontal reactor, the substrate wafer sits on a susceptor in a horizontal tube and reactants flow over it, parallel to the wafer surface. The reactor geometry is designed to allow a laminar flow to develop and to avoid turbulence vortexes within the reactor cells of gas. Usually, the susceptor is ether tilted or rotated to compensate the growth nonuniformity caused by the depletion of the reactants as they flow over the wafer. Horizontal flow reactors have relatively simple construction, which can be easily adapted for particular experimental or technological purposes. For example, various *in situ* characterisation techniques like reflectometry, ellipsometry, x-ray analysis, mass-spectroscopy etc can be readily employed in horizontal flow reactors. Disadvantages of this design include: thickness nonuniformity due to the depletion effect and edge effects of the side walls, deposits on the ceiling, which affect uniformity and surface quality, and a tendency to exhibit recirculation cells.

The Aixtron planetary reactor is the further development of the horizontal flow reactor. The underlying concept encompasses radial flow from centre to the outer rim and planetary motion of wafers, i.e. slow double rotation to achieve averaging of deposition thickness and enhance uniformity. Rotation is achieved by gas that is introduced behind each wafer carrier and is constrained by spiral grooves; this causes the carrier to float and rotate. By the correct choice of geometry and carrier gas flow, the depletion across the susceptor can be made approximately linear, so that with the wafer rotation, good thickness uniformities of 1-2% can be achieved.

The two-flow MOCVD reactor developed by Nakamura [4] can be also regarded as a horizontal flow reactor, as the source gases (main flow) are introduced parallel to the substrate surface. A second flow (sub flow) containing equal amounts of N_2 and H_2 was introduced perpendicular to the substrate surface to suppress any thermal convection arising from the heated substrate and to bring the reactants toward the substrate surface. The suppression of thermal convection is effective enough to allow atmospheric pressure operation.

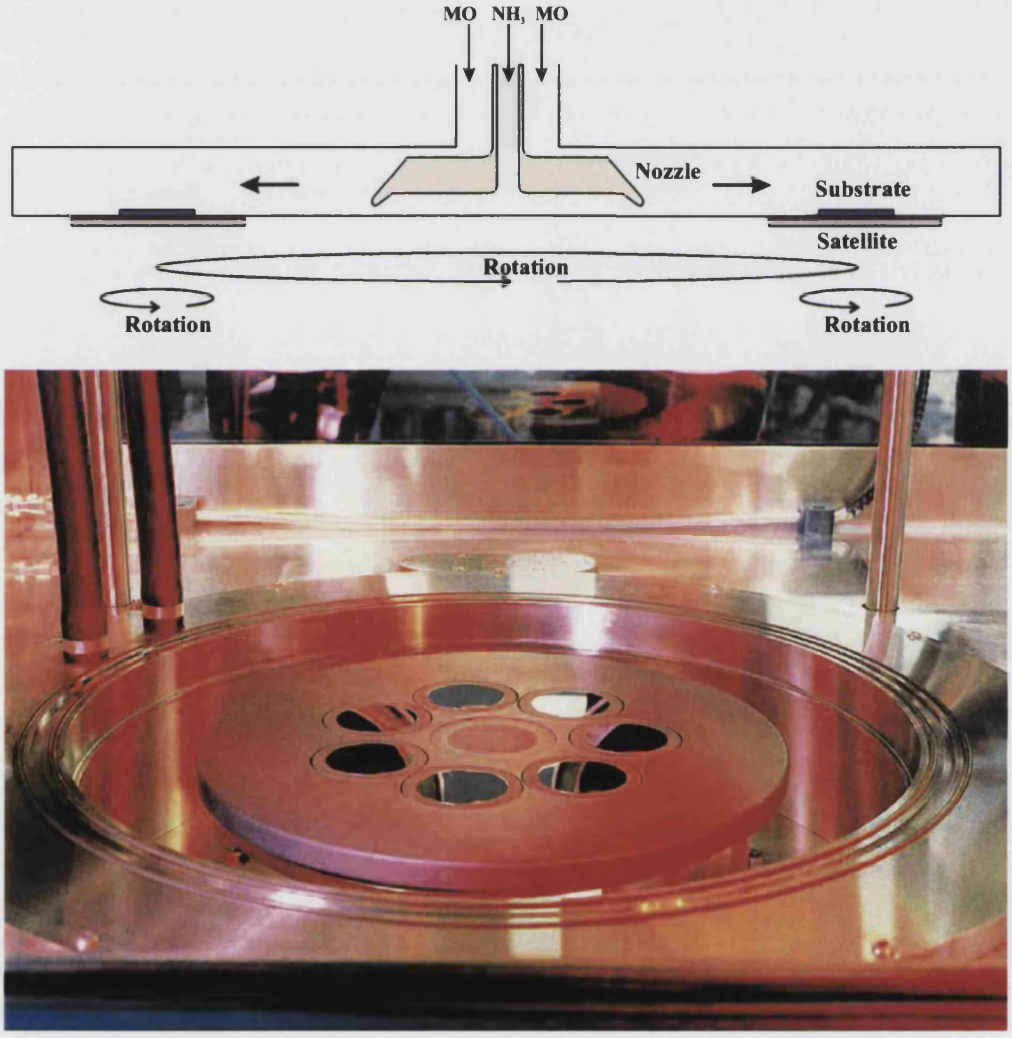

Figure 2.6. Schematic cross-section of the planetary reactor (top). Process chamber of the AIX2000HT for GaN high temperature MOCVD with 7x2" wafer capacity (bottom).

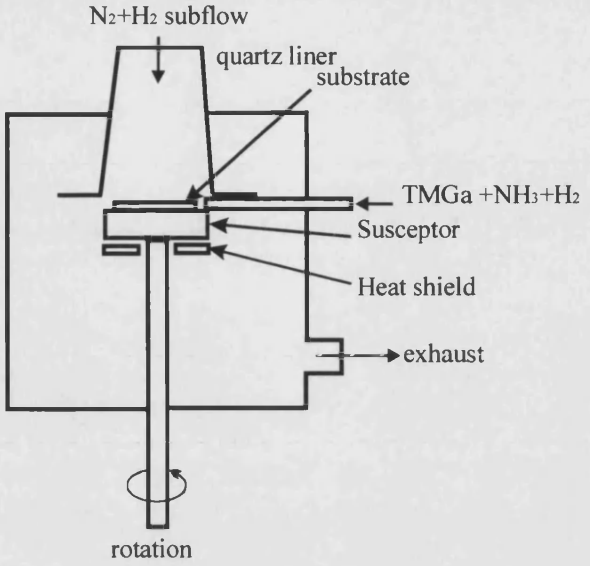

Figure 2.7 Schematic drawing of the two-flow MOCVD reactor

A similar reactor concept was suggested by Wang *et al* [5] who reported on a three-flow reactor. Two parallel carrier gas-flow for Group-III sources and NH_3 separated by a quartz plate which are also parallel to the substrate are used. The N_2, which is used as a sub-flow, flows through a quartz filter perpendicular to the substrate where it meets the two parallel group III and group V source flows. This new flow arrangement enhances the mixture of group III-V sources at the contacting substrate due to the perpendicular direction of the N_2 sub-flow.

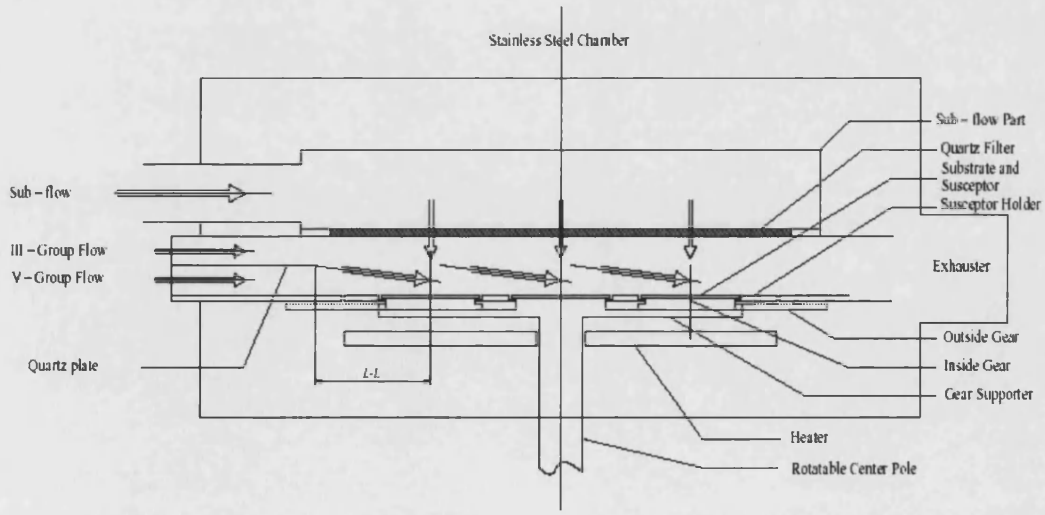

Figure 2.8 Schematic drawing of the three-flow reactor for GaN-based MOCVD.

Two other players on the MOCVD reactor market, Emcore and Thomas Swan (now subsidiary of Aixtron) produce vertical flow reactors. As a rule, vertical reactors are more subjected to formation of recirculation cells and convectional flows because they typically have larger free height above the substrate than horizontal reactors. In Emcore's design, thermal convection is suppressed by a high speed rotating susceptor. The gas layer adjacent to the rotating susceptor is forced out by centrifugal force. This flow is balanced by the axial flow towards the susceptor. In other words, the rotating susceptor produces a pumping action, which effectively suppresses buoyancy forces. In addition, high-speed rotation creates a thin, uniform boundary layer, enhancing the mass-transfer towards the substrate. Thin and adjustable boundary layer facilitates fast change of reaction components and, consequently, the growth of heterostructures with abrupt interfaces. The reagents are delivered into the reactor through the Emcore proprietary Flow Flange® with radial reactant distribution over the susceptor area to achieve both thickness uniformity and high source utilisation efficiency.

A different approach for suppression of thermal convection is used in the Thomas Swan vertical reactor. In this design, the group III and group V elements are injected separately into the reactor through a water-cooled "showerhead" to avoid undesired upstream pre-reactions. The showerhead surface is very close to the to the substrate (less than 2 cm) to avoid the formation of recirculation cells. The very fine mesh (~100 per sq. inch) of injection tubes ensures a very good uniformly gas distribution.

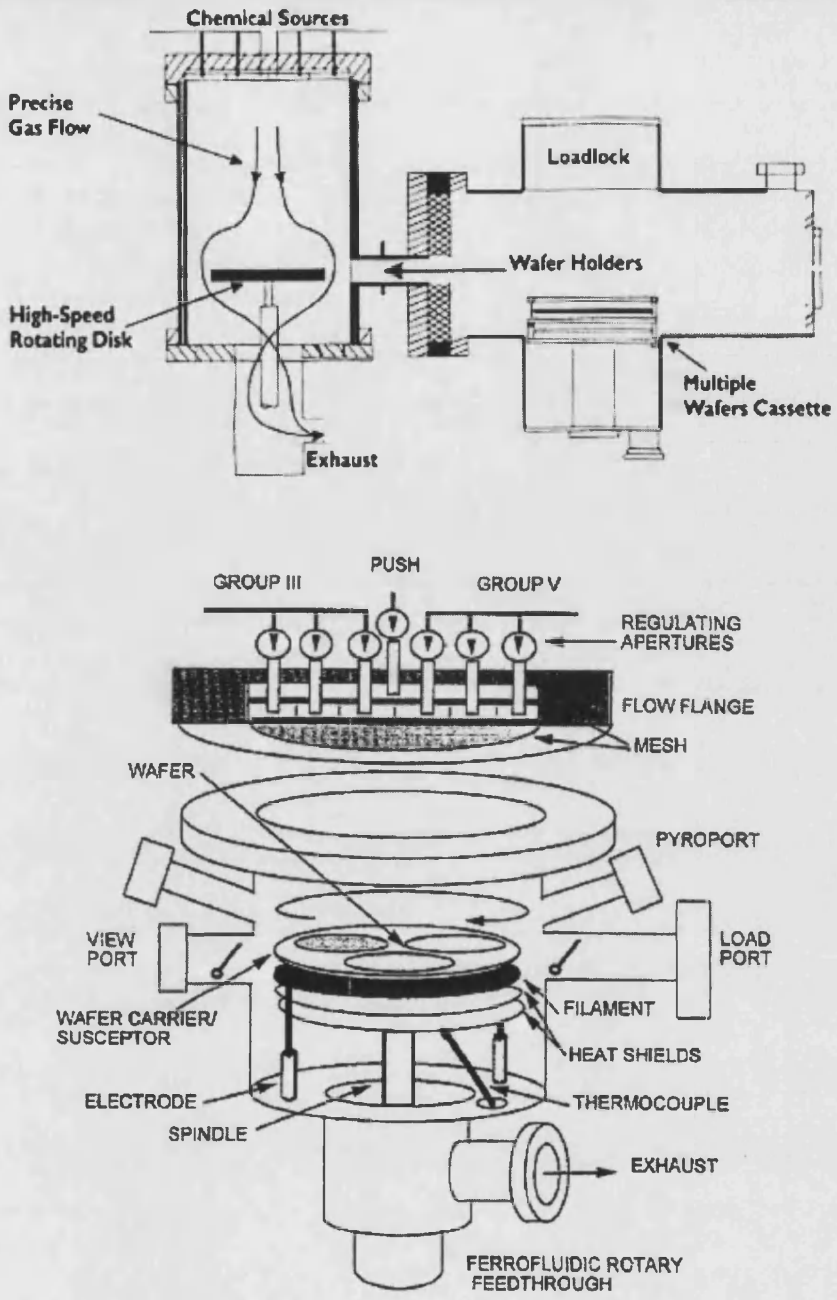

Figure 2.9 Emcore TurboDisc reactor

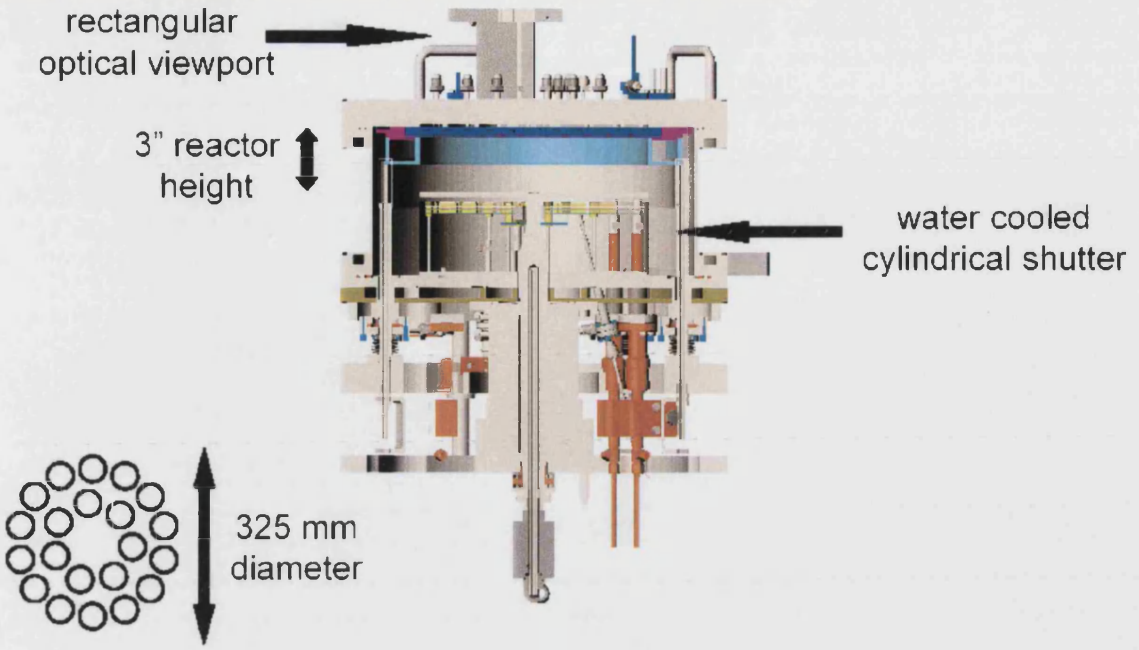

Figure 2.10 Cross-section of the Emcore's large area GaN reactor

A graphite resistance heater is used to raise the temperature of a graphite susceptor up to 1200°C. The temperature is measured with an optical pyrometer looking directly at the substrate or the susceptor. The substrate is placed on a rotating susceptor to achieve improved uniformity and lateral flow regime across the substrate surface. The rotation speed of the susceptor can be varied between 0 and 1500 rpm (typically 800 rpm). The reactor has a wide process window; the deposition can be performed both under atmospheric and low pressure.

It should be noted, that some convergence tendency between Thomas Swan's and Emcore's reactor conceptions can be observed. In recent models of Emcore systems (short jar design) the free height of the reactor was reduced to 3 inches, while Thomas Swan introduced a fast rotation option into their reactors.

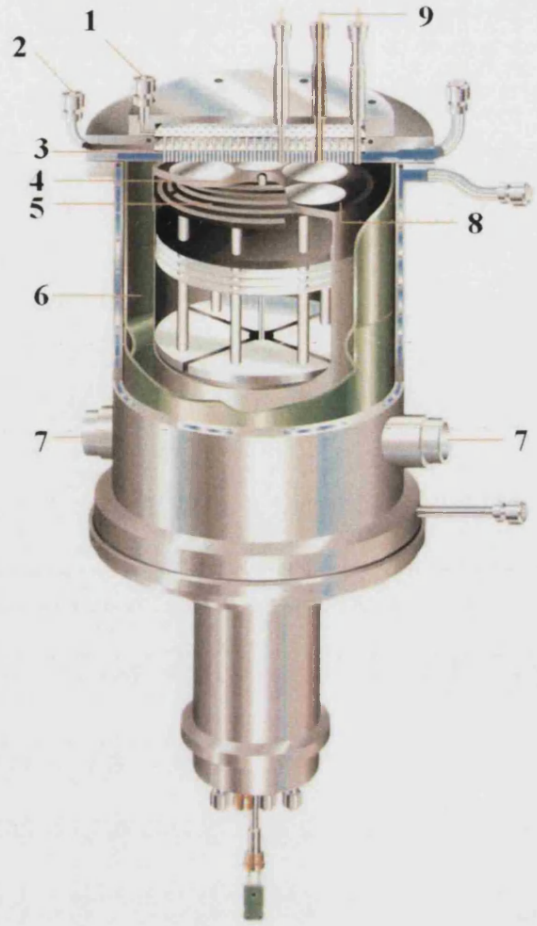

Figure 2.11 Thomas Swan close coupled showerhead reactor. 1 – precursors top plenum; 2 – precursors bottom plenum; 3 – water cooled injector surface; 4 – thermocouple; 5 – three zone heater; 6 – quartz liner; 7 – exhaust; 8 – SiC coated graphite susceptor; 9 – optical probe.

We now discuss in more detail the Aixtron 200/4/HT/RF MOCVD system as it was used in the present work. It is a single 2" wafer horizontal flow research type reactor. The reactor includes a water-cooled stainless steel chamber with internal quartz liner forming a reaction zone. The liner has a rectangular cross-section 130×45 mm^2. Substrates are placed on the rotating SiC or TaC covered graphite susceptor heated by RF coil. The graphite susceptor is rotated by the Gas Foil Rotation® principle. The cross-sectional drawing of the reactor is presented in Figure 2.13. Metalorganic and hydride precursors are injected to the reactor via an injection head. The two flows are prevented from mixing by a separating plate made of quartz. Mixing of the reagents occurs a few centimetres upstream of the wafer.

The setup has a computer controlled gas distribution system with six metalorganic lines (TMGa, TEGa, TMAl, TMIn, TEZn and Cp_2Mg), two ammonia lines, two SiH_4 lines, a propane line and one HCl line for *in situ* etching. All the sources are temperature- and pressure-controlled to ensure constant vapour delivery and all gas flows are controlled with metal-sealed mass-flow and pressure controllers. Hydrogen or nitrogen can be used as a carrier gas.

The system is equipped with *in situ* reflectometry for real time measurements of epilayer thickness, growth rate and surface roughness.

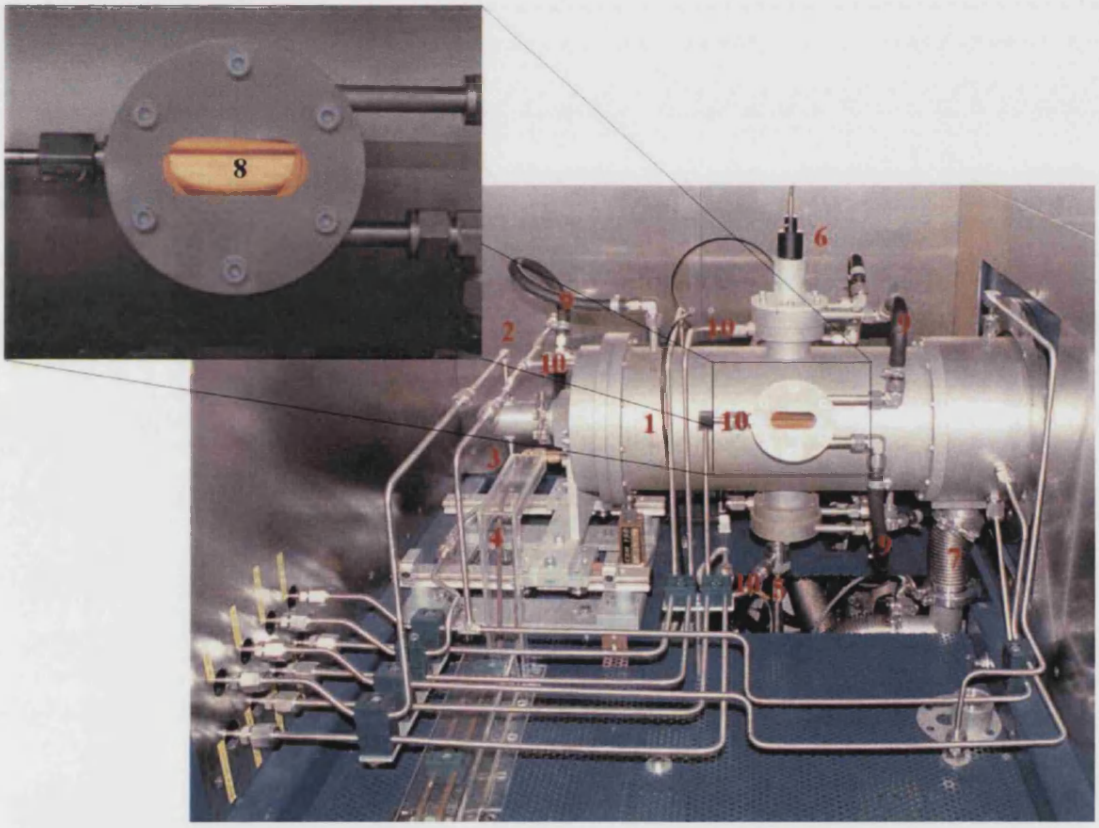

Figure 2.12 Photograph of Aixtron 200/4/HT/RF reactor. 1 – reactor chamber; 2 – MO inlet; 3 – hydride inlet; 4 – RF supply line; 5 – pyrometer; 6 – reflectometer; 7 – exhaust; 8 – viewport; 9 – cooling water supply; 10 – window purge.

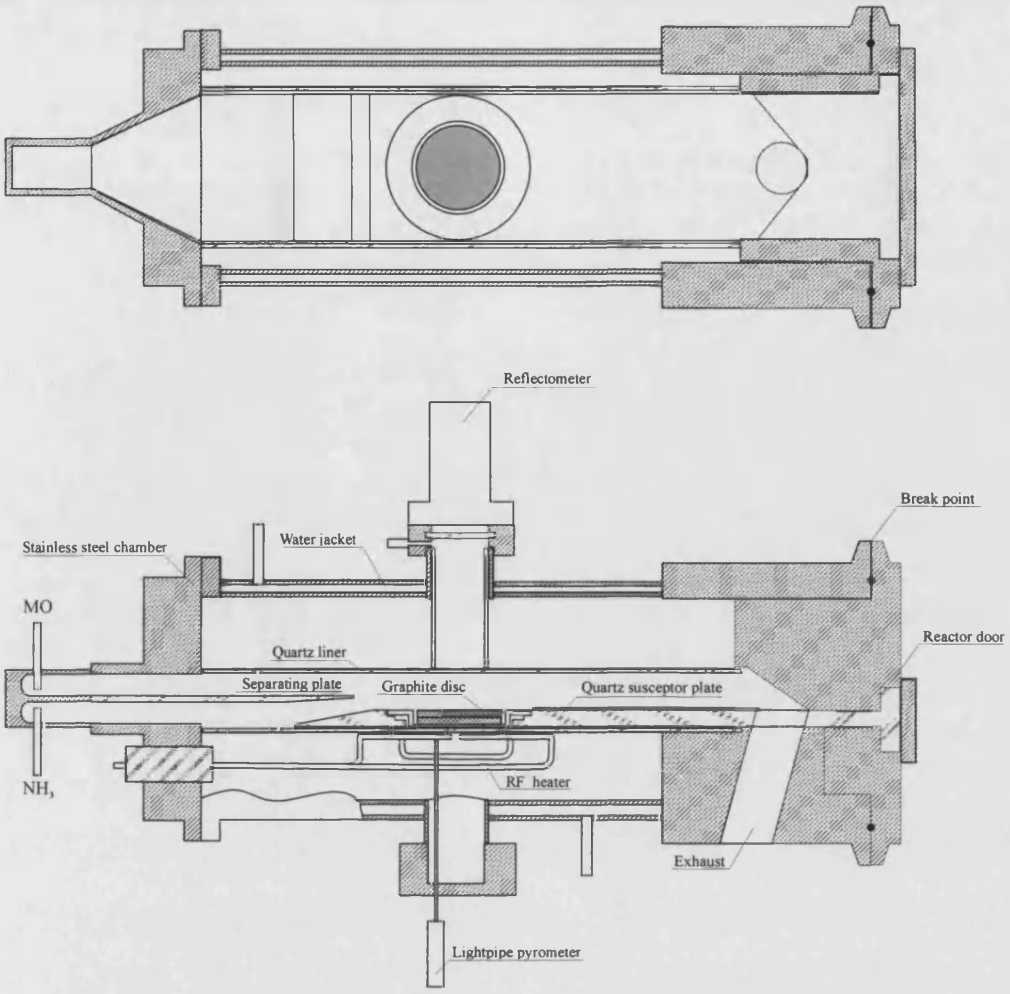

Figure 2.13 Aixtron AIX 200-4/HT/RF reactor

2.4. References

1. H.M. Manasevit, Appl. Phys. Lett. 116 1725(1969)
2. O. Ambacher, J. Phys. D: Appl. Phys. 31 2653 (1998)
3. G.B. Stringfellow, "Organometallic Vapor-Phase Epitaxy: Theory and Practice", Academic Press, London, 1989.
4. Shuji Nakamura, Yasuhiro Harada, Masayuki Seno , Appl. Phys. Lett. 58, 2021-2023 (1991).
5. H.X. Wang, T. Wang ,S. Mahanty, F. Komatsu, T. Inaoka , K. Nishino, S. Sakai Journal of Crystal Growth 218 148 (2000)

3. Nucleation layer

3.1. Introduction

A *c*-plane sapphire is the most common substrate for the GaN growth. The surface energy of the sapphire surface is too high resulting in a low density of nucleation centres. Therefore, the growth by MOCVD of GaN directly on sapphire results in nucleation only on isolated islands and leads to highly defective films with rough morphology. In order to overcome these problems, the two-step growth method was proposed by Amano and co-workers [1]. In this method a high temperature (HT) growth at T>1000°C of GaN was preceded by the deposition of a low temperature (LT) at T≈500–600°C nucleation layer of GaN or AlN. The LT buffer reportedly increased the density of nucleation sites and promoted the lateral growth of GaN. The HT growth first leads to the formation of islands, the coalescence of these islands, and, finally, a quasi-two-dimensional growth. The introduction of a low-temperature nucleation layer has considerably improved the morphology and the crystalline quality of subsequently grown high-temperature GaN films.

3.2. Nucleation and growth mechanisms

Typically, the initiation of GaN growth on sapphire involves the following stages:

- High temperature (~1200°C) desorption of sapphire substrate in hydrogen.
- Growth of the low-temperature (500 – 600°C) nucleation layer
- High temperature (>1000°C) anneal of nucleation layer.
- Growth of GaN at high temperature (>1000°C)

The growth mechanisms involved in this process are not yet understood in full detail; however the following model is generally accepted. At low temperature the supersaturation is high and the mobility of adatoms is low giving rise to high nucleation rates and

promoting uniform dispersion of nuclei along the substrate surface. The as-grown nucleation layer is polycrystalline and consists of grains of highly disordered cubic and wurtzite GaN. Afterwards the deposition is stopped, and the nucleation layer is annealed at high temperature for a short time. During this anneal the nucleation layer recrystallises into GaN seeds. The material is transported by surface diffusion and desorption/re-deposition reactions from smaller seeds to larger seeds, which have smaller surface energy. As a result, the seeds smaller than some critical dimension completely disappear while the other seeds are growing both laterally and vertically.

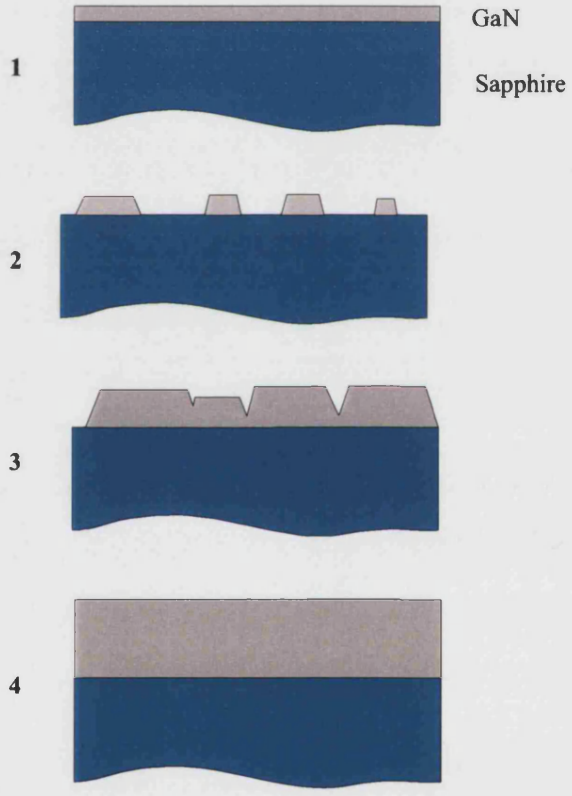

Figure 3.1. Schematic GaN evolution during initial stage of MOCVD growth on sapphire substrate. (1) – deposition of a low-temperature GaN nucleation layer. A uniform distribution of nucleation seeds is achieved during this stage. (2) – high temperature annealing of the nucleation layer. GaN recrystallises and forms isolated islands. (3) – high temperature growth of GaN started. GaN islands grow laterally and vertically. (4) – high temperature growth continued. Coalescence process has finished and a quasi-two-dimensional growth is established.

The microstructure of NL and its transformation during annealing have been studied by a number of authors by using TEM, AFM, elipsometry, RHEED and other methods.

Wickenden *et al* [2] observed that the degree of crystallinity of the LT nucleation layer increases during the temperature ramp and anneal. George *et al* [3] and Wu *et al* [4] examined as-grown and annealed LT nucleation layers by TEM and AFM. Both groups made similar observations that the roughness and average grain size increased after annealing. Wu *et al* [5] and Twigg *et al* [6] have reported that the proper as-grown NL is predominantly cubic in structure and transforms into hexagonal wurtzite phase upon annealing. After annealing the GaN deposition is started again. The growth starts first on these seeds expanding both laterally and vertically and is then continued by their coalescence.

Similar results were published by Munkholm *et al* [7]. They have measured the proportion of the cubic and hexagonal phases throughout the GaN nucleation layers using the grazing incidence x-ray scattering. The as-grown 20nm nucleation layer has the cubic fraction of 0.56. High temperature treatment reduces the cubic fraction to 0.17.

Nakamura *et al* [8,9] reported on the first *in situ* monitoring of the surface roughness and evolution of nucleation layer using an infrared pyrometer. The observed decay and recovery of IR transmission during initial stage of HT growth supports the model of growth evolution discussed above.

In situ real-time reflectivity measurement is a simple, but very useful technique for monitoring of NL properties. It has been successfully used for optimisation of the LT nucleation layer many groups, e.g. by Han *et al* [10] and Koleske *et al* [11]. Figure 3.2 shows the reflectivity recorded during the progress of the process. The reflectivity of a bare sapphire substrate is about 7-8%. During the deposition of the nucleation layer the reflectivity is increasing as a function of layer thickness (1). When the reflectivity reaches ~15%, the deposition of the nucleation layer is stopped and the temperature is ramped to 1140°C. The recrystallisation, inducing a 2D-3D transition, increases the diffuse scattering of the light beam and appears as a continuous decrease of the reflectivity (2). The

reflectivity reaches a minimal value and starts to increase slowly, indicating the completion of the recrystallisation process. At this point TMGa is introduced into the reactor and the growth started again.

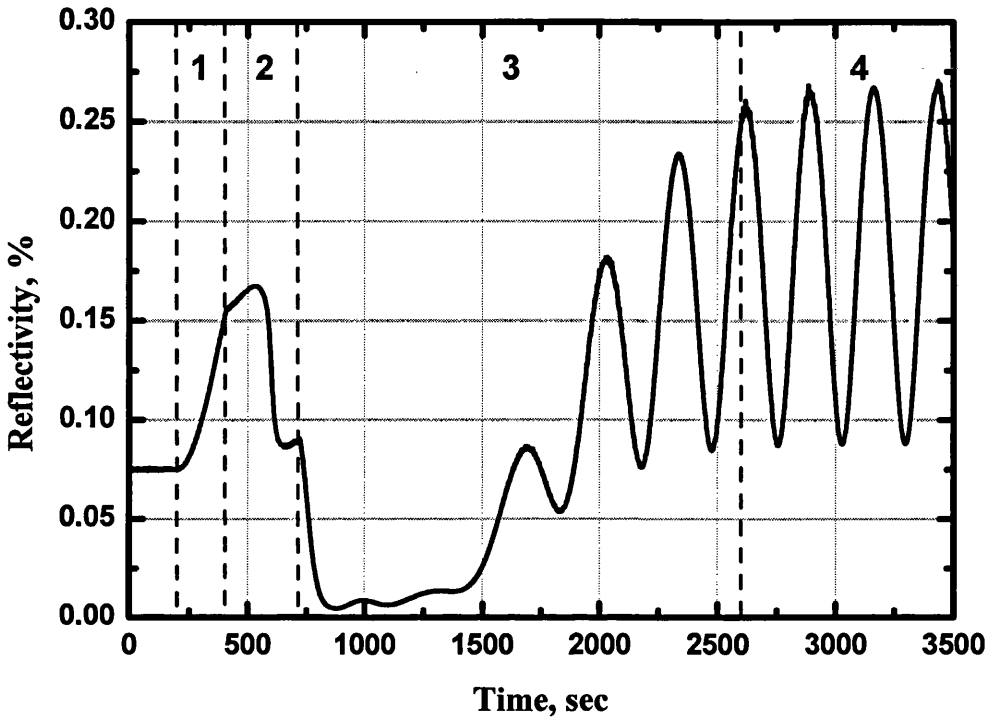

Figure 3.2. Reflectivity recorded during the growth of GaN on sapphire. 1 – nucleation layer growth at 560°C; 2 – anneal nucleation layer at 1140°C; 3 – coalescence; 4 –high temperature GaN buffer.

The nucleation islands continue to expand laterally and vertically; their facets effectively reflect the light sideways causing a profound dip in the reflectivity signal. The subsequent recovery of reflectivity signal reflects the beginning of coalescence process. Interference fringes also appear. The magnitude of interference fringes is increasing (stage 3), as the surface morphology of the growing film improves. At stage 4, the magnitude of oscillations reaches its maximal value indicating that the quasi-two dimensional growth mode is established.

Han *et al* and Koleske *et al* studied the effect of NH_3 partial pressure on morphology evolution of LT nucleation layer. The two reports made similar observations. A higher temperature and a higher NH_3 flow (at a fixed TMGa flow rate) tend to promote lateral growth, thus increasing the coalescence rate and increasing the recovery rate. Also, Han *et al* have demonstrated that H_2 partial pressure strongly affects the coalescence process. Higher H_2 partial pressure slows down the coalescence process and increases the recovery time. Delayed coalescence with slow recovery time leads to the epitaxial layers with narrower XRD rocking curves and higher electron mobility.

Koleske *et al* observed the correlation between the reflectance recovery time and LED output power. By delaying the reflectance recovery time through the use of slow NH_3 flow at the initial stages of HT growth, LEDs with higher output power were fabricated.

Another way to delay the coalescence of GaN islands has been suggested by Haffouz *et al.* [12]. They used a high-temperature SiN treatment before the deposition of a low-temperature GaN nucleation layer. The treatment was carried out by introducing silane together with ammonia in the vapour phase at 1150°C. The treatment modifies the surface energy of the sapphire and increases the mobility of adatoms. As a result, the treatment facilitates the conversion from continuous nucleation layer into isolated truncated hexagonal islands and leads to a 3D growth mode. Such a 3D growth mode improves considerably the material quality and reduces the dislocation density.

The growth temperature of low-temperature nucleation layer also affects the properties of the epitaxial films. The growth rate at low temperatures is limited by the rate of the chemical reaction, which increases exponentially with temperature. Thus, the thickness of nucleation layer has strong dependence on temperature. Yi *et al* [13] studied the effects of growth temperature on the microstructure of GaN nucleation layers by x-ray synchrotron scattering. As the growth temperature was increased from 467°C to 655°C, the stacking of GaN changes from random stacking to a mixture of cubic and hexagonal

stacking. The nucleation layer grown at 505°C shows the best crystalline order in atomic layer positions and the smoothest surface morphology. The GaN grown on 505°C nucleation layer shows only the band edge luminescence, while the GaN films grown on the nucleation layers grown at 467°C and 655°C show a significant amount of the broad yellow luminescence originated from the defect levels.

3.3. Experiment

The samples were grown using low-pressure MOCVD. Before the growth, (0001) sapphire wafers were annealed in H_2 at 1200°C for 10 min. Then a low-temperature GaN nucleation layer was grown at 550°C at 200mbar using 66 μmoles/min TMGa, 3 slm of NH_3, and 9 slm of H_2. Real time *in situ* reflectance monitoring was used to control the thickness and the surface evolution of the GaN layer. The low temperature deposition of GaN nucleation layer was stopped when reflectivity signal at 600 nm reached 15-17%. After that the temperature was ramped for 3 min to 1140-1160°C and stabilised for 4 min prior to high temperature growth. For the samples 539GN and 540GN the NH_3 flow during initial high temperature growth was reduce to 0.5 slm and then ramped to 3 slm for 30 min and 1 min, respectively. All samples were grown to the thickness of about 3 μm. After the growth the samples were characterised by x-ray diffraction, room temperature photoluminescence and resistivity measurements. The reflectance waveforms are presented in Figure 3.3. Note that slowing down the NH_3 flow during initial stage of HT growth results in longer recovery time.

X-ray diffraction experiments were performed using a Bede D1 diffractometer. We measured ω- and ω-2θ scans of (002) reflection in triple axis mode and ω-2θ scan of (114) reflection in double axis mode; (114) scans were collected with open detector. The width of the (002) ω-scans gives information on the tilt component of mosaic spread in the sample. However (002) reflection is not sensitive to the twist component of mosaic spread.

It has been reported that specific dislocation structures in hexagonal III-nitrides may lead to anomalously narrow symmetric rocking curves, although the dislocation density is still very high [14]. For this reason θ-2θ scans of the (114) reflection were also measured. In this case the measurements were performed in double crystal geometry with open detector. Therefore, the width of the (114) θ-2θ scan is the cumulative figure of merit for tilt, twist and inhomogeneous strain in the sample.

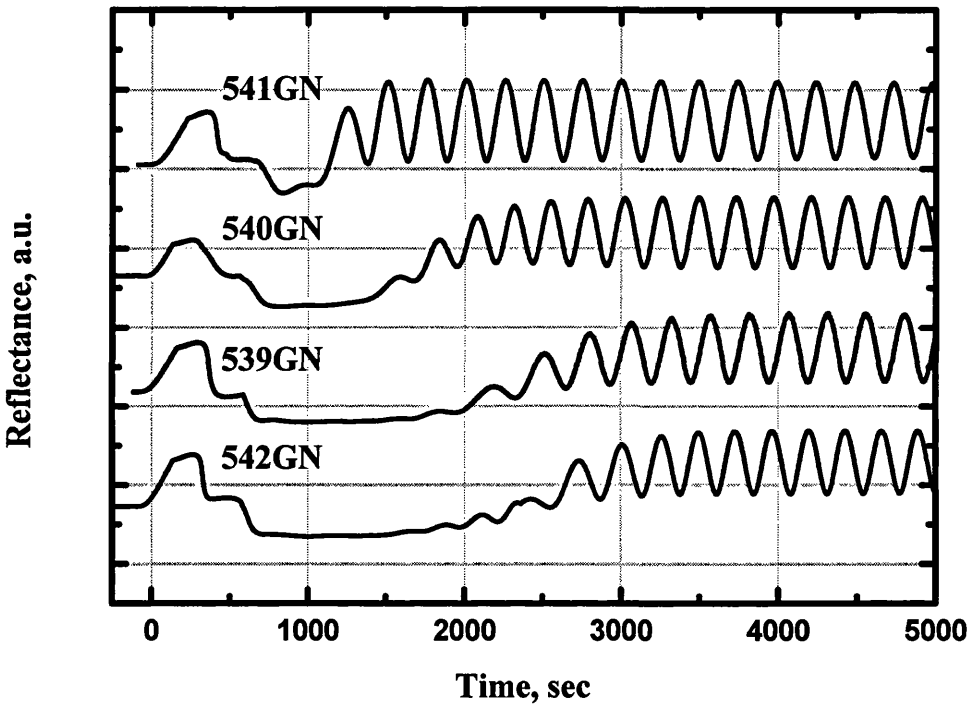

Figure 3.3 Real time reflectance waveforms recorded for GaN samples grown under different growth conditions. Longer recovery time corresponds to slower coalescence process. The monitoring wavelength is 600 nm.

Figure 3.4 depicts ω-2θ scans from GaN epilayers collected in the triple axis mode. All ω-2θ scans consist largely of two components; a sharp central peak occurred near the bulk position of the GaN (002) and a broad component. The sharp central peak is attributed to the thick part of the epitaxial layer where most of the lattice strain was released. Meanwhile the broad component represents the highly strained thinner part of the epitaxial layer. The line breadths of ω-2θ scans are presented in Table 4. Samples grown using the

delayed coalescence process have broader ω-2θ scans, which indicates higher degree of heterogeneous strain in those samples. A possible explanation is that the samples grown under delayed coalescence conditions have lower density of misfit dislocations; therefore strain relaxation in those samples is less effective.

Room temperature photoluminescence spectra were collected using a Renishaw Raman microscope. Photoluminescence was excited by 244 nm radiation generated by a frequency doubled Ar laser. The excitation power density was about 1kW/cm^2. The photoluminescence spectra are presented in Figure 3.5.

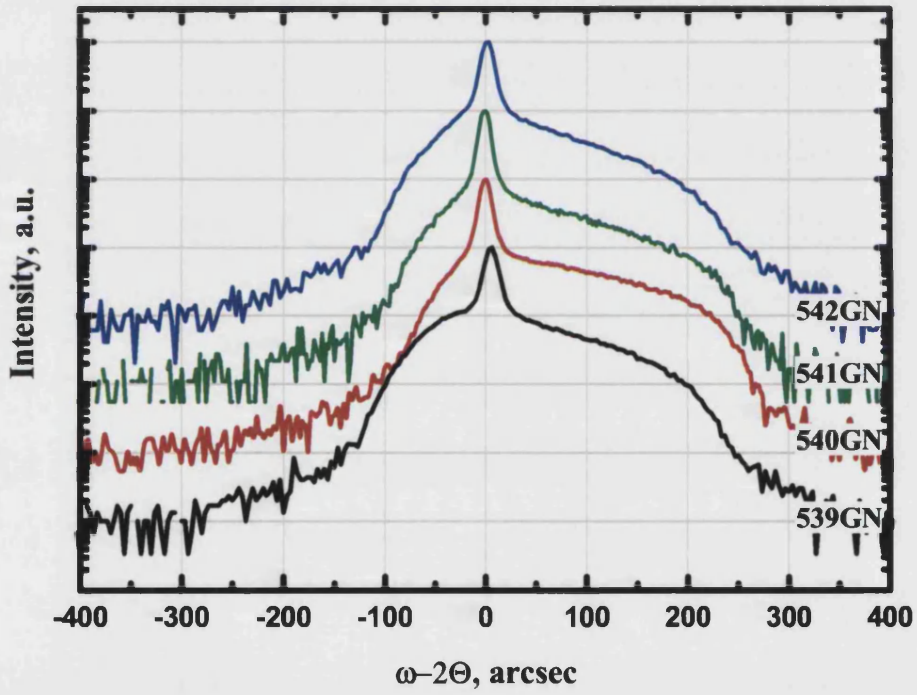

Figure 3.4 Triple axis ω-2θ scans of GaN films on sapphire around (002) reflection. The curves are vertically shifted for clarity.

Resistivity measurements were done using both two-point probe and van der Pauw methods. In case of two-point probe method a narrow stripe (~2×25 mm) was cut from a wafer, then two indium contacts were created on both ends of the sample. Van der Pauw measurements were performed on square ~7×7 mm^2 samples with soldered indium contacts on each corner. Both techniques yield essentially the same results.

The results of PL, XRD and resistivity measurements are summarised in.Table 4 Clear dependence of the properties of epitaxial layers on the reflectance recovery time has been observed. Samples grown under the conditions with longer recovery time have narrower rocking curves, brighter edge photoluminescence, and lower resistivity. This suggests smaller dislocation densities in these samples.

The rate of the coalescence process also affects the surface morphology. Figure 3.6 presents Nomarski phase contrast micrographs of two GaN specimens grown under the conditions of fast coalescence (541GN, left) and slow coalescence (542GN, right). Clearly, GaN epilayer grown in the slow coalescence process has rougher surface morphology than that of the sample grown using the fast coalescence process.

Table 4. Growth conditions and characterisation results for GaN epilayers on sapphire.

Parameter	541GN	540GN	539GN	542GN
Coalescence	fast	medium	slow	slow
Thickness, μm	2.75	2.9	3.1	3.2
NH_3 flow [slm], time [min]	3	0.5→3, 1 min	0.5→3, 30 min	0.2→1, 30 min
Growth temperature	1160	1140	1140	1160
X-ray:				
ω-2θ scan (002), triple-axis	12.8″	13.8″	16.6″	15.4″
ω-scan (002), triple-axis	256″	280″	242″	237″
ω-2θ scan (114), open detector, double-axis	446″	540″	352″	325″
Resistivity, Ωcm	1.73	0.61	0.55	0.4
Edge PL peak intensity, a.u.	1185	1485	3970	4920

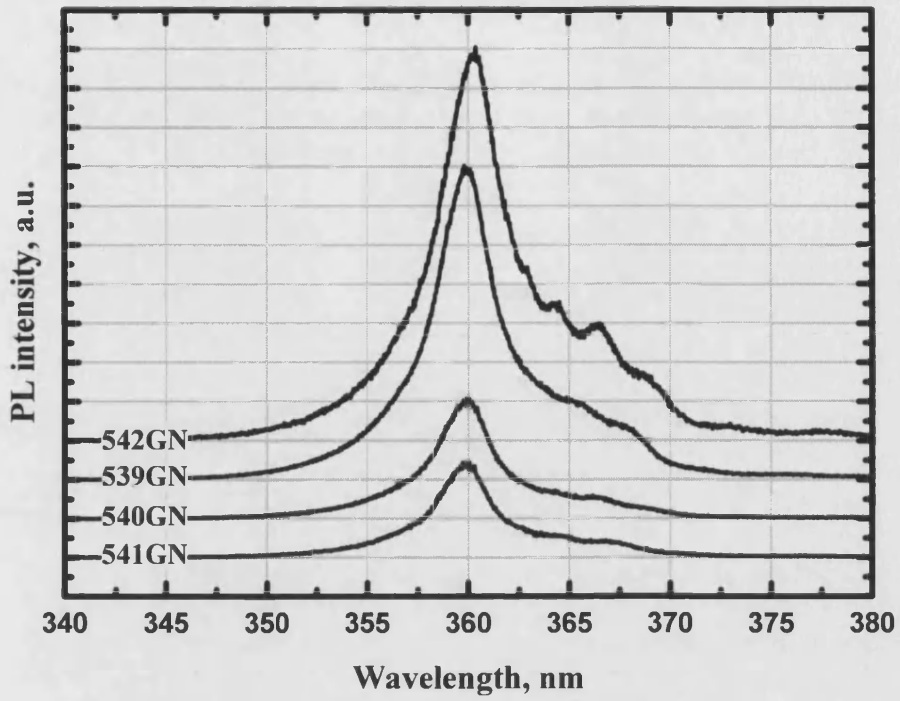

Figure 3.5. Room temperature photoluminescence spectra for GaN epilayers grown under different coalescence conditions. The spectra are vertically shifted for clarity.

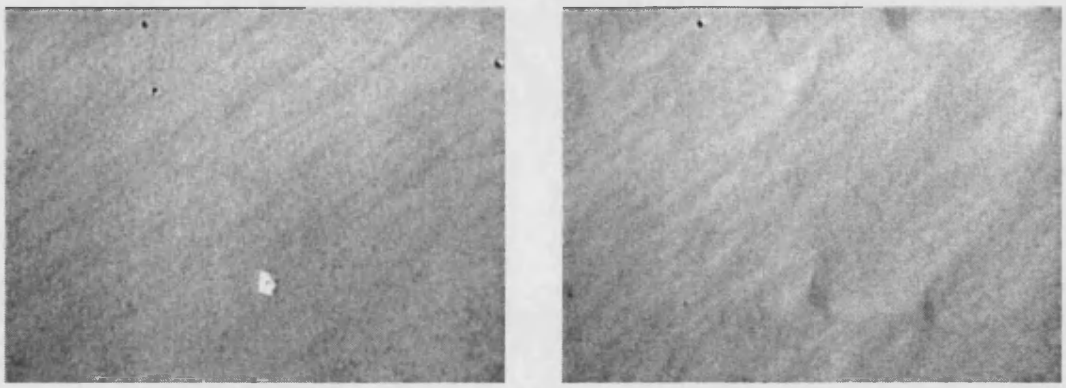

541GN 542GN

Figure 3.6. Nomarski phase contrast micrographs of GaN epilayers grown using fast coalescence process (left) and delayed coalescence process (right). Delayed coalescence leads to rougher surface morphology. Field size is 300x225 μm.

Figure 3.7 presents AFM images for samples 541GN and 542GN. Again, the sample grown under delayed coalescence conditions has rougher surface morphology.

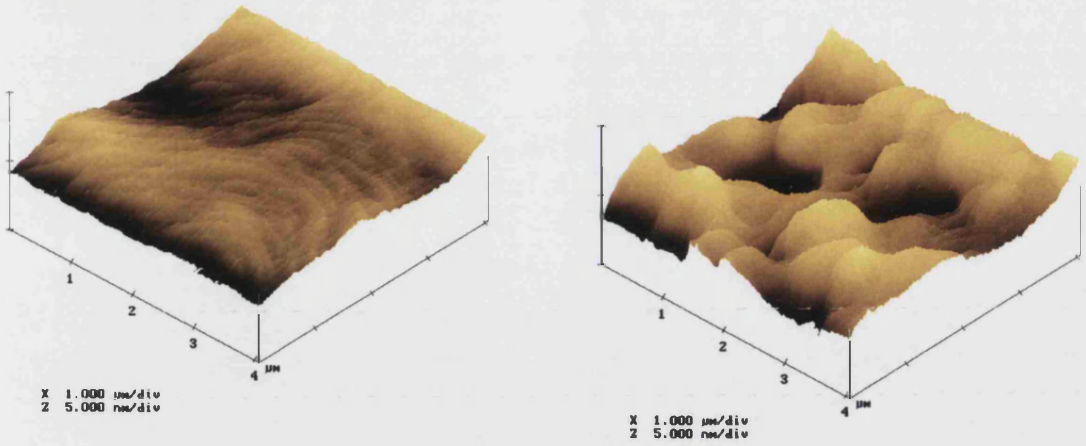

Figure 3.7 AFM images of samples grown with different coalescence rate. Left: 541GN (fast coalescence), right: 542GN (slow coalescence).

The structural properties of the samples 541GN (fastest coalescence) and 542GN (slowest coalescence) were studied in more detailed by high-resolution x-ray diffraction using Williamson-Hall method [15,16]. XRD measurements were made using a Bede D1 diffractometer in triple-axis mode. Angular scans (ω-scans) and radial scans (ω-2θ scans) of the symmetric reflections (002), (004) and (006) have been recorded. In addition, Φ-scans of asymmetric reflection (204) have been performed.

In Chapter 4 we use the double axis XRD analysis to determine structural parameters of GaN epitaxial layers such as dislocation density and misorientation mosaic blocks. Rocking curves measured in the double axis geometry are broadened by a large number of factors including heterogeneous strain, finite coherence length and misorientation of crystallites. Because the impact of different broadening factors is different for different diffracting planes, it is possible to separate those by performing measurements of several symmetric and asymmetric reflections and using special mathematical procedure (see Chapter 4). However, double axis analysis is quite time consuming and requiring a large amount of experimental work.

The analysis can be simplified significantly by using a triple axis diffractometer. The most important advantage of a triple axis diffractometer is its ability to distinguish between

broadening due to misorientation of mosaic blocks and nonuniform strain. In triple axis geometry, a rocking curve (ω-scan) is broadened due to tilt misorientation of subgrains and finite coherence length in the direction parallel to the sample surface. On the other hand, a radial scan (ω-2θ scan) is broadened by the heterogeneous strain along the surface normal and finite transverse coherence length. In most cases instrument broadening can be neglected.

Because crystalline misorientation and heterogeneous strain are already separated by the experimental setup, the mathematical procedure in triple axis analysis straightforward and involves simple linear dependences. We will omit the derivation of the equations used in Williamson-Hall method as they can be found in special literature and Chapter 4.

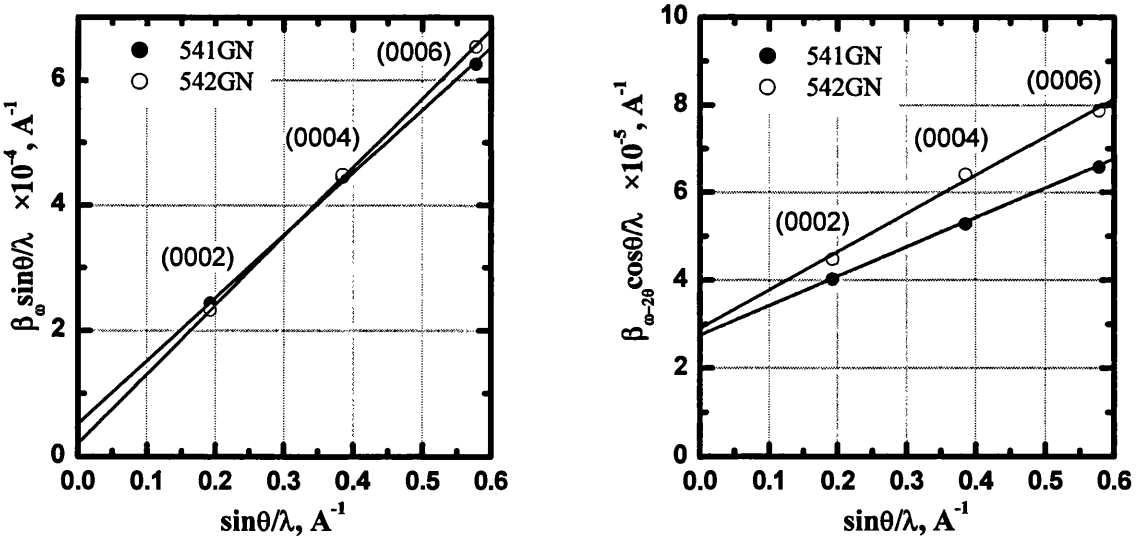

Figure 3.8. Williamson–Hall plots for samples 541GN and 542GN.

In the Williamson-Hall method $\beta_\omega \sin\theta/\lambda$ is plotted against $\sin\theta/\lambda$ for each reflection (so-called Williamson-Hall plot, see Figure 3.8), and fitted by a straight line. θ, λ and β_ω are the Bragg reflection angle, x-ray wavelength, and the FWHM of the ω-scan, respectively. The y-intersection y_0 gives the lateral coherence length.

$$L_{\parallel} = \frac{2\ln 2}{\pi}\frac{1}{y_0} \approx \frac{0.44}{y_0} \tag{3.1}$$

The slope of the line gives the tilt misorientation β_{tilt} of the subgrains. Assuming random distribution of the dislocation lines, the density of the screw dislocations can be obtained from the following equation:

$$D_{screw} = \frac{\beta_{tilt}^2}{2\pi \ln 2 b_{[0001]}^2} \tag{3.2}$$

$$b_{[0001]} = c = 5.187\text{Å}$$

If dislocations are piled up in small angle grain boundaries, the dislocation density is given by:

$$D_{screw} = \frac{\beta_{tilt}}{2\pi \ln 2 b_{[0001]} L_{\parallel}} \tag{3.3}$$

$$b_{[0001]} = c = 5.187\text{Å}$$

where $L_{\parallel}$ is the lateral coherence length.

In the other Williamson–Hall plot, $\beta_{\omega-2\theta}\cos\theta/\lambda$ is plotted against $\sin\theta/\lambda$ for every reflection, and again fitted linearly, where $\beta_{\omega-2\theta}$ is the FWHM of the radial scans. The y-intersection gives the vertical coherence length

$$L_{\perp} = \frac{2\ln 2}{\pi}\frac{1}{y_0} \approx \frac{0.44}{y_0} \tag{3.4}$$

and the line slope is a measure of the heterogeneous strain along the c-axis, $\varepsilon_{\perp}$.

The azimuthal misorientation of the subgrains or twist angle β_{twist} can be measured by performing Φ-scans on asymmetric reflections. The twist angle β_{twist} and the broadening of the Φ-scans are related by the following equation:

$$\beta_{twist} = \beta_{\Phi}\sin\phi \tag{3.5}$$

where ϕ is the inclination angle of asymmetric diffracting plane.

If dislocations are distributed randomly, the density of edge dislocation is given by

$$D_{edge} = \frac{\beta_{twist}^2}{2\pi \ln 2 b_{\frac{1}{3}\langle 11\bar{2}0\rangle}^2} \tag{3.6}$$

$$b_{\frac{1}{3}\langle 11\bar{2}0\rangle} = a = 3.185\text{Å}$$

If dislocations are arranged in small angle grain boundaries, the density of the edge dislocations is given by

$$D_{edge} = \frac{\beta_{twist}}{2\pi \ln 2 b_{\frac{1}{3}\langle 11\bar{2}0\rangle} L_{\parallel}} \tag{3.7}$$

$$b_{\frac{1}{3}\langle 11\bar{2}0\rangle} = a = 3.185\text{Å}$$

Table 5. Analysis summary of XRD measurements of samples 541GN and 542GN

	541GN	542GN
$L_{\parallel}$, μm	0.8	1.8
$L_{\perp}$, μm	1.6	1.5
β_{tilt}, arcsec	204	225
β_{twist}, arcsec	483	357
D_{screw}, cm^{-2}, from Eq (3.2)	0.8×10^{8}	1.0×10^{8}
D^{*}_{screw}, cm^{-2}, from Eq (3.3)	5.5×10^{7}	2.7×10^{7}
D_{edge}, cm^{-2}, from Eq (3.6)	1.2×10^{9}	6.8×10^{8}
D^{*}_{edge}, cm^{-2}, from Eq (3.7)	2.1×10^{8}	6.9×10^{7}
$\varepsilon_{\perp}$ (10^{-5})	6.63	8.79

The results of Williamson-Hall analysis are presented in Table 5. The dislocation densities were estimated under two different assumptions of dislocation arrangement. Values D_{screw} and D_{edge} were calculated assuming random distribution of dislocation lines using equations (3.2) and (3.6). Values D^{*}_{screw} and D^{*}_{edge} were calculated assuming that the dislocations are piled up in small angle subgrain boundaries using equations (3.3) and (3.7). As one can see, sample 542GN has larger coherence length (i.e. larger crystalline

blocks), smaller twist misorientation and lower dislocation density. Both samples have close values of the vertical coherence length; probably because the thickness of the epitaxial film is the limiting factor.

3.4. Summary

In conclusion, we have demonstrated that III-V ratio during initial stage of the high temperature growth can profoundly affect the coalescence process and properties of GaN epilayers. A combination of *in situ* reflectance monitoring and *ex situ* characterisation by photoluminescence, x-ray diffraction and electrical measurements suggests that decreased NH_3 flow during the initial stage of the high temperature growth reduces the coalescence rate. In turn, samples grown under slow coalescence conditions exhibit superior quality in terms of better crystallinity and lower dislocation density. However, the improvement of structural properties is achieved at the expense of slightly rougher surface morphology.

3.5. References

1. H. Amano, N. Sawaki, I. Akasaki, and Y. Toyoda, Appl. Phys. Lett. 48, 353 (1986)
2. A. E. Wickenden, D. K. Wickenden, and T. J. Kistenmacher, J. Appl. Phys. 75, 5367 (1994)
3. T. George, W. T. Pike, M. A. Khan, J. N. Kuznia, and P. Chang-Chien, J.Electron. Mater. 24, 241 (1995)
4. X. H. Wu, D. Kapolnek, E. J. Tarsa, B. Heying, S. Keller, B. P. Keller, U.K. Mishra, S. P. DenBaars, and J. S. Speck, Appl. Phys. Lett. 68, 1371 (1996).
5. X. H. Wu, P. Fini, S. Keller, E. J. Tarsa, B. Heying, U. K. Mishra, S. P.DenBaars, and J. S. Speck, Jpn. J. Appl. Phys., Part 2 35, L1648 (1996)
6. M. E. Twigg, R. L. Henry, A. E. Wickenden, D. D. Koleske, and J. C. Culbertson, Appl. Phys. Lett. 75, 686 (1999)
7. A. Munkholm, C. Thompson, C. M. Foster, J. A. Eastman, O. Auciello, G. B. Stephenson, P. Fini, S. P. DenBaars and J. S. Speck Appl. Phys. Lett., 72, 2972 (1998)
8. S. Nakamura, Jpn. J. Appl. Phys. 30, 1348 (1991)
9. S. Nakamura, Jpn. J. Appl. Phys. 30, 1620 (1991)

10. J. Han, T.-B. Ng, R. M. Biefeld, M. H. Crawford, and D. M. Follstaedt, Appl. Phys. Lett. 71 3114 (1997)

11. D. D. Koleske, A. J. Fischer, A. A. Allerman, C. C. Mitchell, K. C. Cross, S. R. Kurtz, J. J. Figiel, K. W. Fullmer, and W. G. Breilandm, Appl. Phys. Lett., Vol. 81, 1940 (2002)

12. S. Haffouz, H. Lahre` che, P. Venne´ gue` s, P. de Mierry, B. Beaumont, F. Omnes, P. Gibart, Appl. Phys. Lett., 73, 1278 (1998)

13. M. S. Yi, H. H. Lee, D. J. Kim, S. J. Park, D. Y. Noh, C. C. Kim, J. H. Je, Appl. Phys. Lett., 75, 2187 (1999)

14. B. Heying, X.H.Wu, S.Keller, Y.Li, D.Kapolnek, B.P.Keller, S.P.Denbaars, J.S.Speck, Appl. Phys. Lett. 68, 643 (1996)

15. P. Gay, P. B. Hirsch, and A. Kelly, Acta Metall. 1, 315 (1953)

16. H.-M. Wang, J.-P. Zhang, C.-Q. Chen, Q. Fareed, J.-W. Yang, M. Asif Khan, Appl. Phys. Lett., 81, (2002)

4. X-ray measurements of dislocation density in GaN layers

Typical dislocation densities in III-nitrides are in the order of 10^9 cm^{-2}, which is much higher compared to conventional III-V semiconductors like GaAs and GaP. High dislocation density affects the performance of III-N devices. Most device parameters like LED output power, ESD stability, LD threshold current densities etc. can be significantly improved merely by decrease in dislocation density.

High resolution x-ray diffraction (XRD) is a useful technique to characterise the structural quality of epitaxial films. Commonly, the full widths at half maximum (FWHM) of symmetrical reflections are taken as a figure of merit for the crystalline perfection. However, such measurements allow only qualitative comparison between different samples, rather then quantitative analysis of epitaxial film properties. Moreover, specific dislocation structures in hexagonal III-nitrides may lead to anomalously narrow symmetric rocking curves, although the dislocation density is still very high [1]. More accurate analysis should involve measurements of several reflections, including asymmetric ones. Then, using a special mathematical treatment it is possible to derive epitaxial layer parameters such as dislocation density, strain, coherence length etc [2,7]. For instance, Williamson-Hall plots [3,4] can be used for analysis of symmetrical triple-axis rocking curves. The analysis of double-axis rocking curves is even more complicated because it is not possible to distinguish between heterogeneous strain and mosaic spread in this geometry.

In this chapter we will develop a technique to extract epilayer parameters from double-crystal rocking curves.

4.1. Dislocations in GaN

First, we would like to discuss basic properties of dislocations in GaN. GaN has a wurtzite structure with *c* axis oriented parallel to the surface normal. The slip systems to be expected in the wurtzite structure [5,6] are listed in Table 6 and illustrated in Figure 4.3. The TEM diffraction analysis of GaN epitaxial films [7,8] shows that the interfacial layer between the substrate and the epitaxial film has a very high density of misfit dislocations (MD) with their line along the interface. These are geometrically necessary dislocations to account for tilt and twist subgrain misorientation and lattice mismatch between GaN and substrate. The volume of the epitaxial film contains a high density of threading dislocations (TD), which propagate along [0001] direction, i.e. they lie perpendicular to the substrate/GaN interface.

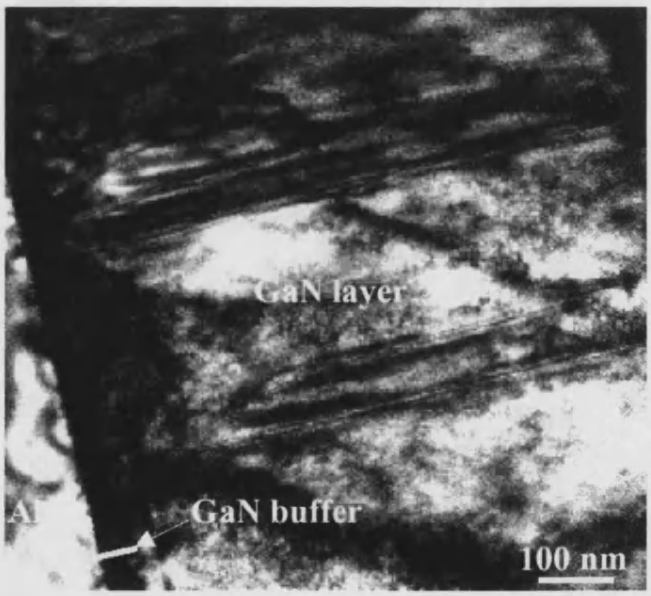

Figure 4.1 Bright field cross-sectional TEM image of the sample with (0002) reflection excited. All the defects observed in the GaN epilayer originate from those in the GaN buffer layer. (From [9])

Threading dislocations in GaN are of three types: **a** type dislocations with Burger's vector perpendicular to [0001] direction, **c** type dislocations with Burger's vector along [0001] direction, and **c+a** type dislocations with $\frac{1}{3}\langle 11\bar{2}3\rangle$ Burger's vector. From the mutual arrangement of the dislocation line and the Burger's vector one can see that **a** type, **c** type

and **c+a** type dislocations must be pure edge, pure screw and mixed dislocations respectively.

Since a dislocation of Burger's type cannot end within the crystal, threading and misfit dislocations are just different segments of the same dislocation lines. The misfit segment lies in the GaN/substrate interface plane. Then the dislocation line bends towards the surface of the film and propagates along [0001] direction, forming the threading segment. Figure 4.2 shows possible dislocations for the wurtzite crystal. For the slip system indicated D1 the misfit segment is a pure screw dislocation, while the threading segment is a pure edge dislocation. The misfit segment can lead to twist misorientation. The threading segment plays no role in misorientation between the subgrains and the substrate.

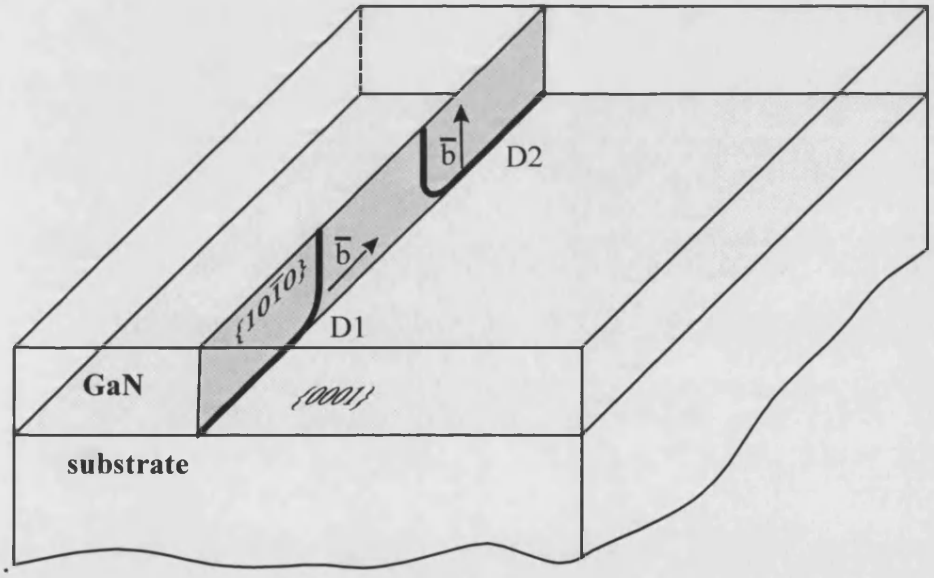

Figure 4.2. Misfit and threading dislocations in GaN crystal

The only way to achieve tilt is to have a dislocation in the basal plate with the Burger's vector out of the basal plane. The dislocation of this kind is indicated as D2. The threading segment of the D2 dislocation is a pure screw dislocation and plays no role in misorientation. The misfit segment is a pure edge dislocation and leads to the tilt misorientation. To summarise, threading dislocations cannot contribute to the subgrain

misorientation directly, but since threading dislocations are related to the misfit dislocations in the interface, tilt is correlated to the density of the screw TD, twist is correlated to the density of edge TD. Threading dislocations of the mixed type lead both to tilt and twist

Table 6. Primary slip systems in GaN.

Slip system	Burger's vector	Slip plane	Dislocation type
D1	$\bar{b} = \pm[110]$ $\bar{b} = \pm[1\bar{2}0]$ $\bar{b} = \pm[\bar{2}10]$	$(1\bar{1}00)$ $(10\bar{1}0)$ $(01\bar{1}0)$	Edge
D2	$\bar{b} = \pm[001]$	$(1\bar{1}0), (110)$ $(100), (1\bar{2}0)$ $(010), (\bar{2}10)$	Screw
D3	$\bar{b} = \pm[101]$ $\bar{b} = \pm[011]$ $\bar{b} = \pm[111]$	(hkl)	Mixed

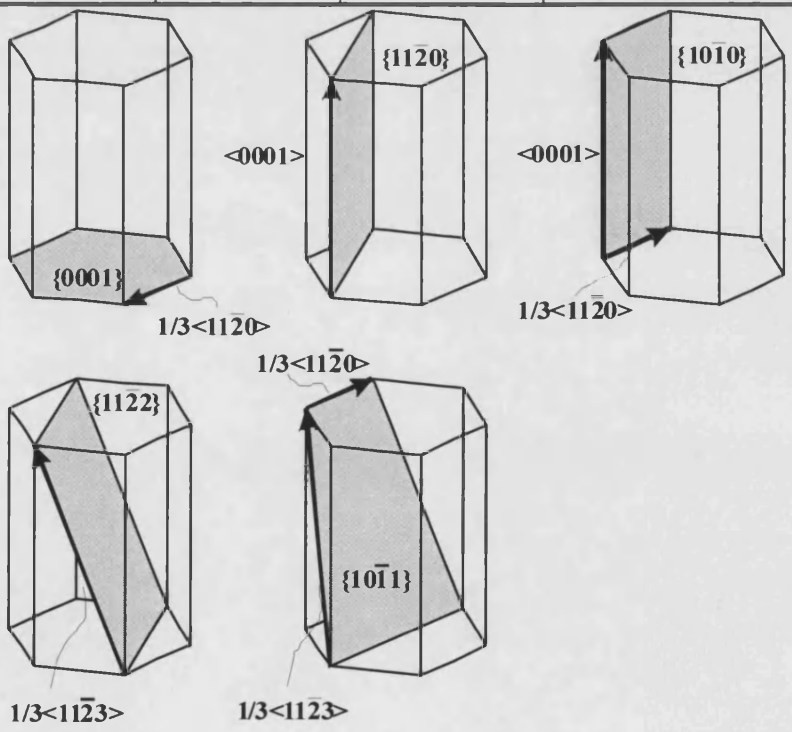

Figure 4.3. Various slip systems in the wurtzite structure

4.2. Broadening components

Here we will develop a simple theory describing the broadening of x-ray rocking curves and relating the width of x-ray peak with parameters of the sample. The broadening of rocking curves is influenced by a large number of factors; some of them are related to the intrinsic parameters of the sample such as dislocation density or non-uniform strain, and others are related to the conditions of the particular experimental setup. For example, the use of a triple-axis diffractometer allows us to distinguish broadening caused by mosaic spread and dilation. The experimental geometry is also very important. For instance, the diffraction from the asymmetrical planes can be measured in three possible ways: symmetrical, grazing incidence and grazing emergence geometries. The XRD data collected using the asymmetric geometry (grazing incidence and/or grazing emergence) are more difficult for analysis. The rocking curves for the same set of diffracting planes measured under grazing incidence and grazing emergence conditions have different widths [10,11].

We will limit our study to the analysis of the x-ray rocking curves obtained with double crystal diffractometer with opened detector using the symmetrical geometry. In this case the broadening of x-ray rocking curves is caused by the following factors:

- The lattice misorientation arising from dislocation tilting,
- The dislocation strain interaction,
- The subgrain particle size,
- The uniform lattice bending,
- The geometrical broadening of instrument,
- The natural broadening of the specimen and the analysing crystals etc.

All these factors could be calculated independently, following the approach suggested by Hordon and Averbach [12]

Let us consider the double-crystal rocking curve as Gaussian in shape. Assuming Gaussian distributions for rocking curve components due to lattice tilting α, lattice strain ε and particle size L, the measured rocking curve full width at half maximum (FWHM) β_M is given by:

$$\beta_M^2 = \beta_0^2 + \beta_\alpha^2 + \beta_L^2 + \beta_\varepsilon^2 + \beta_r^2 \tag{4.1}$$

where β_0, $\beta\alpha$, β_L, β_ε, β_r are the line breadths due to natural broadening, lattice tilting, local strain, particle size and uniform lattice bending, respectively. In case of III-nitride samples natural broadening is much smaller than measured breadth β_M and can be neglected. The wafer is assumed to be flat and broadening due to uniform lattice bending is also neglected.

$$\beta_M^2 = \beta_\alpha^2 + \beta_L^2 + \beta_\varepsilon^2 \tag{4.2}$$

4.2.1. Broadening due to mosaic spread

The broadening component $\beta\alpha$ is the measure of the misorientation of the subgrains. Due to anisotropic nature of the wurtzite structure, the disorientation of the subgrains is also anisotropic. Usually the mosaic structure of an epitaxial film is described in terms of two parameters: the tilt angle and the twist angle. The tilt of the blocks (rotation around the axis parallel to the surface) and twist of them (rotation around c axis) can be separately considered. For symmetrical scanning geometry (see **Figure 7.9**) the broadening due to tilt and twist can be written as:

$$\beta_\alpha^2 = \beta_{twist}^2 \sin^2\phi + \beta_{tilt}^2 \cos^2\phi \tag{4.3}$$

where ϕ is so-called inclination angle (the angle between the surface and the diffracting plane). Symmetrical reflections of the type $(00\cdot l)$ are sensitive only to the tilt component, while reflections from the asymmetric planes are sensitive to both. The impact of the twist broadening component is increasing with the increase of the inclination angle.

The inclination angle is calculated as an angle between the diffracting plane $(hk \cdot l)$ and $(00 \cdot 1)$ plane:

$$\phi = \arccos\left(\sqrt{\frac{\frac{3a^2}{4c^2}l^2}{h^2 + k^2 + hk + \frac{3a^2}{4c^2}l^2}}\right) \tag{4.4}$$

where a and c are the lattice constants of GaN.

$$\begin{aligned} c &= 5.187\text{Å} \\ a &= 3.185\text{Å} \end{aligned} \tag{4.5}$$

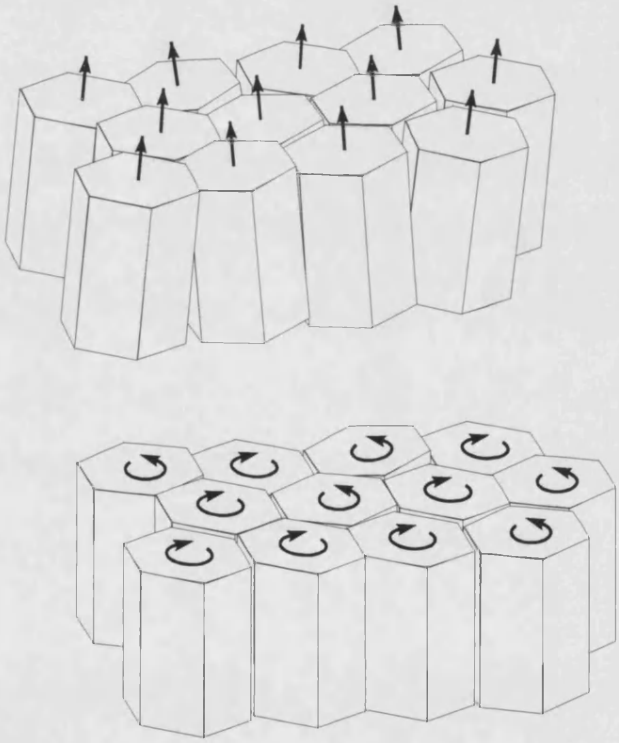

Figure 4.4. Tilt and twist components of subgrain misorientation

4.2.2. Broadening due to finite crystalline size

The broadening component β_L responsible for finite number of diffracting planes is given by Scherrer equation [13].

$$\beta_L^2 = \frac{4\ln 2}{\pi L^2}\frac{\lambda^2}{\cos^2\Theta_b} = C_L\frac{1}{\cos^2\Theta_b} \tag{4.6}$$

where $\lambda = CuK_{\alpha 1} = 1.5405\text{Å}$ is the wavelength of x-ray radiation, L is the particle size, Θ_b is the Bragg's angle.

4.2.3. Broadening due to nonuniform strain

The effect of a nonuniform strain on the rocking curve width can be easily derived from Bragg's law in differential form

$$\frac{\Delta d}{d} = \frac{\Delta\lambda}{\lambda} - \frac{\Delta\Theta}{\tan\Theta} \tag{4.7}$$

The wavelength dispersion $\frac{\Delta\lambda}{\lambda}$ is negligibly small for $CuK_{\alpha 1}$ line, thus

$$\Delta\Theta = -\frac{\Delta d}{d}\tan\Theta \tag{4.8}$$

In differential form

$$\beta_\varepsilon^2 = \varepsilon^2\tan^2\Theta_b = C_e\tan^2\Theta_b \tag{4.9}$$

The nonuniform strain can be described by two independent components: macroscopic strain caused by lattice mismatch and /or difference of thermal expansion coefficients and microscopic strain caused by dislocations.

4.2.4. Broadening due to macroscopic strain

In most cases the macroscopic strain has two components: a biaxial strain $\varepsilon_{\parallel}$ parallel to the sample surface and the corresponding perpendicular strain $\varepsilon_{\perp}$.

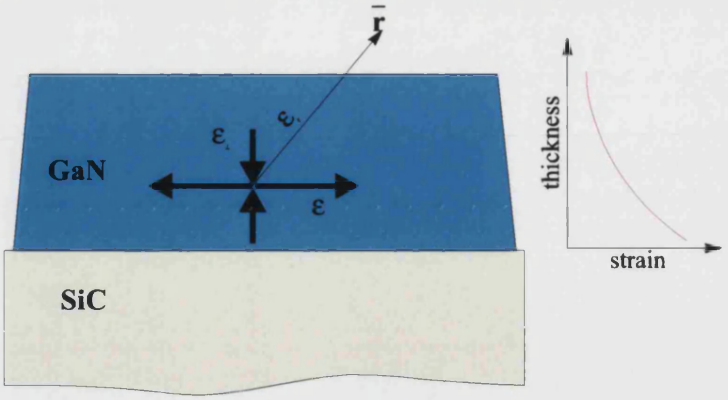

Figure 4.5. Macroscopic strain due to lattice mismatch and TEC difference between substrate and epilayer.

The two components of the strain are related by Poisson's ratio ν

$$\varepsilon_{\perp} = -2\frac{\nu}{1-\nu}\cdot\varepsilon_{\parallel} \tag{4.10}$$

The strain along the direction $\vec{r}$ can be obtained using conventional rotational matrix transformation

$$\varepsilon_r = \varepsilon_{\parallel}\sin^2\phi + \varepsilon_{\perp}\cos^2\phi - 2\varepsilon_{xy}\sin\phi\cos\phi \tag{4.11}$$

The shear strain ε_{xy} is zero, hence

$$\varepsilon_r = \varepsilon_{\parallel}(\sin^2\phi - 2\frac{\nu}{1-\nu}\cos^2\phi) \approx \varepsilon_{\parallel}(\sin^2\phi - 0.44\cos^2\phi) \tag{4.12}$$

where ϕ is the angle between the diffracting plane and the surface of the sample.

The broadening component due to macroscopic strain can be written as

$$\beta_S^2 = K_S(\sin^2\phi - 0.44\cos^2\phi)^2\tan^2\Theta_b \tag{4.13}$$

4.2.5. Broadening due to strain fields of dislocations

For the sake of simplicity we will account only for **c** and **a** type threading dislocations, broadening caused by misfit or **c+a** threading dislocations is neglected. As it was mentioned before, **a**-type threading dislocations are pure edge dislocations with dislocation line along [0001] and Burgers vector $\frac{1}{3}\langle 11\bar{2}0\rangle$. The mean square strain of edge dislocation along direction $\vec{N}$ is given by (see Appendix 1)

$$\overline{\varepsilon_N^{\,2}} = \frac{b^2}{128\pi r^2}\left(5\cos^2\Delta + 17\cos^2\psi\right)\ln\frac{r}{r_0} \tag{4.14}$$

where Δ is the angle between the dislocation glide plane and normal of the diffracting plane N, ψ angle between the Burger's vector $\vec{b}$ and $\vec{N}$. This equation is different from the one used by other authors. Hordon and Averbach [12] suggested the following expression for the mean square strain.

$$\overline{\varepsilon_N^{\,2}} = \frac{5b^2}{64\pi^2 r^2}\left(2.45\cos^2\Delta - 0.45\cos^2\psi\right)\ln\frac{r}{r_0} \tag{4.15}$$

The same equation has been used by Metzger *et al* [7]. However, Hordon and Averbach have used a different expression for ε_{rr} component of the strain

$$\varepsilon_{rr} = \frac{b\sin\theta}{4\pi(1+v)r}, \tag{4.16}$$

This is not correct. The correct expression is given by

$$\varepsilon_{rr} = -\frac{b(1-2v)\sin\theta}{4\pi(1-v)r} \tag{4.17}$$

The detailed calculation of the strain field of the edge dislocation can be found in [16] and in Appendix 1.

C-Type dislocations are pure screw dislocations lying along [0001] and having a Burger's vector [0001]. The mean square strain of screw dislocation along direction $\vec{N}$ is given by (see Appendix 2)

$$\overline{\varepsilon_N^{\,2}} = \frac{b^2}{16\pi^2 r^2}\ln\frac{r}{r_0}\sin^2\psi\cos^2\psi \tag{4.18}$$

Broadening due to dislocations can be written as

$$\beta_D^2 = \left[\frac{b_E^2}{128\pi^2 r_E^2}\ln\frac{r_E}{r_0}\mathrm{f_E}(hkl) + \frac{b_S^2}{16\pi^2 r_S^2}\ln\frac{r_S}{r_0}\mathrm{f_S}(hkl)\right]\tan^2\Theta_b \tag{4.19}$$

where $\mathrm{f}_E(hkl)$, $\mathrm{f}_S(hkl)$ are angular factors for edge and screw dislocation, respectively. Since there are three distinct dislocation systems for pure edge dislocation, the mean

square strain is influenced by all three possible orientations. All possible combinations of slip plane and Burger's vector are presented in Table 7. All these planes and directions are equivalent, thus we assume that all directions are equally possible.

Table 7. Possible edge dislocation systems

Slip Plane, $\{1\bar{1}00\}$ family	Burger's vector $\frac{1}{3}\langle 11\bar{2}0\rangle$ family
$(0\bar{1}0)$	$\pm[100]$
(100)	$\pm[010]$
$(\bar{1}10)$	$\pm[\bar{1}\bar{1}0]$

The angular function for edge dislocations is obtained by summarising over different directions of the Burger's vector and slip planes.

$$\begin{aligned} f_E(hkl) = 5(\cos^2\Delta_{(0\bar{1}0)} + \cos^2\Delta_{(100)} + \cos^2\Delta_{(1\bar{1}0)}) + \\ +17(\cos^2\psi_{[100]} + \cos^2\psi_{[010]} + \cos^2\psi_{[\bar{1}\bar{1}0]}) \end{aligned} \tag{4.20}$$

The mean square strain of the screw dislocation does not depend on the orientation of the slip plane. The Burger's vector has only one possible direction [0001]. Therefore, the angular function for screw dislocations is simply

$$f_S(hkl) = \cos\psi_{[0001]}\sin\psi_{[0001]} \tag{4.21}$$

The angle between the diffracting plane $(h_1k_1\cdot l_1)$ and the slip plane $(h_2k_2\cdot l_2)$ is obtained from the formula:

$$\phi = \arccos\left(\frac{h_1h_2 + k_1k_2 + \frac{1}{2}(h_1k_2 + k_1h_2) + \frac{3a^2}{4c^2}l_1l_2}{\sqrt{\left(h_1^2 + k_1^2 + h_1k_1 + \frac{3a^2}{4c^2}l_1^2\right)\left(h_2^2 + k_2^2 + h_2k_2 + \frac{3a^2}{4c^2}l_2^2\right)}}\right) \tag{4.22}$$

The normal vector $\vec{N} = [uvw]$ to the diffracting plane (hkl) is found from the following equations:

$$u = 2h + k \tag{4.23}$$

$$v = h + 2k$$

$$w = \frac{3}{2}\left(\frac{a}{c}\right)^2 l$$

Note that using above equations one can obtain non-integer values of w, which has no physical sense, but is mathematically correct.

The angle between the diffracting plane normal $\vec{N} = [u_1 v_1 w_1]$ and the Burger's vector $\vec{b} = [u_2 v_2 w_2]$ is given by:

$$\psi = \arccos\left(\frac{u_1u_2 + v_1v_2 - \frac{1}{2}(u_1u_2 + v_1v_2) + w_1w_2\frac{c^2}{a^2}}{\sqrt{\left(u_1^2 + v_1^2 + w^2\frac{c^2}{a^2} - u_1v_1\right)\left(u_2^2 + v_2^2 + w^2\frac{c^2}{a^2} - u_2v_2\right)}} \right) \tag{4.24}$$

Values of Θ_B, ϕ, Δ, ψ_E, ψ_S, $f_E(hkl)$ and $f_S(hkl)$ for different set of diffracting planes are tabulated in Table 8.

Combining all broadening components together we obtain the following expression for the measured rocking curve FWHM: β_M

$$\beta_M^2 = C_{twist}\sin^2\phi + C_{tilt}\cos^2\phi + C_L\frac{1}{\cos^2\Theta_b} + C_{strain}\left(\sin^2\phi - 2\frac{v}{1-v}\cos^2\phi\right)^2\tan^2\Theta_b + \left[C_E f_E(hkl) + C_S f_S(hkl)\right]\tan^2\Theta_b \tag{4.25}$$

Where ϕ is the inclination angle of the diffracting plane, Θ_b is the Bragg's angle, v is the Poisson's ratio, f_E and f_S are the angular factors (see equations (4.20), (4.21)).

Table 8. Values of the Bragg's angle Θ_B, inclination angle ϕ, angle between dislocation slip plane and diffracting plane Δ, angle between Burger's vector and diffracting plane normal ψ , and angular factors f_E and f_S for different diffracting planes in GaN.

Diffracting plane (hkl)	Θ_B, deg	ϕ, deg	Δ, deg slip plane			ψ_E, deg Burger's vector			ψ_S, deg Burger's vector	f_E	f_S
			$(0\bar{1}0)$	(100)	$(\bar{1}10)$	[100]	[010]	$[\bar{1}\bar{1}0]$	[001]		
(002)	17.28	0.00	90.00	90.00	90.00	90.00	90.00	90.00	0.00	0.00	0.00
(004)	36.44	0.00	90.00	90.00	90.00	90.00	90.00	90.00	0.00	0.00	0.00
(006)	63.00	0.00	90.00	90.00	90.00	90.00	90.00	90.00	0.00	0.00	0.00
(102)	24.05	43.22	110.02	46.78	110.02	53.63	90.00	126.37	43.22	15.47	0.25
(103)	31.71	32.06	105.39	57.94	105.39	62.63	90.00	117.37	32.06	9.30	0.20
(104)	41.02	25.17	102.28	64.83	102.28	68.39	90.00	111.61	25.17	5.97	0.15
(114)	49.98	39.14	123.14	56.86	90.00	71.60	71.60	129.14	39.14	13.15	0.24
(204)	54.60	43.22	110.02	46.78	110.02	53.63	90.00	126.37	43.22	15.47	0.25
(105)	52.49	20.60	100.13	69.40	100.13	72.26	90.00	107.74	20.60	4.08	0.11
(205)	68.26	36.93	107.48	53.07	107.48	58.64	90.00	121.36	36.93	11.92	0.23
(106)	69.01	17.39	98.60	72.61	98.60	75.00	90.00	105.00	17.39	2.95	0.08

The equation (4.25) is a linear equation of six unknowns C_{twist}, C_{tilt}, C_L, C_{strain}, C_E and C_S, hence at least six measurements of line breadths of different reflections are required to find the unique solution. For a larger number of experimental points, a suitable minimisation method, e.g. least squares fitting can be used.

In fitting we minimise the following error function:

$$E = \frac{1}{N}\sum_{i=1}^{N}\left|\beta_m^i - \beta_c^i\right| \tag{4.26}$$

where β_m^i and β_c^i are measured and calculated peak widths of i^{th} reflection and N is the number of reflections measured. The natural criterion for satisfactory fit is

$$E \le \Delta\beta \tag{4.27}$$

where $\Delta\beta$ is the average experimental uncertainty in line breadth measurements.

Due to unavoidable experimental error, we cannot obtain exact values of C_{twist}, C_{tilt}, C_L, C_{strain}, C_E and C_S but a range of acceptable values for which the condition (4.27) holds. More accurate determination of fitting constants is limited by the accuracy of rocking breadth curve measurements.

Coefficients C_{twist}, C_{tilt}, C_L, C_{strain}, C_E and C_S have a distinct physical meaning. C_{twist} and C_{tilt} are related to subgrain misorientation, the corresponding tilt and twist angles are calculated as:

$$\beta_{twist} = \sqrt{C_{twist}} \tag{4.28}$$

$$\beta_{tilt} = \sqrt{C_{tilt}}$$

The constant C_L is related to the coherence length (or average crystallite size)

$$L_c = 2\lambda\sqrt{\frac{\ln 2}{\pi C_L}} \tag{4.29}$$

The constant C_{strain} is related to the biaxial nonuniform strain in the plane of the epilayer.

$$\varepsilon_{\parallel} = \sqrt{C_{strain}} \tag{4.30}$$

Constants C_E and C_S are related to the density of threading edge and screw dislocations.

$$C_E = 3\frac{b_E^2}{128\pi^2 r_E^2}\ln\frac{r_E}{r_0} \tag{4.31}$$

$$C_S = \frac{b_S^2}{16\pi^2 r_S^2}\ln\frac{r_S}{r_0}$$

The factor of 3 in the equation for C_E denotes three possible directions of the Burger's vector.

4.3. Dislocation density

4.3.1. Dislocation density and mosaic spread

Fitting equation (4.25) to experimental data one immediately obtains tilt and twist angles describing the mosaicity of the sample. Assuming that subgrains are separated by small angle tilt and twist boundaries, it is possible to relate tilt and twist angles to the dislocation density. First, we will estimate the average angle between two adjacent

subgrains. Assuming Gaussian distribution for the orientations of the subgrains with half-width $\beta\alpha$, the probability density for the subgrain to have an orientation φ is given by:

$$f(\varphi)=\frac{1}{\sqrt{2\pi}\sigma}e^{\frac{\varphi^2}{2\sigma^2}} \tag{4.32}$$

where σ is the standard deviation

$$\sigma=\frac{\beta_\alpha}{2\sqrt{2\ln 2}} \tag{4.33}$$

The average misorientation between two subgrains can be calculated as

$$\overline{|\phi-\varphi|}=\int_{-\infty}^{+\infty}\int_{-\infty}^{+\infty}|\phi-\varphi|f(\phi)f(\varphi)d\phi d\varphi=\frac{1}{2\pi\sigma^2}\int_{-\infty}^{+\infty}\int_{-\infty}^{+\infty}|\phi-\varphi|\exp\left[-\frac{\phi^2+\varphi^2}{2\sigma^2}\right]d\phi d\varphi=\frac{2\sigma}{\pi} \tag{4.34}$$

From equation (4.34)

$$\overline{|\phi-\varphi|}=\frac{\beta_\alpha}{\sqrt{2\pi\ln 2}} \tag{4.35}$$

Next, we estimate the dislocation density from tilt and twist angles using elementary geometrical considerations. A sheet of edge dislocations must be formed between two crystalline blocks to account angular misorientation. The angle between two adjacent subgrains can be expressed as

$$\overline{|\phi-\varphi|}=\frac{b}{h} \tag{4.36}$$

where b is the Burgers vector and h is the average distance between dislocation lines.

The dislocation density is given by

$$D=\frac{1}{Lh} \tag{4.37}$$

where L is the spacing between subgrain boundaries. Assuming random distribution of dislocations $L\approx h$

$$D=\frac{1}{h^2} \tag{4.38}$$

combining equations (4.36) and (4.38) we obtain the following relation between tilt (or twist) angle β and dislocation density D:

$$D = \frac{\beta^2}{2\pi \ln 2b^2} \tag{4.39}$$

If the dislocations are not distributed randomly, but rather piled up in the small angle boundaries, the spacing between subgrain boundaries is approximately equal to the coherence length $L \approx L_c$. In this case the dislocation density is given by

$$D = \frac{\beta}{2\pi \ln 2bL_c} \tag{4.40}$$

Misfit dislocations at the interface between the substrate and the epilayer are responsible for tilt and twist rotations of single crystallites. In order to create a tilt boundary, the misfit dislocation must have a Burger's vector pointing out of the interface plane. Assuming that screw threading dislocations with $b = [0001]$ are related to edge-type misfit with the same Burger's vector, the density of these screw dislocations can be obtained from the following equation:

$$D_{screw} = \frac{\beta_{tilt}^2}{2\pi \ln 2b_{[0001]}^2} \tag{4.41}$$

$$b_{[0001]} = c = 5.187\text{Å}$$

By similar argument, **a**-type threading dislocations mediate an azimuthal rotation of crystallites around surface normal. The density of these dislocations can be derived from twist angle using the equation:

$$D_{edge} = \frac{\beta_{twist}^2}{2\pi \ln 2b_{\frac{1}{3}\langle 11\bar{2}0\rangle}^2} \tag{4.42}$$

$$b_{\frac{1}{3}\langle 11\bar{2}0\rangle} = a = 3.185\text{Å}$$

However, for nitride materials the assumption of assumption of dislocation arrangement in subgrain boundaries is more realistic. In this case the densities of screw and edge dislocations are given by the following equations:

$$D_{screw} = \frac{\beta_{tilt}}{2\pi \ln 2 b_{[0001]} L_c} \tag{4.43}$$

$$b_{[0001]} = c = 5.187\text{Å}$$

$$D_{edge} = \frac{\beta_{twist}}{2\pi \ln 2 b_{\frac{1}{3}\langle 11\bar{2}0\rangle} L_c} \tag{4.44}$$

$$b_{\frac{1}{3}\langle 11\bar{2}0\rangle} = a = 3.185\text{Å}$$

4.3.2. Dislocation density and dislocation strain fields

Another approach to estimate the dislocation density is to use coefficients C_E and C_S. Both of them involve the term $\ln\left(\frac{r}{r_0}\right)$ where r_0 and r are lower and upper limits of integration, respectively. From the physical point of view r_0 is the radius of dislocation core, and r is the maximal extent of the strain field. For a random array of threading dislocations with average spacing h, the strain field of each dislocation effectively acts over a distance $r = h/2$. Consequently, the dislocation density is given by

$$D_{edge} = \frac{1}{4r_E^2} \tag{4.45}$$

$$D_{screw} = \frac{1}{4r_S^2}$$

where effective radii of edge dislocations r_E and screw dislocations r_S are obtained from equations (4.31) It should be noted that determination of the dislocation density from the strain broadening is accurate only to an order of magnitude because it involves r_0.

4.4. Experiment

Here we will illustrate the use of the theoretical model described above for analysis of experimental XRD data. Three GaN samples were grown by MOCVD using the reaction of TMGa and ammonia in the presence of hydrogen as a carrier gas.

Table 9. Properties of GaN epitaxial samples used for x-ray analysis.

	163GN	299SiC	486GN
Substrate	(00·1) Al_2O_3	(00·1) 6H-SiC	(00·1) Al_2O_3
GaN thickness, μm	2.5	1.1	3.6
Nucleation layer	low temp. GaN	high temp. AlN	low temp. GaN

The x-ray diffraction experiments were performed using double crystal Bede D1 diffractometer equipped with four-bounce monochromator. The rocking curves were measured using the symmetric geometry. In this geometry, the sample is rotated in the vertical plane and around the sample normal so that the diffracting planes are brought perpendicular to the diffractometer plane[a]. The rotation in the vertical plane is given by the inclination angle ϕ. The angle of rotation around the vertical axis of the diffractometer ω is given by the Burger's angle Θ_b, and the position of the detector is $2\Theta_b$. Thus, in the symmetric geometry the incidence and diffracted angles are both equal to the Burger's angle Θ_b. The x-ray rocking curves were measured in $\omega - 2\Theta$ geometry without slit in front of the detector (open detector), so the rocking curves were broadened both by tilts and dilatations. The peak width was measured as FWHM of a Gaussian fit to experimental data. The widths of the rocking curves for all three samples are presented in Table 10.

Coefficients C_{twist}, C_{tilt}, C_L, C_{strain}, C_E and C_S were found by fitting equation

[a] The plane containing the x-ray tube, the specimen and the detector.

(4.25) to experimental data. The experimental error in line width measurements is about 10 arc sec. Using condition (4.27) we obtain the admissible ranges for fitting coefficients. Then using equations (4.28), (4.29), (4.30) (4.31) and (4.45) we can calculate tilt and twist angles β_{tilt} and β_{twist}, coherence length L, non-uniform strain $\varepsilon_{\|}$ and density of screw and edge dislocations D_S and D_E.

Table 10. Experimental and calculated line breadths

Reflection	163GN		299SiC		486GaN	
	Measured	Calculated	Measured	Calculated	Measured	Calculated
(002)	324	319	270	267	279	282
(004)	309	320	268	275	276	282.
(006)	328	329	325	329	278	288
(102)	-	-	416	409	517	517
(103)	-	-	369	363	452	440
(104)	461	447	337	339	405	394
(114)	547	566	396	409	-	-
(204)	615	604	433	435	523	533
(105)	427	426	345	337	364	369
(205)	594	595	468	466	527	526
(106)	-	-	402	400	381	374

As one can see, sample 299SiC has the smallest twist and tilt angles, indicating more coherent growth of GaN on SiC. On the other hand, sample 299SiC has the largest non-uniform strain and the smallest coherence length, probably due to small thickness of the GaN epitaxial film. The dislocation density for all three samples is comparable, however for samples 299SiC and 486GN we obtain very wide range for the edge dislocation density (from 0 to 2×10^9 cm^{-2}). This is the intrinsic limitation of the technique because it is difficult to distinguish between broadening caused by mosaic spread and broadening by strain fields of dislocations. For more accurate measurements, a triple axis diffractometer should be used.

Now we would like to check the technique for consistency. The twist angle can be measured by performing Φ-scans on asymmetric reflections, where the sample is rotated

with respect to the surface normal. From simple geometrical considerations the twist angle is given by

$$\beta_{twist} = \beta_{\Phi} \sin\phi \tag{4.46}$$

where β_{Φ} is the FWHM of Φ-scan and ϕ is the corresponding inclination angle.

Table 11. Upper and lower values for twist angle β_{twist}, tilt angle β_{tilt}, coherence length L, non-uniform strain $\varepsilon_{\parallel}$ and density of screw and edge dislocations D_S and D_E.

Parameter	163GN		299SiC		486GN	
	low	**high**	**low**	**high**	**low**	**high**
β_{twist}, arcsec	760	800	480	545	665	720
β_{tilt}, arcsec	310	330	230	260	265	290
L, μm	0.85	∞	0.35	0.27	0.6	∞
$\varepsilon_{\parallel}$	0	6.5×10^{-4}	0	7×10^{-4}	0	6×10^{-4}
[a] D_E, cm^{-2}	2×10^{9}	5×10^{9}	0	2×10^{9}	0	2×10^{9}
[a] D_S, cm^{-2}	1×10^{9}	4×10^{9}	0	2×10^{9}	8×10^{8}	4×10^{9}
[b] D_E, cm^{-2}	5×10^{8}	6×10^{8}	3×10^{8}	4×10^{8}	4×10^{8}	5×10^{8}
[b] D_S, cm^{-2}	1×10^{9}	1×10^{9}	4×10^{8}	6×10^{8}	9×10^{8}	1×10^{9}
[c] D_E, cm^{-2}	0	1×10^{8}	2×10^{8}	3×10^{8}	0	2×10^{8}
[c] D_S, cm^{-2}	0	2×10^{8}	3×10^{8}	4×10^{8}	0	3×10^{8}

Hence, the widths of Φ-scans can be fitted by a linear function $f\left(\frac{1}{\sin\phi}\right)$. The twist angle is found as $\beta_{twist} = f(1)$

[a] Calculated from strain fields using equations (4.45)

[b] Calculated from tilt/twist angles assuming random distribution of dislocations using equations (3.2), (3.6)

[c] Calculated from tilt/twist angles assuming that dislocations are piled up in small angle subgrain boundaries using equations (3.3), (3.7)

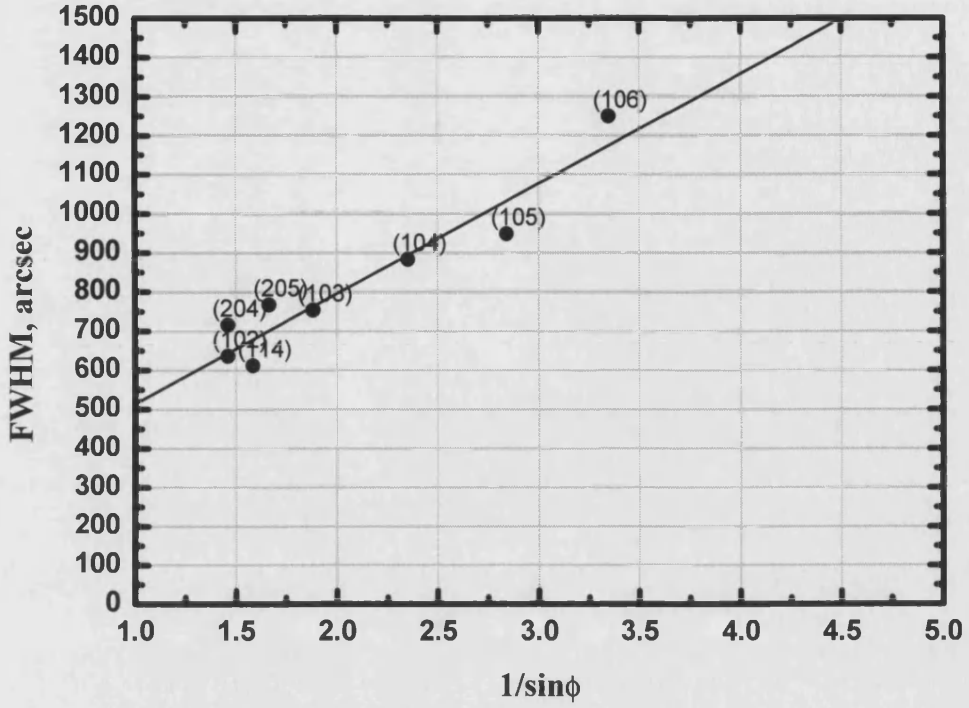

Figure 4.6. Φ-scan widths for sample 299SiC as a function of $1/\sin\phi$, where ϕ is the inclination angle. Intercept with the line x=1 gives the twist angle β_{twist}.

Figure 4.6 illustrates the graphical solution of equation (4.46). Experimental values of Φ-scan widths for sample 299SiC are plotted as a function of $1/\sin\phi$ where ϕ is the inclination angle. Intercept with the line x=1 gives the twist angle β_{twist}. The obtained value of $\beta_{twist} \approx 500$ arcsec is very close to the value estimated by fitting equation (4.25).

4.5. Summary

A technique for analysis of double crystal rocking curves and determination of the epilayer parameters has been developed. The theoretical model is in good agreement with experimental data. The technique allows measuring tilt and twist angles with high degree of accuracy. However, in case of GaN samples the mosaic spread causes most of the broadening and the influence of other components is relatively small. That is why the accuracy of coherence length and dislocation density measurements is not very high. In most cases the model gives only the upper limit for the dislocation density and the lower

limit for the coherence length. For more accurate measurements the triple-axis geometry should be used. In this case broadening due to mosaicity can be separated from the other components.

4.6. Appendix 1. Strain fields of an edge dislocation.

Let us consider a straight edge dislocation running along z axis and having Burgers vector *(b,0,0)*. All displacements are in the *xy*-plane and the theory of plane strain could be applied. According to that theory [14,15,16] stresses are obtained by differentiating a stress function *F*,

$$\sigma_{rr} = \frac{1}{r}\frac{\partial F}{\partial r} + \frac{1}{r^2}\frac{\partial^2 F}{\partial \theta^2}, \quad \sigma_{\theta\theta} = \frac{\partial^2 F}{\partial r^2}, \quad \sigma_{r\theta} = -\frac{\partial^2 F}{\partial r \partial \theta}\left(\frac{F}{r}\right) \tag{4.47}$$

The stress function F is governed by a biharmonic equation:

$$\nabla^4 F = \left(\frac{\partial^2}{\partial r^2} + \frac{1}{r}\frac{\partial}{\partial r} + \frac{1}{r^2}\frac{\partial^2}{\partial \theta^2}\right)F = 0 \tag{4.48}$$

The only solution of that equation which has the essential properties of a dislocation is

$$F = -Dr\sin\theta \ln\left(\frac{r}{b}\right), \qquad D = \frac{bE}{4\pi(1-\nu^2)} \tag{4.49}$$

where ν is the Poisson's ratio and E is the Young's modulus

The stresses are derived from the stress function F

$$\sigma_{rr} = \sigma_{\theta\theta} = -\frac{D\sin\theta}{r}, \quad \sigma_{r\theta} = \frac{D\cos\theta}{r}, \tag{4.50}$$

$$\sigma_{zz} = \nu(\sigma_{rr} + \sigma_{\theta\theta}), \quad \sigma_{rz} = \sigma_{\theta z} = 0$$

The strain components are given in terms of stresses by [14]:

$$\varepsilon_{rr} = \frac{1}{E}(\sigma_{rr} - \nu(\sigma_{\theta\theta} + \sigma_{zz})) = -\frac{b(1-2\nu)\sin\theta}{4\pi(1-\nu)r} \tag{4.51}$$

$$\varepsilon_{\theta\theta} = \frac{1}{E}(\sigma_{\theta\theta} - \nu(\sigma_{rr} + \sigma_{zz})) = -\frac{b(1-2\nu)\sin\theta}{4\pi(1-\nu)r}$$

$$\varepsilon_{zz} = \frac{1}{E}(\sigma_{zz} - \nu(\sigma_{rr} + \sigma_{\theta\theta})) = 0$$

$$\varepsilon_{r\theta} = \frac{1+\nu}{E}\sigma_{r\theta} = \frac{b\cos\theta}{4\pi(1-\nu)r}$$

Let us consider the mean square strain $\overline{\varepsilon_n^2}$ along the direction $\bar{n}$ in the radial plane of the dislocation, where $\bar{n}$ is the radial component of the diffracting plane normal $\bar{N}$. By definition

$$\overline{\varepsilon_n^2} = \frac{1}{\pi r^2}\int_{r_0}^{r}\int_{0}^{2\pi} \varepsilon_{nn}^2 r dr d\theta \tag{4.52}$$

where ε_{nn} is the strain tensor element along $\bar{n}$ direction. It can be found by changing the polar coordinate system (r,θ) to a new rectangular coordinate system (x',y'), defined in such a way that axis x' is parallel to the direction $\bar{n}$. The transformation equations for these two coordinate systems are

$$x' = r\cos(\gamma-\theta), \qquad r = \sqrt{x'^2+y'^2} \tag{4.53}$$

$$y' = r\sin(\gamma-\theta), \quad \theta = \gamma - \tan^{-1}\frac{y'}{x'}$$

where γ is the angle between the Burger's vector $\bar{b}$ and $\bar{n}$. A displacement vector having components U_r and U_θ in the (r,θ) coordinate system is considered to have components $U_{x'}$, $U_{y'}$ in the (x',y') coordinate system. The new components are expressed in terms of the original components by means of transformation equations

$$U_{x'} = U_r\cos(\gamma-\theta) + U_\theta\sin(\gamma-\theta) \tag{4.54}$$

$$U_y' = U_\theta\cos(\gamma-\theta) - U_r\sin(\gamma-\theta)$$

By definition

$$\varepsilon_{nn} = \varepsilon_{xx} = \frac{\partial U_{x'}}{\partial x'} = \left(\frac{\partial r}{\partial x'}\frac{\partial}{\partial r} + \frac{\partial\theta}{\partial x'}\frac{\partial}{\partial\theta}\right)U_{x'} = \tag{4.55}$$

$$= \left(\cos(\gamma-\theta)\frac{\partial}{\partial r} + \frac{1}{r}\sin(\gamma-\theta)\frac{\partial}{\partial\theta}\right)(U_r\cos(\gamma-\theta) + U_\theta\sin(\gamma-\theta)) =$$

$$= \cos^2(\gamma-\theta)\frac{\partial U_r}{\partial r} + \sin^2(\gamma-\theta)\left(\frac{1}{r}\frac{\partial U_\theta}{\partial\theta} + \frac{U_r}{r}\right) + \cos(\gamma-\theta)\sin(\gamma-\theta)\left(\frac{\partial U_\theta}{\partial r} + \frac{1}{r}\frac{\partial U_r}{\partial\theta} - \frac{U_\theta}{r}\right) =$$

$$= \cos^2(\gamma-\theta)\varepsilon_{rr} + \sin^2(\gamma-\theta)\varepsilon_{\theta\theta} + 2\cos(\gamma-\theta)\sin(\gamma-\theta)\varepsilon_{r\theta}$$

Finally, the mean square strain along the direction $\bar{n}$ is given as

$$\overline{\varepsilon_n^{\,2}} = \frac{1}{\pi r^2}\int_{r_0}^{r}\int_{0}^{2\pi}\left[-\frac{b(1-2\nu)\sin\theta}{4\pi(1-\nu)r}+\frac{b\cos\theta}{2\pi(1-\nu)r}\sin(\gamma-\theta)\cos(\gamma-\theta)\right]^2 r\,dr\,d\theta \tag{4.56}$$

Taking the Poisson's ratio ν equal to $\frac{1}{3}$ the above integral become

$$\overline{\varepsilon_n^{\,2}} = \frac{b^2}{128\pi^2 r^2}\left(5+12\cos^2\gamma\right)\ln\frac{r}{r_0} \tag{4.57}$$

It appears that the lower limit of integration r_0 must be non zero value, otherwise the denominator is zero. Thus, we have to consider a hollow tube of material with internal radius r_0 instead of a solid cylinder. It has a direct physical meaning:

First, the material has a discrete nature and the displacement vector r could not be smaller than an atomic spacing. Second, Hook's law assumption of the elastic deformation does not hold at the vicinity of the dislocation line. Usually, r_0 is taken to be an order of magnitude of a few atomic spacings, $r_0 \approx 10^{-7}$ cm.

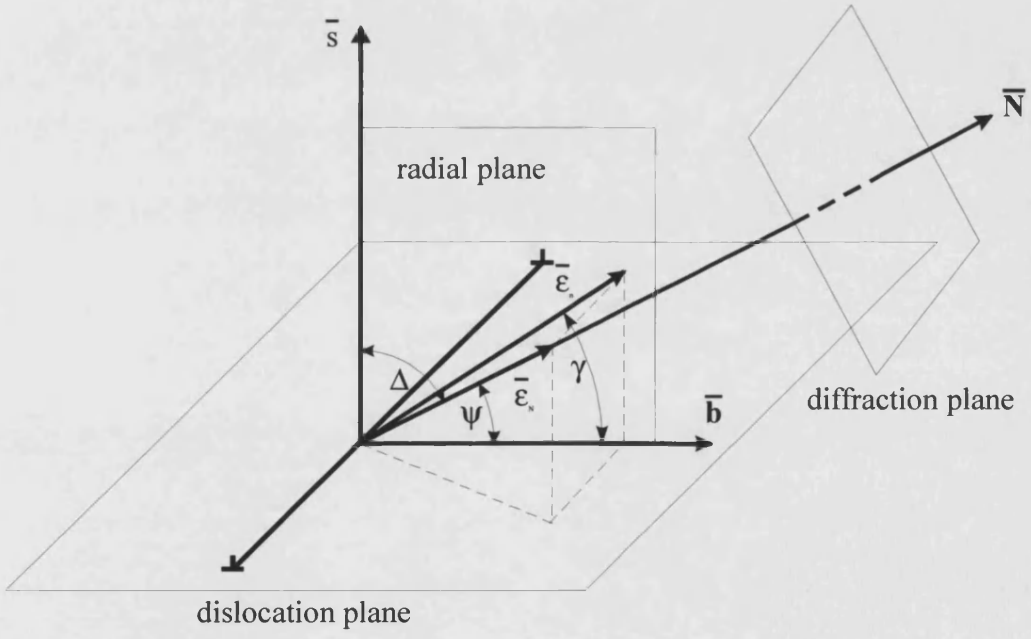

Figure 4.7. Strain field of edge dislocation.

The lattice dilation component along the diffracting plane normal $\overline{N}$ is found from simple geometrical considerations. Defining Δ as the angle between the dislocation glide plane and $\overline{N}$, and ψ as the angle between the Burger's vector $\bar{b}$ and $\overline{N}$, then

$$\overline{\varepsilon_N{}^2} = \overline{\varepsilon_n{}^2}(\cos^2\Delta + \cos^2\psi) \tag{4.58}$$

Noting that

$$\cos^2\gamma = \frac{\cos^2\psi}{\cos^2\Delta + \cos^2\psi} \tag{4.59}$$

The mean square strain along $\overline{N}$ is

$$\overline{\varepsilon_N{}^2} = \frac{b^2}{128\pi^2 r^2}\left(5\cos^2\Delta + 17\cos^2\psi\right)\ln\frac{r}{r_0} \tag{4.60}$$

4.7. Appendix 2. Strain fields of a screw dislocation.

For a screw dislocation lying along z axis the only component of displacement is U_z, being given by

$$U_z = \frac{b}{2\pi}\theta \tag{4.61}$$

Only pure shear strains are involved

$$\varepsilon_{xz} = -\frac{b}{4\pi(x^2+y^2)}y = -\frac{b}{4\pi r}\sin\theta \tag{4.62}$$

$$\varepsilon_{xz} = \frac{b}{4\pi(x^2+y^2)}x = \frac{b}{4\pi r}\cos\theta$$

and all other components vanish [16]

The strain along the diffracting plane normal $\overline{N}$ is found from shear strains by a transition to a new coordinate system (x', y', z') with axes z' parallel to $\overline{N}$ and axis x' lying in the

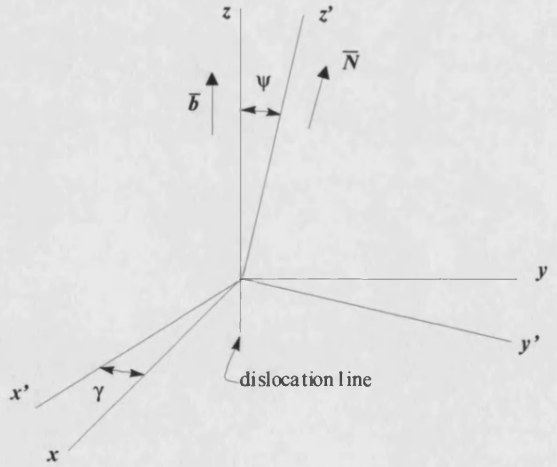

Figure 4.8. Transformation of coordinate system

xy plane. The transformation can be uniquely described in terms of angles ψ and γ, where ψ is the angle between z and z', and γ is the angle between x and x'. Then, the strain along $\overline{N}$ is given by strain component $\varepsilon_{z'z'}$.

The strain components referred to the new set of axes (x', y', z') can be found from first principals, i.e. by differentiating $\frac{\partial U_{z'}}{\partial z'}$ as it was done in Appendix 1. However, here we will use more general approach. By definition, a second order tensor has the transformation law

$$a_{rs} = \sum_{i,j} \ell_{ri} \ell_{sj} a_{ij} \tag{4.63}$$

where ℓ_{ij} are the elements of the rotational matrix T

$$T \equiv [\ell_{ij}] = \begin{bmatrix} \cos(\hat{xx'}) & \cos(\hat{yx'}) & \cos(\hat{zx'}) \\ \cos(\hat{xy'}) & \cos(\hat{yy'}) & \cos(\hat{zy'}) \\ \cos(\hat{xz'}) & \cos(\hat{yz'}) & \cos(\hat{zz'}) \end{bmatrix} \tag{4.64}$$

From equations (4.62), (4.63) we have

$$\varepsilon_{z'z'} = \ell_{z'x} \ell_{z'z} \varepsilon_{xz} + \ell_{z'y} \ell_{z'z} \varepsilon_{yz} \tag{4.65}$$

where

$$\ell_{z'x} = \cos(\hat{z'x}) = -\sin\gamma \sin\psi \tag{4.66}$$

$$\ell_{z'y} = \cos(\hat{z'y}) = \cos\gamma \sin\psi$$

$$\ell_{z'z} = \cos(\hat{z'z}) = \cos\psi$$

Substituting (4.66) into (4.65)

$$\varepsilon_{z'z'} = \sin\psi \cos\psi (\cos\gamma \varepsilon_{yz} - \sin\gamma \varepsilon_{xz}) = \tag{4.67}$$

$$= \frac{b}{4\pi r} \sin\psi \cos\psi (\cos\gamma \cos\theta + \sin\gamma \sin\theta)$$

The mean square strain along $\overline{N}$ is found as

$$\overline{\varepsilon_N^2} = \frac{1}{\pi r^2}\int_{r_0}^{r}\int_{0}^{2\pi}\left[\sin\psi\cos\psi(\cos\gamma\varepsilon_{yz} - \sin\gamma\varepsilon_{xz})\right]^2 r\,d\theta dr = \tag{4.68}$$

$$\frac{b^2}{16\pi^3 r^2}\sin^2\psi\cos^2\psi\int_{r_0}^{r}\int_{0}^{2\pi}\frac{1}{r}(\cos\gamma\cos\theta + \sin\gamma\sin\theta)^2 d\theta dr =$$

$$\frac{b^2}{16\pi^2 r^2}\sin^2\psi\cos^2\psi\ln\left(\frac{r}{r_0}\right)$$

4.8. References

1. B. Heying, X.H.Wu, S.Keller, Y.Li, D.Kapolnek, B.P.Keller, S.P.Denbaars, J.S.Speck, Appl. Phys. Lett. 68, 643 (1996)
2. J. Chaudhuri, C. Ignatiev, S. Stepanov, D. Tsvetkov, A. Cherenkov, V. Dmitriev, Z. Rek, Materials Science and Engineering, B78 (2000) 22–27
3. G. K. Williamson and W. H. Hall, Acta Metall. 1,22 (1953)
4. H.-M. Wang, J.-P. Zhang, C.-Q. Chen, Q. Fareed, J.-W. Yang, and M. A. Khan, Appl. Phys. Lett., 81, 604 (2002)
5. V.Shricant, J.Speck, D.Clarke, J.Appl. Phys., **82**, 4286
6. B.Jahnen, M.Albrecht, W.Dorsh, S.Cristiansen, H.P.Strunk, D.Hanser, R.P.Davis, MRS Internet J.NitrideSemicond. Res. **3**, 39 (1998)
7. T.Metzger, R.Hopler, E.Born, O.Ambacher, M.Stutzmann, R.Stommer, M.Schuster, H.Gobel, S.Christiansen, M.Albreight, H.P.Strunk, Philosophical Magazine A, v.77,1013-1025.
8. P. Vennegues, B. Beaumont and P. Gibart, Mat. Sci. and Eng B, v 43, 274-278
9. P. Visconti, M. A. Reshchikov, F. Yun, K. M. Jones and H. Morkoc A. Passaseo, E. Piscopiello, A. Pomarico and R. Cingolani, M. Lomascolo, M. Catalano, MRS Spring 2001Meeting, E3.8
10. C. Ferrari, L. Francesio, P.Franzosi, S.Gennari, Appl. Phys. Lett., 69, 4233 (1996)
11. D.K. Bowen, B.K. Tanner, "High resolution x-ray diffractometry and topography", Taylor & Francis, 2002
12. M.J. Hordon, B.L. Averbach, Acta Metallurgica, v 9, p237 (1961)
13. B.D. Cullity: Elements of X-ray Diffraction, Addison-Wesley Pub. Co., 1967
14. D.S.Dugdale, "Elements of elasticity", Pergamon Press, 1968.
15. J.H.Hirth, J.Lothe, "Theory of dislocations", McGraw-Hill Inc.,1968
16. F.R.N. Nabarro, "Theory of crystal dislocations", Oxford, Clarendon Press, 1967

5. P-type doping of GaN

5.1. Introduction.

P-type GaN is of a critical importance for high performance optoelectronic devices. Among all other elements, Mg is the only efficient species used as a p-type dopant in MOCVD grown GaN. No other impurity has been so successful in producing p-type conductivity in GaN. Nevertheless, effective p-type doping of III-Nitrides remains to be a challenging task. The activation energy of Mg is relatively high (typically about 150–200 meV), therefore only a few percent of Mg atoms are electrically active at room temperature. Thus, the Mg doping level in around of 10^{19} cm^{-3} is required to achieve the hole concentration in the 10^{17} cm^{-3} range. The corresponding hole mobility is around 10 cm^2/Vs and the specific resistivity of Mg doped films remains high. This limited p-type conductivity is one of the major reasons that hampers further rapid development of nitride-based electronic devices. For efficient light emitting diodes, laser diodes, ohmic contacts etc. doping densities of about $10^{18}cm^{-3}$ are desirable.

The Mg doping of GaN is comprehensively reviewed in the scientific literature. Here we will briefly mention only most important results on Mg doping of GaN. For a more thorough review on doping of III-nitrides one could refer to the publication by Sheu and Chi [1] and references cited. Published results can be roughly divided into three groups: (1) reports on Mg-doped GaN, (2) reports on Mg co-doped GaN, (3) reports on Mg-doped superlattices. For the first group, GaN was doped by Mg only and low-resistivity material was achieved by optimisation of doping level, growth parameters and annealing conditions. For the second group, GaN was co-doped with Mg and other elements (Si, O, Zn, etc), which helps to reduce the activation energy of the acceptor. For the third group, the activation energy of the acceptor was reduced by modification of the zone diagram of GaN using a superlattice structure. A summary of the best published results on Mg-doping

can be found in Table 12. In this chapter we will discuss Mg doping and Mg co-doping. Mg doped superlattice structures will be reviewed in Chapter 10.

Table 12. Review of the best published results on Mg-doping of GaN.

Reference	ρ, Ωcm	p, cm^{-3}	μ_H, cm^2/Vs	Mg, cm^{-3}	Comments
Mg-doped GaN					
Tokunaga *et al* [2]	1.04	8×10^{17}	7.5	8×10^{19}	Horizontal atmospheric system with 3-layered laminar flow gas injection.
Sugiura *et al* [30]	0.8-1.0	$0.8\text{-}2\times10^{18}$	5-10	6×10^{19}	Atmospheric pressure system, H_2-free ambient
C.-R. Lee et al [3]	1.1	3.2×10^{17}	17.5	-	Using SiO_2 cap layer during *ex situ* annealing
Kumakura *et al* [4]	-	6.7×10^{17}	-	3×10^{19}	0.4 μm-thick Mg-doped $In_{0.14}Ga_{0.86}N$ layer grown at 780 C
Mg-codoped GaN					
Kim *et al* [5]	0.72	8.5×10^{17}	10	2×10^{19}	Mg+Zn co-doping, ratio Cp_2Mg:DEZn is about 1000:1 ?
Kim *et al* [13]	1.26	4.5×10^{17}	11	-	Mg+Si co-doping, without Si hole concentration was higher (6.7×10^{17} cm^{-3})
Aoyagi *et al*	-	4.5×10^{18}	-	-	Mg+Si co-doping, ALE epitaxy (Details in Technical Notes)
Korotkov *et al* [12]	0.2	2×10^{18}	16	2×10^{19}	Mg+O co-doping, Oxygen concentration in the reactor 4.0—11.5 ppm
Mg-doped superlattice structures					
Kumakura *et al* [6]	-	3×10^{18}	-	2×10^{19}	25-30 period $Al_xGa_{1-x}N$/GaN (240/120Å) SL, x=0.13–0.30
Kumakura *et al* [7]	0.45	2.8×10^{19}	-	3×10^{19}	45-period $In_xGa_{1-x}N$/GaN (40/40Å) SL, x=0.10 and 0.22
Kozodoy *et al* [8]	-	3×10^{18}	10	-	25-period uniformly doped $Al_{0.2}Ga_{0.8}N$/GaN (80/80Å) SL
Kozodoy *et al* [8]	-	1.9×10^{19}	19	-	Modulation-doped 25-period $Al_{0.12}Ga_{0.88}N$/GaN (80/80Å) SL Plasma-assisted MBE was used for growing this SL on top of MOCVD-grown GaN based layers.

5.2. Mg doped GaN

As we mentioned before, the highest hole concentrations at room temperature in MOCVD grown Mg-doped GaN, as reported by several groups, are in the 5×10^{17}–1×10^{18} cm^{-3} range for doping levels in the mid 10^{19} cm^{-3} range. The specific resistivity of the layers is about 1–2 Ωcm. Achieving higher hole concentrations with Mg as the dopant has proved very difficult. The further increase of the doping level results in the decrease of the hole concentration. Among the possible reasons for difficulties to achieve higher hole concentration different authors have cited:

- Compensation by the residual donor impurities such as oxygen
- Deterioration of the layer crystallinity at very high doping levels
- Limit of Mg solubility and formation of Mg_3N_2
- Self-compensation by formation of Mg-related donor levels

According to the publication of Kozodoy *et al* [9], temperature dependent Hall measurements indicate that concentration of compensating donors in Mg-doped GaN is in the 10^{18}–10^{19} cm^{-3} range. On the other hand, concentration of residual donor impurities such as silicon and oxygen in the undoped GaN is well below 10^{17} cm^{-3}. Therefore, we can conclude that compensation by residual impurities played some role in the early days of GaN epitaxy, but for the modern stage of technology it is definitely not a major issue.

A deterioration of the layer crystallinity is also unlikely to be the cause for the drop of the hole concentration at high doping levels. Firstly, results of x-ray analysis and surface morphology observations suggest that a significant deterioration the layer crystallinity occurs only for a very high Mg doping levels (>10^{20} cm^{-3}). Secondly, as the hole mobility is very sensitive to the degradation of the crystalline structure, one should expect a dramatic decrease of the hole mobility with the increase of the doping level. Nevertheless, experimental results indicate that the hole mobility does not change much with Mg

concentration. Therefore, we can conclude that deterioration of the layer crystallinity does not play a significant role in reduction of the hole concentration.

If the solubility of Mg were the limiting factor, one would expect the hole density to increase with Mg concentration and saturate at maximum value. However, the decrease of the hole concentration for high doping levels is not explained by this theory. Another argument against is that the formation of the second phase Mg_3N_2 is observed only for high Mg doping levels (10^{20}–10^{21} cm^{-3}). We can conclude that for typical doping levels below 10^{20} cm^{-3} solubility of Mg is not the major factor for the decrease of the hole concentration.

Self-compensation is the only remaining possibility to explain the decrease of the hole concentration at high doping levels. Two major arguments support this theory. Firstly, temperature dependent Hall measurements indicate high concentration of compensating donors in Mg-doped layers. Secondly, GaN layers with high Mg concentration exhibit strong donor-acceptor recombination at 2.8 eV. The most natural choice of acceptor is Mg_{Ga} (shallow acceptor), while donor is thought to be a complex of Mg with nitrogen vacancy MgV_N (deep donor).

Nitrogen vacancy is a most common native defect in GaN. It acts as a triple donor and can accept charge q from 0 to $+3\bar{e}$. The formation energy of the nitrogen depends on the position of the Fermi level E_F, In other words, the formation energy of nitrogen vacancies is quite high in n-type GaN, but is significantly lower in p-type GaN. Because of low formation energy, nitrogen vacancies are easily generated during the growth of Mg-doped GaN. According to Haufmann et al [10] the concentration of nitrogen vacancies N_V is given by the following phenomenological equation:

$$N_V \propto \exp\left(\frac{-qE_F}{kT}\right) \tag{5.1}$$

where q is the charge state of the vacancy, i.e. 0 to +3, and E_F is the Fermi level. Thus the concentration of nitrogen vacancies increases exponentially when E_F approaches the valence band, i.e. with increasing hole concentration. In the same manner, the concentration of nitrogen vacancies is rapidly increasing with temperature.

Now we suggest the following mechanism for formation of vacancy MgV_N complexes. First, nitrogen vacancies are generated during the epitaxial growth of Mg-doped GaN at high temperature (T≈1300 K). The nitrogen vacancies are mobile at growth temperatures and positively charged; therefore, they are attracted to negatively charged Mg acceptors forming a V_NMg complex. Because migration of V_NMg complexes is limited, they are more stable than stand-alone nitrogen vacancies. Therefore it is reasonable to assume that after cooling down the equilibrium concentration of V_NMg complexes corresponding to the growth temperature is frozen. For simplicity, we assume that all generated nitrogen vacancies are coupled with Mg atoms. In this case the resulting concentration of acceptors N_A and donors N_D is given by

$$N_A = N_{Mg} - C\exp\left(\frac{-qE_F}{kT}\right) \qquad N_D = C\exp\left(\frac{-qE_F}{kT}\right) \tag{5.2}$$

where N_{Mg} is the doping level and C is some coefficient which depends on density of sites in GaN lattice and entropy of nitrogen vacancy formation. In our phenomenological model we treat C as a fitting parameter. For simplicity, we assume that all nitrogen vacancies are in the charge state +3. The position of the Fermi level is found from the electroneutrality equation:

$$N_{cond} f(E_g,T) + m_A N_A f(E_A,T) - N_{val}(1-f(0,T)) - m_D N_D (1-f(E_D,T)) = 0 \tag{5.3}$$

where N_{cond}, N_{val} are the effective densities of states in conduction and valence bands, respectively, m_A and m_D are the multiplicity factors, and $f(E,T)$ is the Fermi distribution function:

$$N_{cond} = 0.43 \cdot 10^{15} \cdot T^{3/2} \ (\text{cm}^{-3}) \qquad N_{val} = 8.9 \cdot 10^{15} \cdot T^{3/2} \ (\text{cm}^{-3}) \qquad (5.4)$$

$$m_A = 1 \qquad m_D = 2$$

$$f(E,T) = \frac{1}{1 + \exp\left(\frac{E - E_F}{kT}\right)} \qquad (5.5)$$

For p-type material $E_F << E_g$, $E_F << E_N$ holds and the equation (5.3) can be simplified

$$(N_{Mg} - N_D) f(E_A,T) - N_{val}(1 - f(0,T)) - 2N_D = 0 \qquad (5.6)$$

Strictly speaking, the acceptor activation energy E_A depends on the doping level and varies from 100 meV to 250 meV. For the sake of simplicity, a constant value of 160 meV is used here. Solving equation (5.6) for $T \approx 1300\,\text{K}$ we can find the position of the Fermi level at growth temperature. Then the concentration of acceptors N_A and compensating donors N_D can be readily calculated using equation (5.2). After that we solve equation (5.6) for $T \approx 300\,\text{K}$ to find the position of the Fermi level at room temperature. Finally, the room temperature hole concentration is given by

$$p = N_{val}(1 - f(0,T)) \qquad (5.7)$$

In the above calculations the fitting parameter C in the equation (5.2) was arbitrary chosen to be 5×10^{21} cm^{-3} as this value gives reasonably good agreement with experiment. Figure 5.1 shows the calculated dependence of the hole concentration versus the doping level. Two cases were considered: one in which donor concentration is negligibly small $N_D = 0$, and another where Mg doping generates V_NMg donors. Although this crude model is not accurate enough in a quantitative sense, it allows making some important qualitative observations. First, due to large activation energy, the hole concentration is increasing much slower than the doping level. Hole density in the beginning of the 10^{17} cm^{-3} range can be easily achieved with a moderate Mg concentration in the 10^{17}–10^{18} cm^{-3} range. However, in order to increase hole concentration 10 times one should

increase Mg doping level 50-100 times. Second, the influence of self-compensating effects is negligible for Mg concentrations below 10^{19} cm^{-3}, but becomes progressively more significant with increase of the doping level.

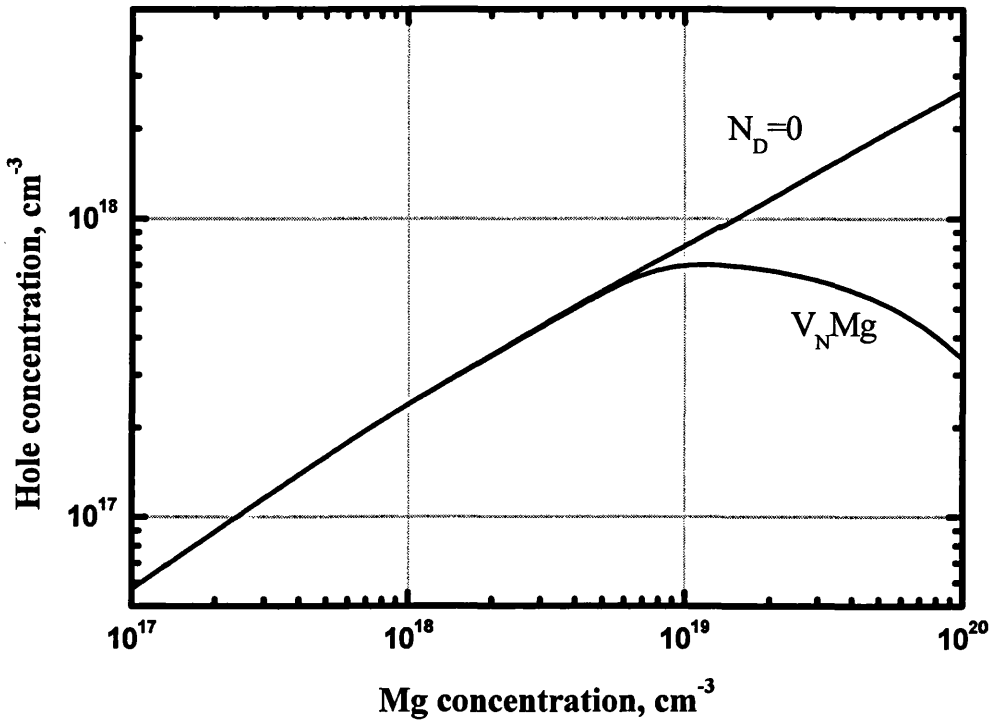

Figure 5.1. Calculated hole concentration versus Mg doping level

5.3. Co-doped GaN

Recently, there was a number of theoretical [11] and experimental [12,13,14] publications on co-doping of GaN, in which both n- and p-type dopants are introduced into the GaN layer. The co-doping method is considered to form meta-stable acceptor-donor complexes, which have lower activation energy, than acceptor alone. Additionally, the carrier mobility of co-doped samples is believed to increase due to the replacement of long-range Coulomb scattering in the case of a simple doping, by short-range dipole scattering.

Using Mg+O co-doping Korotkov et al [12] reduced the resistivity of the p-type layer from 8 Ωcm to 0.2 Ωcm and increased the hole density from 1×10^{17} cm^{-3} to 2×10^{18} cm^{-3},

while reducing the activation energy to 135 eV. Reverse engineering of Nichia's commercially available white LED revealed, that the p-type cladding layer contained a high concentration of Mg ($\sim 2\times10^{20}$ cm^{-3}) and O ($\sim 1\times10^{20}$ cm^{-3}) [11]. Just a few publications on successful Mg+Si co-doping are available. Kim et al [13] reported increase of the hole concentration from 4.3×10^{17} cm^{-3} to 8.5×10^{17} cm^{-3} with Mg+Si co-doping. However, higher flow of Si resulted in n-type material. It could be argued that Mg+Si co-doping is not efficient due to a chemical interaction between Si and NH_3 during the growth. Ammonia affects the surface diffusion of Si adatoms and prevents the formation of Mg-Si complex. To overcome this problem, an alternative co-doping method has been proposed [14]. In this method, GaN is grown by alternative supply of TMGa and NH_3 with a sequence of 1 sec and 3 sec interval for each source gas in a low pressure MOCVD reactor. Mg doping material (Cp_2Mg) is supplied during TMGa feeding and Si doping material (TESi) is supplied just after the feeding of Mg source within the purging time of TMGa before NH_3 feeding time.

According to publications of Kim [5,13] and Cho [15] Mg+Zn co-doping increases the hole concentration (up to 8.5×10^{17} cm^{-3}) and improves the structural quality of GaN as compared to the only Mg-doped GaN layer. In addition, the specific contact resistance for Mg+Zn co-doped GaN (5.0×10^{-4} Ωcm^2) is lower by one order of magnitude than that for Mg-doped only GaN film (1.9×10^{-3} Ωcm^2). Interestingly, the Cp_2Mg flow was 0.643 μmol/min (Mg/Ga ratio of 7.6×10^{-3}) and the DEZn flow was only 0.616 nmol/min (Zn/Ga ratio of 7.3×10^{-6}). According to our SIMS measurements and Amano's data on Zn incorporation [16] the solid-vapour ratio of Zn to Ga at typical growth temperatures (~1000°C) is about 1×10^{-3}. This means that with given Zn/Ga ratio of 7.3×10^{-6} in the gas phase the Zn/Ga ratio in the solid will be 7.3×10^{-9}, which corresponds to Zn concentration of 3×10^{14} cm^{-3}. Such a low concentration can hardly have any effect on electrical or

structural properties of the material. We have carried out similar experiments on Mg+Zn co-doping but have not observed any improvement of p-type doping.

5.4. Mg activation

Another particularity of Mg doping during MOCVD growth is the necessity of a special activation procedure. Generally, as-grown Mg-doped GaN films exhibit insulating behaviour. According to commonly adopted theory, in as-grown samples Mg atoms are passivated by hydrogen forming electrically neutral complexes. The formation of Mg-H complexes is supported by experiments of Theys *et al* [17]. They have studied deuterium diffusion in GaN layers when they are exposed to a remote deuterium plasma at 500°C. They have found that deuterium diffuses deeply in Mg doped GaN samples altering the native hydrogen profile. On the other hand, in the same plasma conditions, deuterium does not diffuse significantly in non-intentionally doped samples. For detailed study on various hydrogen related complexes in GaN one should refer to the work of Reboredo *et al* [18]. Due to formation of these complexes, magnesium tends to incorporate in GaN in electrically inactive form. The activation of Mg can be achieved by thermal annealing or by electron beam irradiation. Amano *et al* [19] have demonstrated that Mg atoms can be activated by low energy electron beam irradiation after the growth. Later, Nakamura *et al* [20] showed that the same effect can be achieved by thermal annealing in hydrogen-free ambient.

Usually, temperature in the range 600°C–900°C is required to activate Mg acceptors. As a rule, annealing temperature and annealing time are interdependent, i.e. lower annealing temperature requires longer annealing time and vice versa. It has been widely discussed that too high annealing temperature can generate defects reducing hole concentration. Fujita *et al* [21] have studied successive dehydrogenation and hydrogenation of Mg acceptors in GaN by N_2 and H_2 annealing, respectively, at different

temperatures. The authors have found that the higher annealing temperature reduces the number of unfavourable scattering centres originating from Mg-H bondings. Annealing at the temperature higher than the growth temperature results in compensation but does not enhance the generation of scattering centres. Even if the GaN experiences thermal damage by high temperature annealing, it is not destructive and can be well recovered by appropriate hydrogenation/dehydrogenation treatments afterwards. It has been reported [22,23] that rapid thermal annealing (RTA) has certain advantages for Mg activation compared to conventional furnace annealing. High ramp up rates in temperature (up to 100°C/s), allow an efficient activation of the Mg dopant but avoid the formation of nitrogen vacancies, which may eventually compensate the p-type conductivity.

Waki *et al* [24] reported on successful activation of Mg by deposition of a Ni film on the sample surface and performing a low-temperature annealing in nitrogen at 200°C. These results suggest that the Ni film significantly enhances hydrogen desorption from the GaN film, which results in the activation of Mg-doped GaN at quite low temperatures.

Lee *et al* [25] have studied the annealing effect of Mg-doped GaN epilayers capped with SiO_2 layer. The samples were annealed in nitrogen at various temperatures, after that the SiO_2 was removed by chemical etching. The hole concentration of the GaN:Mg epilayers capped with SiO_2 after annealing was much higher than that of the layer annealed without SiO_2 at any temperatures. The authors explained this phenomenon by reduced out-diffusion of cracked Mg from MgH complex in the samples with SiO_2 layer during annealing.

Recently, it has been found that magnesium can be activated by thermal annealing in oxygen atmosphere [26]. The authors have found that when activated in O_2 containing ambient, the resistivity was considerably lower, at any given temperature, than that of samples activated in pure N_2. This phenomenon is believed to result from chemical interaction of oxygen with hydrogen, which is responsible for passivation of Mg acceptors.

5.5. Mg doping during MOCVD growth

5.5.1. Mg precursors

A priori, two magnesium precursors are available, the bis(cyclopentadienyl)magnesium (Cp_2Mg) and the bis(methylcyclopentadienyl)magnesium ($(MeCp)_2Mg$). The Cp_2Mg is commonly used to obtain Mg-doped GaN. However, the Cp_2Mg is solid at practical temperatures (melting point of 176°C) and has those typical problems, which are common to all solid sources, i.e. non-equilibrium vapour pressure, poor stability and efficiency degrading with time. Furthermore, significant memory effects have been experienced when using a solid Cp_2Mg source due to low transport efficiencies resulting in uncontrollable doping levels.[27]

The $(MeCp)_2Mg$ has lower melting point (29°C) and potentially does not have these drawbacks. However, this precursor is much more reactive compared to the Cp_2Mg. It reacts in the gas phase with ammonia producing tiny solid particles, reducing magnesium incorporation and deteriorating the epilayer [28].

Several commercial manufactures of metalorganic precursors for MOCVD growth have addressed these problems by offering an efficient magnesium precursor system where solid Cp_2Mg is suspended in an extremely low vapour pressure hydrocarbon liquid[a]. The behaviour of this system is expected to be very similar to TMIn solution [29]. The solvent forms a liquid layer over the solid Cp_2Mg and it is assumed that the Cp_2Mg is vaporized directly from the solution. A dynamic equilibrium establishes between the solid Cp_2Mg, Cp_2Mg in the vapour and the Cp_2Mg dissolved in the hydrocarbon solvent. [27] As Cp_2Mg is vaporized from the solution a similar quantity of solid Cp_2Mg dissolves into the solvent, maintaining a constant saturated liquid phase concentration.

The Cp_2Mg solution offers the following advantages:

---

[a] For example Solution Magnesocene™ manufactured by Epichem

- Constant output of Cp_2Mg over nearly the entire life of the source
- Speedy response like other liquid metalorganics
- Vapour pressure effectively the same as that of Cp_2Mg
- More contact time between the carrier gas (hydrogen) and the Cp_2Mg
- Reduced memory effects due to increasing transport efficiency

Recent work on solution Cp_2Mg in comparison with $(MeCp)_2Mg$, showed that solution Cp_2Mg increased by twofold the efficiency of Mg incorporation and gave a reliable delivery [28]. We have carried out experiments on p-type doping of GaN using both solid Cp_2Mg source and liquid Cp_2Mg source.

5.5.2. P-type doping using solid Cp_2Mg source.

The Mg-doped epilayers were grown on (0001) sapphire substrates. Before the growth, substrates were annealed at 1200°C in hydrogen. A low temperature GaN nucleation layer was deposited at 540-560°C. Then the substrate temperature was raised to 1160°C for the growth of 1.5μm thick nominally undoped GaN buffer layer. After that, the temperature was lowered to 1070°C for the deposition of Mg-doped GaN layer (~0.5 μm thick). The reactor pressure was 200 mbar during the growth of undoped GaN buffer and 100 mbar during the growth of Mg-doped GaN. The source materials were TMGa (for undoped GaN buffer), TEGa (for Mg-doped GaN), NH_3 and Cp_2Mg. Hydrogen was used as a carrier gas. During the growth of p-type GaN, the TEGa flow was kept constant at 34 μmol/min for all samples, while Cp_2Mg flow was varied from 62 nmol/min to 168 nmol/min. The details of the growth conditions and results of electrical measurements are presented in Table 13 and Figure 5.2.

Table 13. Growth conditions and electrical properties of Mg-doped GaN samples.

Growth run	Mg flow, nmol/min	ρ, Ωcm	μ_H, cm^2/Vs	p, cm^{-3}	T_{growth}, °C
134	82.5	2.2	7.1	3.9×10^{17}	1070
135	168.0	3.1	5.1	4.0×10^{17}	1070
191	82.5	2.9	10	2.2×10^{17}	1070
192	168.0	6.0	7.8	1.3×10^{17}	1070
193	118.0	3.9	11	1.4×10^{17}	1070
194	62.5	3.9	11	1.4×10^{17}	1070
195	168.0	2.5	11	2.2×10^{17}	1070
196	82.5	1.9	16	2.0×10^{17}	1070
197	82.5	3.0	12	1.7×10^{17}	1050
198	118.0	2.2	9	3.1×10^{17}	1070

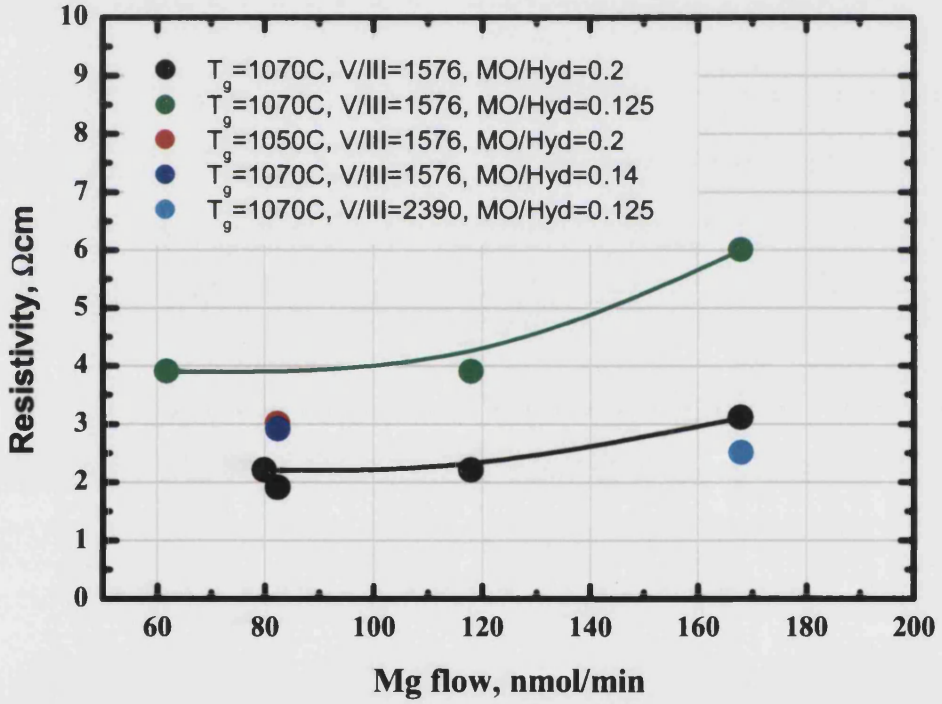

Figure 5.2. Resistivity of Mg-doped GaN layers versus Cp_2Mg flow.

5.5.3. P-type doping using Solution Magnesocene

Mg-doped GaN layers were grown on (0001) sapphire substrates using a similar deposition procedure to the one described above. The growth sequence included the annealing in hydrogen, the growth of the low temperature nucleation layer (30 nm), the growth of undoped GaN layer (~1 μm), the growth of a Zn-doped layer (~1 μm) and the

growth of Mg-doped layer (0.5 μm). The insulating Zn-doped layer was added to the structure to prevent current leakage through the buffer layer during electrical measurements. GaN:Mg layer was deposited at 1070°C and 100 mbar. The sources of Ga, N and Mg were TEGa/TMGa, NH_3 and Cp_2Mg solution, respectively. Samples 348–356 were grown using TEGa precursor with TEGa flow being 31.5 μmol/min. Samples 543–549 were grown using TMGa precursor with TMGa flow being 17.7 μmol/min. The Cp_2Mg flow was varied from 69 nmol/min to 743 nmol/min. The samples grown using TMGa precursor exhibit similar properties to that of specimens grown using TEGa precursor. It is interesting to note, that in terms of growth rate TMGa is almost twice more efficient precursor than TEGa.

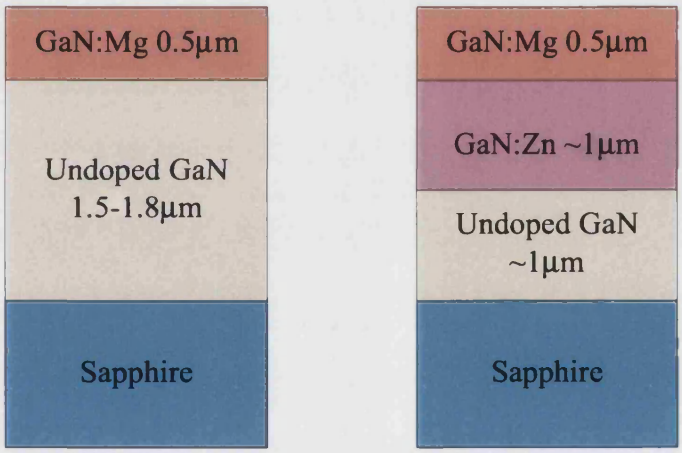

Figure 5.3. GaN:Mg structures without insulating layer (left) and with insulating layer (right).

After the growth, the samples were annealed in nitrogen (or oxygen) ambient for activation of acceptors. The annealing procedure will be is discussed later on in more detail. The samples were characterised using a secondary ion mass spectroscopy (SIMS), photoluminescence (PL), Hall effect and resistivity measurements. The details of the growth parameters and electrical properties are summarized in Table 14.

Table 14. Growth conditions and electrical properties of Mg-doped GaN samples, grown with Solution Magnesocene source.

Sample	Mg flow, nmol/min	NH_3 flow, slm	ρ, Ωcm	μ_H, cm^2/Vs	p, cm^{-3}
348	743.4	1.2	5.1	8	1.5×10^{17}
349	739.3	1.2	high	—	—
350	210.3	1.2	2.7	11	2.2×10^{17}
351	220.1	1.2	3.4	9	2.0×10^{17}
352	151.4	1.2	2.2	14	2.0×10^{17}
353	100.9	1.2	1.7	15	2.4×10^{17}
354	69.1	1.2	0.09	193	3.5×10^{17}
355	85.1	1.2	3.4	9	2.1×10^{17}
356	100.9	1.2	3.6	10	1.6×10^{17}
543	105	3	5.0	-	-
544	91	3	4.9	10	1.3×10^{17}
546	240	3	2.8	18	1.3×10^{17}
547	78.6	1.2	2.3	7	4×10^{17}
548	58.2	1.2	2.2	14	2.4×10^{17}
549	78.6	1.2	1.7	12	3×10^{17}

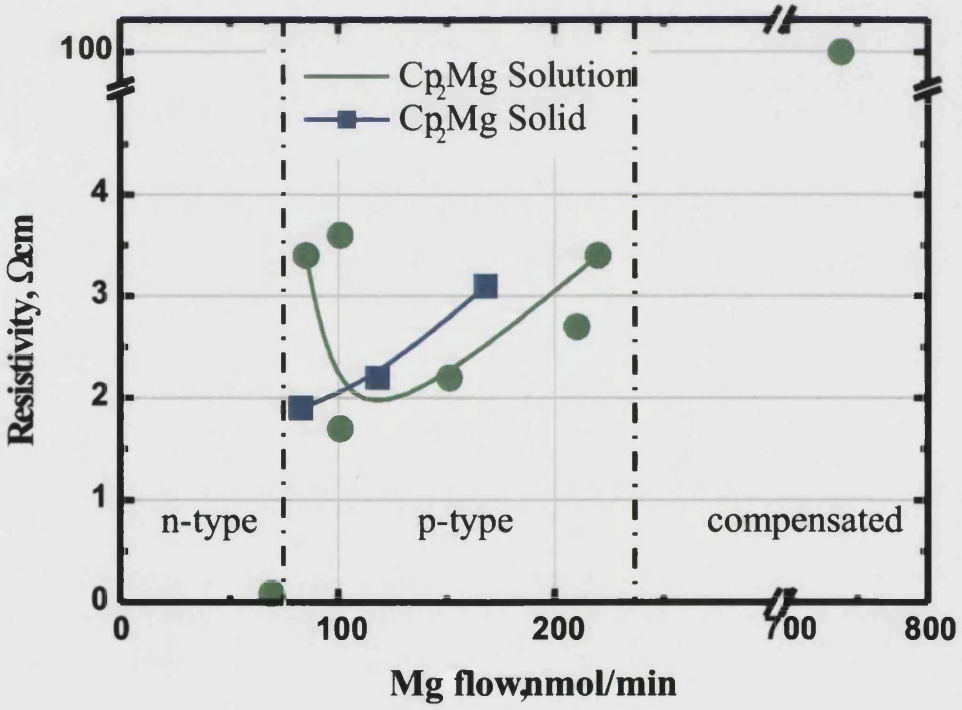

Figure 5.4. Resistivity of Mg-doped GaN layers versus Cp_2Mg flow. ■ – samples grown using solid Cp_2Mg source. ● - samples grown using Cp_2Mg solution.

The behaviour of a liquid Cp_2Mg source was very similar to that of a solid Cp_2Mg source. Using a liquid source we have repeated the results obtained using a solid source

(see Figure 5.4). However, we have found that with a liquid source the results were more reproducible. The usage of liquid Cp_2Mg source enabled our further studies of the whole Mg flow "window" from n-type to compensated material. The specific resistivity has a minimum at Cp_2Mg flow about 100 nmol/min. Further increase of doping level results in increasing resistivity. Such behaviour can be explained by self-compensation by the formation of Mg related deep donors [10,31].

As one can see from Table 14 Mg doping is strongly affected by ammonia flow. With all other parameters being kept constant, an increase of ammonia flow results in a decrease of the hole concentration. Higher Cp_2Mg flow is required to achieve the same level of Mg doping. This phenomenon is well explained by homogeneous prereaction between NH_3 and Cp_2Mg. Higher ammonia flow results in increased gas phase reactions, which reduce the effective Cp_2Mg concentration in the deposition zone.

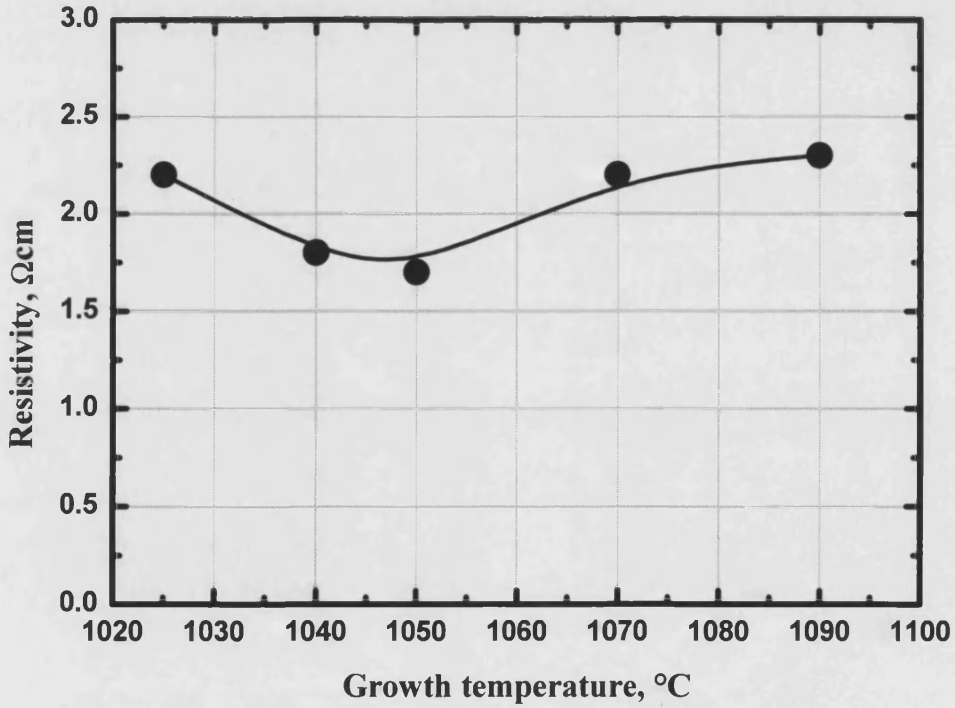

Figure 5.5. Resistivity of Mg-doped GaN layers versus growth temperature.

The growth temperature also influences the doping process. Figure 5.5 shows the dependence of specific resistivity of magnesium doped GaN films on the growth

temperature. The optimum growth temperature corresponding to the lowest resistivity is about 1050°C. It should be noted that the actual temperature on the substrate surface differs from the pyrometer reading and depends on large number of factors. When the conditions inside the reactor are changed, for example after the change of the quartzware, temperature corrections are often required. For this reason it is correct to compare growth temperatures only between experiments from the same series.

5.5.4. Growth in nitrogen ambient.

Sugiura *et al* [30] have studied the influence of the carrier gas on electrical properties of GaN films. They have obtained a low-resistivity p-type GaN with the resistivity of 0.8-1 Ωcm and the carrier concentration of $0.8\text{-}2\times10^{18}$ cm^{-3} by H_2-free growth without any post-treatments. The small amount of H_2 gas in a reactor strongly influenced the electrical properties of the Mg-doped GaN films.

We have conducted an experiment on GaN:Mg growth under N_2 rich conditions. Figure 5.6 shows the reflectance versus time signal measured during the growth of GaN/GaN:Mg structure. During the growth of undoped GaN buffer layer under H_2 (region A) the magnitude of oscillations is high, indicating good quality of the film. For Mg-doped GaN the carrier gas was changed to H_2/N_2 mixture (60% of N_2) and the magnitude of oscillations drops rapidly, indicating roughening of the surface. When the carrier gas was changed back to H_2 the reflectance signal partially recovers, yet not to the original level (region C). The growth rate with N_2-rich carrier gas (0.35 μm/h) is slower than that for H_2 carrier gas (0.6 μm/h).

Figure 5.7 shows micrographs done with Nomarski microscope for samples grown under N_2+H_2 mixture (right) and under H_2 (left). The film grown under hydrogen has a very smooth surface. On the contrary, film grown under nitrogen-rich conditions has much rougher surface.

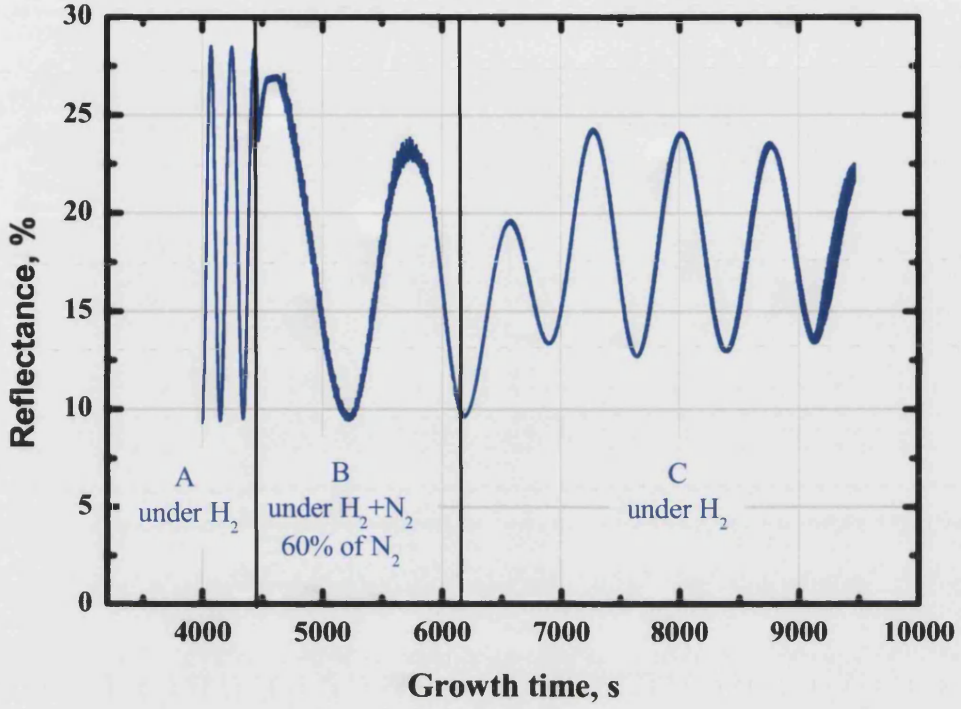

Figure 5.6. Optical reflectance at 600 nm versus time recorded during the growth of Mg doped GaN. A - growth of UD GaN buffer layer under H_2, B - growth of GaN:Mg under N_2 (60%) + H_2(40%) gas mixture, C growth of GaN:Mg under H_2

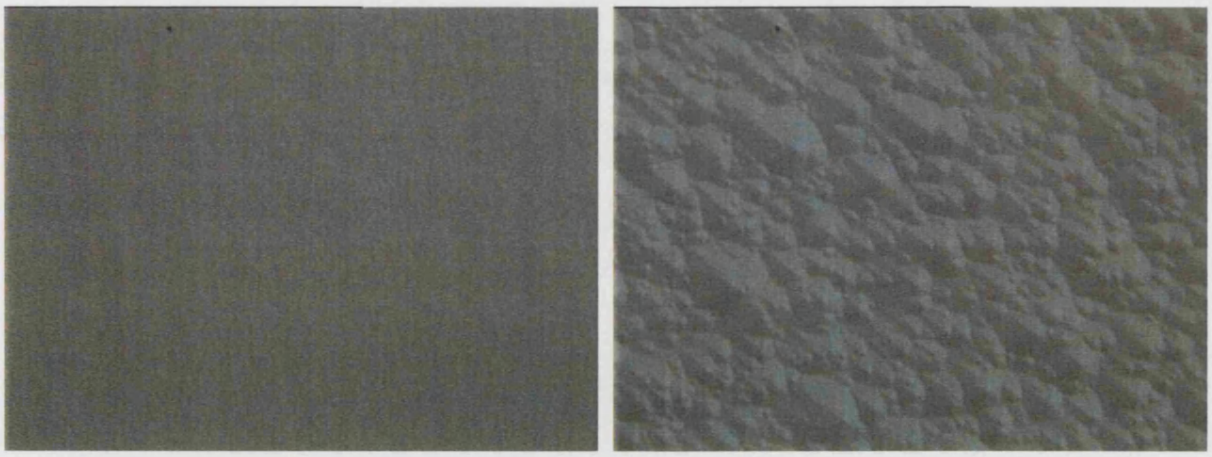

Under H_2 Under H_2+N_2

Figure 5.7. Nomarski micrographs of the surface of GaN:Mg samples grown under H_2 (left) and under N_2 +H_2 mixture (right). The field size is 200×300 μm.

To summarise, GaN deposition under H_2-free ambient requires more detailed optimisation of the growth parameters. Simple change of the carrier gas from H_2 to N_2 does not improve p-type doping but leads to a defective film with a very rough morphology.

5.6. Optimisation of annealing.

In the present research, we used the following annealing techniques:

- *In situ* annealing in the MOCVD reactor at reduced (400-500 mbar) nitrogen pressure
- *Ex situ* annealing in the open flow furnace under nitrogen
- *Ex situ* annealing in the open flow furnace under oxygen

The advantage of the *in situ* annealing technique is that it can be easily integrated with the growth process. However, *ex situ* techniques are more flexible and offer better control of gas ambient and temperature.

Samples before run 348GN-p were grown using *in situ* annealing in nitrogen at 900°C for 25 min. Not to escape one's attention is the fact that in our MOCVD system the lightpipe pyrometer controls the temperature of the lower graphite disc. The real temperature on the surface of the wafer is 50-100°C lower.

5.6.1. Annealing in nitrogen

For detailed investigation of annealing effects GaN:Mg films were grown without *in situ* annealing. After that the 2" wafer was cut into 7×7 mm^2 pieces and they were annealed in nitrogen for 10 min at various temperatures. The effect of annealing temperature on the specific resistivity of the Mg doped GaN is presented in Figure 5.8. The lowest value of the resistivity (1.6 Ωcm) corresponds to annealing temperature of 800-840°C

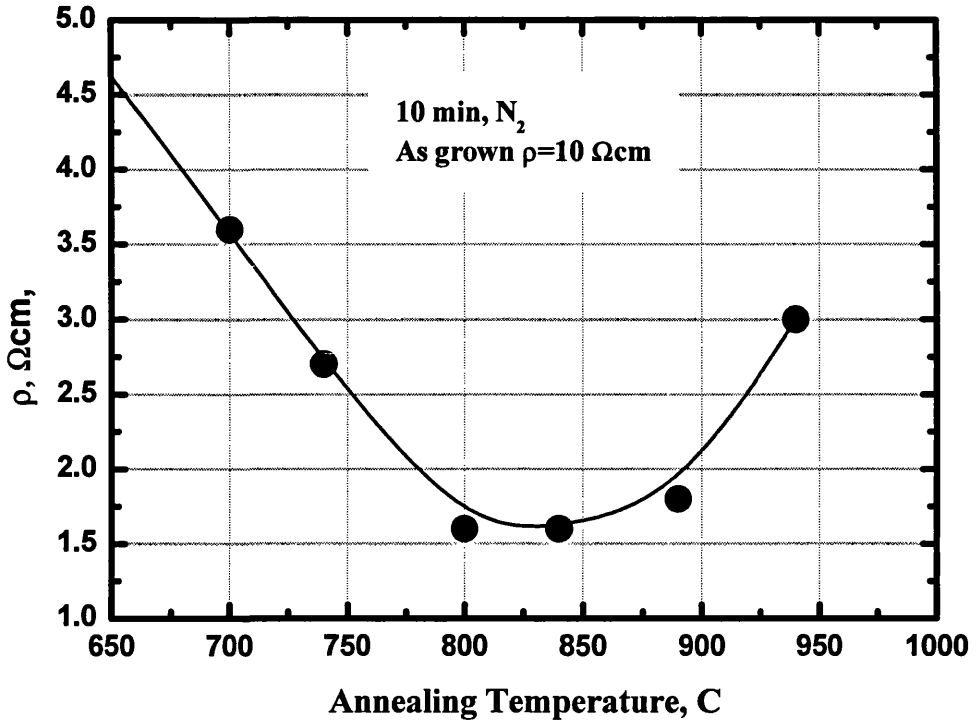

Figure 5.8. Effect of the annealing temperature on resistivity of Mg doped GaN films.

5.6.2. Annealing in oxygen[a]

Pieces of Mg doped GaN wafers were annealed in oxygen at 550°C. Figure 5.9 presents the dependence of specific resistivity on annealing time. As one can see, resistivity saturates after first 40 min.

Table 15 compares properties of GaN films with different Mg doping level annealed in nitrogen and oxygen. Samples annealed in oxygen exhibit lower specific resistivity than that of the samples annealed in nitrogen. It should be noted that in annealing in oxygen requires much lower temperature, therefore, it can be considered less damaging in terms of thermal decomposition and creation of nitrogen vacancies.

[a] Experiments performed by A.Andreev at Ioffe Institute, St.Petersburg, Russia

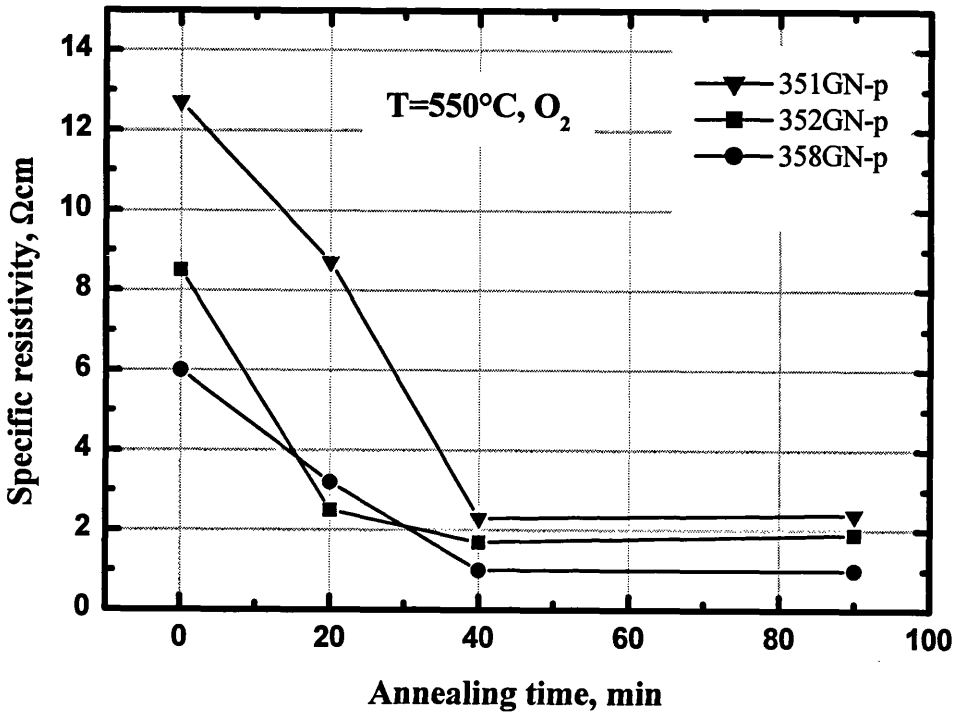

Figure 5.9. Dependence of specific resistivity of Mg doped GaN films on annealing time in O_2 at 550°C.

Table 15. Comparison of Mg activation in nitrogen and oxygen ambient.

Sample, Cp_2Mg flow	Specific resistivity, Ωcm	
	Annealing in N_2, 15 min, 800°C	Annealing in O_2, 40 min,550°C
Sample A, 95nmol/min	1.9	0.95
Sample B, 155nmol/min	2.2	1.7
Sample C, 211nmol/min	3.4	2.3

5.7. SIMS measurements.

Secondary Ion Mass Spectroscopy (SIMS) measurements were performed by MATS, UK. Figure 5.11 shows SIMS profiles of two Mg-doped samples grown with different Mg fluxes. Sample 348GN-p was grown with Cp_2Mg flux of 743 nmol/min using a conventional Cp_2Mg solid source. Sample 350GN-p was grown with Cp_2Mg flux of 210 nmol/min using a liquid Cp_2Mg source.

Both samples appeared to be heavily doped with Mg. The average concentration of magnesium was 1-2×10^{20} cm^{-3} and 2.5-3.5×10^{20} cm^{-3}, for samples 350GN-p and 348GN-p, respectively. It is noteworthy that magnesium incorporation was very effective. The incorporation coefficient was 29% and 51% for samples 348GN-p and 350GN-p, respectively. (see Table 16)

Table 16. Mg/Ga ratio in gas and solid phase and calculation of the segregation coefficient.

Sample #	Cp_2Mg flux, nmol/min	TEGa flux, µmol/min	Mg/Ga, (gas phase)	Mg_{solid} at/cm^3	Mg/Ga (solid)	$\frac{Mg/Ga_{solid}}{Mg/Ga_{gas}}$
348GNp	743	31.5	2.36×10^{-2}	3×10^{20}	6.8×10^{-3}	0.29
350GNp	210	31.5	6.66×10^{-3}	1.5×10^{20}	3.4×10^{-3}	0.51

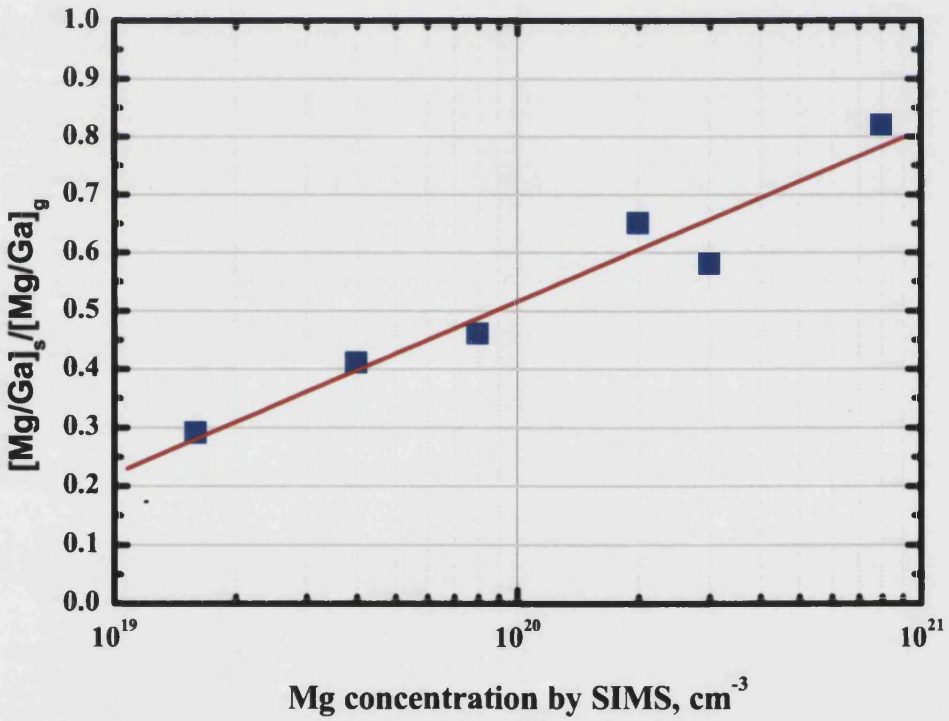

Figure 5.10. Published data on Mg incorporation efficiency. (from Kozodoy *et al* [9])

The efficiency of magnesium incorporation for our system is very similar to the results published by Kozodoy [9]. It is interesting to note that efficiency of Mg incorporation increases with increasing Mg concentration (Figure 5.10).

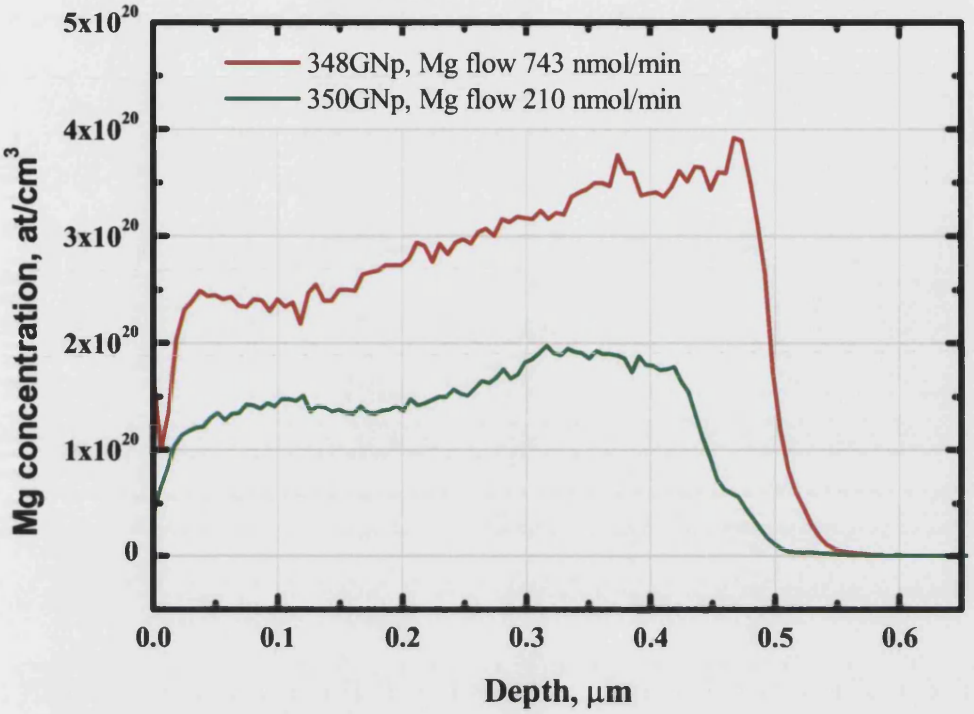

Figure 5.11. SIMS profiles of two Mg-doped GaN samples, with different Cp_2Mg fluxes. 348GNp – Cp_2Mg flow=743nmol/min, solid source, 350GNp – Cp_2Mg flow=210nmol/min, Cp_2Mg solution source.

On both samples the magnesium concentration increases with increasing depth. This gradient is not an artefact because the signal of interest (24Mg) was ratioed against a matrix signal (14N). This means that the magnesium levels do appear to have a real gradient. This is possibly related to Mg out-diffusion after the growth. Zn concentration in the Zn-doped sublayer was about 1×10^{18} cm^{-3}. This is very close to the expected value and proves that our calculations on efficiency of Zn incorporation were correct.

5.8. PL measurements.

The photoluminescence measurements were performed using two experimental setups. The first system included Oriel M260 spectrograph, Andor CCD array and collimating optics. The photoluminescence was excited with the 325 nm line from a Kimmon He-Cd laser. The maximum excitation power density is estimated to be of the order of 1 kW/cm^2. Smaller excitation densities were achieved by defocusing of the laser

beam. PL experiments at higher power densities were performed using Renishaw microraman system. A frequency-doubled argon laser (λ=244nm) was used as an excitation source. The excitation power density was about 10 kW/cm^2. In both cases, PL measurements were performed at room temperature.

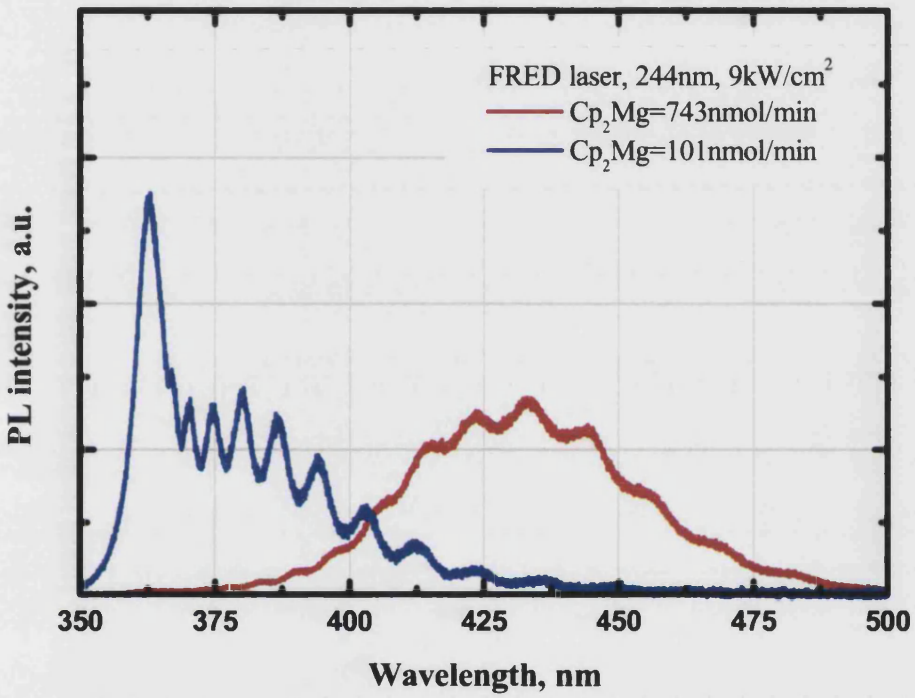

Figure 5.12. PL spectra for GaN sample with different concentration of Mg.

Figure 5.12 shows photoluminescence spectra from Mg-doped samples with different doping level. The sample with high Mg concentration exhibits a wide peak centered around 430-440 nm (2.8 eV). Under the same experimental conditions, the sample with lower Mg concentration reveals only near edge emission at 365 nm (3.4 eV) and Mg-related band at 380 nm (3.2 eV). Samples without annealing also have a broad red line centered at 700nm (1.8 eV) (see Figure 5.14). In contrast to undoped or Si-doped GaN, Mg-doped samples show no yellow luminescence at 600 nm (2.1 eV).

Figure 5.13 presents PL spectra from Mg-doped GaN measured at different excitation power densities. Three samples with different concentration of Mg were measured. The lowest Mg concentration corresponds to n-type material ("underdoped"

sample), the average Mg concentration corresponds to p-type material, and the highest Mg concentration corresponds to compensated material ("overdoped" sample) The "overdoped" sample shows only 2.8 eV line, while two other show both 2.8 eV and 3.2 eV luminescence.

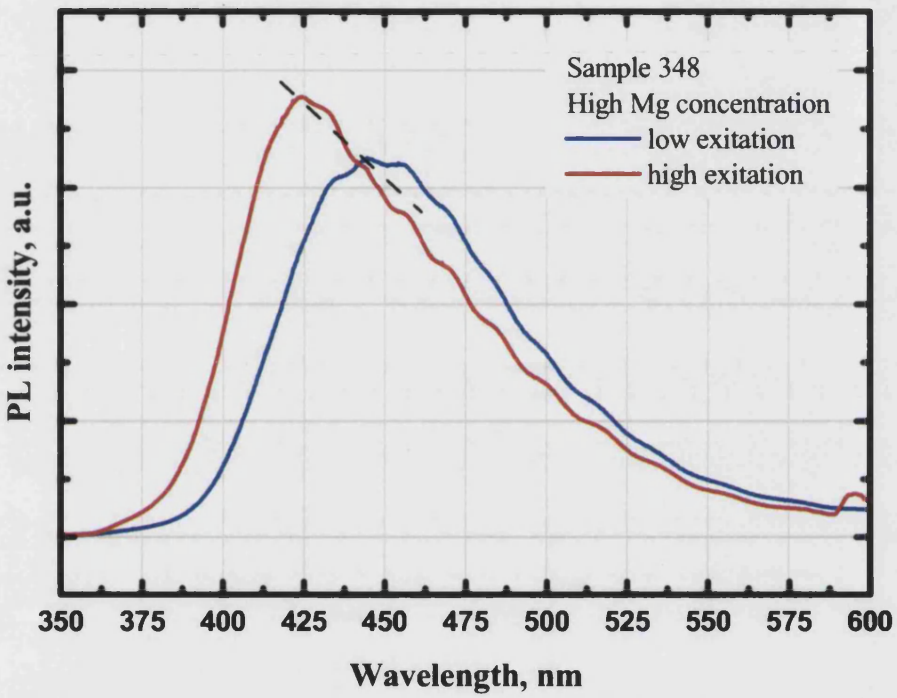

Figure 5.13a. PL spectra for the "overdoped" GaN:Mg sample obtained at various excitation intensities. Only 2.8 eV defect-related peak is observed.

The 3.2 eV line does not change much its position with the increase of excitation power density. At the same time, 2.8 eV line shifts remarkably to higher energies with increasing power density. At high excitation intensity, the 2.8 eV luminescence band saturates and 3.2eV line dominates in the PL spectra.

The magnesium related blue luminescence has been well studied by a number of authors [31,32,33,34,35]. The 3.2 eV line is usually observed in samples doped in lover 10^{19} cm^{-3} and is assigned to capture free electrons at neutral Mg acceptors (Mg_0, e) [36,37,38]. Most of the authors conclude, that the 2.8 eV line is a donor-acceptor pair (DAP) emission involving a deep donor and shallow acceptor. The shallow acceptor is

Mg_{Ga} and a deep donor is thought to be a complex of nitrogen vacancy with magnesium or hydrogen (e.g Mg_i-V_N, Mg_{Ga}-V_N, V_N-H).

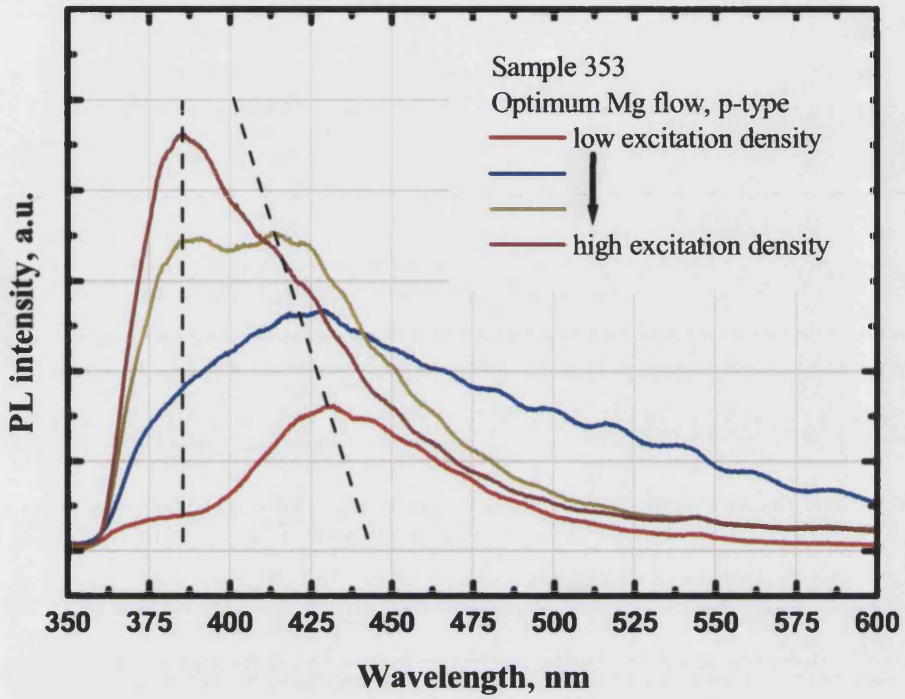

Figure 5.13b. PL spectra for the sample with optimum Mg concentration obtained under various excitation intencities. The 2.8 eV band dominates at low excitation power density. At higher excitation PL switches to 3.2 eV band.

Two major facts support the DAP model. First, the 2.8 eV line is observed only for the samples with high Mg concentration (10^{19}-10^{20} cm^{-3}) when average distance between acceptors and donors is small enough (15-30Å). The close location of pair components results in a high probability for DAP type transitions in spite of strong localization of the electron and the hole bound to the deep defect. Second, there is a distinct shift of the 2.8 eV line to higher energy with increasing excitation power density. The intensity of the 2.8 eV line saturates with increasing excitation density. The intensity of 2.8 eV line saturates at high excitation densities The reason for this behaviour is the Coulomb interaction of an ionised DAP

$$h\nu = E_g - (E_d + E_a) - \frac{e^2}{\varepsilon \cdot r} \tag{5.8}$$

The mean separation r between donors and acceptors in neutral pairs decreases with increasing excitation density. Consequently, the Coulomb term in the above-mentioned equation increases and $h\nu$ shifts to higher energy. Authors [39] suggest that 2.8 eV luminescence is related to a defect complex composed of the nitrogen vacancy and the Mg interstitial at a nearby empty site in p-type GaN. This defect complex forms deep donor levels positioned around 2.8 eV above valence band.

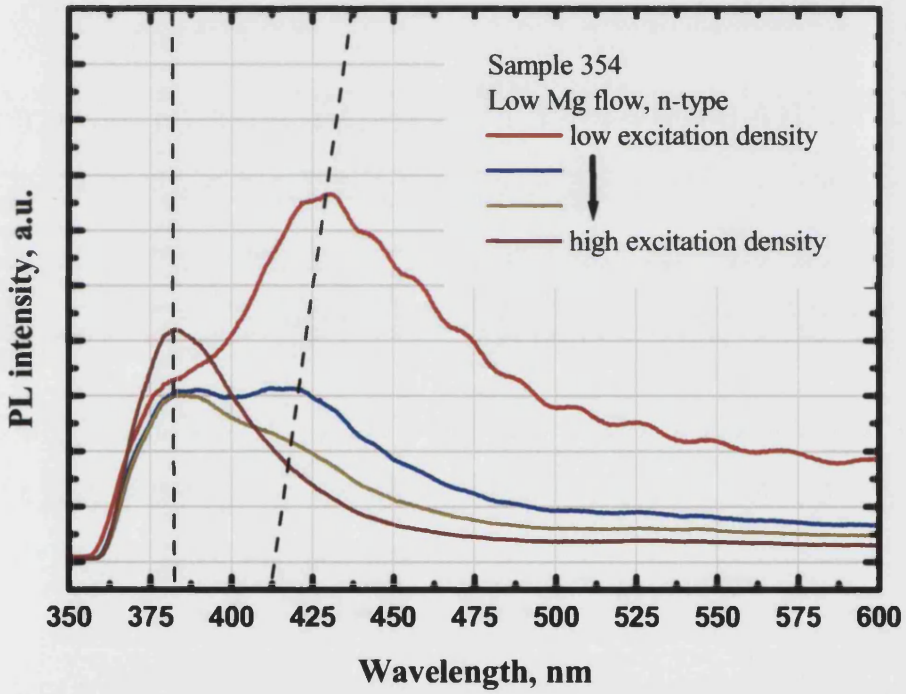

Figure 5.13c. PL spectra of the "underdoped" GaN:Mg sample obtained under various excitation intencities.

The red luminescence at 700 nm (1.8 eV) was observed only on the samples without annealing. After annealing even at moderate temperature (about 700°C), the intensity of the 1.8 eV line drops below the detection limit of our system (see Figure 5.14). The 1.8 eV red emission has been observed in Mg-doped GaN by other authors [40, 41]. It has been reported that the emission is increased by co-doping of Si+Mg. The 1.8 eV luminescence

has been also observed in nominally undoped GaN grown by HVPE [42]. Hofmann et al [43] demonstrated that the presence of high amounts of C and O also leads to the presence of 1.8 eV band. This suggests that the chemical nature of dopants has no strong influence on the chemical nature of the red emission. It is likely that the red band is related to native defects such as vacancies or native interstitial atoms, possibly paired with impurities. It can be speculated that the red 1.8 eV and the blue 2.8 eV emission bands are related to the same Mg-induced deep donor (e.g. $[Mg_{Ga}\text{-}V_N]$). The other centre involved in the red emission band is some deep centre, possibly $[V_{Ga}\text{-}Si]$ complex.

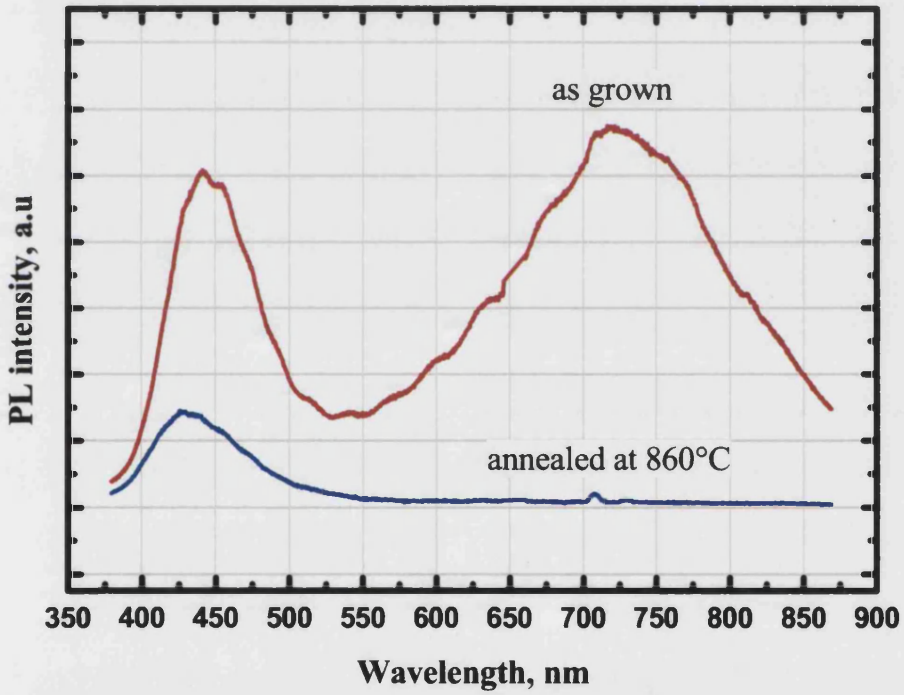

Figure 5.14. Red luminescence (1.8 eV band) from Mg-doped GaN.

Figure 5.15 shows PL spectra for Mg doped GaN films annealed at different temperatures. The intensity of the edge luminescence and Mg-related 3.2 eV line is constantly decreasing with increase of the annealing temperature. This annealing effect can be attributed to the surface decomposition, which is known to result in the degradation of PL signals.

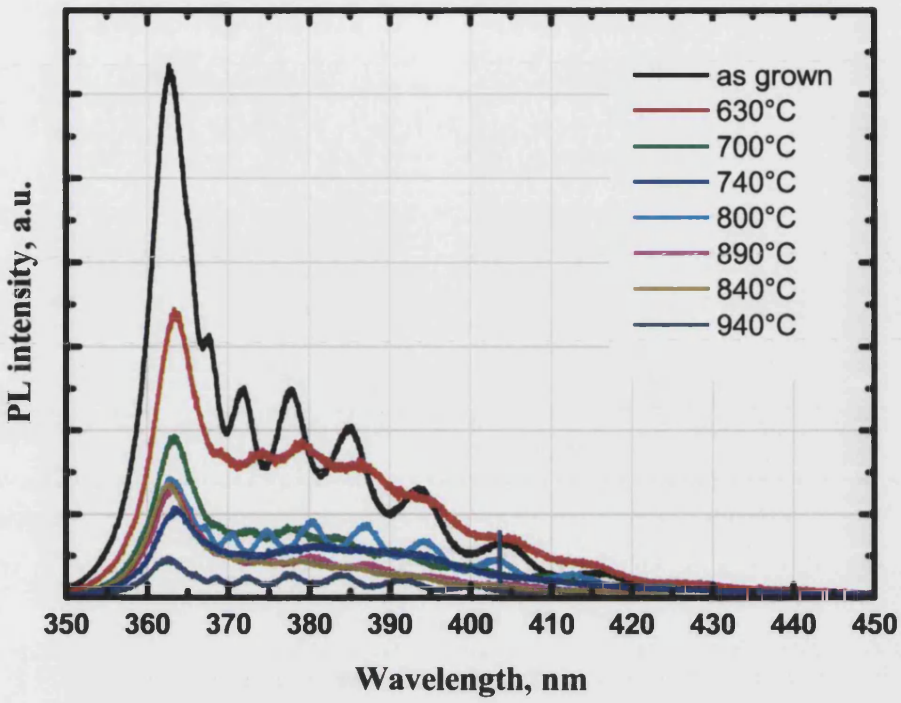

Figure 5.15. PL spectra of Mg doped GaN samples annealed at various temperatures

5.9. Summary

We have successfully grown Mg-doped GaN layers by MOCVD using solid and liquid Cp_2Mg sources. Magnesium concentration up to 3×10^{20} cm^{-3} and hole density up to 5×10^{17} cm^{-3} have been achieved. We have studied the electrical and optical properties of Mg-doped GaN as a function of doping level, growth temperature, NH_3 flow and annealing conditions.

5.10. References

1. J K Sheu, G C Chi, J. Phys.: Condens. Matter 14 R657 (2002)
2. H. Tokunaga, I.Waki, A.Yamaguchi, N.Akutsu, K.Matsumoto, J.Cryst.Growth,189/190 519-522.
3. C.-R. Lee *et al,* J. Crystal Growth 216 (2000) 62-68
4. K.Kumakura, T.Makimoto, N.Kobayashi, Jpn. J. Appl. Phys. 39 (2000) L337

5. K. S. Kim, M. S. Han, G. M. Yang, C. J. Youn, H. J. Lee, H. K. Cho and J. Y. Lee, Appl. Phys. Lett. 77,1123 (2000)
6. K.Kumakura, N.Kobayashi, Jpn. J. Appl. Phys. Vol.38(1999) L1012
7. K.Kumakura, T.Makimoto, N.Kobayashi, Jpn. J. Appl. Phys. Vol.39(1999) L195
8. P. Kozodoy, Yu.P. Smorchkova, M.Hansen, H.Xing, S.P.DenBaars, U.K.Mishra, A. W. Saxler, R. Perrin, W. C. Mitchel, Appl. Phys. Lett. 75(1999), p. 2444
9. P.Kozodoy, H.Xing, S.P.DenBaars, U.K. Mishra, A.Sahler, R.Perrin, S.Elhamri and W.C. Mitchel, J. Appl. Phys., v. 87, p. 1832.(2000)
10. U. Kaufmann, P. Schlotter, H. Obloh, K. Köhler, M. Maier. Phys. Rev. B, 62, 10 867, (2000)
11. H.Katayma-Yoshida, Tnishimatsu, T,Yamamoto and N.Orita, J. Phys.:Condens. Matter, v 13, p. 8901
12. R. Y. Korotkov, J. M. Gregie, and B. W. Wessels, Appl. Phys. Lett., v.78, p. 222
13. K.S. Kim, C.S. Oh, M.S. Han, C.S. Kim, G.M. Yang*, J.W. Yang, C.-H. Hong, C.J.Youn, K.Y. Lim, and H.J. Lee, MRS Internet J. Nitride Semicond. Res. 5S1, W3.84 (2000)
14. Y. Aoyagi, S. Iwai, A. Kinoshita, H. Hirayama, International Workshop on Nitride Semiconductors (IWN2000), Sept. 2000 (Nagoya)
15. H.K.Cho, J.Y.Lee, K.S. Kim, G.M.Yang, Solid-State Electronics, 45 (2001), p.2023
16. H.Amano, K.Hiramatsu, M.Kito, N.Sawaki, I.Akasaki, J. Cryst. Growth, v.93, p. 79
17. B Theys, Z Teukam, F Jomard, P de Mierry, A Y Polyakov, M Barb'e, Semicond. Sci. Technol. 16 L53 (2001)
18. F. A. Reboredo, S. T. Pantelides, Phys. Rev. Lett. 82, 1889, (1999)
19. H.Amano, M. Kito, K. Hiramatsu and I. Akasaki, Japan. J. Appl. Phys. 28 L2112 (1989)
20. S. Nakamura, T. Mukai and M. Senoh, Japan. J. Appl. Phys. 31 L139 (1991)
21. S. Fujita, M. Funato, D.-C. Park, Y. Ikenaga, S. Fujita, MRS Internet J. Nitride Semicond. Res. 4S1, G6.31(1999)
22. K.S. Ahn, D.J. Kim, Y.T. Moon, H.G. Kim, S.J. Park, Proceedings of Second International Symposium on Blue Lasers and Light Emitting Diodes, Chiba, Japan, p. 556. (1998)
23. H.Y.A. Chung,, A. Pelzmann, M. Drechsler, M Scherer, V. Schwegler, M. Seyboth, C. Kirchner, M. Kamp, J. Crystal Growth 230, 549 (2001)
24. I. Waki, H. Fujioka, M. Oshima, H. Miki and A. Fukizawa, Appl. Phys. Lett., 78, 2899 (2001)
25. C.R. Lee, J.Y. Leem, B.G. Ahn, Journal of Crystal Growth 216, 62 (2000)
26. B.A. Hull, S.E. Mohney, H.S. Venugopalan, and J.C. Ramer, Appl. Phys. Lett. 76, 2271, (2000)
27. Y.Ohba, A.Hatano, J. Crystal Growth, v145(1994) p 214-218

28. P. de Mierry, B. Beaumont, E. Feltin, H.P.D. Schenk, Pierre Gibart, F. Jomard, S. Rushworth, L. Smith and R. Odedra, MRS Internet J. Nitride Semicond. Res. 5, 8 (2000).

29. M R Ravetz, Journal of Electronic Materials, Vol. 29, No.1, 2000, p157

30. L.Sugiura, M.Suzuki, J.Hishio, Appl. Phys. Lett, v. 72, p. 1748

31. U.Kaufmann, M.Kunzer, M.Maier, H.Obloh, A.Ramakrishnan, B.Santic, P. Schlotter, Appl. Phys. Lett, v. 72, p. 1326

32. M. A. Reshchikov, G.-C. Yi, and B. W. Wessels, MRS Internet J. Nitride Semicond. Res. 4S1, G11.8 (1999)

33. F.Shahedipour, B.W.Wessels , MRS Internet J. Nitride Semicond. Res. 6, 12 (2001).

34. F. Shahedipour , B. W. Wessels , Appl. Phys. Lett., v.76, p.3011

35. S. M. Jeong, H. W. Shim, H. S. Yoon, M. G. Cheong, R. J. Choi, E.-K. Suh, and H. J. Lee, J. Appl. Phys. 91, 9711 (2002)

36. M. Lachab, D.-H. Youn, R.S. Qhalid Fareed, T. Wang, S. Sakai, Solid-State Electronics 44, 1669 (2000)

37. T. W. Kang, S. H. Park, H. Song, T. W. Kim, G. S. Yoon, and C. O. Kim, J. Appl. Phys. 84, 2082 (1998)

38. A. K. Viswanath, E. Shin, J. I. Lee, S. Yu, D. Kim, B. Kim, Y. Choi, and C.-H. Hong, J. Appl. Phys. 83, 2272 (1998)

39. S.-G. Lee and K. J. Chang, Semicond. Sci. Technol. 14 138, (1999).

40. U.Kaufmann, M.Kunzer, H.Obloh, M.Maier, A.Ramakrishnan, B.Santic, Phys. Rev. B 59 5561 (1999)

41 M.W. Bayerl, M.S. Brand, E.R.Glaser, A.E.Wickenden, D.D. Koleske, R.L.Henry M.Stutzmann, Phys. Stat. Sol. (b) 216, 547 (1999)

42. E.M.Goldys, M. Godlewski, T. Paskova, G. Pozina, B. Monemar, MRS Internet J. Nitride Semicond. Res. 6, 1 (2001).

43. D.M. Hofmann, B.K. Meyer, H.Alves, F.Leiter, W.Burkhard, N.Romanov, Y.Kim, J.Krüger, E.R.Weber, Phys Stat. Sol (a) 180, 261 (2000)

6. Growth of AlGaN

6.1. Introduction

The AlGaN alloy is a solid solution over the whole range of composition and has a direct band gap from 3.4 to 6.2 eV. Nitride-based device structures for electronic and optoelectronics applications usually incorporate layers of $Al_xGa_{1-x}N$. For instance, AlGaN alloys form the thick cladding layers in nitride-based injection lasers, AlGaN/GaN heterostructures are used in III-nitride heterojunction field effect transistors, AlGaN/GaN superlattices found wide application for efficient acceptor activation and mobility improvement.

However, most research to date has indicated that AlGaN alloys are more difficult to grow than pure GaN due to problems of strain, increased parasitic reactions in the gas phase, and doping. As a rule, the number of challenges in AlGaN growth significantly increases with increasing Al content.

To obtain high quality AlGaN for electronic applications it is necessary first to study the growth mechanisms and to optimise the growth conditions. Therefore, we have grown AlGaN layers in a wide range of compositions by varying the gas phase composition.

6.2. AlGaN Growth by MOCVD

MOCVD technique is capable of growing AlGaN layers with Al content ranging from 0% to 100%. However, increased reactivity of Al-based metalorganic compounds compared to that of Ga-based metalorganic compounds implies certain limitations on the usable range of the growth parameters. TMAl tends to prereact with NH_3 in the gas phase. This parasitic reaction reduces the incorporation of Al and leads to the formation of tiny particles in the gas phase, which may deteriorate the quality of the layer. To minimise this effect, AlGaN layers are commonly grown at smaller V/III ratio and reduced pressure.

6.2.1. Experiment

AlGaN films were grown on (0001) sapphire substrates by the low-pressure MOCVD using TMGa, TMAl and NH_3 as precursors. Hydrogen was used as a carrier gas. The deposition sequence included the growth of a low temperature nucleation layer followed by the growth of a 1-2 μm thick GaN buffer layer. The AlGaN layer was grown either directly on GaN buffer layer, or using an intermediate compliance layer to prevent cracking.

Table 17. Typical conditions used for AlGaN growth

TMGa flow	15-20 μmol/min
TMAl flow	0-40 μmol/min
NH_3 flow	500-1500 sccm
Temperature	1000-1100
Pressure	100 mbar
Carrier gas	H_2, total flow 5000 sscm

The composition of AlGaN films was determined by x-ray diffraction, assuming that the variation of the lattice parameter c between GaN and AlN is linearly proportional to the Al concentration. The calculations were done using the assumption of fully relaxed AlGaN epilayers.

6.2.2. Results and discussion

For the epitaxial growth of AlGaN the relationship between the concentration of TMAl in the supplied gas phase and the resulting Al composition in the solid state is very important.

The experimental dependence of the Al content in AlGaN layers versus the input concentration of TMAl is presented in Figure 6.1. As one can see, the dependence exhibits a sublinear behaviour, especially for high input concentration of TMAl. The efficiency of Al incorporation increases with decrease of NH_3 flow and growth pressure. On the contrary, increase of the total molar flow of group III precursors (fast growth rate

conditions) results in reduced Al composition. Such type of growth behaviour is explained by increased premature reactions of TMAl with NH_3 in the gas phase.

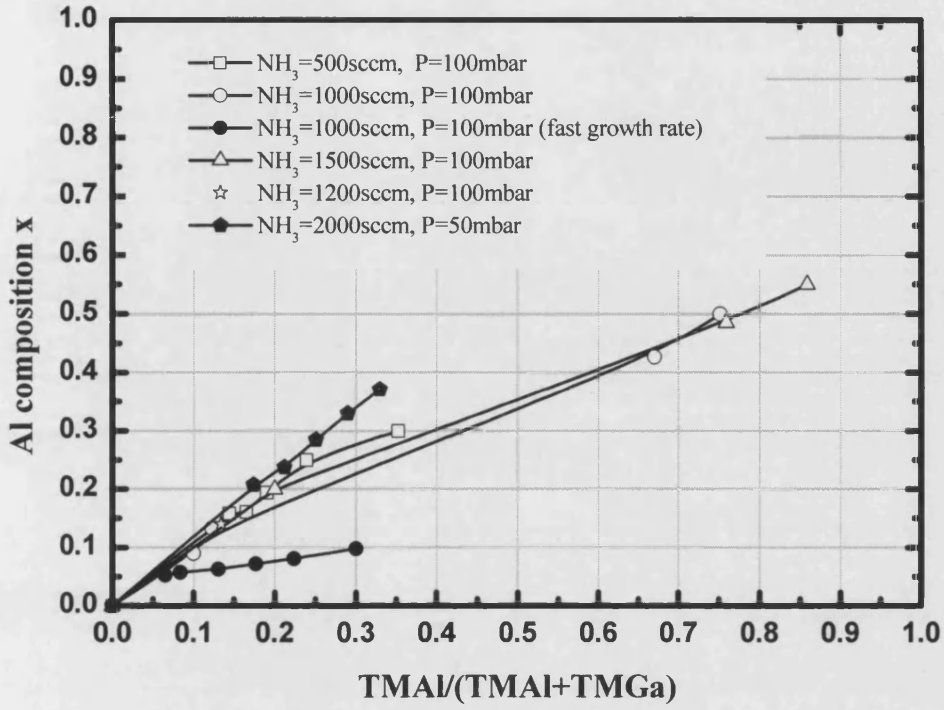

Figure 6.1 Al content versus input TMAl/(TMAl+TMGa) ratio

The growth AlGaN can be described by a simple model [1,2], which assumes that the deposition process is mass-transport limited. If there are no pre-reactions in the gas phase, the ratio of Al to Ga in the solid phase is linearly proportional to the ratio of TMAl to TMGa molecules injected into the gas phase.

$$\frac{x_{Al}}{x_{Ga}} = k\frac{v_{TMAl}}{v_{TMGa}} \tag{6.1}$$

where x_{Al}, x_{Ga} are concentrations of Al and Ga in the solid, and v_{TMAl}, v_{TMGa} are molar flows of TMAl and TMGa injected into the gas phase. The coefficient k is given by the ratio of incorporation efficiencies of Al to Ga.

$$k = \frac{i_{Al}}{i_{Ga}} \tag{6.2}$$

In the presence of gas phase reactions, the effective concentration of TMAl in the gas phase will be reduced. Therefore, equation (6.1) has to be rewritten in terms of effective flow of TMAl v'_{TMAl} which is given by the following expression

$$v'_{TMAl} = v_{TMAl} e^{-\alpha t} \tag{6.3}$$

Where t is the time required for a volume of gas to travel from the reactor inlet to the substrate. Reaction constant α describes the number of effective collisions between TMAl and NH_3 molecules and depends on pressure, temperature, V/III ratio and other factors. The volume collision rate is proportional to p^2 and the transfer time t is proportional to p. These results in

$$v'_{TMAl} = v_{TMAl} e^{-\alpha' p^3} \tag{6.4}$$

Equations (6.1), (6.2) and (6.4) yield

$$\frac{x_{Al}}{x_{Ga}} = \frac{i_{Al}}{i_{Ga}} \frac{v_{TMAl}}{v_{TMGa}} e^{-\alpha' p^3} \tag{6.5}$$

Denoting $x_{solid} \equiv x_{Al}$, $x_{vapour} \equiv \frac{v_{TMAl}}{v_{TMGa} + v_{TMAl}}$ and bearing in mind that $x_{Ga} = 1 - x_{Al}$, we can rewrite equation (6.5) as

$$x_{Al} = \frac{1}{1 + \frac{i_{Ga}}{i_{Al}} e^{\alpha' p^3} \left(\frac{1}{x_{vapour}} - 1 \right)} \tag{6.6}$$

Equation (6.6) relates the Al content x in $Al_xGa_{1-x}N$ with injected TMAl to total MO flow ratio x_{vapour} and growth pressure p. The exponent constant α' and the ratio of incorporation efficiencies $\frac{i_{Ga}}{i_{Al}}$ can be found by fitting the model to the experimental data.

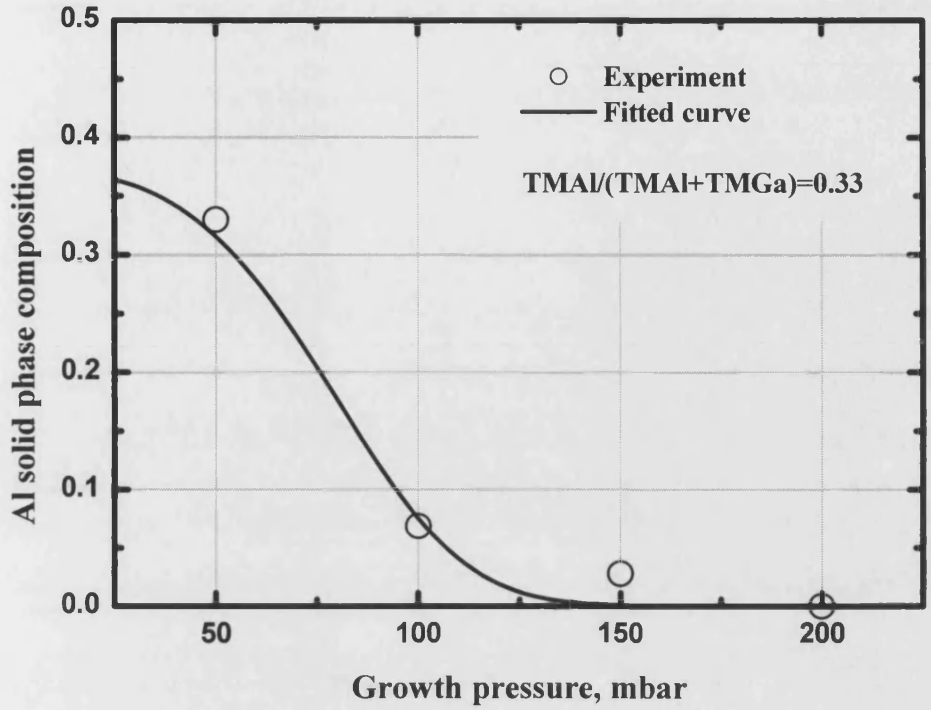

Figure 6.2 AlGaN solid composition versus growth pressure. Circles represent experimental data fitted by our model (continuous line).

Figure 6.2 presents the dependence of AlGaN composition on the growth pressure. As one can see, Al incorporation is drastically reduced at growth pressures above 200 mbar. On the other hand, below 50 mbar gas phase pre-reactions can be neglected. Figure 6.3 shows the experimentally measured dependence (circles) of Al composition in the solid on gas phase composition. The continuous line represents to the best fit of the model to the experimental data.

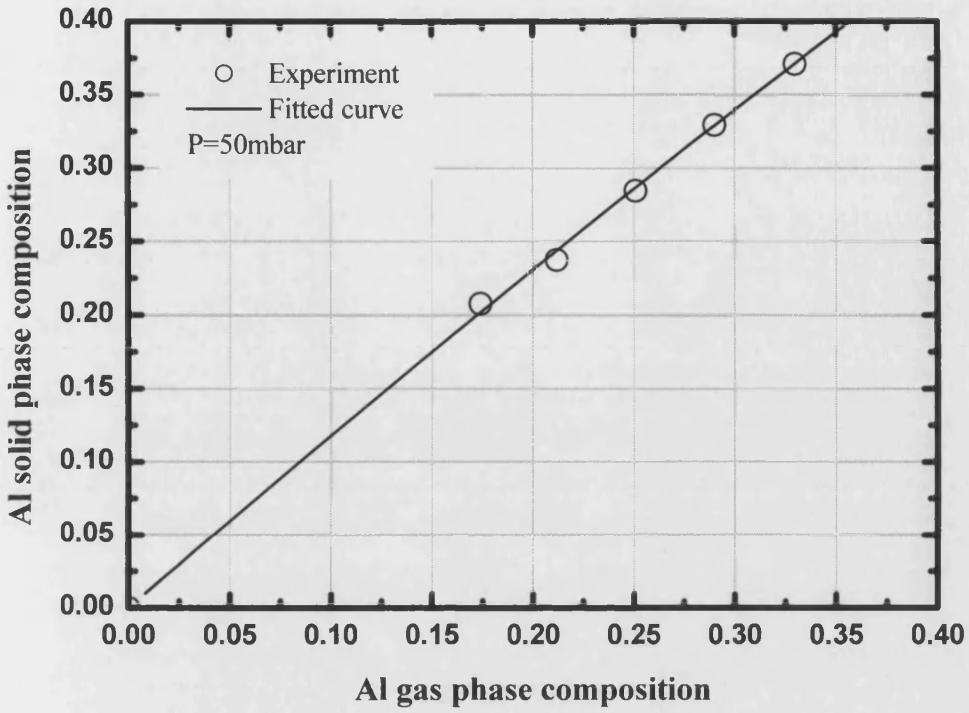

Figure 6.3 AlGaN solid composition versus gas phase composition. Circles represent experimental data fitted by our model (continuous line).

Fitting equation (6.5) to the experimental data we have obtained $\frac{i_{Ga}}{i_{Al}} = 0.834$ and $\alpha' = 1.98 \times 10^{-6}$ mbar^{-3}. These values are very close to ones reported by other authors [1,2].

Homogeneous pre-reactions strongly affect the growth rate of AlGaN layers. The growth rate is decreasing with increase of the growth pressure (Figure 6.5) and with increase of the input TMAl ratio (Figure 6.5). It is interesting to note, that the growth rate of AlGaN can be even smaller than that of GaN at the same flow TMGa. This observation suggests that the presence of TMAl facilitates homogeneous reactions involving TMGa and other species. One of the possible mechanisms is the reaction between TMAl adducts and TMGa leading to formation of AlGaN powder in the gas phase.

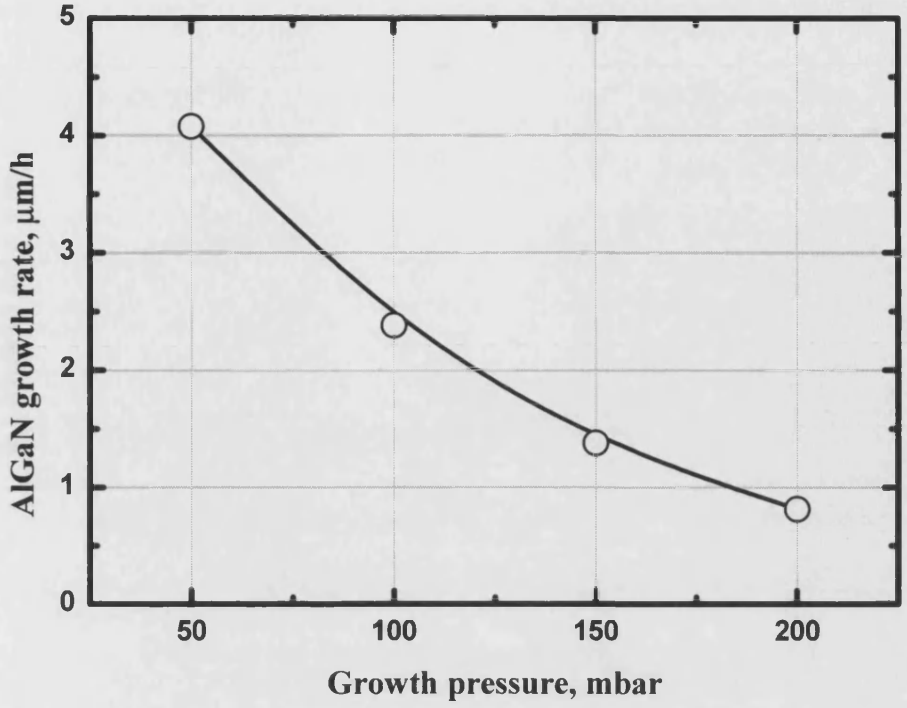

Figure 6.4 Pressure dependence of incorporation efficiency and growth rate.

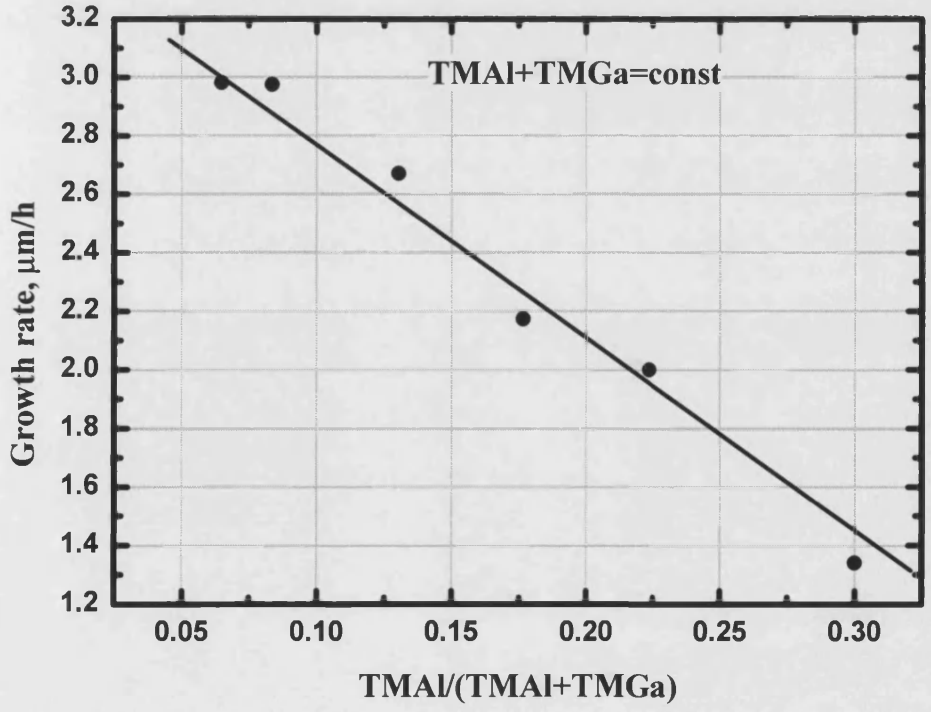

Figure 6.5 AlGaN growth rate versus input TMAl/(TMAl+TMGa) ratio

6.3. Optical Characterisation of AlGaN layers

Room temperature PL spectra from AlGaN samples are presented in Figure 6.6. The measurements were performed using Renishaw micro Raman system. A frequency doubled Ar laser (λ=244 nm) was used as an excitation source. Besides the shift of the emission peak to the shorter wavelengths, one can also notice a decrease of PL intensity and broadening of the PL peak. This can be explained by the alloy broadening and lower material quality of AlGaN layers with high Al content.

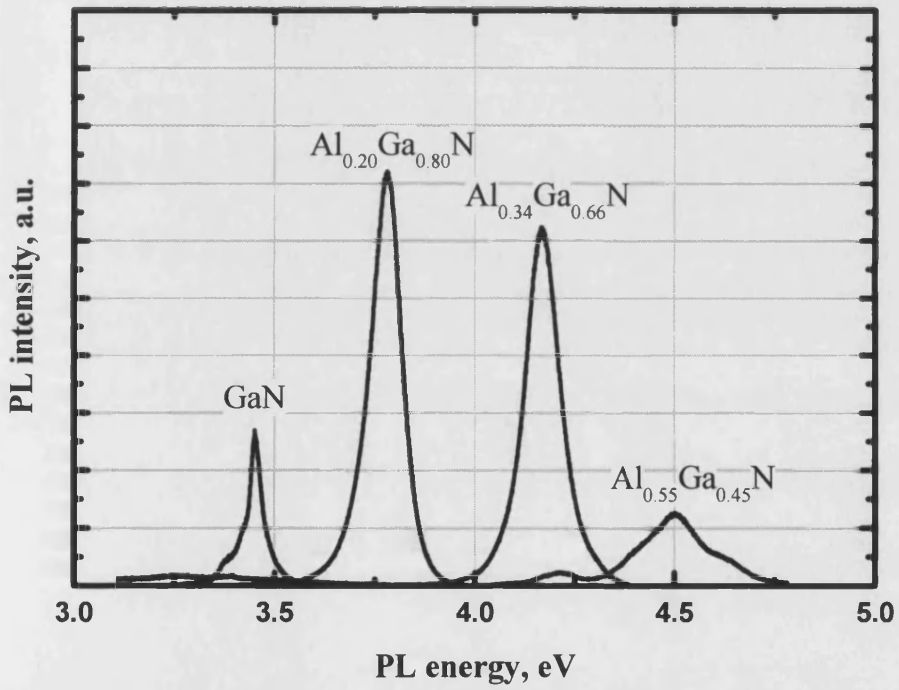

Figure 6.6 PL spectra from AlGaN layers of different composition.

The dependence of the PL peak position on Al composition is presented in Figure 6.7. The experimental points follow the parabolic compositional dependence for the band gap

$$E_g(x) = 3.4(1-x) - 1(1-x)x + 6.2x \qquad (6.7)$$

where the bowing parameter responsible for the magnitude of the parabolic nonlinearity is +1 eV. Published data for the bowing parameter in AlGaN are scattered from –0.8 eV to +2.6 eV. A detailed survey of published values of the bowing parameter for the AlGaN system has been done by Lee *et al* [3]. According to them, extant data suggest that the intrinsic band-gap bowing parameter for AlGaN alloys is b=+0.62(±0.45) eV.

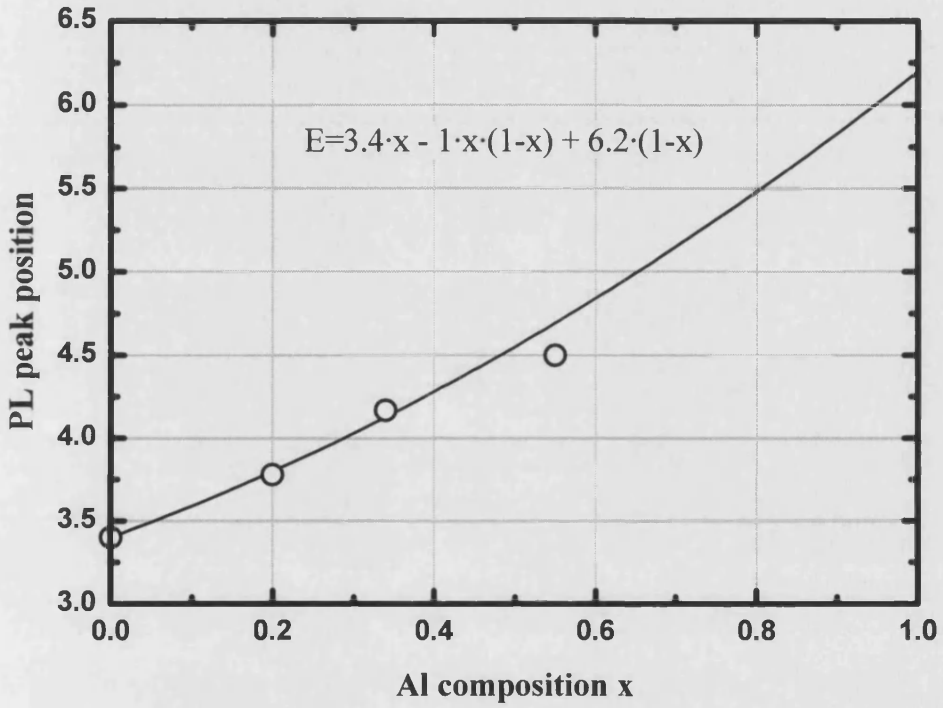

Figure 6.7. PL peak position versus Al composition.

6.3.1. Crack formation

The formation of cracks is one of the most severe problems in AlGaN growth. Misfit dislocations do not easily afford stress relief during strained heteroepitaxy of the (0001)-oriented, wurtzite, III-nitrides. Difficulty of misfit-dislocation formation in AlGaN crystals is due to the absence of effective slip systems. Therefore, the relaxation of tensilely stressed AlGaN on GaN can proceed only through the generation of crack network (see Figure 6.8).

Various types of interlayers have been reported to facilitate the crack-free growth of AlGaN. Nakamura and Fasol [4] reported the use of an InGaN layer before the growth of

AlGaN cladding layers in laser diode structures to avoid cracking. Amano et al [5] and Han et al [6] demonstrated that the introduction of a low temperature AlN interlayer on a high temperature GaN epilayer facilitates subsequent crack-free growth of HT AlGaN.

We have successfully employed GaN→AlGaN gradient layers to control and eliminate cracking of subsequent AlGaN layers.

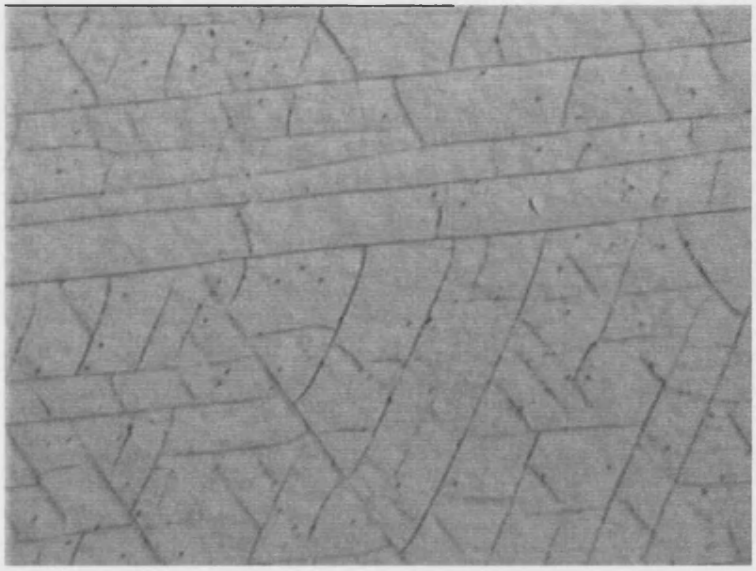

Figure 6.8 Optical micrograph of $Al_{0.33}Ga_{0.67}N$ layer, a cracking network is clearly observed.

6.4. P-type AlGaN

Magnesium doped p-type AlGaN layers are used as carrier emitters in optoelectronic devices. However, it is difficult to achieve high p-type conductivity in p-type AlGaN alloys due to high activation energy of Mg dopants as well as reduced crystalline quality of the alloys. Because these materials are of great importance in realizing nitride-based optoelectronic devices, studies that could provide better understanding and realization of highly conductive p-type AlGaN are urgently needed. A few studies have been reported on Mg-doped p-type AlGaN [7,8,9,10]. Most of the authors reporting on p-type AlGaN conclude that the activation energies of Mg acceptors increase with the increase in Al content.

Due to the increased Mg activation energy, it has been difficult to achieve p-type conductivity in AlGaN with high Al content. Suzuki et al [11] reported that $Al_{0.15}Ga_{0.85}N$ has a hole concentration and a thermal activation energy of about 6.6×10^{16} cm^{-3} and 250 meV, respectively. Li et al [12] have demonstrated p-type AlGaN layers with the Al content up to 0.27. The activation energy of Mg acceptors N measured by variable temperature Hall technique increased linearly from 150 meV for p-GaN to 310 meV for p-$Al_{0.27}Ga_{0.73}N$.

6.5. Experiment

P-type AlGaN samples were grown by the low pressure MOCVD on (0001) sapphire substrates. The deposition sequence included the growth of the following layers: the low-temperature nucleation layer, the 2-3 μm thick undoped GaN buffer layer, the 1 μm thick GaN:Zn layer, the 0.5 μm thick AlGaN:Mg layer, 0.05 μm thick GaN:Mg contact layer. In this structure the zinc doped layer acts as an insulation layer to prevent current leakage via GaN buffer during electrical characterization. Thin p-GaN on the top prevents oxidation of AlGaN and facilitates the preparation of ohmic contacts.

Table 18. Growth conditions for p-AlGaN.

TMGa flow	17.7 μmol/min
TMAl flow	0.5-1.5 μmol/min
NH_3 flow	1000 sccm
Cp2Mg flow	250-360 nmol/min
Temperature	1070°C
Pressure	100 mbar
Carrier gas	H_2, total flow 5000 sscm

The doping level for GaN:Zn layer was in the 10^{18} cm^{-3} range. According to our own observations and published data [13] such Zn doping produces effectively insulating material with specific resistivity of 10^6-10^{12} Ωcm. The growth conditions for p-type AlGaN are presented in Table 18. The Cp_2Mg flow during the growth of p-AlGaN layer was 250-360 nmol/min instead of 70-100 nmol/min normally used for p-GaN growth.

After the growth the samples were annealed at 800°C in nitrogen for 15 min to activate Mg. The Al composition measured by x-ray diffraction varied from 0.09 to 0.13.

Figure 6.9 Layout of AlGaN structure used for electrical measurements.

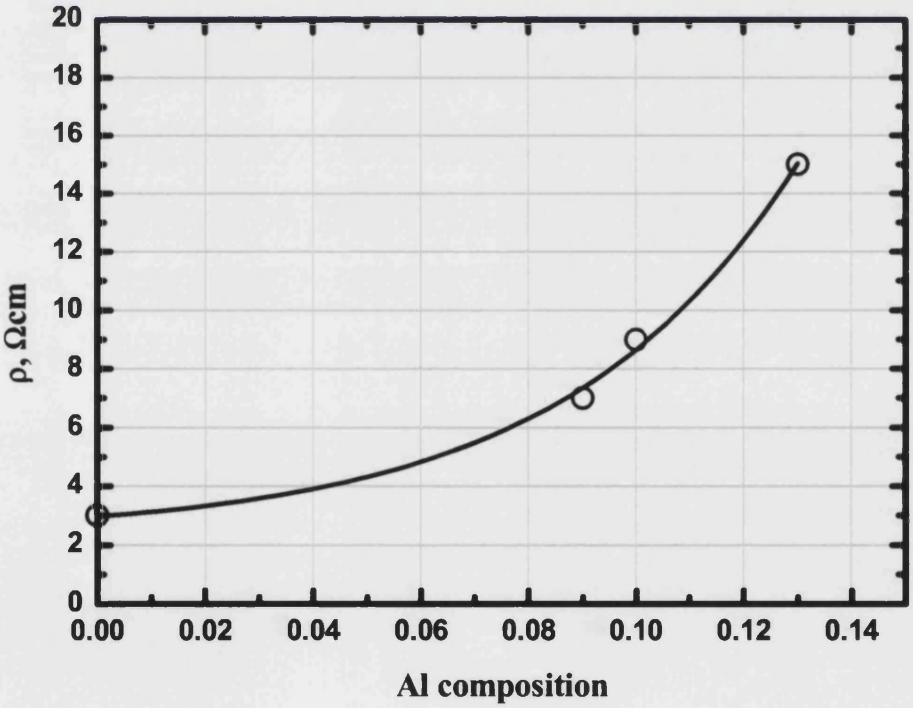

Figure 6.10. Specific resistivity of AlGaN layers versus Al composition.

The carrier concentration, the hall mobility and the specific resistivity of the samples were determined by room temperature Hall effect measurements using the van der Pauw

geometry. The hole concentration for all samples was about 10^{17} cm^{-3}. The mobility was 4-7 cm^2/Vs, which is about 2 times lower than that in p-GaN. The reduction of the mobility is probably explained by the increased scattering and lower crystalline quality of AlGaN material. The specific resistivity of p-AlGaN layers was from 7 Ωcm to 15 Ωcm, which is high compared to 2-3 Ωcm for p-GaN samples. As one can see on Figure 6.10 the specific resistivity of AlGaN layers is rapidly increasing with increase of Al composition.

6.6. Summary

We have grown AlGaN epitaxial layers with Al composition ranging from 0 to 55%. The layers were characterised by means of XRD, PL and optical microscopy. Considering that the growth mechanism is mass-transport limited and the composition is determined by the relative Al and Ga fluxes reaching the interface by diffusion, we have developed a model describing incorporation from the gas phase to the solid AlGaN. It was found that homogeneous gas-phase pre-reactions strongly affect the growth AlGaN alloys. The effect of premature reactions can be minimised by using low-pressure growth conditions (<50mbar).

We have obtained p-type conductivity in Mg-doped $Al_xGa_{1-x}N$ for x up to 0.13. It was found that the resistivity of the layers is rapidly increasing with increase of Al content.

6.7. References

1. S. Ruffenach-Clur, O. Briot, B. Gil, R.L. Aulombard, J. L. Rouviere, MRS Internet J. Nitride Semicond. Res. 2, 27(1997).
2. M. Seyboth , C. Kirchner, Annual Report 1999, Dept. of Optoelectronics, University of Ulm (1999)
3. S. R. Lee, A. F. Wright, M. H. Crawford, G. A. Petersen, J. Han, R. M. Biefeld, Appl. Phys. Lett., 74, 3344 (1999)
4. S. Nakamura and G. Fasol, The Blue Laser Diode, Springer, Berlin, 1997.
5. H. Amano, M. Iwaya, N. Hayashi, T. Kashima, S. Nitta, C. Wetzel, and I.Akasaki, Phys. Status Solidi B 216, 683 (1999).

6. J. Han, K. E. Waldrip, S. R. Lee, J. J. Figiel, S. J. Hearne, G. A. Petersen, and S. M. Myers, Appl. Phys. Lett., Vol. 78, 67 (2001)

7. T. Tanaka, A. Watanabe, H. Amano, Y. Kobayashi, I. Akasaki, S.Yamazaki, and M. Koike, Appl. Phys. Lett. 65,593 (1994).

8. I. Akasaki and H. Amano, Mater. Res. Soc. Symp. Proc. 242,383 (1991).

9. M. Suzuki, J. Nishio, M. Onomura, and C. Hongo, J. Cryst. Growth 189, 190, 511 (1998)

10. L. Sugiura, M. Suzuki, J. Nishio, K. Itaya, Y. Kokubun, and M. Ishikawa, Jpn. J. Appl. Phys., Part 1 7, 3878 (1998).

11. Suzuki M, Nishio J, Onomura M and Hongo C 1998 J. Cryst. Growth 188/189 511

12. J. Li, TN. Oder, M.L. Nakarmi, JY. Lin, and H.X. Jiang, Appl. Phys. Lett., Vol. 80, 1210 (2002)

13. N. I. Kuznetsov, A. E. Nikolaev, and A. S. Zubrilov, Yu. V. Melnik, V.A. Dmitriev, Appl. Phys. Lett., 75, 3138, (1999).

7. Growth of InGaN

7.1. Introduction

The high efficiency of luminescence from InGaN/GaN heterostructures has underpinned recent developments in blue–green optoelectronics. InGaN alloy constitutes the active region in the form of quantum well (QW) and emits light by the recombination of electrons and holes injected into the InGaN. The thickness of the InGaN layers in these devices ranges from 3-5 nm in conventional quantum-well structures to 10-50 nm in charge asymmetric resonance tunnelling structures [1].

7.2. MOCVD growth and thermal stability of InGaN

The growth of high quality InGaN films with a large indium mole fraction is difficult, because of the compositional unstable nature of the alloy or the deposition of indium droplets. This problem arises from the significantly higher vapour pressure of nitrogen over InGaN [2], and low thermal stability of InGaN. Rapid decomposition of InN occurs above 700°C. Trainor and Rose [3] observed dissociation of thin InN films at temperature as low as 500°C at atmospheric pressure. In turn, In incorporation is drastically reduced at high temperatures due to high volatility of indium nitride. For that reason, low temperature conditions are preferred for the growth of InGaN. Lowering the growth temperature, however, usually results in an inferior material quality, because the decomposition rate of NH_3 is very low. For the efficient activation of ammonia, the growth temperature should exceed 550°C (N-H bond strength is 3.9 eV). Additionally, at too low substrate temperature the mobility of adatoms is too slow, resulting in highly defective material, which is not desirable for device applications. The above-mentioned considerations limit the usable temperature window for InGaN growth to 550-850°C.

In contrast to conventional III-V alloy systems like AlGaAs where the solid composition is a linear function of the input mole ratio of the Group III metalorganic precursors at constant partial pressure of Group V gas, the solid composition of InGaN deviates significantly from a linear function at high substrate temperatures. Figure 7.1 presents theoretical curves [4,5] showing the solid composition x of $In_xGa_{1-x}N$ as a function of the input mole ratio of the indium metalorganic sources In/(In+Ga), as well as a survey [6,7] of experimental results on InGaN growth by MOCVD. As one can see, the deviation of solid composition from a linear function is increasing with increasing growth temperature. An important feature in the figure is that the isotherm lines change in a complex manner at high temperatures. This indicates that the deposition of compounds with several solid compositions is expected for a given input mole ratio of the group III metalorganic source. For example, for 790°C isotherm the solid composition from x=0.2 to x=0.8 are unreachable for any input ratio and formation of inhomogeneous composition is possible for input ratios from 0.85 to 0.95. Authors [6,7] predict from thermodynamic analysis that the compositional inhomogeneity occurs under the conditions of high growth temperature, high mole fraction of H_2, low input partial pressure of the group III metalorganic sources and low input V/III ratio.

Besides temperature, gas ambient is another important factor affecting the composition of InGaN alloy. Hydrogen used as the transport gas can also significantly reduce the incorporation of indium. The detailed mechanism as to how hydrogen affects indium incorporation is not clear. Presumably, hydrogen forms volatile InH_x compounds, shortening the lifetime of reactive indium species at the surface, and consequently reducing the amount of indium being incorporated into the growing film. Another possibility is that hydrogen affects the concentration of contaminants at the growing surface, such as carbon, which could in turn affect the In content of InGaN.

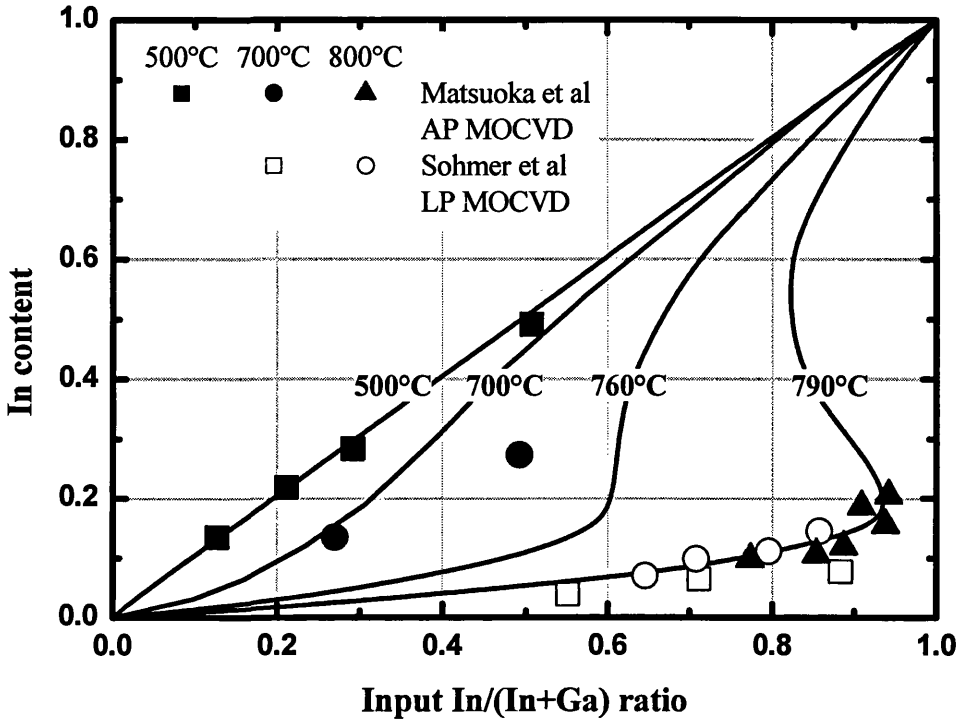

Figure 7.1 Theoretically predicted compositions of InGaN alloys for different input In/(In+Ga) gas phase ratios [4,5] are compared with experimental data for different substrate temperatures (Matsuoka [6], Scholz [7]). (From Ambacher [8])

Apart from hydrogen partial pressure, input indium ratio and the substrate temperature, the incorporation of indium can be influenced by the strain. Group-III nitrides binary compounds have crystalline lattice constants differing significantly from each other. For example, the mismatch between GaN and InN is 10.7% and 15.0%, for *a* and *c* lattice parameters, respectively. Such a large difference in the lattice parameters results in a considerable internal strain arising in ternary nitrides. Even small additions of some group-III elements into a ternary compound changes its lattice constant remarkably. As a result, a layer of ternary compound grown on an underlying binary wafer becomes highly strained. This not only influences the properties of grown material but also can affect just the growth process. For example, indium incorporation efficiency can be reduced due to so-called "compositional pulling effect". In the presence of strain, indium atoms are excluded

from the InGaN lattice to reduce the deformation energy. Compositional pulling effect was observed for other systems, such as LPE-grown InGaP/GaAs and InGaP/GaAsP and MBE-grown InAlAs/InP. Shimizu *et al* [9,10] reported on observation of compositional pulling in InGaN.

Table 19 summarises general trends between deposition parameters and structural qualities and the In incorporation in InGaN.

Table 19. General trends of the In content of epitaxial InGaN film growth in dependence of various MOCVD parameters. ↑–increasing; ↓–decreasing; 0–weak influence. From Ambacher [8]

Parameter		Indium content
Substrate temperature	↑	↓
Growth rate	↑	↑
In/(In+Ga) input ratio	↑	↑
Hydrogen partial pressure	↑	↓
Ammonia partial pressure	↑	0
Total pressure	↑	0
Biaxial compressive stress	↑	↓

Another interesting strain-related effect is considerable suppression of phase separation in the strained InGaN layers [11]. Because the enthalpy of mixing for InGaN alloy is positive, at temperatures below a certain temperature a single homogeneous phase has a higher free energy than a mixture of two phases. This dictates that at equilibrium, the single phase will decompose into a mixture of two phases. The decomposition process can be either *spinodally*, with no energy barrier, or *binodally*, with energy barrier. On the T-x phase diagram the boundaries of unstable regions are described by spinodal and binodal curves, respectively. Below the spinodal curve the solid can decompose spontaneously; in the region between spinodal and binodal the alloy is metastable. According to [12,13] the critical temperature corresponding to InGaN spinodal decomposition of InGaN is 1200°C, and the stable ternary compound with In content higher than 10% can not be obtained up to the growth temperature of 800°C. These results have been obtained using the Valence

Force Field approach for the analysis of lattice distortion. Other authors gave even more hard estimates for critical temperature: 2460°C in [14] and 1950°C in [15]. Despite the strict limitation caused by spinodal decomposition, the InGaN ternary compounds with high In content up to 30% have been repeatedly grown inside the miscibility gap. Normally, the application of the Valence Force Field model to conventional III-V compounds gives results close to experimental ones; this means that some other mechanism providing suppression of the phase separation exist. One such possible mechanism refers to additional elastic energy accumulated in a uniformly strained epitaxial layer. This energy modifies the Gibbs free energy, and as a result the miscibility gap shifts remarkably into the area of higher InN concentration and becomes an asymmetric shape (see Figure 7.2 and Figure 7.3).

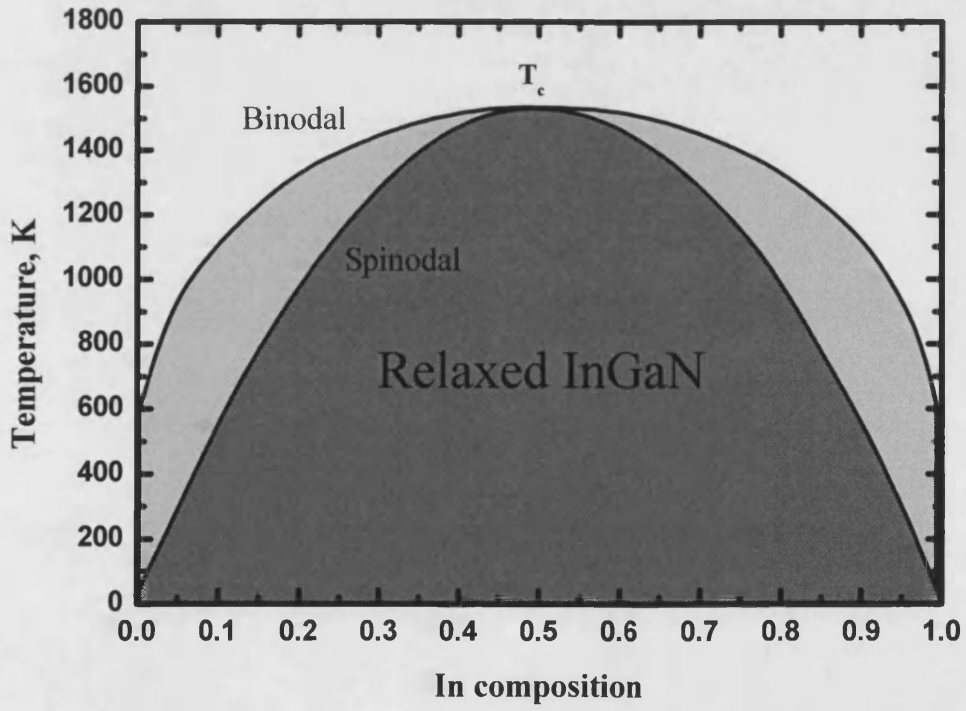

Figure 7.2. T-x phase diagram for relaxed InGaN alloy

The results obtained by Karpov [11] show that elastic strain affects dramatically the phase separation in InGaN ternary compounds. The effect is predicted to lower the critical temperature from 1135°C down to 735°C.

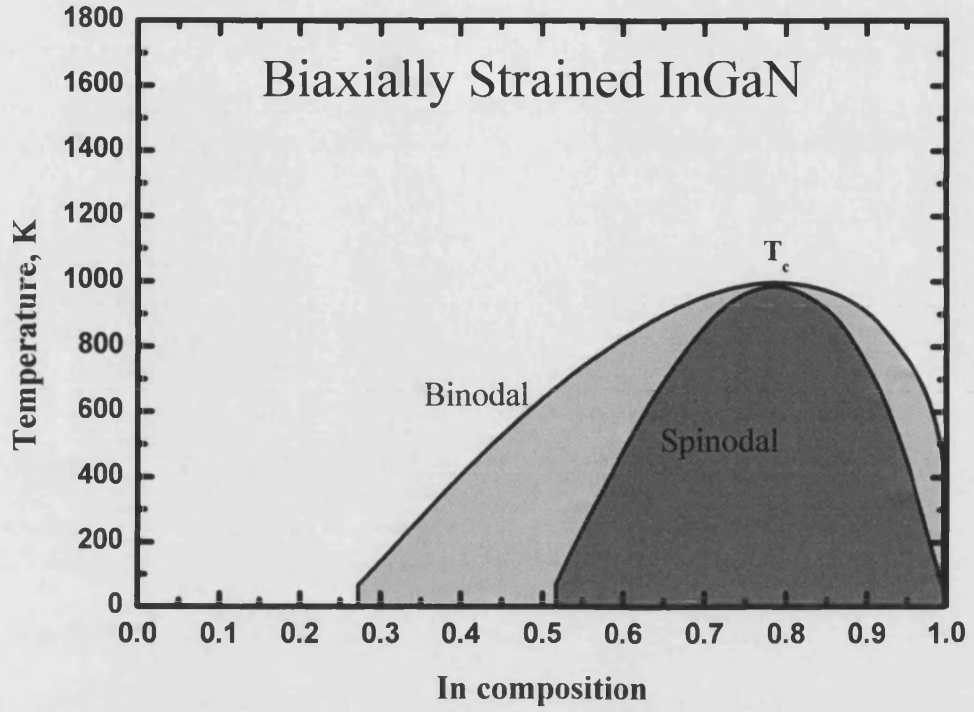

Figure 7.3. T-x phase diagram for biaxially (0001)-strained InGaN alloy

7.3. Experiment. MOCVD growth of InGaN layers

Sets of samples have been grown by low pressure MOCVD on (0001)-oriented 2" sapphire substrates. TMGa/TEGa, TMIn, NH_3 were employed as precursors and H_2/N_2 as gas carriers. The growth pressure was 200 mbar. The structures consisted of a low temperature GaN nucleation layer, 1.2 μm-thick GaN buffer layer and upper $In_xGa_{1-x}N$ layers with thickness 15-70 nm. The growth of GaN buffer was conducted using hydrogen as a carrier gas due to superior quality of GaN films grown under hydrogen ambient. In contrast, the growth InGaN was conducted in nitrogen in order to improve the incorporation of indium.

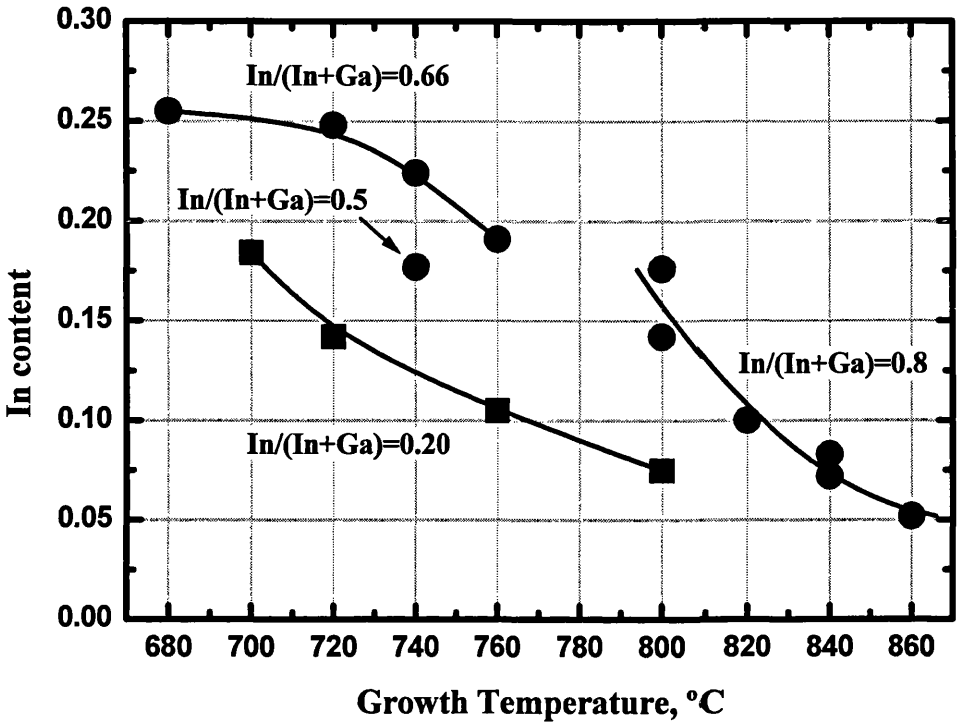

Figure 7.4. Indium content versus growth temperature for different In/(In+Ga) input ratios

The alloy composition of the InGaN layer was controlled by changing the input In/(In+Ga) ratio from 0.2 to 0.8 and the growth temperature from 680°C to 860°C. The indium content was measured by x-ray diffraction (see details below) and was in the range 0.05-0.25.

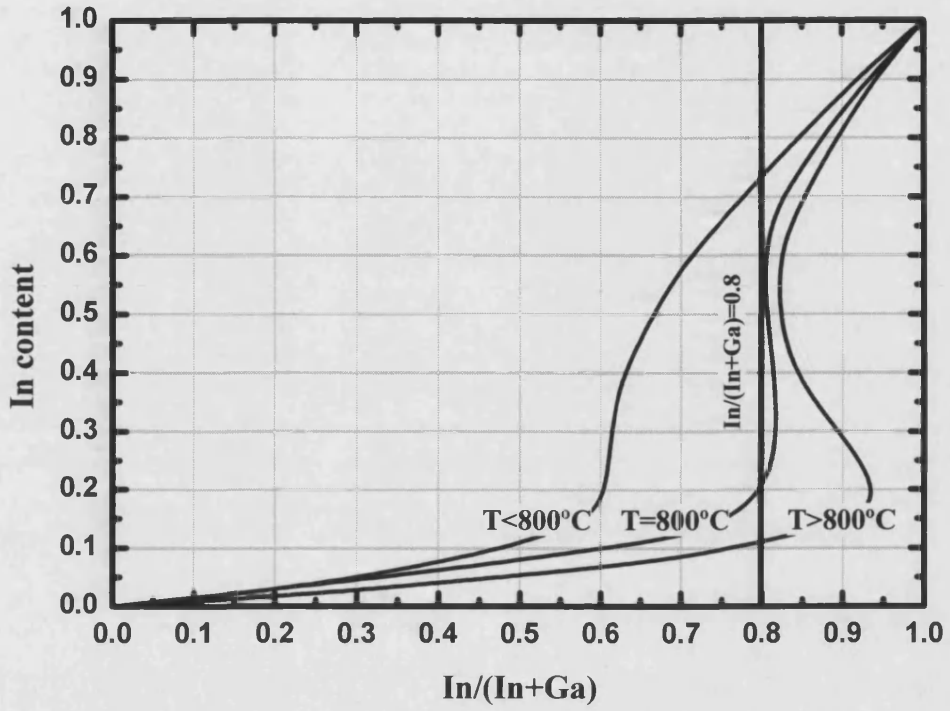

Figure 7.5. Illustration of unstable InGaN growth for the input ratio In/(In+Ga)=0.8 and the growth temperature of 800°C

Figure 7.4 illustrates the dependence of the indium composition on the growth temperature. As one can see, the indium incorporation into the InGaN film strongly increases with decreasing growth temperature. The dependence is stronger for high input ratios, which agrees well with theoretical thermodynamic calculations (see Figure 7.1). We have found it difficult to control In composition for input ratio In/(In+Ga)=0.8 for temperatures below 800°C. The explanation of this phenomenon can be readily seen in Figure 7.5.

For growth temperatures higher than 800°C the indium content is uniquely defined by the intersection of the vertical line In/(In+Ga)=0.8 and the corresponding isotherm curve. For growth temperature of 800°C the input concentration of 0.8 corresponds to the unstable region of the isotherm, resulting in abrupt increase of In composition and multiphase growth.

The discrepancy between isotherm temperatures in Figure 7.1 and Figure 7.5 is explained by the difference of temperature definitions. In the Figure 7.1 we refer to the temperature of the substrate surface used in thermodynamic calculations, while in Figure 7.5 we deal with the susceptor temperature measured by the pyrometer. The difference between pyrometer readings and actual substrate temperature is about -60°C under these conditions.

7.4. AFM measurements

The surface morphology of InGaN layers was characterised by means of Atomic Force Microscopy (AFM). As one can see in Figure 7.6, there is a clear dependence of the surface morphology on the growth temperature. InGaN layers grown at the highest temperature (800°C) have a smooth surface with some occasional "bumps". At this point, it would be speculative to draw any conclusions on the nature of these "bumps". Most likely they are three-dimensional InGaN crystallites. The average size of the "bumps" decreases with decreasing growth temperature (increasing In content), until they fully vanish at 720°C. At the same time, the atomic growth steps are getting more pronounced with temperature decrease. The sample grown at the lowest temperature (720°C) has a large density (10^9–10^{10} cm^{-2}) of pinholes caused either by the patterning of dislocation lines or formation of In droplets.

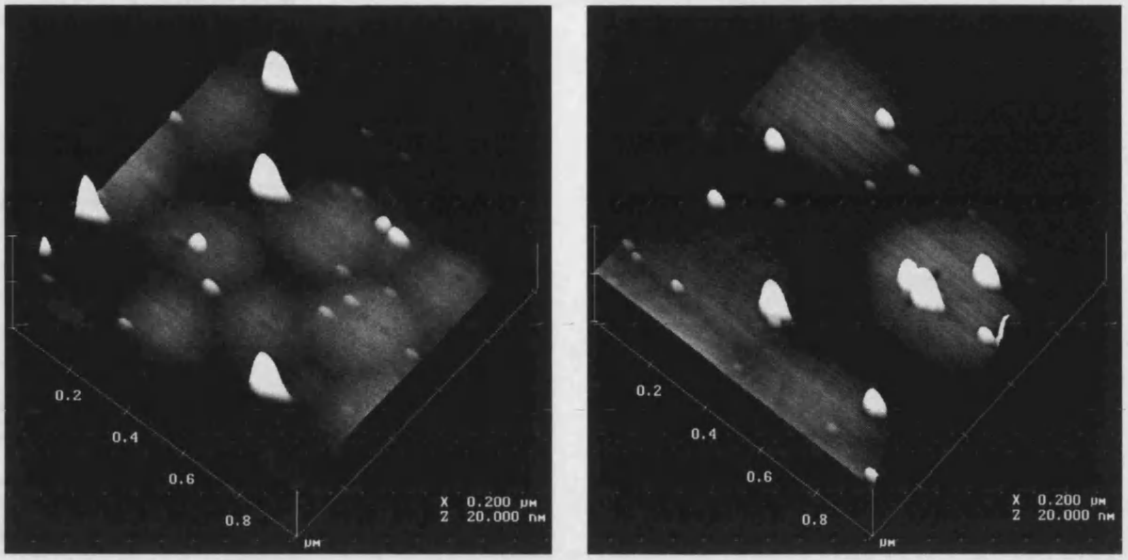

800°C 760°C

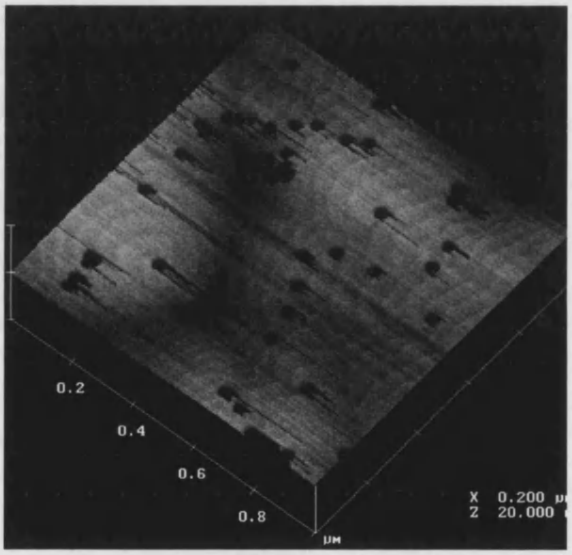

720°C

Figure 7.6. AFM images of InGaN epilayers grown at various temperatures

7.5. Photoluminescence

Room-temperature photoluminescence (PL) spectra were measured to obtain emission wavelength of the InGaN layers. A 0.1-1 mW He-Cd laser was used as the excitation light source for PL. Figure 7.7 presents room temperature PL spectra from InGaN films with different In content. All samples show strong sharp emission peaks with narrow FWHM of about 50-100 meV. All PL peaks showed the excitation power

dependence due to built-in piezoelectric field. No evidence of the phase separation in the InGaN layers has been observed by PL measurements.

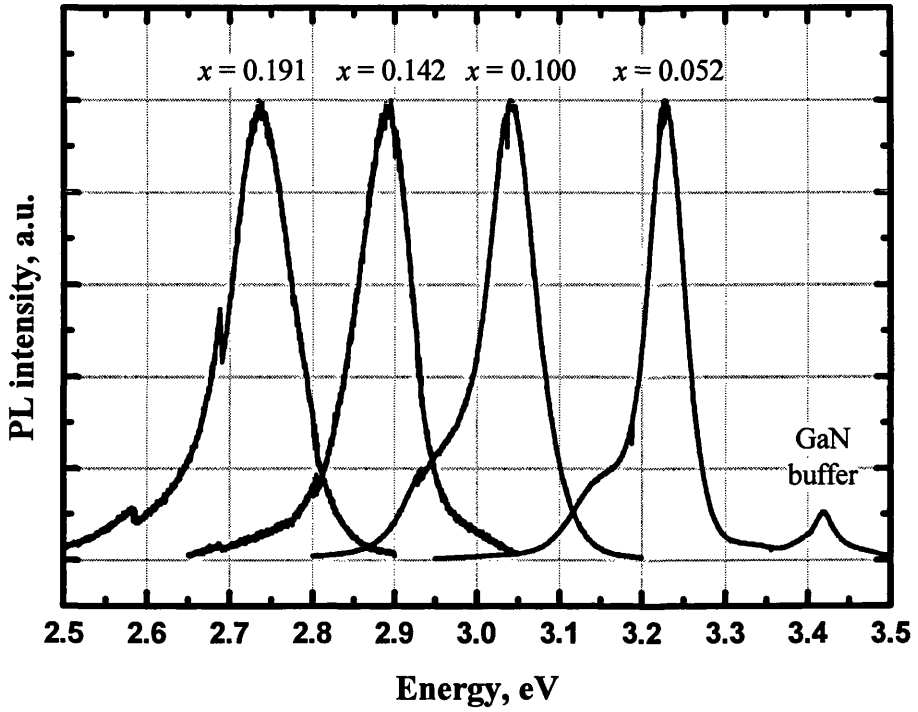

Figure 7.7. Room-temperature PL spectra for the InGaN layers grown on GaN.

7.6. X-ray characterisation of InGaN films

High resolution X-ray diffraction (HRXRD) techniques are widely used to measure very accurately and non-destructively the lattice constant of alloys, making possible the determination of the composition x when the dependence with the lattice constant is known. In many systems, this dependence is assumed to be linear (Vegard's Law). In this case, it is sufficient to measure one of the lattice constants, usually in the direction perpendicular to the surface of the epilayer, to calculate the alloy composition.

However, Vegard's law is valid only for relaxed crystals, which in most cases is not a valid assumption for InGaN epilayers. Due to difficulty of dislocation formation at typical InGaN growth temperatures, InGaN layers with thickness much larger than the critical thickness remained pseudomorphic to GaN [16,25,27,32,35] and no misfit

dislocations were formed at InGaN/GaN interface. Thus, the In content needs to be corrected with respect to elastic properties of the layers. For strained layers the change of the lattice constants due to biaxial stress must be considered. Both c and a lattice parameters, have to be measured to separate the influence of strain and composition on the lattice constants.

7.6.1. Measurements of lattice constants

For the correct determination of a and c lattice constants it is required to measure at least two reflections from non-parallel diffracting planes. In practice, it is convenient to measure one symmetric reflection from $(00 \cdot l)$ plane, and one asymmetric reflection from $(hk \cdot l)$ plane. Symmetric reflections are sensitive only to the c lattice constant, while asymmetric reflections are sensitive to both a and c lattice constants. The c lattice constant can be readily found from the position of the symmetric reflection. Afterwards, using the obtained value for c, the a lattice constant is found from the position of the asymmetric reflection.

Reflections from the planes not parallel to the sample surface can be measured in two different ways. In the first approach, the sample is rotated about the axis perpendicular to the plane containing the incident and diffracted beams to accommodate angle between the plane and the sample surface. In this geometry the primary beam makes angle $\Theta - \varphi$ (low incidence) or $\Theta + \varphi$ (high incidence) with sample surface, where Θ and φ are the Bragg's angle and the angle between the plane of reflection and sample surface, respectively. This is so-called asymmetric geometry, as incident and reflected angles are different.

In the second approach, asymmetric reflections are measured in a symmetric experimental geometry. In this geometry the sample is tilted by angle φ about an axis in the plane containing the incident and diffracted beams.

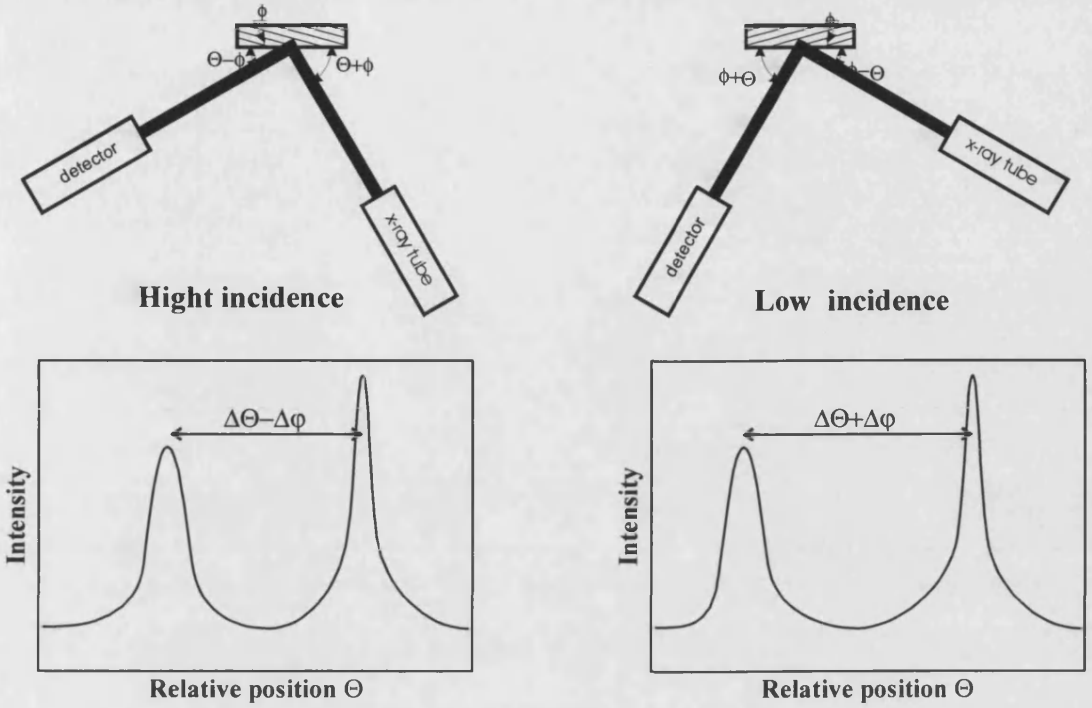

Figure 7.8 High and low incidence asymmetric geometries

It is very difficult to measure the absolute value of the Bragg's angle; for epitaxial layers it is more convenient to measure the separation between the epilayer and substrate peaks. For InGaN/GaN samples, the reflection from GaN can be used as an internal reference for Bragg's angle position. The thick GaN buffer is assumed to be relaxed with the *a* and *c* lattice constants equal to those for bulk GaN. The separation between GaN and InGaN peaks can be measured experimentally with a high degree of accuracy.

In asymmetric geometry this separation is either $\Delta\Theta - \Delta\varphi$ or $\Delta\Theta + \Delta\varphi$, where $\Delta\Theta$ is difference of Bragg angles $\Delta\Theta = \Theta_{GaN} - \Theta_{InGaN}$ and $\Delta\varphi$ is angle between planes in GaN and in InGaN $\Delta\varphi = \varphi_{GaN} - \varphi_{InGaN}$. In general, planes of the set $(hk \cdot l)$ in GaN are not parallel to the planes of the same set $(hk \cdot l)$ in InGaN, because the ratio of lattice constants a/c is different for GaN and InGaN. Consequently, $\Delta\varphi$ is non-zero. Moreover, $\Delta\varphi$ depends on the degree of relaxation of the InGaN layer and for the fully strained layer can be as high as 0.1°–0.3°. It should be noted, that it is possible to eliminate the influence of $\Delta\varphi$ performing two scans with high and low angle of incident beam and averaging the

separation between GaN and InGaN peaks from these two scans. In this case $\pm\Delta\varphi$ terms cancel each other out

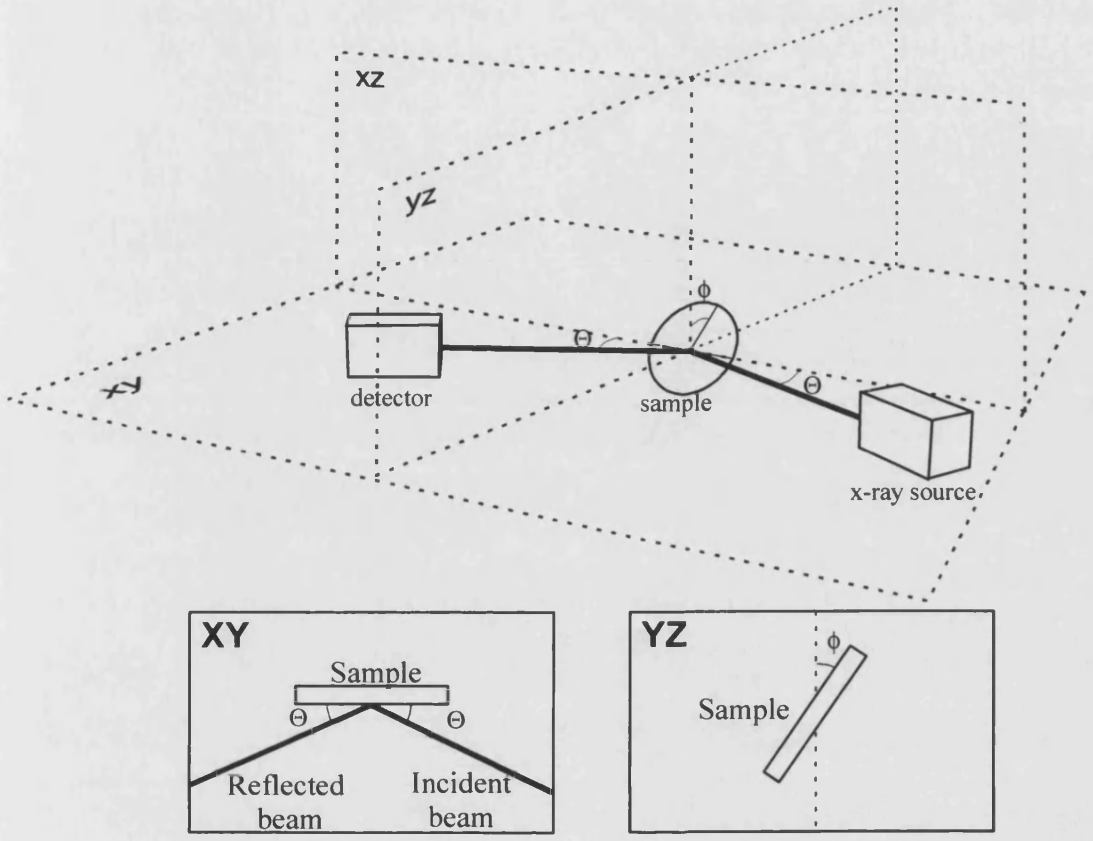

Figure 7.9. Symmetric geometry

$$\Delta = \frac{\Delta\Theta + \Delta\varphi + \Delta\Theta - \Delta\varphi}{2} = \Delta\Theta \qquad (7.1)$$

Nevertheless, we have found this approach too complicated and not precise enough for our purposes. In contrast, in symmetric geometry the angular separation between GaN and InGaN peaks gives us the exact value of $\Delta\Theta$ without any additional calculations. Since that, XRD measurements of InGaN films were performed in symmetric geometry. High-order reflections are more sensitive to small variations of the lattice constant; hence $(00\cdot6)$ reflection was used for *c* parameter measurements. The results were also validated by $(00\cdot2)$ reflection scans. In plane lattice constant *a* was measured using $(10\cdot4),(10\cdot5),(20\cdot5)$, and $(11\cdot4)$ reflections. The resulting *a*-lattice constants for the layer were calculated after averaging the values calculated from each of these three

reflections. Symmetric and asymmetric reflections were measured using a high-resolution Bede D1 diffractometer with Cu $K\alpha_1$ radiation. Figure 7.10 presents an example of the XRD Θ-2Θ scan for symmetric (00.6) and asymmetric (20.5) reflection from one of the InGaN samples. In both reflections GaN- and InGaN- related Gaussian-like diffraction peaks are clearly seen. The FWHM of corresponding (00.2) InGaN reflection peaks is about 4-8 min. The FWHM for thicker InGaN layers is slightly lower than for thinner layers.

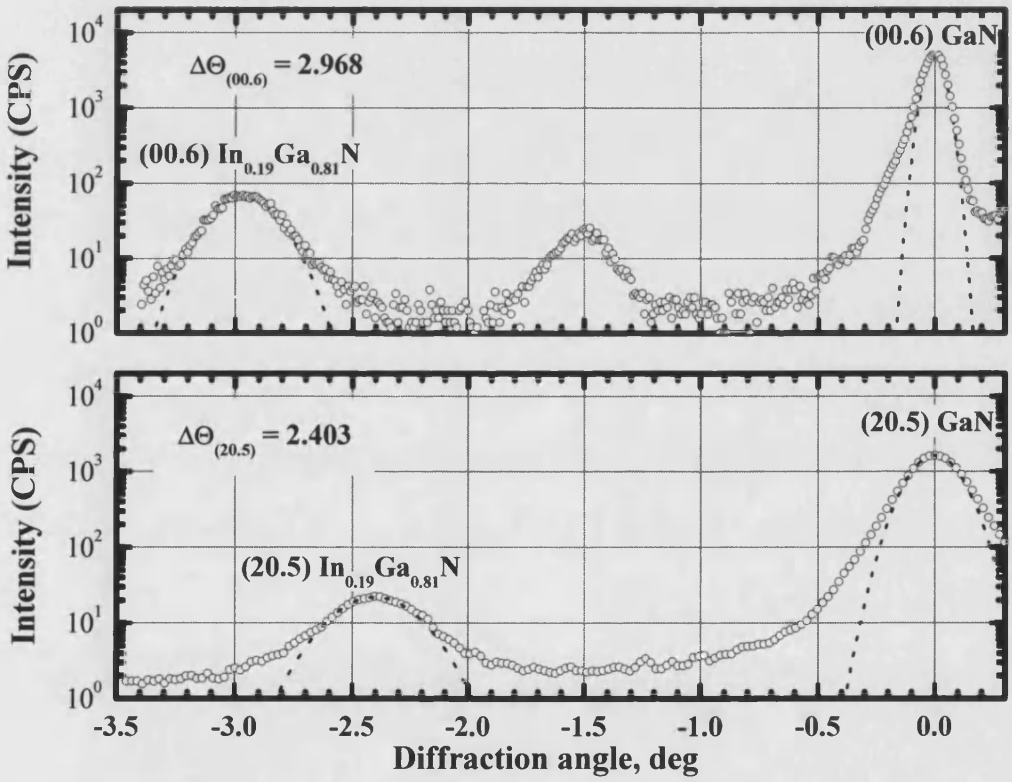

Figure 7.10. XRD rocking curves of symmetric $(00\cdot6)$ **and asymmetric** $(20\cdot5)$ **reflections for 40 nm – thick $In_{0.19}Ga_{0.81}N$ layer grown on GaN.**

For a hexagonal crystal, the distance d_{hkl} between adjacent $(hk\cdot l)$ planes is related with lattice parameters a and c by the following expression

$$\frac{1}{d_{hkl}^2} = \frac{4}{3}\left(\frac{h^2 + hk + k^2}{a^2}\right) + \frac{l^2}{c^2} \tag{7.2}$$

In turn, the plane spacing d_{hkl} can be found from the angular position of x-ray diffraction peak Θ_b using Bragg's law:

$$d_{hkl} = \frac{\lambda}{2\sin\Theta_B} \tag{7.3}$$

where λ is the wavelength of x-ray radiation. In our case $\lambda = CuK_{\alpha 1} = 1.54059\text{Å}$

As we mentioned before, it is more convenient to measure the angular separation $\Delta\Theta_B$ between GaN and InGaN reflections rather than the absolute value of Bragg's angle Θ_B. In this case the equation (7.3) can be modified as follows

$$d_{hkl} = \frac{d_{hkl}^{(GaN)}}{1 + 2\sin\frac{\Delta\Theta_B}{2}\sqrt{\left(\frac{2d_{hkl}^{(GaN)}}{\lambda}\right)^2 - 1}} \tag{7.4}$$

Knowing the interplanar spacing d_{hkl} one can readily calculate the lattice parameters. The interplanar spacing for $(00\cdot l)$ planes immediately gives the c lattice parameter

$$c = l \cdot d_{00l} \tag{7.5}$$

The a lattice parameter is found from interplanar spacing of asymmetric diffracting planes $(hk\cdot l)$ using the obtained value of the c lattice parameter.

$$a = \sqrt{\frac{4}{3}\left(h^2 + hk + k^2\right) \Big/ \left(\frac{1}{d_{hkl}^2} - \frac{l^2}{c^2}\right)} \tag{7.6}$$

The results on lattice constant calculations are presented in Figure 7.11. The a lattice parameters for all InGaN samples are close to that of the GaN, indicating that the InGaN layers are pseudomorphic to underlying GaN buffer layer.

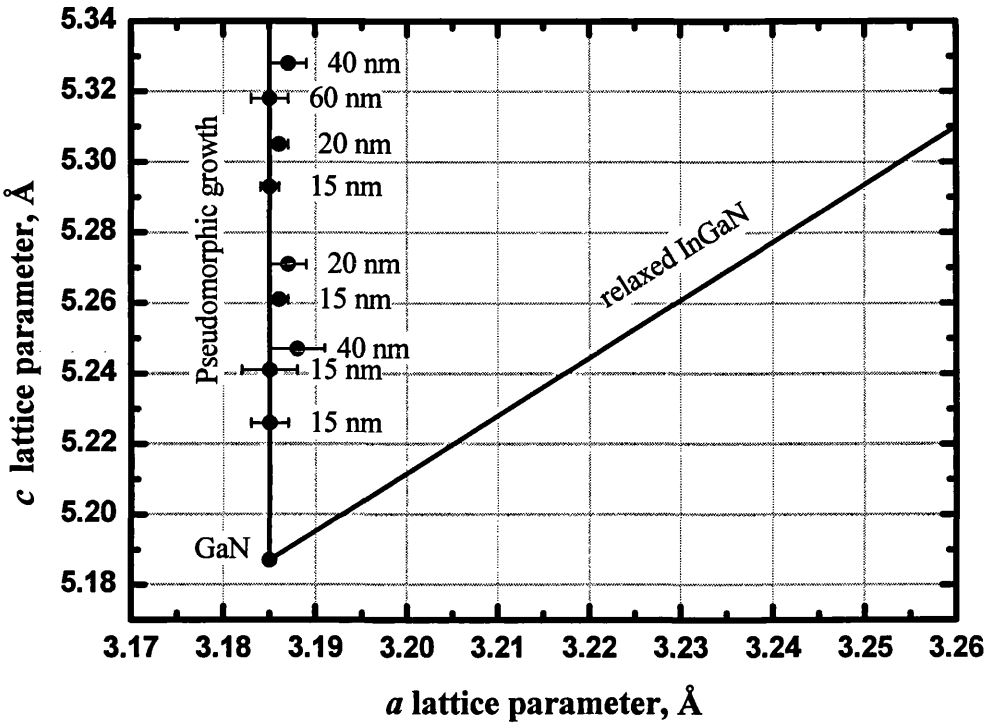

Figure 7.11 The *c*-lattice parameter versus the *a*-lattice parameter for the InGaN layers on GaN. The vertical line marks GaN *a*-lattice parameter. The diagonal line corresponds to relaxed InGaN.

The maximal measured strain relaxation degree for the InGaN layers is only 4%, while typical is about 0-2%. No visible change in the relaxation degree is observed even for 60-70 nm thick InGaN layers as compared to 15-20 nm thick InGaN layers.

7.6.2. Calculation of In content

We assume that the Vegard's law is valid for InGaN system, i.e. relaxed a and c lattice parameters are changing linearly with In content x.

$$c_0 = c_0^{(GaN)} \cdot (1-x) + c_0^{(InN)} \cdot x \qquad (7.7)$$
$$a_0 = a_0^{(GaN)} \cdot (1-x) + a_0^{(InN)} \cdot x$$

In the limiting case of a fully relaxed InGaN layer on the GaN substrate, the experimentally measured lattice parameters are equal to unstrained ones. Using equation (7.7) one can find the indium content x.

$$x^{(\max)} = \frac{c - c_0^{(GaN)}}{c_0^{(InN)} - c_0^{(GaN)}} \tag{7.8}$$

Only one measurement of symmetric plane $(00 \cdot l)$ is required as the equation (7.8) includes only the c lattice constant. As we discussed earlier, if the thickness of InGaN layers is below certain critical value, the formation of misfit dislocations doesn't occur. Consequently, the InGaN film is biaxially stressed and the lattice parameters are different from unstressed values. Nevertheless, the equation. (7.8) is still useful even for strained layers as it gives the upper estimate of indium composition.

The biaxial compressive strain $\varepsilon_{\parallel}$ in the InGaN layer induces the corresponding perpendicular strain $\varepsilon_{\perp}$. The two components of strain are interdependent and related by the following expression.

$$\varepsilon_{\perp}(x) = -2\frac{\nu(x)}{1-\nu(x)} \cdot \varepsilon_{\parallel}(x) \tag{7.9}$$

where $\nu(x)$ is the Poisson's ratio. For hexagonal layers grown along (00.1) axis the Poisson's ratio is expressed through elastic constants C_{13} and C_{33} as

$$\frac{\nu(x)}{1-\nu(x)} = \frac{C_{13}(x)}{C_{33}(x)} \tag{7.10}$$

Rewriting Eq (7.9) in terms of lattice parameters, we obtain the following expression

$$\frac{c - c_0(x)}{c_0(x)} = -2\frac{\nu(x)}{1-\nu(x)} \cdot \frac{a - a_0(x)}{a_0(x)} \tag{7.11}$$

For an ideal wurtzite structure, the ratio of lattice parameters is fixed $c_0/a_0 = 1.633$. For real crystals, the ratio can deviate from 1.633 due to non-ideality of the structure. For example, for GaN this ratio is $c_0^{(GaN)}/a_0^{(GaN)} = 1.6259$ and for InN $c_0^{(InN)}/a_0^{(InN)} = 1.6114$. However, the variation of this ratio is small and can be neglected. As a first order approximation, we can assume that the ratio of lattice parameters of GaN and InGaN is the same.

$$\eta = \frac{c_0^{(GaN)}}{a_0^{(GaN)}} = \frac{c_0(x)}{a_0(x)} = const \tag{7.12}$$

$$c_0(x) = \eta a_0(x)$$

Applying equation (7.12) to equation (7.9), we obtain

$$\frac{c - c_0(x)}{c_0(x)} = -2\frac{\nu(x)}{1-\nu(x)} \cdot \frac{\eta a - c_0(x)}{c_0(x)} \tag{7.13}$$

The relaxed lattice parameters of InGaN can be calculated from the Vegard's law equations (7.7)

$$c - c_0^{(GaN)} - x\left(c_0^{(InN)} - c_0^{(GaN)}\right) = -2\frac{\nu(x)}{1-\nu(x)} \cdot \left[\left(\eta a - c_0^{(GaN)}\right) - x\left(c_0^{(InN)} - c_0^{(GaN)}\right)\right] \tag{7.14}$$

We solve this for x, which gives

$$x = \frac{1-\nu(x)}{1+\nu(x)} \cdot \frac{c - c_{\mathrm{GaN}}}{c_{\mathrm{InN}} - c_{\mathrm{GaN}}} + \frac{2\nu(x)}{1+\nu(x)} \cdot \frac{a - a_{\mathrm{GaN}}}{a_{\mathrm{InN}} - a_{\mathrm{GaN}}} \tag{7.15}$$

Two marginal cases of fully strained layer and fully relaxed layer should be discussed in more detail. For InGaN layers pseudomorphic to GaN the in-plane lattice parameter of InGaN is equal to that of GaN $a = a_{GaN}$, and the second term in equation (7.15) vanishes. In the case of fully relaxed layer, which formally corresponds to zero Poisson's ratio $\nu = 0$, equation (7.15) reduces to equation (7.8) for unstrained layers. In these two particular cases, when it is possible *a priori* to make some assumption about the degree of the strain (0% strain or 100% strain) in the layer, only the c lattice parameter is required for calculation of the In composition. In the general case of indefinite strain the equation contains both lattice parameters a and c. It is important to note that the In content depends also on the value of the Poisson's ratio used for calculations. Therefore, for the correct determination of the In content in strained InGaN layers, one should have some additional information about elastic properties of the material.

7.6.3. Poisson's ratio

Information on the elastic properties of InGaN alloy is incomplete and inaccurate. Görgens *et al* [17] used a linear interpolation between GaN and InN, which yields quite a sophisticated expression for In composition *x*. However, their approach gives essentially the same results as compared to experimental uncertainty. Therefore, we neglect the dependence of the Poisson's ratio on the indium composition and assume that the same value can be used for GaN and near-GaN InGaN alloys.

Published theoretical and experimental data on the elastic constants of GaN are quite scattered. Theoretical calculations [18,19] predict that in GaN the ratio $2C_{13}/C_{33}$ is about 0.51, which corresponds to the Poisson's ratio of about 0.20. Calculation with this value yields, however, a lower In content as compared to direct measurement by SIMS [32] or RBS [25]. The measured Poisson's ratio in the case of RBS In-content determination should be 0.18. Several experimental works were performed for measuring the Poisson's ratio. Detchprohm *et al* [20] reported $2C_{13}/C_{33} = 0.38$ ($\nu = 0.16$) after fitting their data on *c*- and *a*- lattice constants for thick relaxed GaN layers on sapphire. Deger *et al* [21] reported $2C_{13}/C_{33} = 0.56$ ($\nu = 0.22$) of GaN from the surface acoustic-wave measurements on epitaxial AlGaN films. Yamaguchi *et al* [22] reported $2C_{13}/C_{33} = 0.60$ ($\nu = 0.23$) from the Brillouin scattering study of epitaxial GaN films. This value was widely used by many authors for determination of the bowing parameter. The Brillouin scattering study for bulk GaN [24, 23] gave $2C_{13}/C_{33} = 0.42$ ($\nu = 0.17$). However, as it was mentioned by Yamaguchi *et al.* [24], the measured elastic constants of thin GaN epitaxial films can differ significantly from actual values due to the presence of residual strains in epitaxial layers. In addition, epitaxial films have high dislocation densities, invariability affecting properties of GaN.

Therefore, the most reliable values of the Poisson's are the ones that were measured either for bulk GaN [22,23] or for thick relaxed layers [20], or obtained by correlating

XRD data with independent measurements of In content by other methods [25]. As it is seen, the most reliable data on the Poisson's ratio measurements, give the same results as compared to the admissible Poisson's ratio uncertainty (see section 7.8.3). In our calculations, we use $\nu = 0.17$ as an average between these data.

Table 20. Elastic constants (GPa) for wurtzite GaN

	C_{13}	C_{33}	$2C_{13}/C_{33}$	$\nu = \frac{C_{13}}{C_{33}+C_{13}}$
Kim *et al* [18]	100	392	0.51	0.20
Polian *et al* [26]	106	398	0.53	0.21
Wright *et al* [19]	103	405	0.51	0.20
Romano *et al* [25]	-	-	-	0.18
Detchprohm *et al* [20]	-	-	0.38	0.16
Deger *et al* [21]	110	390	0.56	0.22
Yamaguchi *et al* [22]	114	381	0.60	0.23
Yamaguchi *et al* [24]	80	387	0.42	0.17
Deguchi *et al* [23]	80.4	387	0.42	0.17

7.7. Dependence of emission energy on alloy composition

Figure 7.12 presents the dependence of the PL emission energy on the In content in the InGaN layers. Error bars illustrate the dependence of In content on the degree of relaxation of the InGaN layer. The right end of the bar corresponds to the fully relaxed material and the left end corresponds to the fully strained material.

7.8. Bowing parameter in InGaN alloys[a]

7.8.1. Review of published results

The dependence of the emission wavelength on the In content in InGaN layers is important for device design. Emission energy of an $In_xGa_{1-x}N$ alloy system is usually described by

$$E(x) = (1-x)E_{GaN} + xE_{InN} - b \cdot x(1-x) \qquad (7.16)$$

[a] Published in MRS Internet J. Nitride Semicond. Res. 6, 6 (2001).

where b is a bowing parameter. This dependence has been measured by many groups [25,27,28,29,30,31,32], and significantly "different" results have been obtained.

The bandgap energy of GaN is measured with good accuracy and a value of 3.4 eV is generally accepted. In contrast, there is large discrepancy in the values of InN bandgap energy. In this chapter we assume InN bandgap to be 1.95eV as this value was used in all publications cited here. However, it should be noted that recent study [33] strongly suggests that a wurtzite InN single crystal has a true bandgap of 0.7-1 eV.

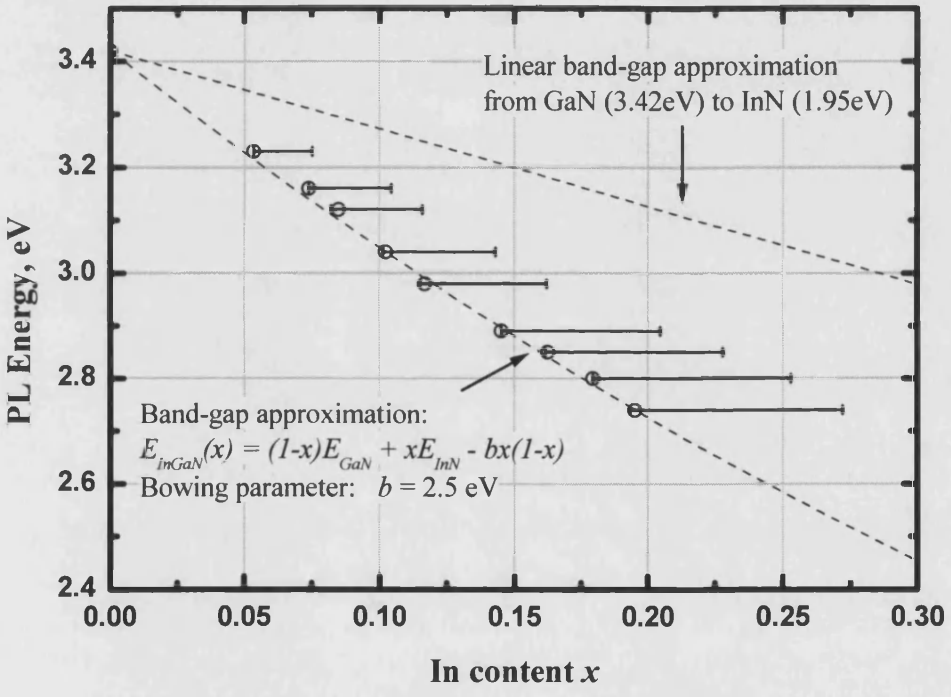

Figure 7.12. PL emission energy versus In content in the InGaN layers. Horizontal bars represent the possible In content range (as measured from *c*-lattice constant) depending on the relaxation degree of the InGaN layers. The right end of the bar (maximal In content) in error bars corresponds to fully relaxed InGaN layers, while the left end (minimal In content) corresponds to InGaN layers pseudomorphically strained to GaN.

The bowing parameter has been measured to be from 1 eV to 3.2 eV (see Table 21). The possible reasons of "scatter" in bowing parameter values were widely discussed. It has been pointed out that determination of the In content by x-ray diffraction (XRD), using the linear interpolation of the c lattice parameter between GaN and InN (Vegard's law), may

result in a systematic overestimation of the In content, and low values of bowing parameter. This determination implicitly assumes that InGaN layers are relaxed. It was observed, however, that due to difficulty of dislocation formation at typical InGaN growth temperatures, InGaN layers with thickness much larger than the critical thickness remained pseudomorphic to GaN [25,27,32,34,35], and no misfit dislocations were formed at InGaN/GaN interface. Thus, the In content needs to be corrected with respect to elastic properties of the layers resulting in higher values of bowing parameter. The "scatter" in bowing parameter exists, however, even in this case. Direct measurement of the In content by Rutherford back-scattering spectrometry (RBS) [25] and secondary ion mass spectroscopy (SIMS) with calibrated standards [32] confirms some of XRD results but differs significantly from others. Besides, it has been proved that the bowing parameter depends also on the method of optical transition measurement. Photoluminescence (PL) [27,28,36] gives typically lower values of energy than optical transmission (OT) [29,25], photothermal deflection spectroscopy (PDS) [31], photorefraction (PR) [30,32,36] and spectroscopic ellipsometry (SE) [37]. This difference, however, as well as uncertainty in energy measurement due to possible In content fluctuation is not large enough to explain "scatter" in the published values of bowing parameter.

Table 21. Values of bowing parameter for strained InGaN layers obtained by various groups. Recalculated values with consideration of the same Poisson's ratio $\nu = 0.17$ ($2C_{13}/C_{33} = 0.41$) are also given. For references [25] and [29] the bowing parameter is calculated from given experimental points.

	Composition measurement	Poisson's ratio	In content	Energy measurement	Bowing parameter (eV)	
					measured	recalculated
Present work	XRD	0.17	0 – 0.2	PL	2.5	2.5
Takeuchi et al. [27]	XRD	0.23+0.10·x	0 – 0.2	PL	3.2	2.6
Nakamura [28]	XRD	0	0 – 0.33	PL	1.0	2.1
McCluskey et al. [29] and Romano et al. [25]	RBS & XRD	(0.18)	0 – 0.11	OT	2.5	-
Wetzel et al. [30]	XRD	0.23+0.05·x	0 – 0.2	PR	2.6	2.1
				PL	3.2	2.6
Scholz et al. [31]	XRD	0	0 – 0.13	PDS	1.1	2.2
Wagner et al. [32]	SIMS	-	0 – 0.15	PR	2.0	-

7.8.2. Admissible uncertainty of bowing parameter

The accuracy of bowing parameter measurements is limited by two main factors. The first is the InGaN composition fluctuations over the sample surface. The second is the energy-position fluctuations in room-temperature PL measurements. We assume that both these factors have approximately the same influence on experimental accuracy, so that the uncertainty in emission-energy measurements is $\Delta E \approx kT$. It gives the bowing parameter measurement uncertainty $\Delta b \geq 4\Delta E \approx 0.1$ eV. The uncertainty depends on maximal In content measured. The lower In content, the higher uncertainty. For example, for InGaN layers with maximal In content of only 0.10-0.12, the uncertainty should be about 0.25 eV. For layers with maximal In content of 0.20, the uncertainty should be about 0.15 eV.

7.8.3. Admissible uncertainty of Poisson's ratio

X-ray diffraction is the most widely used technique for evaluation of the composition of ternary alloys. As it was mentioned above, the deformation of the unit cell in InGaN affects the interpretation of the In content from XRD measurements. Thus, the calculated In content depends on the Poisson's ratio. Knowing the admissible uncertainty of the bowing parameter, we can estimate the required accuracy of the Poisson's ratio. The acceptable precision of the In content calculation Δx can be estimated from (7.16) as follows:

$$\frac{\Delta x}{x} \approx -\frac{\Delta b}{E_{GaN} - E_{InN} + b} \tag{7.17}$$

Thus, the admissible Poisson's ratio uncertainty for measuring the bowing parameter of strained InGaN alloys with In content up to 0.2 can be estimated from (7.15) and (7.17) as

$$|\Delta \nu| \approx \frac{1-\nu^2}{2} \cdot \frac{\Delta b}{E_{GaN} - E_{InN} + b} \approx 0.01 \div 0.02 \tag{7.18}$$

7.8.4. Discrepancy in published values of the bowing parameter

In most of published reports on determination of the bowing parameter in InGaN authors measured In content by means of x-ray diffraction. The values of the Poisson's ratio used by various groups in their calculations are listed in Table 21. In several works, InGaN layers were assumed relaxed which formally corresponds to $\nu = 0$ in equation (7.15). As we mentioned before, neglecting the strain in epitaxial InGaN layers results in systematic overestimation of In content and, consequently, low values of the bowing parameter. Other authors have considered the strain effects in calculation of In composition. However, they used different values of Poisson's ratio, which results in different values of the bowing parameter.

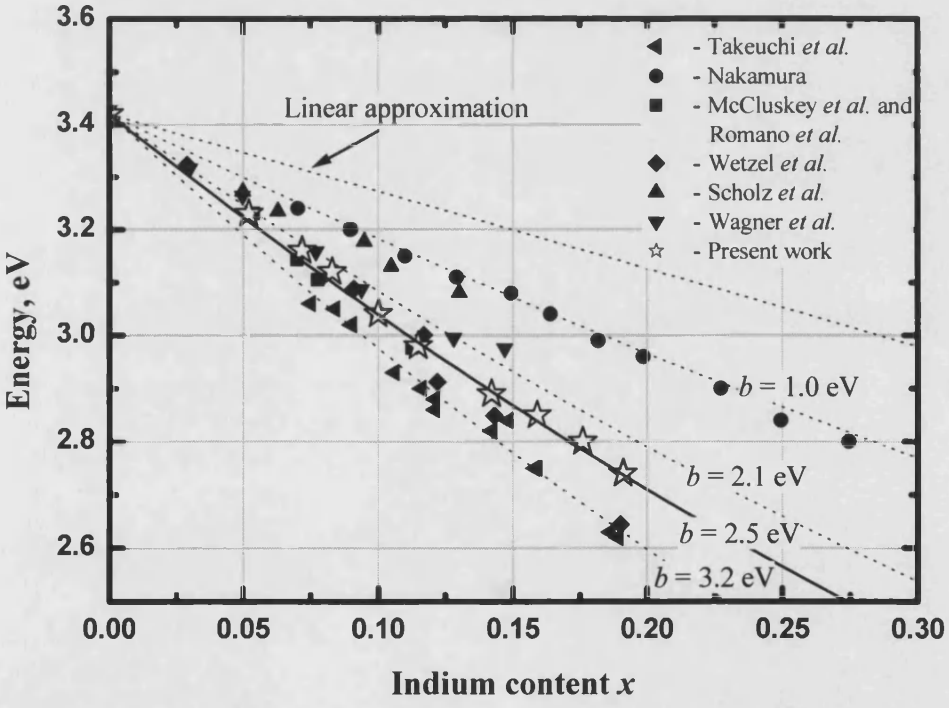

Figure 7.13. Emission energy of InGaN layers versus In content. Experimentally measured and "as is" published data are shown.

The comparison of our experimental data on PL energy dependence on the In content with previously published data is presented in Figure 7.13. As one can see, there is large discrepancy in measured dependencies. The bowing parameter varies from 1 eV [28] to

3.2 eV [27,30]. In Figure 7.14, the published data are recalculated with respect to the same Poisson's ratio $\nu = 0.17$ and the same GaN emission energy of 3.42 eV. In the above calculation we have implicitly assumed that the InGaN layers are pseudomorphically strained to GaN. As one can see, the recalculated points lie much closer to each other. Consequently, the scattering in the values of the bowing parameter is reduced to 2.1–2.6 eV. This proves that the major reason of different values of the bowing parameter is the Poisson's ratio used for calculation of In content. It interesting to note, that all PL measurements (except Nakamura [28]) typically give larger values of the bowing parameter of 2.6–2.5 eV, while OT, OR and PDS techniques yield the bowing parameter of 2.1–2.2 eV. Additional changes in measured dependencies can be made after correction to the same lattice parameters of GaN and InN.

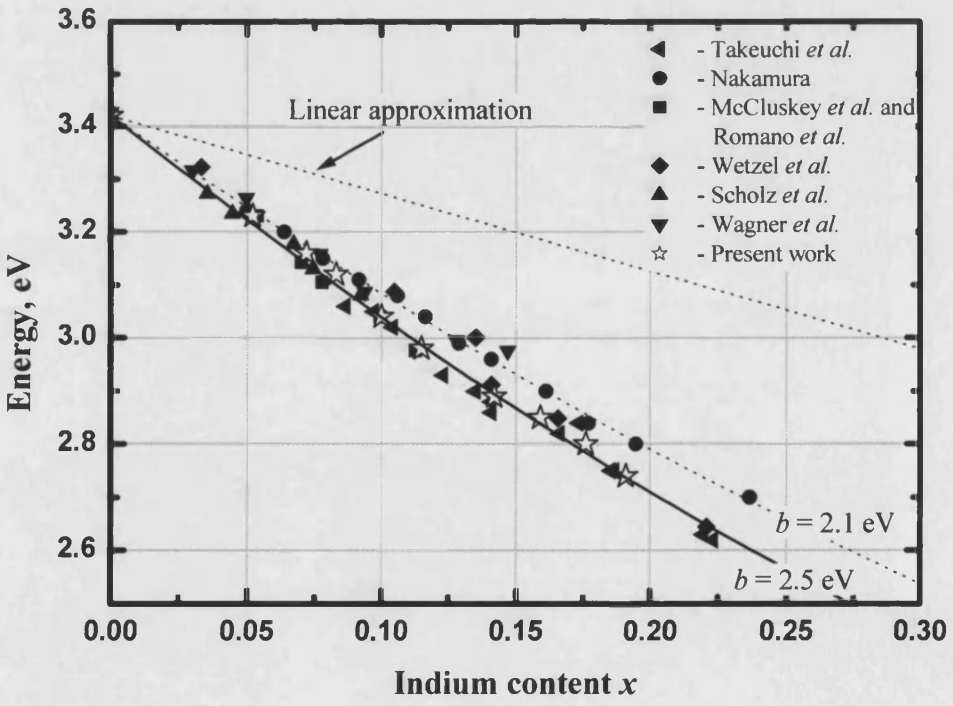

Figure 7.14. Emission energy of InGaN layers versus In content. Published data are recalculated with respect to the same Poisson's ratio ν=0.17.

7.9. Summary

The RT emission energy dependence on the In content (*c*-lattice constant) of the pseudomorphically strained InGaN layers grown on GaN is measured. It is shown that the existing "scatter" in various published data on this dependence originates mostly from strong uncertainty in Poisson's ratio values used. After correction to the same Poisson's ratio value, all published data on the bowing parameter in strained InGaN layers yield essentially the same results as compared to experimental uncertainty in emission energy and lattice constant measurements.

7.10. References

1. Y.T. Rebane, Y.G. Shreter, B.S. Yavich, V.E. Bougrov, S.I. Stepanov, W.N. Wang, *Phys. Stat. Sol. A* **180**, 121 (2000).
2. T. Matsuoka, T. Sasaki, and A. Katsui, Optoelectron 5, 53 (1990).
3. Trainor J W and Rose K J. Electron. Mater. 3 821 (1974)
4. A. Koukitu, N. Takahashi, T. Taki and H. Seki, Japan. J. Appl. Phys. 35 L673(1996)
5. T. Irisawaa, A. Koukitub, H. Seki, The Third Symposium on Atomic-Scale Surface and Interface Dynamics 3-4 March, Across-Fukuoka, (1999)
6. Matsuoka T, Yoshimoto N, Sakai T and Katsui A J. Electron. Mater. 21 157 (1992)
7. Sohmer A et al Mater. Res. Soc. Inter. J. Nit. Semi. Res. 2 14 (1997)
8. O Ambacher, J. Phys. D: Appl. Phys. 31 2653–2710. (1998)
9. M. Shimizu, Y. Kawaguchi, K. Hiramatsu, N. Sawaki, Sol. St. Electr. 41, 145 (1997).
10. K. Hiramatsu, Y. Kawaguchi, M. Shimizu, N. Sawaki, T. Zheleva, Robert F. Davis,H. Tsuda, W. Taki, N. Kuwano, K. Oki, MRS Internet J. Nitride Semicond. Res. 2, 6 (1997)
11. Yu. Karpov, MRS Internet J. Nitride Semicond. Res. 3, 16 (1998).
12. I. Ho, G.B. Stringfellow, Appl. Phys. Lett. 69, 2701-2703 (1996).
13. I. H. Ho, G. B. Stringfellow, Mater. Res. Soc. Symp. Proc. 449 , 871 (1997).
14. V.A. Elyukhin, S.A. Nikishin, Semicond. Sci. Technol. 11, 917 (1996).
15. M. van Schilfgaarde, A. Sher, A.-B. Chen, J. Cryst. Growth 178, 8-31 (1997).
16. J. Off, A. Kniest, C. Vorbeck, F. Scholz, O. Ambacher, *J. Cryst. Growth* ***195***, 286 (1998).
17. L. Görgens, O. Ambacher, M. Stutzmann, C. Miskys, F. Scholz and J. Off, Appl. Phys. Let., Vol. 76, No. 5, pp. 577–579, (2000)

18. K. Kim, W.R.L. Lambrecht, B. Segall, Phys. Rev. B 53, 16310 (1996).

19. A.F. Wright, J. Appl. Phys. 82, 2833 (1997).

20. T. Detchprohm, K. Hiramatsu, K. Itoh, I. Akasaki, Jap. J. Appl. Phys. 31, L1454 (1992).

21. C. Deger, E. Born, H. Angerer, O. Ambacher, M. Stutzmann, J. Hornsteiner, E. Riha, G. Fischerauer, Appl. Phys. Lett. ***72***, 2400 (1998).

22. M. Yamaguchi, T. Yagi, T. Azuhata, T. Sota, K. Suzuki, S. Chichibu, S. Nakamura, J. Phys. C 9, 241 (1997).

23. T. Deguchi, D. Ichiryu, K. Toshikawa, K. Sekiguchi, T. Sota, R. Matsuo, T. Azuhata, M. Yamaguchi, T. Yagi, S. Chichibu, S. Nakamura, J. Appl. Phys. ***86***, 1860 (1999).

24. M. Yamaguchi, T. Yagi, T. Sota, T. Deguchi, K. Shimada, S. Nakamura, J. Appl. Phys. 85, 8502 (1999).

25. L.T. Romano, B.S. Krusor, M.D. McCluskey, D.P. Bour, K. Nauka, *Appl. Phys. Lett.* ***73***, 1757 (1998)

26. A. Polian, M. Grimsditch, and I. Grzegory, J. Appl. Phys. 79, 3343 (1996)

27. T. Takeuchi, H. Takeuchi, S. Sota, H. Sakai, H. Amano, I. Akasaki, , *Jap. J. Appl. Phys.* ***36***, L177 (1997).

28. S. Nakamura, *Sol. St. Comm.* ***102***, 237 (1997)

29. M.D. McCluskey, C.G. Van de Walle, C.P. Master, L.T. Romano, N.M. Johnson, *Appl. Phys. Lett.* ***72***, 2725 (1998)

30. C. Wetzel, T. Takeuchi, S. Yamaguchi, H. Katoh, H. Amano, I. Akasaki, *Appl. Phys. Lett.* ***73***, 1994 (1998)

31. F. Scholz, J. Off, A. Sohmer, V. Syganow, A. Dörnen, O. Ambacher, *J. Cryst. Growth* ***189/190***, 8 (1998).

32. J. Wagner, A. Ramakrishnan, D. Behr, M. Maier, N. Herres, M. Kunzer, H. Obloh, K.-H. Bachem, MRS Internet J. Nitride Semicond. Res. 4S1, G2.8 (1999).

33. Takashi Matsuoka, Hiroshi Okamoto, Masashi Nakao, Hiroshi Harima, and Eiji Kurimoto, *Appl. Phys. Lett.* ***81***, 1246 (2002)

34. J. Off, A. Kniest, C. Vorbeck, F. Scholz, O. Ambacher, *J. Cryst. Growth* ***195***, 286 (1998).

35. L. Görgens, O. Ambacher, M. Stutzmann, C. Miskys, F. Scholz, J. Off, *Appl. Phys. Lett.* ***76***, 577 (2000).

36. C. Wetzel, S. Nitta, T. Takeuchi, S. Yamaguchi, H. Amano, I. Akasaki, , *MRS Internet J. Nitride Semicond. Res.* ***3***, 31 (1998).

37. J. Wagner, A. Ramakrishnan, D. Behr, H. Obloh, M. Kunzer, K.-H. Bachem, *Appl. Phys. Lett.* ***73***, 1715 (1998).

8. Series resistance and current distribution in GaN-based LEDs and LDs

8.1. Introduction

In this chapter we address the problem of current spreading and estimate the series resistance of III-nitride based LEDs and LDs. The most conventional substrate material for the growth of III-nitrides is sapphire. However, sapphire substrates are insulating and mesa structures with a lateral current injection geometry have to be used. The use of lateral current injection, however, can lead to non-uniform current distribution. This leads to poor uniformity of light emission and may deteriorate the ESD stability of the devices.

Another important parameter for the LEDs and LDs is the series resistance. First, series resistance increases the forward voltage and reduces the efficiency due to Joule heat generation. Second, the dissipated power raises the temperature of the active region, reducing both the lifetime and the efficiency. The latter problem is even more important for LDs, where high power dissipation can even destroy the device.

8.2. Components of the series resistance

Next, we analyse components of the series resistance in a p-side-up mesa LED structure and structure parameter requirements. For the sake of simplicity we limit our study to the one-dimensional problem, and analyse the structure with two n-type contacts on both sides of a mesa (Figure 8.1) instead of a ring contact around the mesa. Some components of the series resistance in our case are neglected as compared to other components. We neglect the resistance of metal films, the resistance of isotype junctions, and the resistance of thin layers in the active region. The only important components for us are:

1. The contact resistance to the n-GaN layer.

2. The spreading n-GaN resistance under n-contact.

3. The n-GaN layer resistance between mesa and the metal contact.

4. The spreading resistance of n-GaN layer under the mesa.

5. The transversal resistance of the p-GaN layer.

6. The contact resistance to the p-GaN layer.

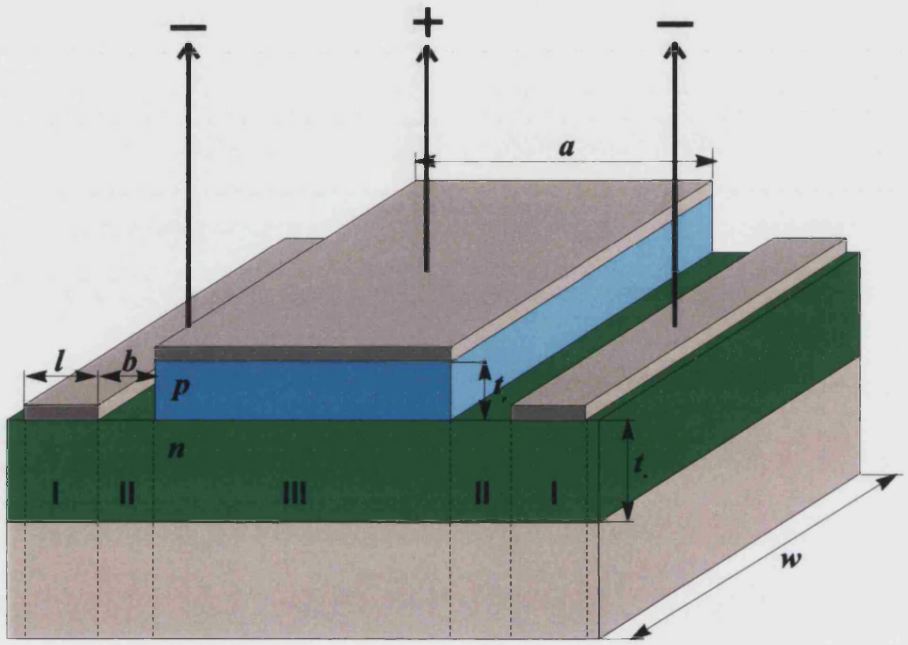

Figure 8.1. Schematic of GaN/InGaN mesa structure with lateral current path

The total series resistance is a sum of the mentioned above components:

$$R_{total} = \sum_i R_i \qquad (8.19)$$

The LED structure can be divided into three parts: the region under the n-type contact (denoted as region I in the figure); the region between the n-type contact and the mesa (region II) and region under the mesa (region III)

The n-contact resistance and the spreading resistance under n-contact are accounted by the formula[a]:

[a]See Appendix 1. In case of 2-sided contact $R_{1,2} = \frac{1}{2}R$

$$R_{1,2} = \frac{\sqrt{\rho_c^{(n)} \frac{\rho^{(n)}}{t}}}{2w\left(1-\exp\left(-\sqrt{\frac{\rho^{(n)}}{\rho_c^{(n)} t}}a\right)\right)}, \tag{8.20}$$

where $\rho_c^{(n)}$ is the n-contact specific resistivity, $\rho^{(n)}$ is the specific resistivity of the n-type layer l is the width of the contact pad, w is the width of the mesa structure.

The resistance of the n-GaN between the mesa and the metal contact is given by:

$$R_3 = \frac{1}{2}\frac{\rho^{(n)} \cdot b}{w \cdot t_n}, \tag{8.21}$$

where $\rho^{(n)}$ is the specific resistivity of the n-GaN layer, t_n is the thickness of the n-layer, b is the distance between the mesa and the contact, $w-$ the width of the mesa structure. The factor of $\frac{1}{2}$ originates from the presence of two n-contacts in the symmetrical LED structure.

The resistance of the p-contact (6), the transverse resistance of the p-layer (5) and the spreading resistance of the n-layer under the mesa (4) are accounted by the formula:

$$R_{4,5,6} = \frac{\sqrt{\frac{\rho^{(n)}}{t_n}(\rho_c^{(p)} + \rho^{(p)} \cdot t_p)}}{2w\tanh\left(\sqrt{\frac{\rho^{(n)}}{t_n \cdot (\rho_c^{(p)} + \rho^{(p)} t_p)}}\frac{l}{2}\right)}, \tag{8.22}$$

where $\rho^{(p)}$ is the specific resistivity of the p-type layer, $\rho^{(n)}$ is the specific resistivity of the n-type layer, $\rho_c^{(p)}$ is the specific resistivity of the p-contact t_p is the p-type layer thickness, t_n is the p-type layer thickness, l and w are the dimensions of the mesa.

The total series resistance is given by:

$$R_{total}=\frac{1}{2w}\left(\frac{\sqrt{\rho_c^{(n)}\frac{\rho^{(n)}}{t_n}}}{\left(1-\exp\left(-\sqrt{\frac{\rho^{(n)}}{\rho_c^{(n)}t_n}}a\right)\right)}+\frac{\rho^{(n)}\cdot b}{t_n}+\frac{\sqrt{\frac{\rho^{(n)}}{t_n}(\rho_c^{(p)}+\rho^{(p)}\cdot t_p)}}{\tanh\left(\sqrt{\frac{\rho^{(n)}}{t_n\cdot(\rho_c^{(p)}+\rho^{(p)}t_p)}}\frac{l}{2}\right)}\right) \tag{8.23}$$

Next, we wish to examine the problem quantitatively using real values. Typical dimensions of the mesa structure are:

$$w=l=3\cdot10^{-2}\text{cm},\ a=3\cdot10^{-3}\text{cm},\ b=1\cdot10^{-3}\text{cm} \tag{8.24}$$

$$t_n=3\cdot10^{-4}\text{cm},\quad t_p=5\cdot10^{-5}\text{cm}$$

The specific contact resistances for n- and p-GaN are:

$$\rho_c^{(n)}=10^{-4}\Omega\text{cm}^2,\rho_c^{(p)}=10^{-2}\Omega\text{cm}^2 \tag{8.25}$$

In case of Si-doped GaN with free electron concentration of 5×10^{18} cm^{-3} and mobility of 100–200 $\text{cm}^2\text{V}^{-1}\text{s}^{-1}$ the specific resistivity is:

$$\rho^{(n)}=\frac{1}{en\mu}\approx10^{-2}\Omega\text{cm} \tag{8.26}$$

For Mg-doped p-GaN the hole concentration is about 5×10^{17} cm^{-3} and mobility is about 15 $\text{cm}^2\text{V}^{-1}\text{s}^{-1}$.

$$\rho^{(p)}\approx1\,\Omega\text{cm} \tag{8.27}$$

With above values the equation gives the total series resistance of an LED structure of 15 Ω. This is close to the experimental value of ~10 Ω.

To estimate the contribution of resistance components to the total series resistance we varied the specific resistance of the contacts and layers from 10% to 100% of the values mentioned above. The results are presented in Figure 8.2.

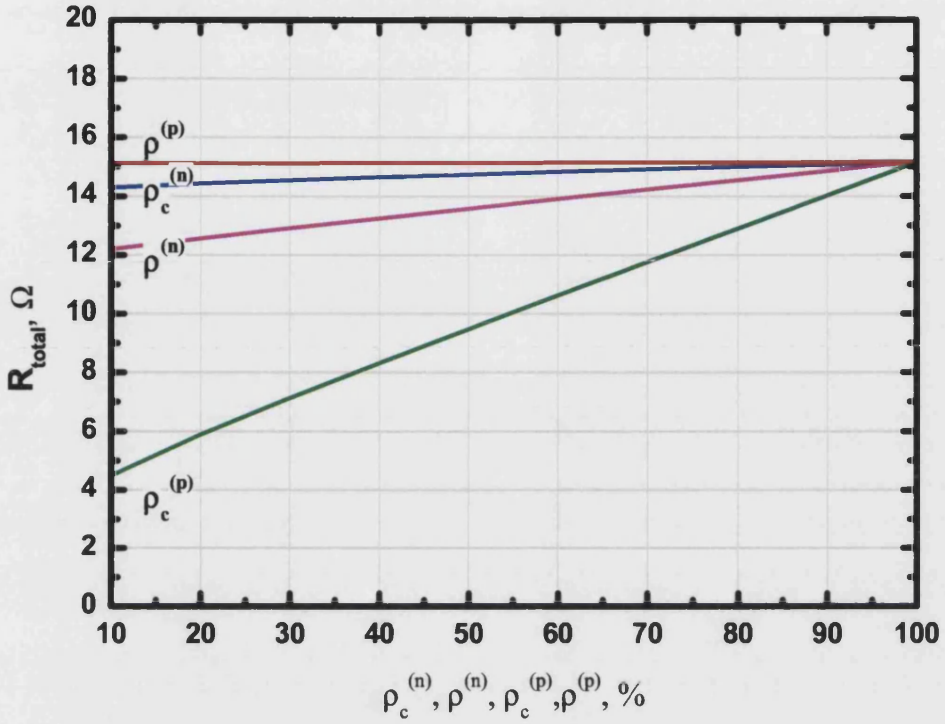

Figure 8.2. Influence of n-contact resistivity, n-layer resistivity, p-contact resistivity and p-layer resistivity on the total series resistance of an LED structure. Each parameter was varied from 10% to 100%, while other parameters were fixed at 100% ($\rho_c^{(n)} = 10^{-4}$ Ωcm^2, $\rho_c^{(p)} = 10^{-2}$ Ωcm^2, $\rho^{(n)} = 10^{-2}$ Ωcm, $\rho^{(p)} = 1$ Ωcm)

As one can see, the impact of series resistance of the p-layer is almost negligible, while p-contact resistance has the strongest effect on the total series resistance. The series resistance components can be ranged from most to least important in the following order:

1. p-contact resistance
2. n-layer lateral resistance
3. n-contact resistance
4. p-layer transverse resistance

It should be noted that, despite the resistivity of p-layer having a negligible effect on the series resistance of the structure, the resistivity of p-layer has very strong effect on p-contact resistivity. That is why efficient p-type doping is of crucial importance for reducing the total series resistance of the structure.

8.3. Current spreading

Next, we estimate the current spreading uniformity. In lateral geometry the finite resistance of the n-type material causes the current to "crowd" near the edge of the n-contact. Current crowding in lasers and LEDs has been addressed in several publications [1, 2, 3]

Applying our model (see Appendix 2) current distribution in the mesa structure is given by:

$$I(x)=\frac{V(x)-V_D}{R_v}=\frac{(V_0-V_D)}{\rho_c^{(p)}+\rho^{(p)}t_p}\frac{\cosh\left(\sqrt{\frac{\rho^{(n)}}{t_n\cdot(\rho_c^{(p)}+\rho^{(p)}t_p)}}x\right)}{\cosh\left(\sqrt{\frac{\rho^{(n)}}{t_n\cdot(\rho_c^{(p)}+\rho^{(p)}t_p)}}\frac{a}{2}\right)} \tag{8.28}$$

The current distribution in the active region is shown in Figure 8.3.

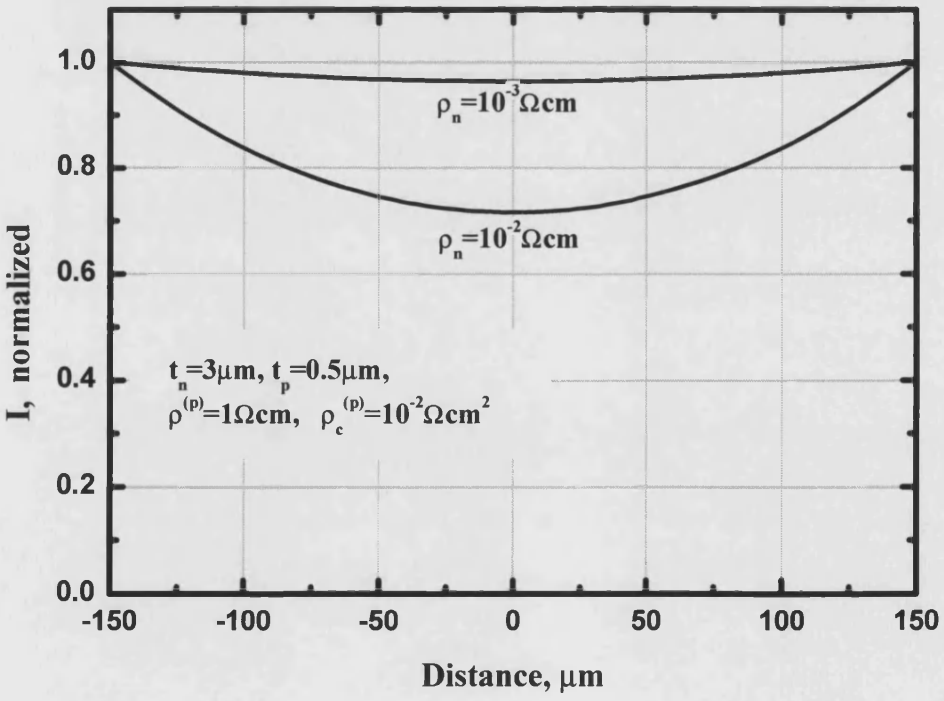

Figure 8.3. Calculated current distribution across the active region.

The LED parameters used in the figure are as follows: thickness of the n-type and p-type layers layer are $t_n=3\,\mu m$ and $t_p=0.5\,\mu m$, resistivity of the p-type layer

$\rho^{(p)} = 1\,\Omega\text{cm}$; the specific p-type contact resistance $\rho_c^{(p)} = 10^{-2}\,\Omega\text{cm}^2$; the size of the mesa is $300\times300\,\mu\text{m}^2$. In Figure 8.3 there are two curves, each representing the current distribution for resistivity of n-type layer of $\rho^{(n)} = 10^{-2}\,\Omega\text{cm}$ and $\rho^{(n)} = 10^{-3}\,\Omega\text{cm}$. One can see that in the case of low specific resistivity the current distribution is much more uniform.

The uniformity of the current distribution may be described by the ratio of the minimal current density to the maximal current density:

$$\frac{I_{\min}}{I_{\max}} = \frac{I(0)}{I(\frac{a}{2})} = \frac{1}{\cosh\left(\sqrt{\frac{\rho^{(n)}}{t_n\cdot(\rho_c^{(p)}+\rho^{(p)}t_p)}}\,\frac{a}{2}\right)} \tag{8.29}$$

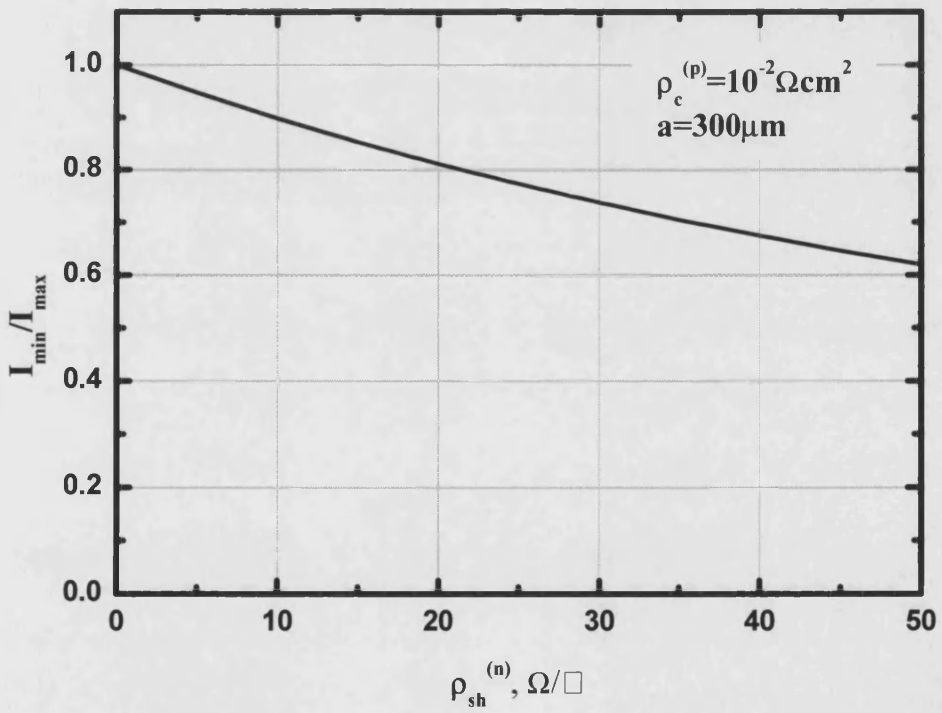

Figure 8.4. Calculated current uniformity as a function of the n-type sheet resistivity.

Again, for a typical GaN-based LED resistivity of the p-type layer may be neglected.

$$\rho_c^{(p)} >> \rho^{(p)}t_p, \qquad \frac{\rho^{(n)}}{t_n} = \rho_n^{(sh)} \tag{8.30}$$

$$\frac{I_{\min}}{I_{\max}} \approx \frac{1}{\cosh\left(\sqrt{\frac{\rho_{sh}^{n}}{\rho_{c}^{(p)}}}\frac{a}{2}\right)} \tag{8.31}$$

This equation implies that the uniformity of the current distribution can be improved by increase of p-type contact resistance. On the other hand, high p-type contact resistance is not desirable for the devices since it increases total series resistance and generates heat. The only practical way to improve the uniformity of the current distribution is the reduction of the n-type layer sheet resistivity.

Figure 8.4 shows the dependence of the current uniformity on the sheet resistivity of the n-type layer. For the current uniformity of 90% the n-type layer sheet resistivity of 10 Ω/ is required. With improvement of the p-type contact and large device sizes the contact crowding becomes increasingly severe.

Sheet resistivity is given by $\rho_{sh} = \frac{1}{e\mu nt}$, where e is the elementary charge, μ is the carrier mobility, n is the carrier concentration, t is the thickness of the film. Thus, the sheet resistivity of n-type layer can be decreased by:

1. Increase of carrier concentration
2. Increase of carrier mobility
3. Increase of n-type layer thickness

The highest concentration of free electrons in Si-doped GaN is on the order of 10^{20} cm^{-3}. However, high concentration of Si deteriorates the crystalline quality of n-GaN buffer and subsequent layers. Thus, in practical devices the free electron concentration is limited by 5×10^{18} - 10^{19} cm^{-3}. The mobility is also related to the carrier concentration. For example, Gotz and co-workers [4] have found that the mobility of the carriers decreased from 500 to 135 cm^{2}V^{-1}s^{-1} when the concentration of free electrons was increased from

5×10^{17} cm^{-3} to 1.5×10^{19} cm^{-3}. Similar values are given by Gaskill *et al.* [5] who summarized data on electron mobility and carrier concentration values for hexagonal GaN grown by various techniques (see Figure 8.5).

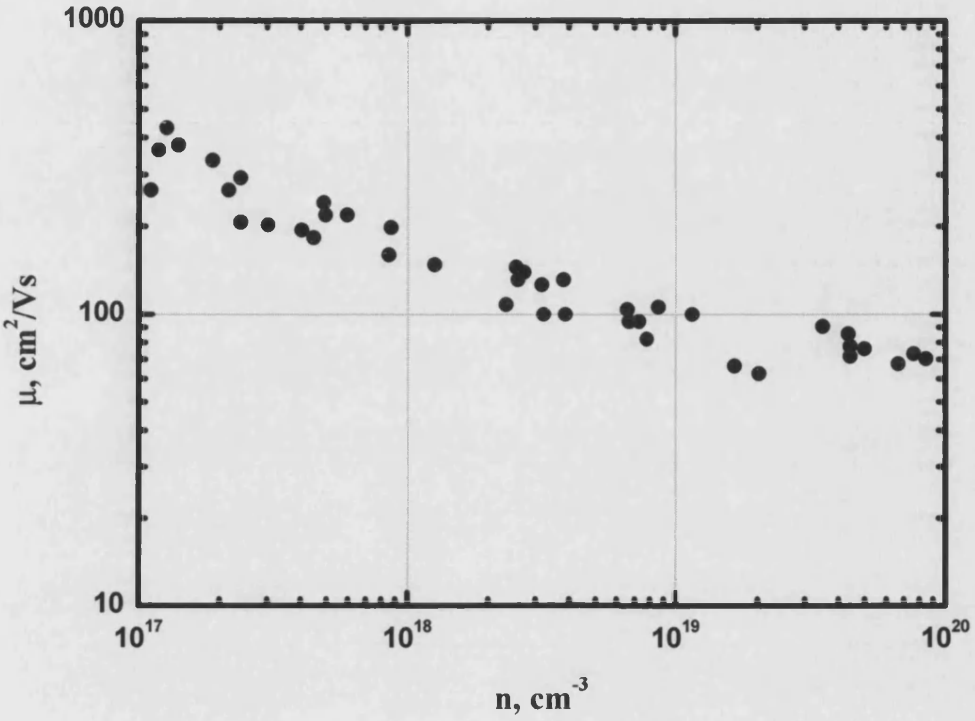

Figure 8.5. A survey of 300 K GaN electron Hall mobility values as reported by various authors (From [6])

Figure 8.6 shows the dependence of specific resistivity of n-type GaN on the carrier concentration. One can see that for the concentration of free electrons of 10^{19} cm^{-3} the resistivity is greater than 5×10^{-3} Ωcm. Thus, to provide satisfactory current uniformity. the thickness of the n-type layer should be more than 5 μm.

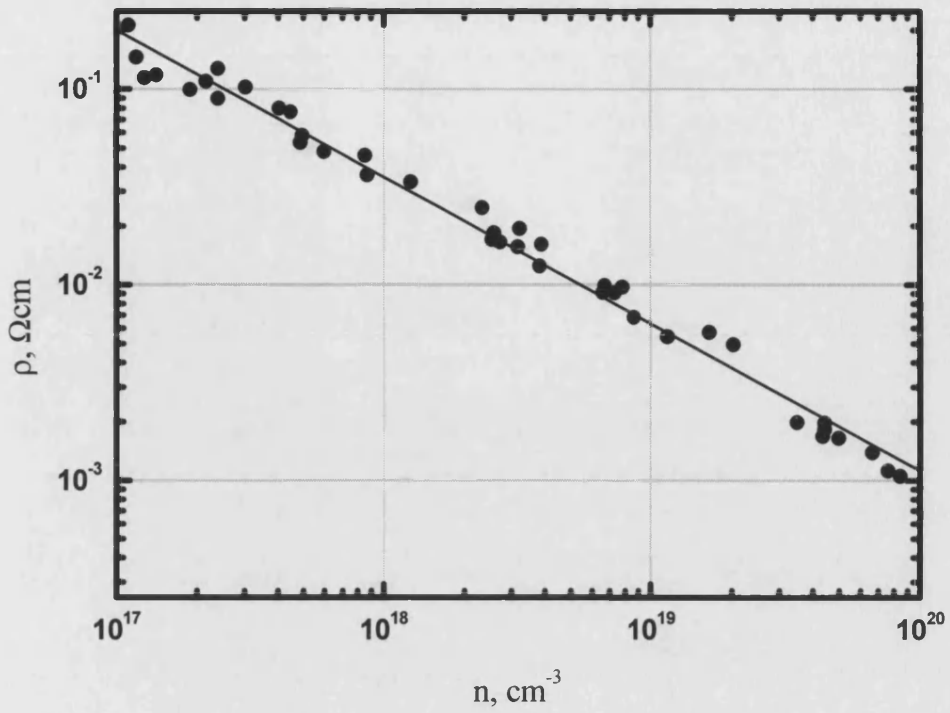

Figure 8.6. Specific resistivity of n-type GaN versus free electron concentration (Recalculated from [6])

8.4. Summary

The impact of the specific resistivity of the n- and p-type layers and contacts on the total device series resistance has been analysed. It has been demonstrated p-contact resistance makes the major contribution to the to the total series resistance. The sheet resistance of the n-type layer does not affect much the serial resistance, but is very important for good current spreading. Even in case of high doping level (up to 10^{19} cm^{-3}) a thick (>5 μm) n-type layer is required to provide current uniformity of 90%.

8.5. Appendix 1. Contact to conductive layer on insulating substrate

Consider a layer of a conductive material of thickness t and specific resistivity ρ. A metal stripe of width w and length l is placed on top of the conductive material (see Figure 8.7). The metal forms ohmic contact to the conductive layer with contact specific resistivity ρ_c. The specific resistivity of the metal contact is much smaller than that of the conductive layer and may be neglected. Also we assume that the layer of conductive material is thin, i.e. its thickness is small compared to lateral dimensions of the contact.

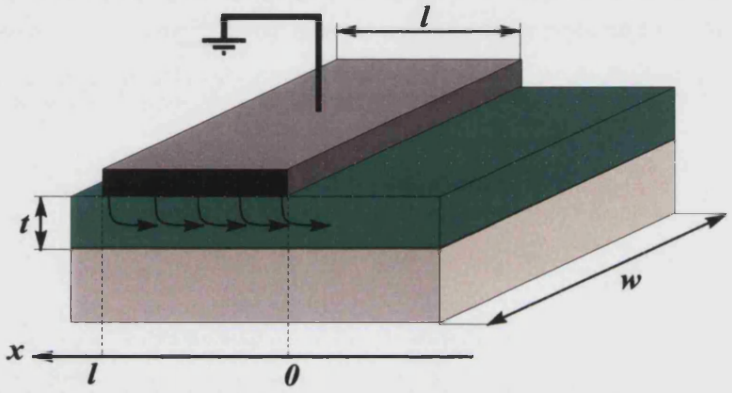

Figure 8.7. Schematic of a metal contact to a conductive layer on insulating substrate.

In this case current spreading can be accounted by the circuit model shown in Figure 8.8.

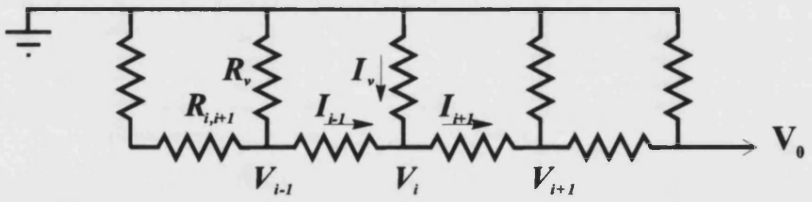

Figure 8.8. Equivalent circuit used for analysis.

Vertical resistors denote the contact resistivity and horizontal resistors denote the specific resistivity of the layer. Applying Kirchhoff's current law to the i^{th} node of the circuit we can write an expression:

$$I_{i-1} - I_{i+1} = I_v \tag{8.32}$$

$$R_{i-1,i} = R_{i,i+1} = \frac{\rho \cdot \Delta x}{t \cdot w} \tag{8.33}$$

$$R_v = \frac{\rho_c}{w \cdot \Delta x} \tag{8.34}$$

$$I = \frac{\Delta V}{R}, \tag{8.35}$$

$$\frac{t \cdot w}{\rho}\left(\frac{V_i - V_{i+1}}{\Delta x} - \frac{V_{i+1} - V_i}{\Delta x}\right) = \frac{V_i \cdot w}{\rho_c}\Delta x \tag{8.36}$$

For Δx approaching zero, we can rewrite equation (8.36) in differential form:

$$\frac{d^2V(x)}{dx^2} = \frac{\rho}{t \cdot \rho_c}V(x) \tag{8.37}$$

The boundary conditions are:

$$V(0) = V_0 \qquad V(\infty) = 0 \tag{8.38}$$

The solution of the differential equation is:

$$V(x) = V_0 \exp\left(-\sqrt{\frac{\rho}{t \cdot \rho_c}}x\right) \tag{8.39}$$

The total current through the contact can be found from the integral:

$$I = \int_0^l \frac{w}{\rho_c}V(x)dx = \frac{wV_0}{\rho_c}\int_0^l \exp\left(-\sqrt{\frac{\rho}{t \cdot \rho_c}}x\right)dx \tag{8.40}$$

And the spreading resistance can be calculated as

$$R = \frac{V(0)}{I} = \frac{\rho_c}{w\int_0^l \exp\left(-\sqrt{\frac{\rho}{t \cdot \rho_c}}x\right)dx} = \frac{\sqrt{\rho_c \frac{\rho}{t}}}{w\left(1 - \exp\left(-\sqrt{\frac{\rho}{\rho_c t}}l\right)\right)} \tag{8.41}$$

In the limiting case of $\rho = 0$ the equation reduces to the definition of the contact resistivity:

$$\lim_{\rho \to 0} R = \lim_{\rho \to 0} \frac{\sqrt{\rho_c \frac{\rho}{t}}}{w\left(1 - \exp\left(-\sqrt{\frac{\rho}{\rho_c t}}l\right)\right)} = \frac{\rho_c}{wl} \tag{8.42}$$

8.6. Appendix 2. Current spreading under mesa

Consider a *pn*-junction structure formed with n-type layer of thickness t_n and specific resistivity $\rho^{(n)}$, p-type layer of thickness t_p and specific resistivity $\rho^{(p)}$. A mesa structure with lateral sizes $l \times w$ is formed to expose n-type layer. A metal contact is deposited over on top of the mesa.

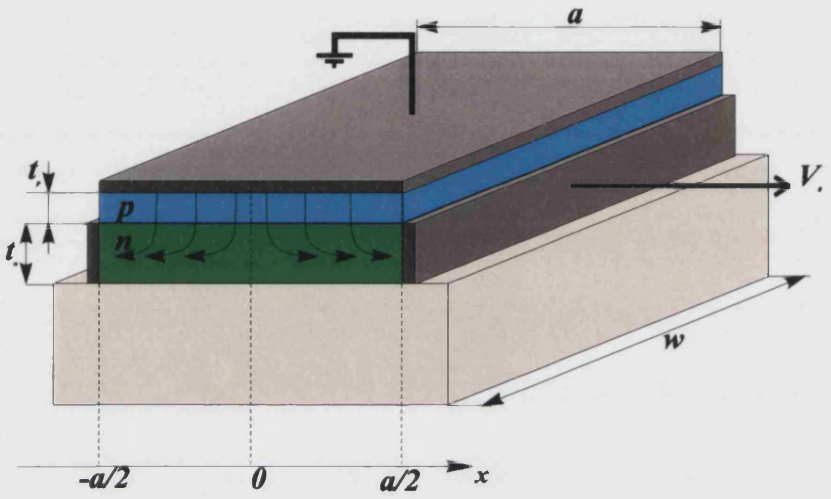

Figure 8.9. Schematic of a pn-junction on an insulating structure.

The metal forms ohmic contact to the p-type layer with contact specific resistivity ρ_c. The specific resistivity of the metal contact is small and may be neglected. Also we assume that all layers are thin, i.e. its thickness is small compared to lateral dimensions of the structure.

In this case current spreading can be accounted by the circuit model shown in Figure 8.10.

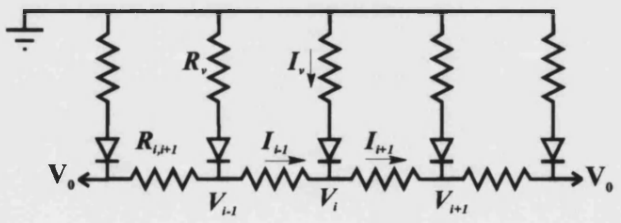

Figure 8.10. Equivalent circuit model used for analysis.

For the sake of simplicity we assume that at working current the pn-junction is fully opened and current is limited by series resistance of the structure. In this case the analysis is similar to that used in Appendix 1.

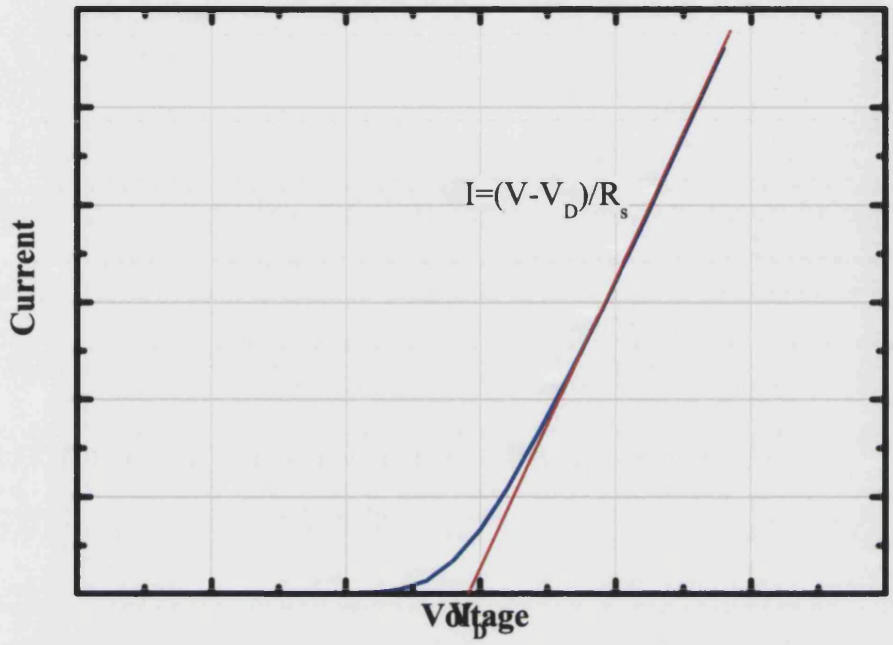

Figure 8.11. Typical I-V curve for an LED. At working currents the curve may be approximated by a straight line.

A linear approximation can be used for the vertical current:

$$I_v = \frac{V_i - V_D}{R_v} \tag{8.43}$$

where the resistance is the sum of the p-type contact resistance and the transversal resistance of p-type layer:

$$R_v = \frac{\rho_c^{(p)}}{w \cdot \Delta x} + \frac{\rho^{(p)} \cdot t_p}{w \cdot \Delta x} \tag{8.44}$$

Again, the application of Kirchhoff's current law yields:

$$\frac{d^2V(x)}{dx^2} = \frac{\rho^{(n)}}{t_n \cdot (\rho_c^{(p)} + \rho^{(p)} t_p)} (V(x) - V_D) \tag{8.45}$$

Boundary conditions are symmetric (n-contact on both sides of the mesa):

$$V(-\frac{a}{2}) = V_0, \quad V(\frac{a}{2}) = V_0 \tag{8.46}$$

The solution of the differential equation is:

$$V(x) = (V_0 - V_D)\frac{\cosh\left(\sqrt{\frac{\rho^{(n)}}{t_n \cdot (\rho_c^{(p)} + \rho^{(p)} t_p)}}\, x\right)}{\cosh\left(\sqrt{\frac{\rho^{(n)}}{t_n \cdot (\rho_c^{(p)} + \rho^{(p)} t_p)}}\, \frac{a}{2}\right)} + V_D \tag{8.47}$$

The resistance is calculated as:

$$R = \frac{dV}{dI} = \frac{\rho_c^{(p)} + \rho^{(p)} \cdot t_p}{w} \cdot \frac{V_0}{\int_{-l/2}^{l/2} V(x)dx} = \frac{1}{w} \cdot \frac{\sqrt{\frac{\rho^{(n)}}{t_n}(\rho_c^{(p)} + \rho^{(p)} \cdot t_p)}}{2\tanh\left(\sqrt{\frac{\rho^{(n)}}{t_n \cdot (\rho_c^{(p)} + \rho^{(p)} t_p)}}\, \frac{l}{2}\right)} \tag{8.48}$$

8.7. References

1. X.Guo, E.F. Shubert, J. Appl. Phys., Vol 90, (8), 4191
2. H. Kim, J.-M. Lee, C. Huh, S.-W. Kim, D.J. Kim, S. Park, H. Hwang, Appl. Phys.Lett., 77, (12), 1903
3. I. Eliashevich, Y. Li, A. Osinsky, C. A. Tran, M. G. Brown, Part of the SPIE Conference on Light-Emitting Diodes: Research, Manufacturing and Applications III, San Jose, California, Proc. SPIE 3621, 28
4. W. Gotz, N.M. Johnson, C.Chen, H. Liu, H.Kuo, W. Imler, Appl. Phys. Lett., 68, 3144
5. D. K. Gaskill, K. Doverspike, L. Rowland, and D. L. Rode, 21st Interna-tional Symposium on Compound Semiconductors, San Diego, 18–28 September 1994 unpublished.
6. D. L. Rode, D. K. Gaskill, Appl. Phys. Lett. 66 (15), 10

9. Si-doped AlGaN/GaN Superlattice Structures

9.1. Introduction

As we discussed before, a low resistance n-type buffer layer is important for the uniformity of current and EL distributions, as well as for ESD stability of LEDs and LDs. However, the electron mobility in bulk GaN rapidly decreases with increase in the doping level resulting in the saturation of the n-type GaN resistivity. Therefore, thick (≥5 μm) n-GaN buffer layer is required to provide good current spreading. Doped AlGaN/GaN superlattice structures offer an alternative to the use of bulk GaN layers as a current spreading layer. Experimental data [1,2,3] and mobility calculations [4,5] show that the 2D electron mobility in AlGaN/GaN heterostructures is much higher than that for bulk GaN and AlGaN. Also, the mobility decreases little with doping, thus the lateral resistivity of AlGaN/GaN structures is lower than that for bulk GaN. A higher value of the mobility in the 2D gas is primarily related to the decrease of ionised impurity scattering caused by separation from the ionised donors and by screening effects in a high-density 2DEG.

The built-in electric fields in play an important role in the formation of 2DEG in AlGaN/GaN superlattices. We will start our study from the analysis of built-in polarization fields in AlGaN/GaN heterostructures.

9.2. 2DEG and built-in polarization fields in AlGaN/GaN heterostructures

The wurtzite material system has a strain-independent (spontaneous) built-in electric field [6]. In addition, because of large piezoelectric coefficients and lattice mismatch between III-nitride materials, a strain induced (piezoelectric) field [7] is generated in strained heterostructures. The two polarizations add algebraically to reinforce or partially cancel one another. These effects largely influence the electrical properties of the semiconductors such as the potential profile and the electron density.

In the case of a freestanding slab of GaN the adsorption of ambient ions will create surface charges which will entirely neutralize internal electric field. In case of AlGaN/GaN heterostructures upper and lower surfaces have different polarization charges and surface charges cannot entirely eliminate internal electric field [8] The difference of two charges at lower and upper surfaces determines the induced electron density at the interface to satisfy the condition of overall charge neutrality.

First, consider a thin AlGaN layer grown pseudomorphically on a thick strain-relaxed GaN buffer (see Figure 9.1). The GaN buffer layer has only the spontaneous polarization, which is directed in $[000\bar{1}]$ direction. The AlGaN has both spontaneous and piezoelectric polarizations. The strain induced piezoelectric field in the AlGaN layer also points in $[000\bar{1}]$ direction.

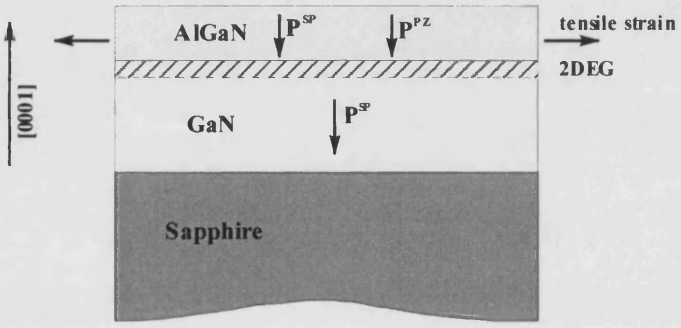

Figure 9.1. Spontaneous and piezoelectric polarizations in pseudomorphic GaN/AlGaN heterostructure with Ga-face polarity.

By convention the [0001] direction is given by a vector pointing from a Ga atom to a nearest-neighbour N atom. In case MOCVD growth on c-sapphire GaN is Ga-faced and [0001] corresponds to the growth direction. Thus, both piezoelectric and spontaneous fields are directed towards the substrate.

Spontaneous polarizations for GaN and AlN are -0.029 Cm^{-2} and -0.081 Cm^{-2} [9], respectively. The spontaneous polarization of AlGaN can be described by a linear approximation between the spontaneous polarizations of GaN and AlN:

$$P^{SP}_{AlGaN}(x) = -0.029 - 0.052x \tag{9.1}$$

Table 22. Spontaneous polarization, piezoelectric coefficients, elastic constants, lattice parameters and dielectric constants for AlN and GaN.

	AlN	GaN
Spontaneous polarization P^{SP}, [C/m^2]	-8.1×10^{-2}	-2.9×10^{-2}
Piezoelectric coefficients: [9]		
e_{33}, [C/m^2]	1.46	0.73
e_{31}, [C/m^2]	-0.60	-0.49
e_{15}, [C/m^2]	-0.48	-0.3
Elastic constants: [10,11,12]		
C_{13}, [GPa]	99	106
C_{33},[GPa]	389	398
Lattice parameters: [9]		
a_0,[Å]	3.112	3.189
c_0,[Å]	4.982	5.185
Dielectric constants		
ε_{11}	9.0	9.5
ε_{33}	10.7	10.4

The piezoelectric polarization can be calculated using the piezoelectric coefficients e_{33} and e_{13} as

$$P^{PZ} = e_{33}\varepsilon_z + e_{31}(\varepsilon_x + \varepsilon_y) \tag{9.2}$$

where ε_z is the strain along c-axis ε_x and ε_y are in-plane strain components. The shear strain is neglected. Assuming that the layer is under isotropic biaxial strain:

$$\varepsilon_z = (c - c_0)/c_0, \qquad \varepsilon_x = \varepsilon_y = (a - a_0)/a_0 \tag{9.3}$$

The relation between the tensile and lateral strain is given by:

$$\varepsilon_z = -2\frac{C_{13}}{C_{33}}\varepsilon_x \tag{9.4}$$

Using equations (9.3) and (9.4), the amount of piezoelectric polarization along the c axis can be determined by:

$$P_{AlGaN}^{PZ} = 2\frac{a-a_0}{a_0}\left(e_{31} - e_{33}\frac{C_{13}}{C_{33}}\right) \tag{9.5}$$

The lattice constant of relaxed AlGaN obeys the Vegard's law:

$$a_0 = a_0^{(GaN)} \cdot (1-x) + a_0^{(AlN)} \cdot x \tag{9.6}$$

The a lattice constant of pseudomorphically grown AlGaN is equal to that of underlying GaN buffer. Thus, the piezoelectric polarization is given by:

$$P_{AlGaN}^{PZ}(x) = 2\frac{(a_0^{(GaN)} - a_0^{(AlN)})x}{a_0^{(GaN)} - (a_0^{(GaN)} - a_0^{(AlN)})x}\left(e_{31} - e_{33}\frac{C_{13}}{C_{33}}\right) \tag{9.7}$$

Using the following set of linear interpolations between physical properties of GaN and AlN [13,14]:

Elastic constants:

$$C_{13}(x) = 99x + 106(1-x), \text{(GPa)} \tag{9.8}$$

$$C_{33}(x) = 389x + 398(1-x), \text{(GPa)} \tag{9.9}$$

Piezoelectric constants:

$$e_{31}(x) = -0.60x - 0.49(1-x), (\text{C/m}^2) \tag{9.10}$$

$$e_{33}(x) = 1.46x + 0.73(1-x), (\text{C/m}^2) \tag{9.11}$$

The amount of spontaneous, piezoelectric and total polarization is calculated using equations ((9.1), (9.7), (9.8), (9.9), (9.10) and (9.11) (see Figure 9.2).

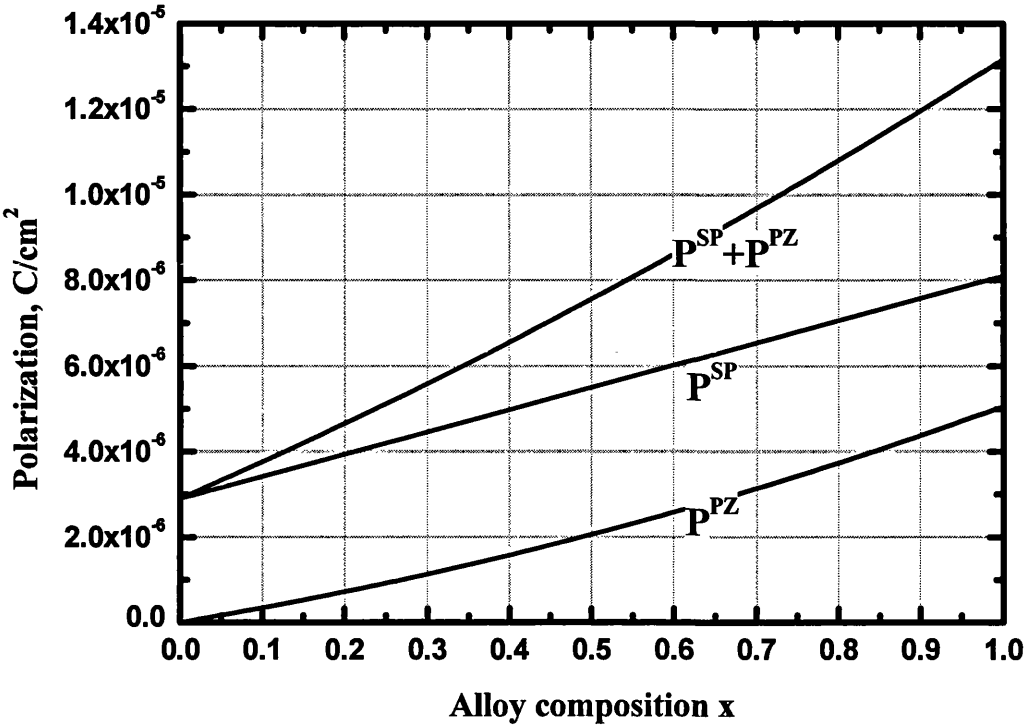

Figure 9.2. Spontaneous, piezoelectric and total polarization of $Al_xGa_{1-x}N$ versus alloy composition x.

Abrupt change of polarization at the AlGaN/GaN interface gives rise to the formation of polarization charge. A positive sheet charge is formed at AlGaN/GaN interface and a corresponding negative sheet charge is formed at the top of AlGaN layer. The charge density is defined as:

$$\sigma(P^{SP}+P^{PZ}) = P(AlGaN) - P(GaN) = P^{PZ}(x) + P^{SP}(x) - P^{SP}(0) \qquad (9.12)$$

where $P^{SP}(x)$ and $P^{PZ}(x)$ are given by equations ((9.1) and (9.7) respectively. Figure 9.3 shows the calculated sheet charge σ/e at the AlGaN/GaN interface versus alloy composition.

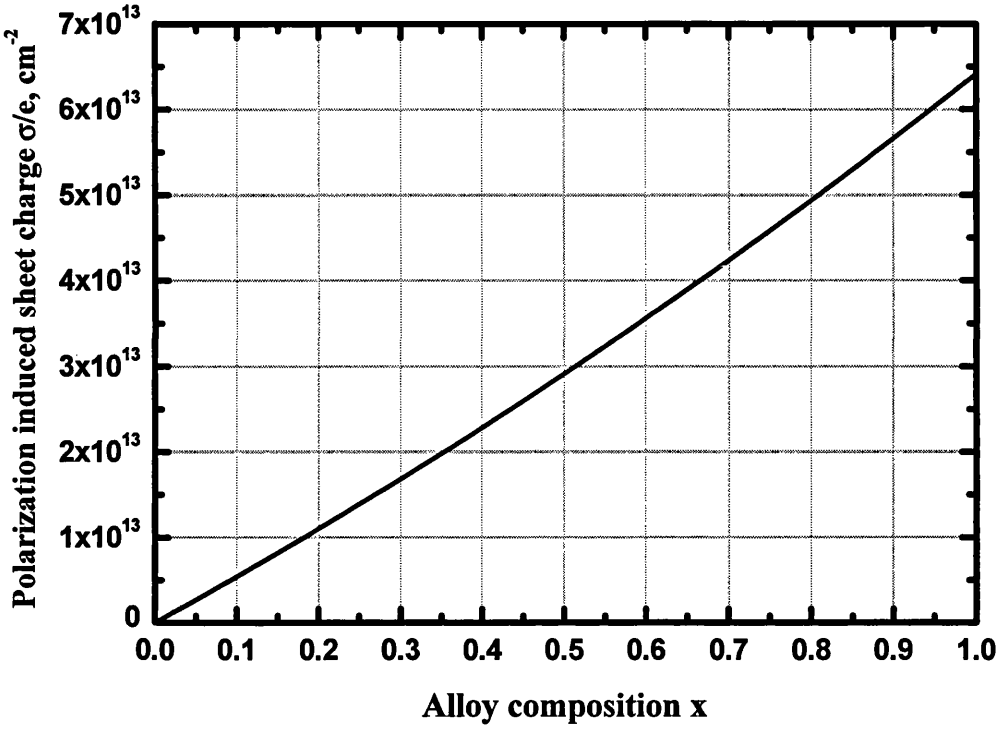

Figure 9.3. Calculated polarization induced sheet charge density at the interface of $Al_xGa_{1-x}N$/GaN heterostructure versus alloy composition x.

Attracted ambient ions and/or charged surface states at the upper AlGaN and the bottom GaN surfaces and give rise to the formation of surface charges $+\sigma_{s1}$ and $+\sigma_{s2}$, respectively. Since the polarization charges of AlGaN and GaN are different, consequently, the surface charges are not equal. The induced charge electron density is $\sigma_{s1}-\sigma_{s2}$ to obtain overall charge neutrality. These electrons fill a triangular quantum well at the AlGaN/GaN interface and form a two dimensional electron gas.

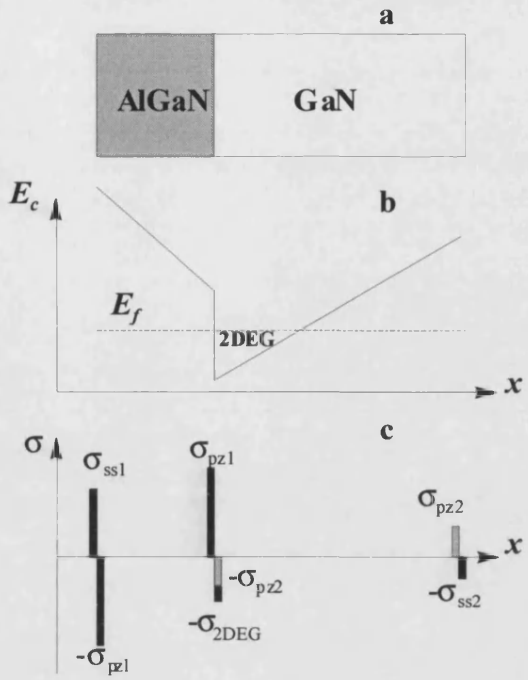

Figure 9.4. a – schematic diagram of a GaN/AlGaN heterostructure; b – conduction band diagram; c – diagram of charge distribution.

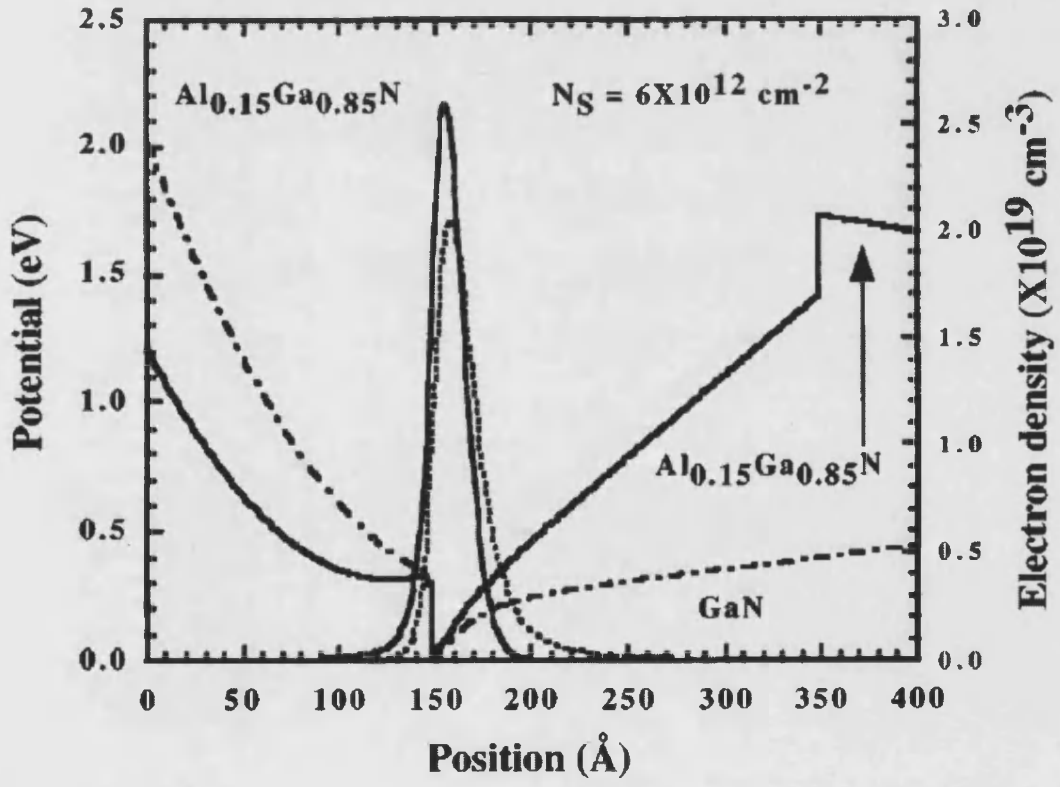

Figure 9.5. Potential profiles and 2DEG distributions in AlGaN/GaN heterostructure with differing N_s . Solid and dotted lines correspond to $N_s = 7\times10^{12}$ and 6×10^{12} cm^{-2}, respectively (after Maeda *et al* [15]).

The induced electron density can be obtained by self-consistently solving the Schrodinger's and Poisson's equations. First, the electrical fields in the structure are calculated from the known polarization charges. Then, requiring that voltage difference across the structure vanishes, the surface charge density is deducted. The voltage difference will include the depth of the quantum well, which, in turn, will depend on induced electron density.

Maeda *et al* [15] have calculated potential profile and 2DEG distribution in the similar structure by self-consistently solving the Schrodinger's and Poisson's equations. The results are shown in Figure 9.5. Their modelling suggests that the space charge at AlGaN/GaN interface is confined within 30–50 Å from the interface.

The electron density at the interface can be as high as 10^{13} cm^{-2} and mobilities up to 2000 cm^2/Vs have been reported [13]. The lowest sheet resistivity of the single channel is about 300-600 Ω/□. However, this value is too high for the use as a current spreading layer. The simplest way to reduce the sheet resistivity is to use a multiple channel structure, i.e. a superlattice.

9.3. N-type AlGaN/GaN superlattice structures

The analysis of the 2DEG formation in the AlGaN/GaN superlattice structure is very similar to the one discussed above. Again, the polarization field creates a periodic saw-tooth variation in the band diagram as shown in Figure 9.6. A two-dimensional electron gas (2DEG) with the sheet electron density on the order of 10^{13} cm^{-2} is formed in the triangular quantum well at the GaN/AlGaN interface. However, the boundary conditions are slightly different. The exact conduction band profile and charge distribution can be found only by solving Schrodinger's and Poisson's equations numerically using a computer. Here we present a quite crude electrostatical model that describes the effect of spontaneous and piezoelectric polarization on 2DEG formation. The latter approach lacks

the precision, but gives more insight into the physics of the process. For the sake of simplicity the following assumptions are made:

5. The AlGaN/GaN superlattice structure has infinite number of periods.

6. AlGaN layers are uniformly n-type doped and are entirely depleted of electrons.

7. GaN layers are undoped and free of electrons.

8. All electrons are contained in the 2DEG at the interface.

9. The 2DEG it is treated as a sheet charge of zero width

10. GaN layers are relaxed and AlGaN layers are pseudomorphically strained.

Upon the condition of infinite number of periods, natural boundary conditions would be a requirement of periodicity for the electric field and the zero voltage difference across one period of the superlattice. Assumptions 6 and 7 are valid for highly doped structures, when background electron concentration may be neglected. Assumptions 8 and 9 are justifiable for relatively thick GaN layers. Assumption 10 is applicable if AlGaN layers are thinner than GaN layers and Al composition is not too high.

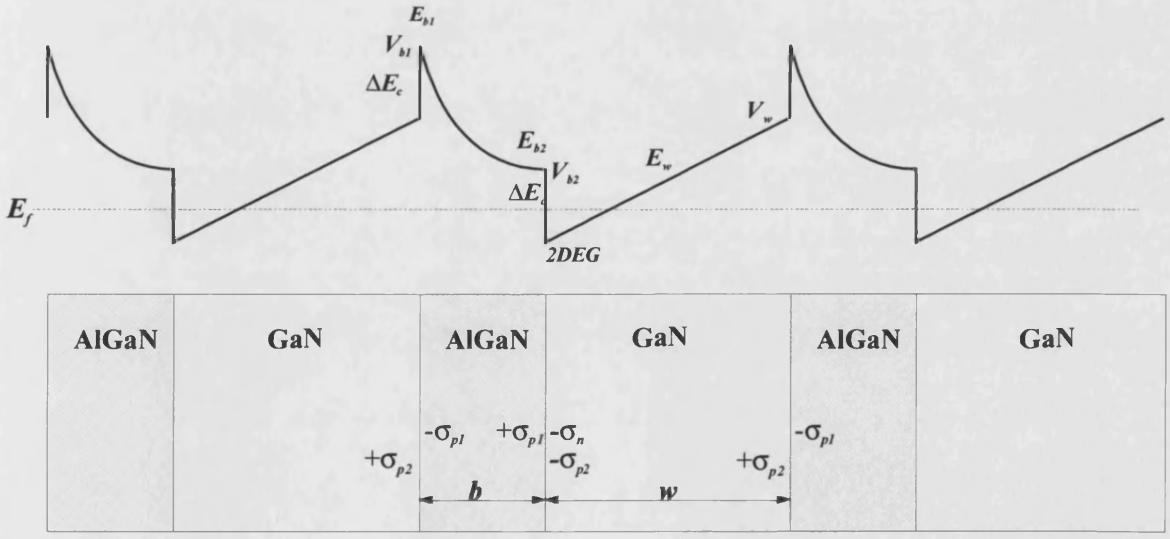

Figure 9.6. Schematic conduction band dependence through an AlGaN/GaN superlattice. The magnitude of sheet charges is depicted by σ.

Beginning from the left, we denote the electric field immediately at the GaN/AlGaN interface, AlGaN/GaN interface and GaN as E_{b1}, E_{b2} and E_w respectively. The electric

field in the barrier changes linear function of x due to space charge of the ionised donors. Since the well is free of electrons and ionised donors, the electric field is constant. If ε_b is the electric permittivity of the AlGaN barrier, and ε_w is the electric permittivity of the GaN well, the electric fields are given by:

$$\varepsilon_b E_{b1} = \varepsilon_w E_w + \sigma_w - \sigma_b \tag{9.13}$$

$$\varepsilon_b E_{b2} = \varepsilon_b E_{b1} + eN_d b \tag{9.14}$$

$$\varepsilon_w E_w = \varepsilon_b E_{b2} + \sigma_b - \sigma_w - \sigma_n \tag{9.15}$$

From equations (9.13), (9.14), (9.15) immediately follows that

$$\sigma_n = eN_d b \tag{9.16}$$

The triangular quantum well is formed only if $E_w > 0$, also requiring $E_{b2} \leq 0$ and using equations (9.15) we obtain that the 2DEG charge density should not exceed the polarization charge density.

$$\sigma_n \leq \sigma_b - \sigma_w \tag{9.17}$$

The latter statement is a direct consequence of the assumptions made and is valid only to some degree. For example 2DEG is formed in lattice matched cubic III-V semiconductors without piezoelectric charge. Nevertheless, it is a good approximation because the 2DEG charge density in III-nitrides is at least one order of magnitude larger than that in conventional cubic III-V semiconductors.

The system of equations (9.13), (9.14), (9.15) is not sufficient to find the unique solution for E_{b1}, E_{b2} and E_w. The additional equation is found from the requirement of zero voltage change across one period of the superlattice. The voltage change across the barrier is obtained by integrating the Poisson's equation:

$$V_{b2} = V_{b1} - E_{b1} b - \frac{eN_d b^2}{2\varepsilon_b} \tag{9.18}$$

The voltage change across the well is

$$V_w = E_w w \tag{9.19}$$

where w is the width of GaN layer.

The voltage difference is zero, $V_w = V_{b1}$, or

$$E_w w = -E_{b1} b - \frac{eN_d b^2}{2\varepsilon_b} \tag{9.20}$$

Using equations (9.13), (9.14), (9.15) and (9.20), and noting that $\sigma_b - \sigma_w$ is the polarization charge $\sigma(x)$ from equation (9.12), we obtain E_w

$$E_w = \frac{b}{2}\frac{2\sigma(x) - eN_d b}{w\varepsilon_b + b\varepsilon_w} \tag{9.21}$$

If the 2DEG charge is approaching the maximal value of $\sigma_n = eN_d b = \sigma(x)$ the equation (9.21) simplifies to

$$E_w = \frac{b}{2}\frac{\sigma(x)}{w\varepsilon_b + b\varepsilon_w} \tag{9.22}$$

Assuming that the electrons occupy the lowest subband of the quantum well, the Fermi level position is given by

$$E_f = E_0 + \frac{\pi\hbar^2}{m^*} n_s \tag{9.23}$$

Where E_0 is the ground energy level in the triangular quantum well

$$E_0 = \left(\frac{\hbar^2}{2m^*}\right)^{\frac{1}{3}}\left(\frac{9\pi e E_w}{8}\right)^{\frac{2}{3}} \tag{9.24}$$

The Fermi level should not exceed the band offset between GaN and AlGaN, otherwise the 2DEG is not contained in the quantum well and electrons overflow to the barrier. The band offset between $Al_xGa_{1-x}N$ and GaN is

$$\Delta E_c = 0.7\left(E_g(x) - E_g(0)\right) \tag{9.25}$$

Where the band gap of AlGaN is measured to be

$$E_g(x) = xE_g^{AlN} - x(1-x)b + (1-x)E_g^{GaN} = \quad (9.26)$$
$$= x \cdot 6.1eV - x(1-x) \cdot 1.0eV + (1-x) \cdot 3.4eV$$

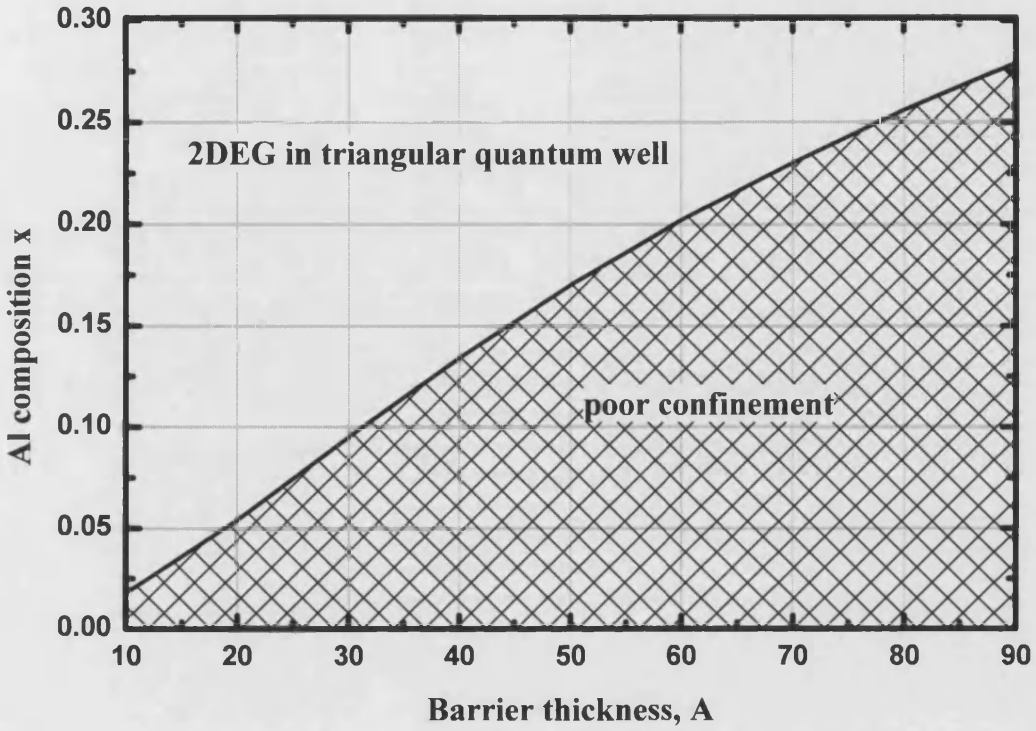

Figure 9.7. Minimal Al composition versus barrier thickness. The well is 100 Å thick.

Using equations (9.22), (9.23), (9.24), (9.25), (9.26) we calculate the minimal Al concentration in the barrier to satisfy the condition $E_f < \Delta E_c$. The results are presented in Figure 9.7 and Figure 9.8. For Al concentrations above the curve the condition $E_f < \Delta E_c$ is satisfied and 2DEG is established. For Al concentrations below the curve (hatched area) the triangular quantum well is not deep enough to contain all the carriers. Some electrons overflow to the barrier. Thus, for Al concentrations below the minimal value, we should expect lower mobility.

It should be mentioned that the calculations above should be treated only as qualitative prediction of a trend. The exact solution is more complicated because the potential well is of finite depth and is not triangular.

Next, we estimate the specific resistivity of n-type SL structures. The specific resistivity is given by

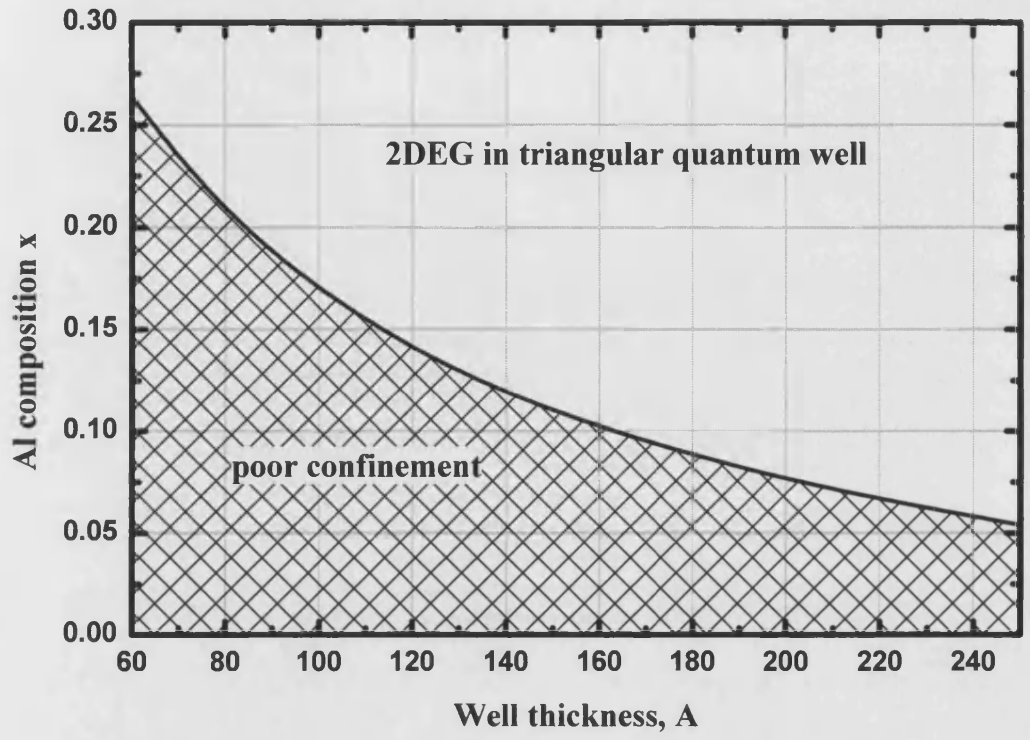

Figure 9.8. Minimal Al composition versus well thickness. The barrier thickness is 50 Å.

$$\rho = \frac{1}{\mu n e} = \frac{T}{\mu n_{sh} e} \tag{9.27}$$

Where T is the period of the superlattice, μ is the electron mobility, n_{sh} is the sheet electron concentration and e is the elementary charge. Using realistic values $T = 100\text{A}$, $\mu = 500\ \text{cm}^2/\text{Vs}$, $n_{sh} = 10^{13}\ \text{cm}^{-2}$ we obtain the specific resistivity $\rho = 1.25\times10^{-3}\ \Omega\text{cm}$. For comparison, the specific resistivity of bulk GaN with carrier concentration of $10^{19}\ \text{cm}^{-3}$ and mobility of $100\ \text{cm}^2/\text{Vs}$ is only $6.25\times10^{-3}\ \Omega\text{cm}$.

On one hand, the specific resistivity is proportional to the period of the superlattice, thus shorter period should result in lower value of specific resistivity. On the other hand, carrier confinement is less efficient in short period superlattice structures resulting in lower

mobility values. Consequently, there must be an optimum value of the superlattice period that gives the minimal value of specific resistivity.

To summarise, we can write down some guidelines for the growth of low resistivity superlattice structures:

1. The maximum doping level is given by equation (9.17), higher doping will not increase the 2DEG concentration.
2. The minimum Al composition is given by equations (9.22), (9.23), (9.24), (9.25), (9.26), for lower Al composition the band offset is too small to provide good carrier confinement.
3. The well to barrier ratio is chosen from equation (9.22), (9.23), (9.24), (9.25), (9.26). Structures with narrow barriers and wide wells have better carrier confinement.
4. The optimum period of the superlattice is a compromise between the condition of carrier confinement (equations (9.22-9.26)), and the condition of low specific resistivity (equation (9.27)).
5. The interfaces should be as smooth as possible to provide high mobility.
6. Relaxation of AlGaN layers should be avoided. First, for relaxed layers the piezoelectric field and, consequently, the 2DEG density is smaller. Second, relaxation generates high density of misfit dislocations at the interfaces, which affect the electron mobility.

9.4. Experiment

The AlGaN/GaN superlattice structures were grown by low pressure MOCVD on sapphire substrates. First, a ~1 μm GaN buffer layer was deposited following the standard procedure. Then, an AlGaN/GaN SL was grown on the top of the GaN buffer. TMGa, TMAl and NH_3 were used as sources of III and V element groups, SiH_4 was used as a dopant and hydrogen was used as a carrier gas. The flows of TMGa, TMAl, NH_3 and SiH_4

were 13.3 μmol/min, 0.93 – 10.4 μmol/min, 53 mmol/min and 2.6 – 26 nmol/min for, respectively. The periodicity of the SL structure was varied from 80 Å to 280 Å, the number of AlGaN/GaN pairs was 30 to 70 and the total thickness of the SL was about 0.5 μm.

Three different types of SLs were grown:

A. Continuously doped SL without interruption of the growth at the interfaces.

B. Modulation doped SL without interruption of the growth at the interfaces.

C. Modulation doped SL with interruption of the growth at the interfaces.

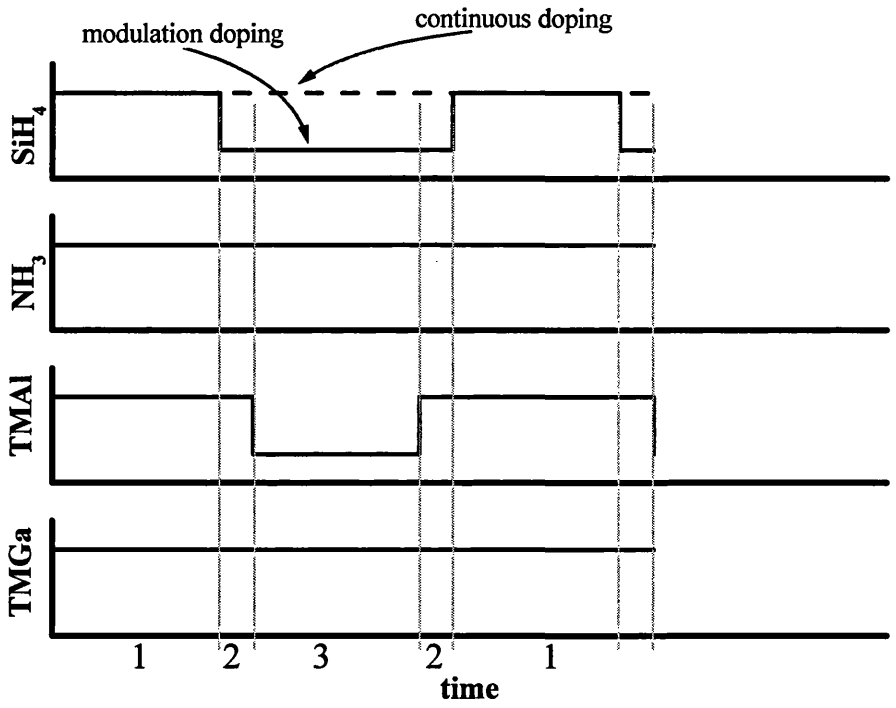

Figure 9.9. Gas flow diagram for the structure without growth interruption. (1) AlGaN barrier, (3) GaN well, (2) undoped spacer (for modulation doping only)

In the case of modulation doping, only the central part of the barrier was doped, the well and thin (5-10 Å) AlGaN spacers were grown without intentional doping to reduce scattering on ionised impurities. The gas flow diagram for modulation doping with growth interruption is shown in Figure 9.10.

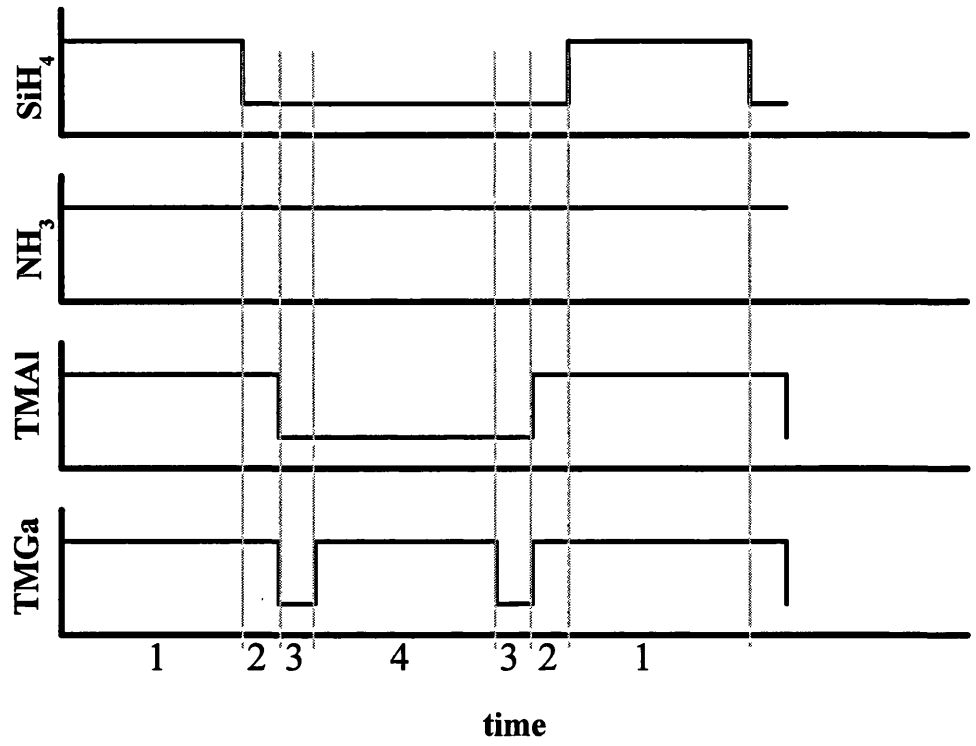

Figure 9.10. Gas flow diagram for the structure with modulation doping and growth interruption. (1) – AlGaN:Si barrier, (2) – AlGaN undoped spacer, (3) – growth interruption, (4) – undoped GaN well.

After the growth the structures were characterised by means of x-ray diffraction and Hall effect measurements. The Al composition in the barrier, well and the barrier widths were extracted from x-ray rocking curves using RADS Mercury dynamic simulation software. Hall measurements were conducted at room temperature using Van der Pauw method. Indium dots were used as contacts. The results are presented in Table 23.

Table 23. Parameters of n-type SL samples.

Sample	Number of pairs	SiH_4 flow, nmol/min	XRD				Hall		
			GaN, Å	AlGaN, Å	Period, Å	Al, %	μ, cm^2/Vs	n_{sh}, cm^{-2}	ρ, Ωcm
377	70	5	55	25	80	13	167	1.3×10^{13}	2.4×10^{-3}
378	70	4	53	25	78	13	224	3.6×10^{12}	6.1×10^{-3}
382	60	5	52	38	90	13	358	5.3×10^{12}	3.0×10^{-3}
384	40	10	52	44	96	13	303	9.5×10^{12}	2.2×10^{-3}
401	60	10	52	43	95	15	399	8.0×10^{12}	2.2×10^{-3}
402	40	10	56	45	101	17	431	9.0×10^{12}	1.6×10^{-3}
403	30	10	97	45	142	17	485	1.0×10^{13}	1.7×10^{-3}
404	30	10	93	45	138	20	531	1.2×10^{13}	1.4×10^{-3}
405	30	10	91	46	137	24	693	9.3×10^{12}	1.4×10^{-3}
406	30	10	98	12	110	100	820	6.6×10^{12}	1.2×10^{-3}
407	30	26.5	91	48	139	20	367	1.8×10^{13}	1.3×10^{-3}
430	30	10	146	43	189	17	564	9.3×10^{12}	2.4×10^{-3}
432	30	10	240	40	280	17	576	8.3×10^{12}	3.6×10^{-3}
460	30	10	100	47	147	22	702	9.3×10^{12}	1.4×10^{-3}
461	30	2.67	100	44	144	23	755	1.6×10^{12}	7.7×10^{-3}
462	30	10	100	42	142	30	798	9.7×10^{12}	1.2×10^{-3}

Sample 377 was continuously doped and has electron mobility of 167 cm^2/Vs. Relatively small value of mobility can be explained by increased scattering of electrons on ionised donors. This is supported by the following observations. First, when the doping level was decreased only by ~20% (sample 378) the mobility increased to 224 cm^2/Vs. Second, the modulation doped SL (sample 382) has higher mobility than that for the continuously doped SL (sample 378), though the carrier concentration in the modulation doped sample is higher than that for the continuously doped sample. In the case of modulation doping the electron scattering is reduced due to spatial separation of the carriers and ionised donors, thus the mobility is higher.

Another interesting observation is that the mobility is increasing with an increase of the Al composition in the barrier (see Figure 9.11). This is explained by better confinement of the electrons in the triangular potential well for higher Al composition in the barrier. For

low Al composition the potential well at the interface is not deep enough to contain all the electrons. Some of them overflow to the barrier and undergo scattering on ionized donors. At certain Al composition the band offset between GaN and AlGaN is large enough to prevent carrier overflow to the barrier and mobility saturates. The critical Al composition calculated from equations (9.22), (9.23), (9.24), (9.25), (9.26) for 45 Å/100 Å AlGaN/GaN superlattice is 15%.

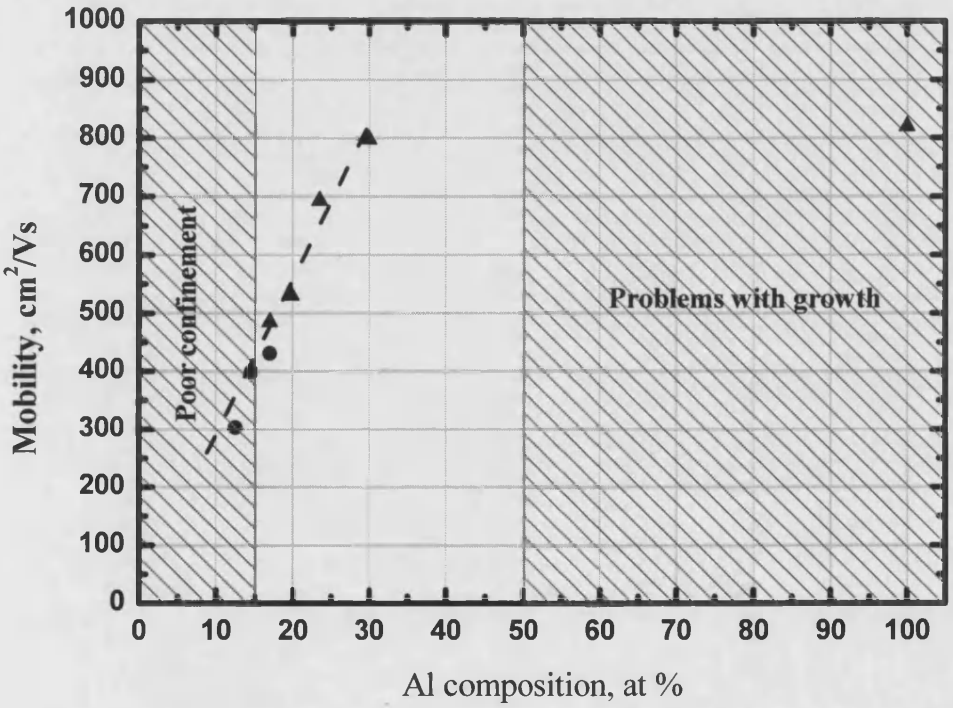

Figure 9.11. Mobility versus Al composition in the barrier.

The growth of AlGaN/GaN superlattice structures with high Al content is complicated from the technical point of view. The quality of the interfaces worsen with increase of Al composition, and this in turn can also affect the mobility. For example, the change of Al composition from 30% (sample 462) to 100% (sample 406) increased the mobility only by ~3%.

As one can see in Figure 9.12, the mobility is also increasing with increase of the well width. The dependence is almost linear in the range 50 – 150 Å, but for wider wells the mobility saturates at ~570 cm^2/Vs. Such behaviour is in good agreement with

theoretical predictions (see Figure 9.8). Using equations (9.22)...(9.26) it is possible to calculate that for the 45 Å thick $Al_{0.17}Ga_{0.83}N$ barrier the condition of carrier confinement is satisfied for wells wider than 90 Å. For wells narrower than that some electrons overflow to the barrier reducing the mobility. Once the well is wide enough to provide sufficient confinement, all electrons are contained in the 2DEG and the mobility saturates at a maximum value.

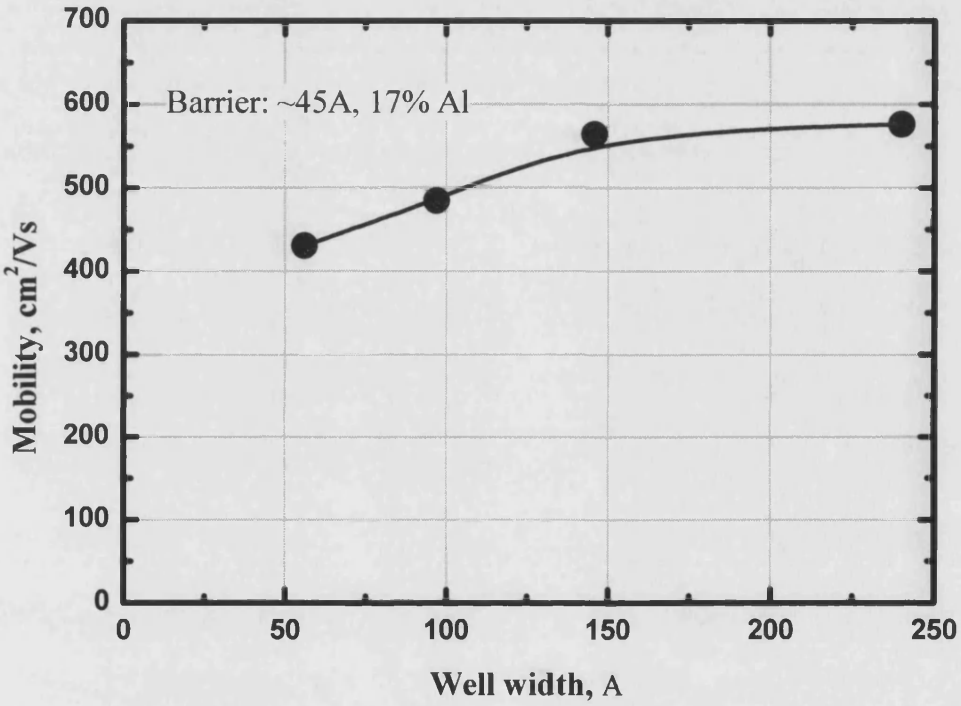

Figure 9.12. Mobility versus well width. Barrier is ~45 A thick and contains ~17% Al.

The measured sheet charge density is in the range $1.6\times10^{12} - 2\times10^{13}$ cm^{-2}. Experimental values are presented in Figure 9.13. The 2DEG charge must be smaller than the polarization charge $\sigma(x)$ (see equation 9.17), otherwise the whole assumption of the triangular well formation is not valid. Thus for the points above the curve $\sigma(x)$ the 2DEG is not formed and the electrons behave like normal 3D carriers with low mobility.

In the case of low Al composition (<15%) the band offset is not sufficient to provide good carrier confinement. Too high Al concentration (>50%) is not practical from the

growth point of view. In the latter case the lattice mismatch is too large and the formation of cracks and misfit dislocations is highly possible. To summarise, high mobility is expected for the points below the curve $\sigma(x)$ and with Al composition from 15% to 50% (white area in the plot)

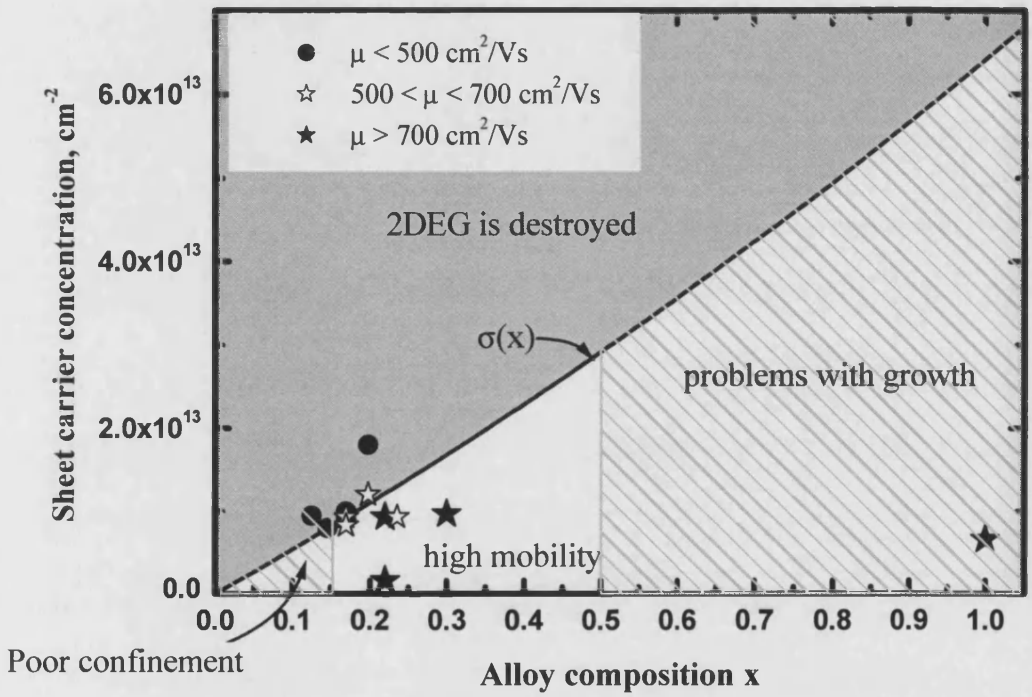

Figure 9.13. Experimental data on sheet carrier concentration versus Al composition. The curve $\sigma(x)$ denotes the piezoelectric charge density. High mobility is expected for the points below the curve $\sigma(x)$ and with Al composition in the range 15% – 50%.

Figure 9.14 illustrates the mobility dependence on the difference between experimentally measured sheet carrier concentration and the maximal allowed 2DEG concentration given by polarization charge density $\sigma(x)/e$.

The dependence has a marked threshold behaviour. The mobility is high when $n_{sh} - \sigma(x)/e$ is negative and all the carriers are contained in the 2DEG at the interface. The mobility decreases rapidly when $n_{sh} - \sigma(x)/e$ is approaching zero. For positive $n_{sh} - \sigma(x)/e$ values the mobility is low because the 2DEG is not formed.

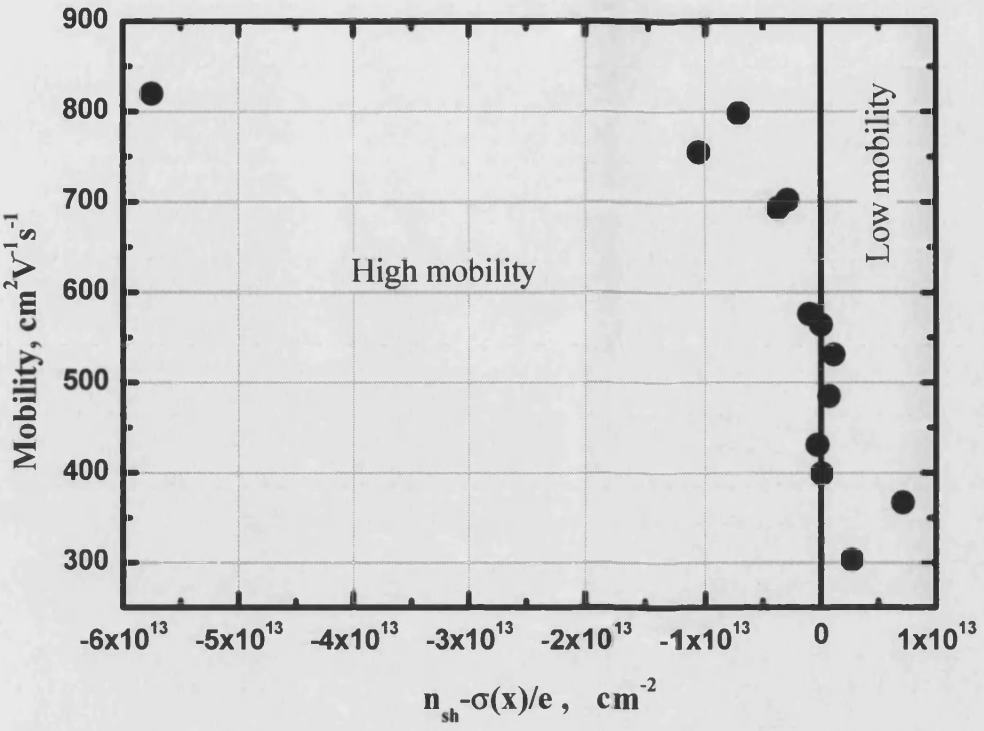

Figure 9.14. Electron mobility versus excess carrier concentration $n_{sh} - \sigma(x)/e$

9.5. Summary

In this chapter we have presented theoretical and experimental studies on n-type doped AlGaN/GaN superlattice structures. The effect of Al concentration, Si doping, well/barrier width on electron mobility and specific resistivity has been studied. The experimental results are in good agreement with theoretical predictions.

High sheet charge density of 10^{13} cm^{-2} and increase of the electron mobility up to 820 cm^2/Vs due to formation of 2DEG have been observed. Low specific resistivity of 1.2×10^{-3} Ωcm has been achieved.

The most important result of the present study is that III-nitride superlattice structures have unique physical properties due to the presence of built-in electric fields. Traditional approaches valid for conventional III-V semiconductors are not applicable to III-nitrides. For example, the optimum well width for AlGaN/GaN superlattices is 100-150 Å, which is much larger than that in AlGaN/GaN superlattices. Also, we should

emphasise the fact, that in case of III-nitride superlattices the maximal doping level is limited by the polarisation charge density. Doping higher than that destroys the 2DEG and reduces the mobility. Consequently, for overdoped samples the specific resistivity is higher.

Now it is worth to summarise the current results and to discuss the directions for further improvement of AlGaN/GaN superlattices.

- Barriers and wells should be about 40-50 Å and 100-150 Å, respectively.
- Higher Al concentration gives better results, but the growth of AlGaN with high Al content is complicated from the technical point of view.
- The doping level should be close, but not exceeding the limit imposed by polarisation charge.

Future work should be concentrated on the optimisation of the growth conditions,material quality, structure parameters and interface roughness.

9.6. References

1. R.Gaska, M.S. Shur, D. Bykhovski, A.O. Orlov, L. Snider, Appl. Phys. Lett. 74, 287
2. I.P. Smorchkova, C.R.Elsass, J.P. Ibbetson, R.Vetury, B. Heying, P. Fini, E. Haus, S.P. DenBaas, J.S. Speck , U.K. Mishra, J.Appl.Phys., 86, 4520
3. S.Yamaguchi, Y. Iwamura, Yasuhiro Watanabe, M. Kosaki, Y. Yukawa, S. Nitta, S. Kamiyama, H. Amano,I. Akasaki, Appl. Phys. Lett., 80, 802
4. Y.Zhang, I.P.Smorchkova, C.R. Elsass, S.Keller, J.P. Ibbetson, S. Denbaars, U.K. Mishra, J.Singh, J. Appl. Phys., 87, 7981
5. Tsung-Hsing Yu, K.F.Brennan, J. Appl. Phys., 89,3827
6. F. Bernardini and V. Fiorentini, Phys. Rev. B, 56 10024
7. A. Bykhovski, B. Gelmont, and M.S. Shur, J.Appl. Phys. 74, 6734
8. B. K. Ridley, Appl. Phys. Lett., Vol. 77, 990
9. O.Ambaher J. Phys. D: Appl. Phys. 31, 2653
10. Polian, A., M. Grimsditch, I. Grzegory, J. Appl. Phys. 79(6) (1996), 3343-3344
11. Wright, A.F, J. Appl. Phys. 82. 6 (1997), 2833-2839.
12. McNeil, L.E, Grimsditch M., French R.H., J. Am. Ceram. Soc. 76, 5 (1993), 1132-1136

13. O. Ambacher, J. Smart, J.R. Shealy, N.G. Weimann, K. Chu, M. Murphy, W.J. Schaff, L.F. Eastman, R. Dimitrov, L. Wittmer, M. Stutzmann, W. Rieger, J. Hilsenbeck, J. Appl. Phys. 85, 3222

14. O.Ambacher, B. Foutz, J. Smart, J.R. Sheally, N.G. Weimann, K. Chu, M. Murphy, A.J. Sierakowski, W.J. Schaff, L.F. Eastman, R. Dimitrov, A. Mitchell, M. Stutzmann, J. Appl. Phys, 87,334.

15. N. Maeda, T. Saitoh, K. Tsubaki, T. Nishida, N. Kobayashi, Appl. Phys. Lett., Vol. 76, 3118

10. Mg doped AlGaN/GaN superlattice structures

10.1. Introduction

Recently, it has been theoretically [1,2] and experimentally [3,4,5] demonstrated that doped superlattice structures increase the free hole concentration as compared to homogeneous p-type GaN and AlGaN. The modulation of the chemical composition leads to a variation of the valence band energy and reduction of the acceptor activation energy. Also, a strain-induced piezoelectric field may be produced. It has been reported [5] that the piezoelectric field can greatly reduce the activation energy of Mg-acceptors.

P-type AlGaN/GaN SLs have been successfully used in light emitting diodes [6] and laser diodes [7,8]. Experimental results indicate superior properties of devices with SLs as compared to devices with homogeneous p-type GaN or AlGaN layers. The use of p-type SLs results in lower operating voltage and higher efficiency of LEDs. A major breakthrough in III-nitride laser diodes has been done using p-type SLs instead of bulk AlGaN cladding layers.

10.2. Review of published results

Goepfert *et al.* [6,9] reported on uniformly Mg-doped AlGaN/GaN. superlattices consisting of 20 periods of equally thick $Al_xGa_{1-x}N$ barriers (100 Å) and GaN wells (100 Å). The AlGaN and GaN layers were uniformly doped with Mg at a level of $N_{Mg} \approx 10^{19}$ cm^{-3}. The Al mole fraction was x=0.10 and x=0.20. At room temperature, the carrier concentration of the doped SL structures were 2×10^{18} cm^{-3} and 4×10^{18} cm^{-3} for an Al mole fraction x=0.10 and x=0.20, respectively. The mobility for both samples was about 1 cm^2/Vs. The acceptor activation energy was extracted from temperature-dependent Hall effect measurements. The activation energy was 200 meV for bulk p-type GaN, 70 meV for SLs with x=0.10 and 58 meV for SLs with x=0.20.

Shew *et al* [10] reported on p-type SL consisted of a 160 Å thick $Al_{0.15}Ga_{0.85}N$ barrier and 80 Å thick GaN in one period. The room temperature free hole concentration was 3×10^{18} cm^{-3} and Hall mobility 5 cm^2/Vs.

Kumakura *et al* [4] studied the dependence of sheet hole concentration per period of the SLs versus period thickness. The thickness of $Al_{0.15}Ga_{0.85}N$ barrier to GaN well was fixed at two. The doping level N_{Mg} was almost constant at 2×10^{19} cm^{-3} for each sample. The sheet hole concentration initially increased as the SL period thickness increased up to 360 Å (240 Å/120 Å) and reached 8×10^{12} cm^{-2}. This sheet concentration corresponds to the hole concentration of 3×10^{18} cm^{-3}. For the period thickness longer than 360 Å it was almost constant or even decreased. The sheet hole concentration increased as the Al mole fraction increased up to 0.15 and then saturates for x ranging between 0.15 and 0.30

Polyakov *et al* [11] presented the results of electrical and optical measurements on p-type SLs grown by MBE technique. The SL structures consisted of 20 periods of AlGaN/GaN. The thickness of the $Al_{0.25}Ga_{0.75}N$ barriers and GaN wells was close to 100 Å. The Mg doping in the barriers was some 10^{19} cm^{-3}. The wells were not intentionally doped; however some Mg doping of these regions may be present due to memory effect of the system. The SL structures were grown on the top of GaN buffer or AlGaN buffer with Al mole fraction close to that in the barriers (x=0.25). The SL grown on the GaN buffer layer had bulk hole concentration of 8×10^{17} cm^{-3} and Hall mobility of 31.3 cm^2/Vs. The hole concentration of the SL grown on the AlGaN buffer was 7.8×10^{17} cm^{-3}, however the mobility was only 2.2 cm^2/Vs. For comparison, the carrier concentration and the mobility in bulk p-type GaN films grown under similar conditions were 2×10^{17} cm^{-3} and 6 cm^2/Vs, respectively.

Saxler et al [12] reported on short period AlGaN/GaN SL doped with Mg. The thickness of AlGaN barriers and GaN wells was varied from 8 Å to 23 Å and from 8 Å to

39 Å, respectively. The Al composition was 30% and 45%. In such type short period SL structures the wave functions can propagate through thin barriers leading to the formation of minibands. The activation energy of Mg acceptors was calculated from temperature-dependent Hall effect and resistivity measurements. The smallest activation energy of 116 meV was measured for the sample with the widest well (39 Å) and the thinnest barrier (8 Å). The SL with 8 Å well and 17 Å barrier had the largest activation energy of 268 meV.

Kozodoy et al [5] studied the dependence of the hole concentration on the SL period and the effect of modulation doping at alternate interfaces. The SL structures of the first type were grown by MOCVD and consisted of $Al_{0.2}Ga_{0.8}N$ barriers and GaN wells of equal thickness L. The Mg doping was applied uniformly through the SL. The SL dimension L was varied from 20 Å to 140 Å. The hole concentration initially increased with increasing L and saturated (or perhaps even decreased) for L longer than 80 Å. The mobility exhibited a weak dependence on L and was about 10 cm^2/Vs. The SL structures of the second type were grown by MBE and consisted of 80 Å thick $Al_{0.12}Ga_{0.88}N$ barriers and 80 Å thick GaN wells. The Mg doping was applied through only half of the structure, either region A or region B (see Figure 10.1). The sample doped only in region A exhibited a higher hole concentration of 1.9×10^{18} cm^{-3} and a higher mobility of 19 cm^2/Vs. For the sample doped in region B the hole concentration was only 6.8×10^{17} cm^{-3} and the mobility 5.6 cm^2/Vs. This observation is the direct evidence of the critical role of polarization fields in the SL band structure.

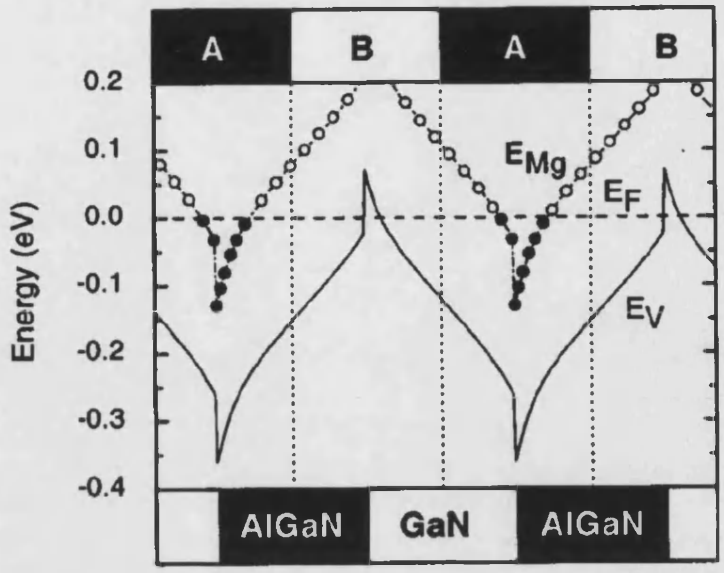

Figure 10.1. Calculated valence-band diagram for the Mg-doped $Al_{0.2}Ga_{0.8N}$/GaN superlattice with spontaneous and piezoelectric polarization fields taken into account. The thickness of each layer is 80 Å. The dashed line indicates the Fermi energy, and the circles represent the energy of the Mg acceptor solid when ionised. Regions A and B defining each interface are indicated. The sapphire substrate is on the left and the free surface of the film is on the right. (From [5])

10.3. Experiment

P-type SL structures were grown on c-face sapphire substrates by low pressure MOCVD. First, we grew a ~1 μm-thick GaN layer at 1160°C on a low-temperature GaN nucleation layer. Then, we grew a ~1 μm-thick GaN:Zn insulating layer. Then a thin (500 Å) p-type GaN cladding layer was deposited to stabilise the growth conditions. After that we grew AlGaN/GaN SL structures with various well and barrier thicknesses. The molar flows TMGa, TMAl, NH_3 and Cp_2Mg during superlattice growth were 17.7 μmol/min, 2.7 μmol/min, 22 mmol/min and 251.5 nmol/min, respectively. Hydrogen was used as a carrier gas. The growth temperature was 1070°C. A thin (500 Å) p-GaN layer was grown above the SL to prevent oxidation of AlGaN layers, followed by the deposition of 100-200 Å p+ contact layer (see Figure 10.2).

The SLs were modulation doped by Mg by switching Cp_2Mg flow on and off during the growth. The SL structures were grown continuously, i.e. without growth interruptions

at interfaces. For that reason one may expect smearing of the doping profile due to memory effects in the reactor. Most of the samples were modulation doped only in AlGaN barriers and no intentional doping was used in GaN wells. For samples 479 and 480 the profiles of Mg and Al were shifted by half of the period with respect to each other, so that half of the barrier and half of the well were doped. The sample 479 was doped only at GaN/AlGaN interfaces (counting from the substrate) and AlGaN/GaN interfaces were undoped. On the contrary, the sample 480 was doped at AlGaN/GaN interfaces and GaN/AlGaN interfaces were undoped. The detailed outline of the structure is presented in Table 24.

Table 24. Typical conditions used for AlGaN/GaN SL growth

TMGa flow	17.7 μmol/min
TMAl flow	2.7 μmol/min
NH_3 flow	500 sccm
Cp_2Mg flow	251.5 nmol/min
Temperature	1070°C
Pressure	100 mbar
Carrier gas	H_2, total flow 5000 sscm

The Al mole fraction, well and barrier thickness were extracted from x-ray diffraction measurements using RADS Mercury simulation software. The van der Pauw-Hall effect measurements using In contacts were carried out to find out the hole concentration, the resistivity and the Hall mobility of SL structures at room temperature. Room temperature PL was measured using a Renishaw micro Raman system equipped with 244 nm frequency doubled Ar laser.

The samples were annealed under nitrogen to activate Mg dopant. The optimum annealing temperature was determined empirically. Wafer 474SL-p was cut into pieces which were annealed for 15 minutes at various temperatures in the range from 580°C to 890°C in an open-flow furnace in nitrogen ambient. Then the Hall effect measurements were performed. The dependence of the hole concentration, the Hall mobility and the resistivity on annealing temperature is presented in Figure 10.3. The hole concentration

continuously increases with increasing temperature, and the Hall mobility approaches a maximal value for samples annealed at 740°C. The resistivity has a minimum at 750-800°C. Basing on these observations, we have chosen the optimum annealing temperature to be around 800°C. The rest of p-type SL samples were annealed for 15 min at 800°C.

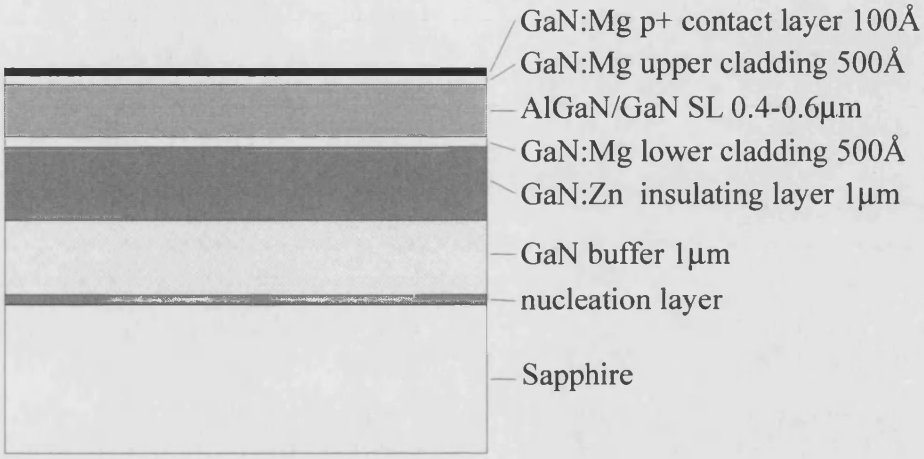

Figure 10.2. Layout of a typical p-type SL structure

Table 25. Sample data including superlattice layer thicknesses, composition of AlGaN layer, doped region and electrical properties.

Sample	**GaN, Å**	**AlGaN, Å**	**Al%**	**# of pairs**	**Doping**	**p cm^{-3}**	**μ cm^2/Vs**	**ρ Ωcm**
474	112	115	12	30	AlGaN	8.3×10^{17}	10	0.77
475	213	109	12	20	AlGaN	8.4×10^{17}	11	0.67
476	206	52	12	20	AlGaN	8.8×10^{17}	13	0.55
477	110	110	13	30	AlGaN	8.1×10^{17}	7	1.00
478	221	217	12	20	AlGaN	7.3×10^{17}	10	0.87
479	100	115	12	30	GaN/AlGaN	5.3×10^{17}	9	1.2
480	100	100	12	30	AlGaN/GaN	6.9×10^{17}	8	1.1
481	119	59	12	25	AlGaN	6.5×10^{17}	12	0.81

The lowest resistivity of 0.55 Ωcm has been measured for 20-period AlGaN/GaN SL with 206 Å thick wells and 52 Å thick $Al_{0.12}Ga_{0.88}N$ barriers. The hole concentration for this sample was 8.8×10^{17} cm^{-3}, with mobility of 13 cm^2/Vs. Both the Hall mobility and the hole concentration increase with decreasing width of AlGaN barrier (see Figure 10.4).

One should note that the Cp_2Mg flow was kept constant, thus Mg concentration per unit volume in SLs with thinner AlGaN barriers is lower. Larger carrier concentration in the thin-barrier structures can be explained by higher strain in AlGaN barriers.

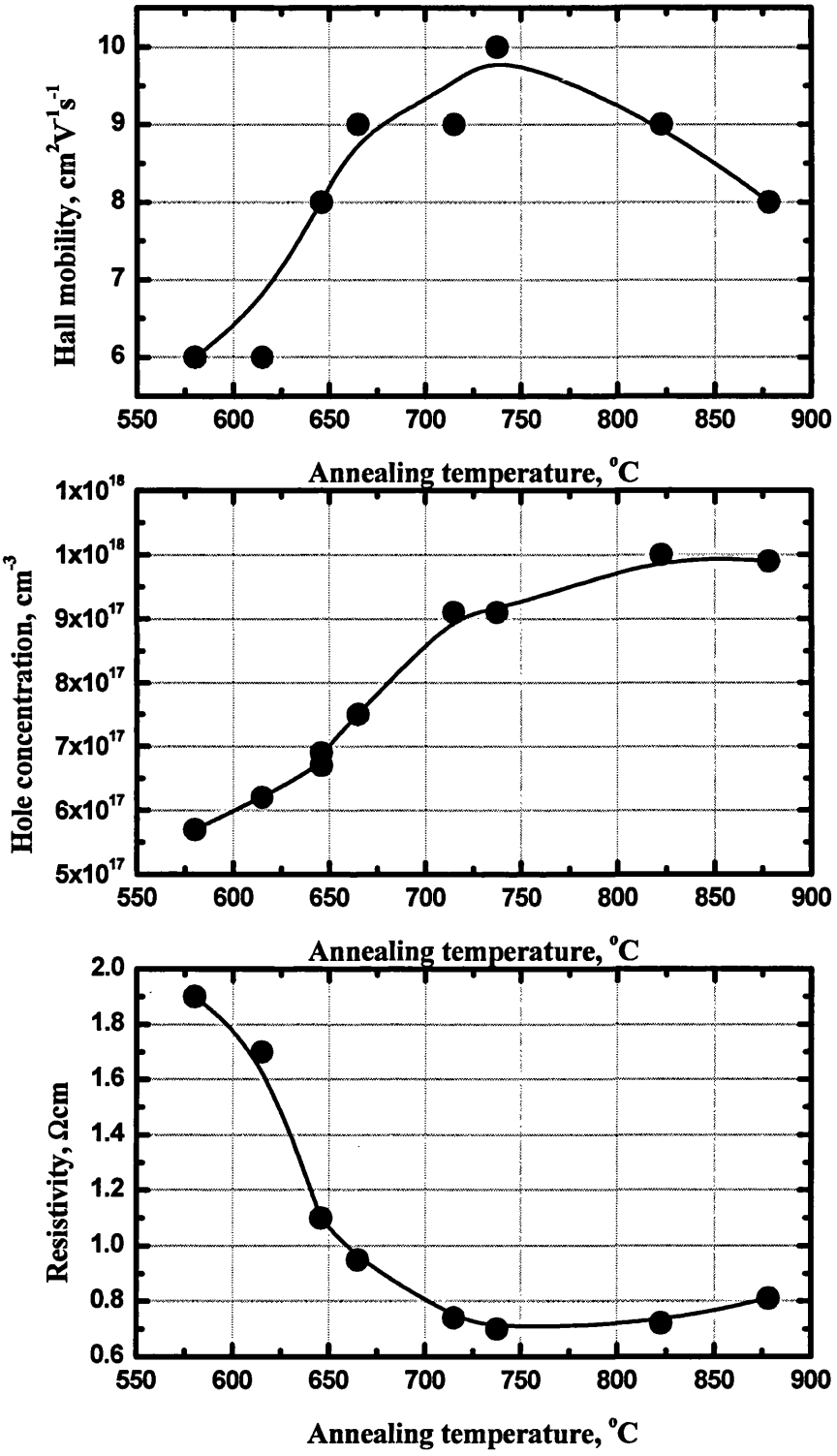

Figure 10.3. Hall mobility, hole concentration and resistivity of Mg-doped AlGaN/GaN superlattice (sample 474) versus annealing temperature.

Higher mobility can be explained by better crystalline quality of the thin AlGaN barriers and better confinement of the two-dimensional hole gas (2DHG) at the interface for thin barriers (see chapter 9).

On the contrary, the resistivity of the samples is decreasing with increasing well width (see Figure 10.5). This phenomenon is also in good agreement with the piezoelectric field model: thicker layers yield larger potential changes from the polarization fields, and therefore higher hole concentrations.

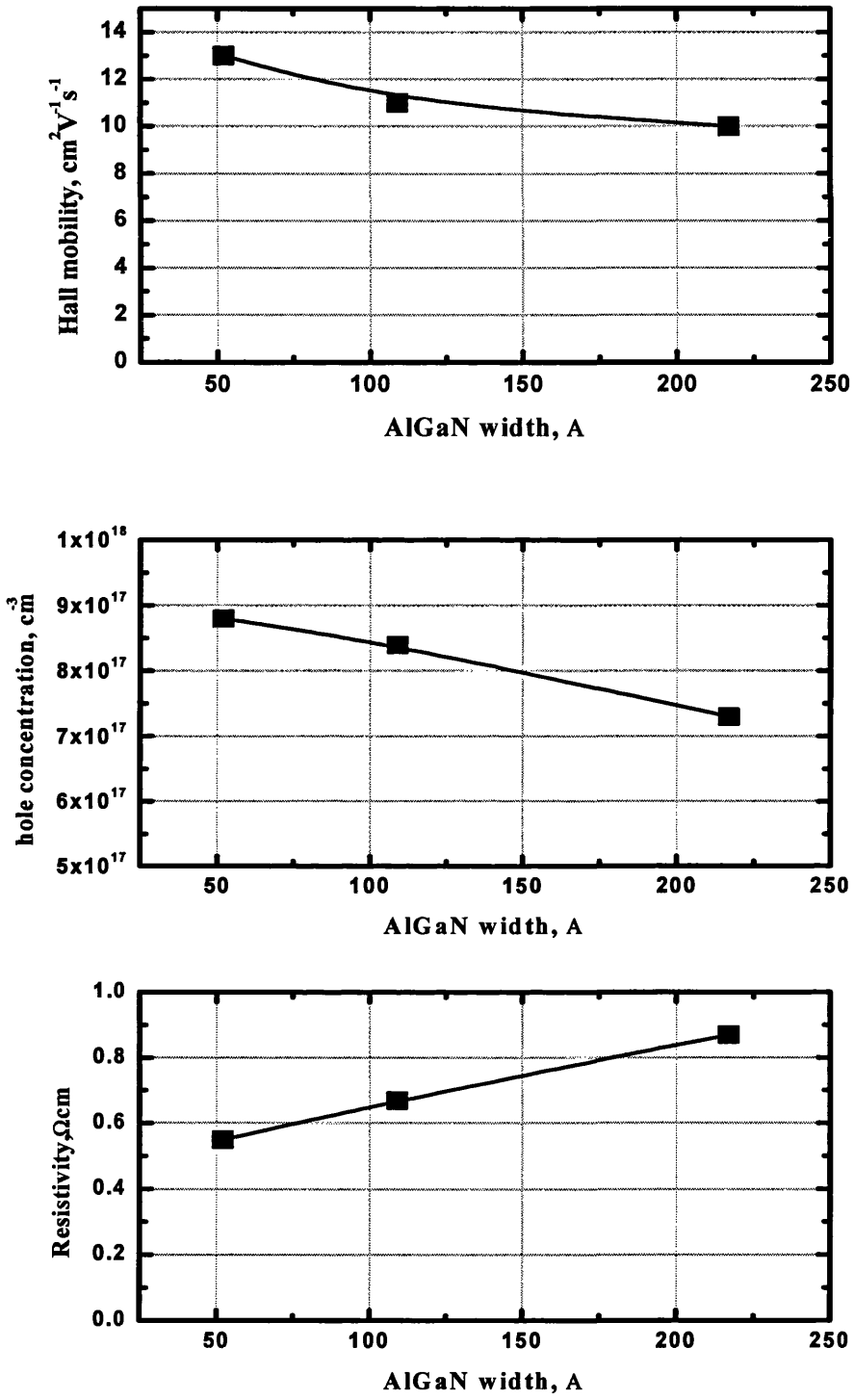

Figure 10.4. Room temperature Hall effect measurements on Mg-doped $Al_{0.12}Ga_{0.88}N$/GaN superlattices. The thickness of AlGaN barrier is varied. The thickness of GaN well is about 210 Å.

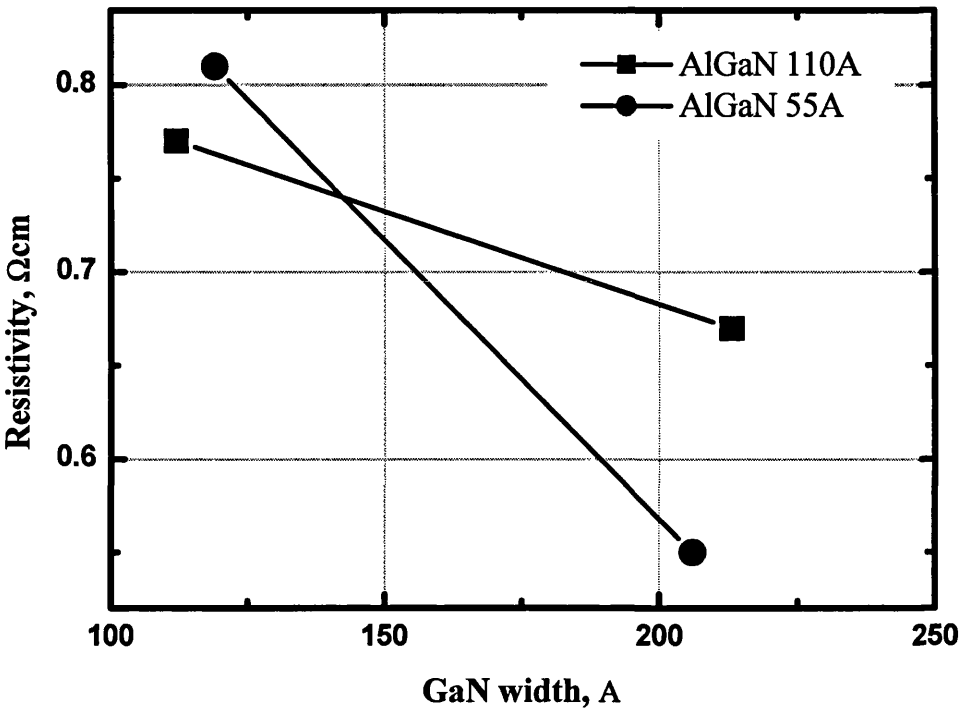

Figure 10.5. Resistivity of AlGaN/GaN SL structures versus GaN well width. The thickness of AlGaN barrier is ~110 Å and ~55 Å.

Figure 10.6 shows room temperature PL spectra for Mg-doped SL structures. The PL spectra are very similar to PL spectra for Mg-doped GaN. In addition to GaN edge emission peak at ~ 361 nm there is a broad Mg-related emission at 380 – 450 nm. As it has been reported by many authors [13] the blue emission at 380 nm (3.2 eV) is related to transitions involving shallow acceptor, while broad blue band around 440 nm is so-called 2.8 eV line, which is related to the transitions involving some deep defect state, either deep acceptor or deep donor. It is interesting to note, that the intensity of these lines strongly correlates with the Hall mobility. For SL structures having low mobility the 2.8 eV line dominates. The intensity of the edge-peak and 3.2 eV increases with increasing mobility. This observation is in line with suggested model of blue emission band. The formation of the deep states gives rise to 2.8 eV line, the increased scattering on the same centres leads to decrease of the Hall mobility.

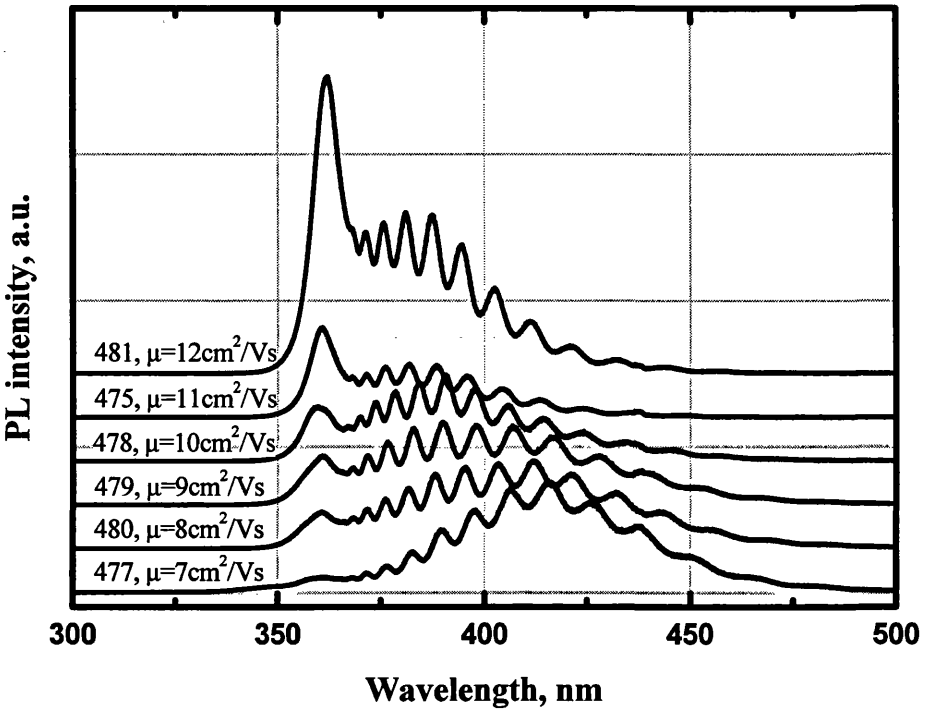

Figure 10.6. Room temperature PL spectra of Mg-doped superlattice structures. The shape and position of PL peaks exhibit strong correlation with the Hall mobility.

10.4. Summary

We have successfully grown modulation Mg-doped AlGaN/GaN superlattice structures. These structures reveal superior electrical properties in terms of lower specific resistivity and higher net hole concentration compared to that of p-type GaN. The highest hole concentration of 8.8×10^{17} cm^{-3} has been demonstrated. The strong dependence of electrical properties on thicknesses of AlGaN and GaN layers indicates that piezoelectric field greatly influences the band structure in AlGaN/GaN superlattices. Therefore, for obtaining a high hole concentration it is necessary to balance well and barrier thicknesses, periodicity of the superlattice and Al mole fraction.

10.5. References

1. E.F. Schubert, W.Grieshaber, I.D.Goepfert, Appl. Phys. Lett., v.69, p.3737, (1996)

2 . L. Hsu, W. Walukiewicz, Appl. Phys. Lett, v74, (1999), 2405

3. K.Kumakura, T.Makimoto, N.Kobayashi, Jpn. J. Appl. Phys. Vol.39(1999) L195

4. K.Kumakura, N.Kobayashi, Jpn. J. Appl. Phys. Vol.38(1999) L1012

5. P. Kozodoy, Yu.P. Smorchkova, M.Hansen, H.Xing, S.P.DenBaars, U.K.Mishra, A. W. Saxler, R. Perrin, W. C. Mitchel, Appl. Phys. Lett. 75(1999), p. 2444

6. I. D. Goepfert, E. F. Schubert, A. Osinsky, P. E. Norris, N. N. Faleev, J. Appl. Phys., 88 (2000), 2030

7. S. Nagahama, T. Yanamoto, M. Sano, and T. Mukai, Appl. Phys. Lett. 79 (2001), 1948

8. S. Nakamura, M. Senoh, S. Nagahama, N. Iwasa, T.Yamada, T. Matsushita, H. Kiyoku, Y. Sugimoto, T. Kozaki, H. Umemoto, M. Sano, and K. Chocho, Appl. Phys. Lett. 72 (1998), 2014

9. I. D. Goepfert, E. F. Schubert, A. Osinsky, P. E. Norris, MRS Internet J. Nitride Semicond. Res. 5S1, W3.85 (2000).

10. J.K.Sheu, C.H.Kuo, C.C. Chen, G.C. Chi, M.J. Jou, Solid-State Electronics 45(2001) 1665

11. A. Y. Polyakov, N. B. Smirnov, A. V. Govorkov, A. V. Osinsky, P.E.Norris,S.J. Pearton, J. Van Hove, A. Wowchak, and P. Chow, Appl. Phys. Lett. 79 (2001), 4372

12. A. Saxler, W. C. Mitchel, P. Kung, M. Razeghi, Appl. Phys. Lett. 74(1999) 2023

13. See references in Chapter 5

11. InGaN/GaN MQW structures

11.1. Introduction.

InGaN quantum wells (QWs) are the key element of LED active region. Despite the remarkable progress in device development, the growth of high quality InGaN/GaN QWs is still very challenging and many fundamentally important issues remain to be addressed. A clear understanding of the quality of InGaN QWs is necessary for the improvement of the properties of these structures. In this chapter, we report on the growth of MQW structures by MOCVD and describe the results of the analysis of these structures by photoluminescence (PL) and x-ray diffraction (XRD).

The primary challenge facing the grower in InGaN/GaN system is that the growth conditions for InGaN and GaN are very different. For example, high quality GaN is grown at high temperature (about 1100°C) using hydrogen as a carrier gas. On the contrary, InGaN growth requires much lower temperature (usually below 850°C) and nitrogen ambient.

The growth at low temperatures results in highly defective GaN films. GaN epilayers grown under nitrogen have rough morphology. At higher growth temperature the incorporation of indium is reduced a lot. Moreover, InGaN is not stable at temperatures above 1000°C and can decompose into indium, gallium and nitrogen. The presence of hydrogen also reduces the indium incorporation and facilitates decomposition of InGaN presumably due to formation of volatile In_xH_y compounds. Therefore, the optimum growth conditions for InGaN/GaN MQW structures require the technique to compromise between good crystalline quality and good In incorporation.

11.2. Experiment

Multiple quantum well structures composed of five periods of InGaN/GaN were grown by the low pressure MOCVD on (0001) sapphire substrates. The growth sequence included the deposition of a low-temperature nucleation layer, the deposition of a 1-2 μm GaN buffer layer, the growth of MQW region, and the growth of a capping layer. A schematic diagram of the MQW structure is presented in Figure 11.1.

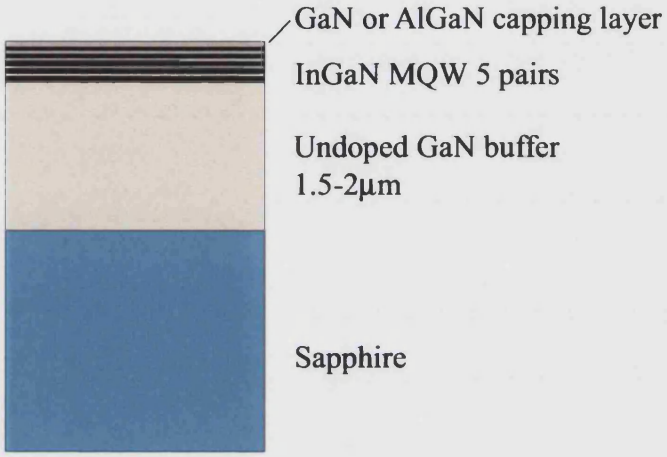

Figure 11.1. Layout of MQW structure.

The nucleation layer and buffer layer were grown using hydrogen carrier gas and TMGa and NH_3 precursors. The deposition temperature for the low-temperature GaN nucleation layer was about 540°C. The GaN buffer layer was grown at 1140-1160°C. During the MQW growth the carrier gas was changed to N_2 and the growth temperature was reduced to 700-850°C to increase the indium incorporation in InGaN layers. The details of the growth conditions of the MQW region are summarised in Table 26.

After the growth the structures were characterised by means of room temperature photoluminescence and x-ray diffraction. The photoluminescence signal was excited by 325 nm line of He-Cd laser (continuous wave, average power of 30mW) or 337 nm line of N_2 (pulse duration of 300 ps, average power of 0.5mW). In the case of the He-Cd laser the excitation power density was in the range 1–5000 W/cm^2, depending on the laser spot size. With the nitrogen laser we were able to achieve the power density up to 10 MW/cm^2.

Table 26. Growth conditions for MQW region.

Ga precursor used	TMGa or TEGa
In precursor used	TMIn
TMGa/TEGa flow	5-20 μmol/min
TMIn flow	3-40 μmol/min
In/(In+Ga) ratio	0.3-0.8
NH_3 flow	6 slm
Temperature	670-850°C
Pressure	100-200mbar
Carrier gas	Nitrogen
Growth rate	2.5-12 Å/min

11.3. Different growth regimes for MQW structures

Several approaches for the growth of MQW InGaN/GaN structures are possible. In the first approach, the barriers and wells are grown at the same temperature and In composition in the solid is varied by changing In/(In+Ga) ratio in the gas phase. In the second approach the In/(In+Ga) ratio is constant for wells and barriers and In composition is controlled by changing growth temperature. The third approach is the combination of the first two when both In/(In+Ga) input ratio and temperature are varied.

We have experimentally studied the different growth regimes of MQW structures. In the case of sample 391MQW, both In input concentration and growth temperature were different for wells and barriers. For sample 421MQW wells and barriers were grown at the same temperature and In content was varied by modulation of the TMIn flow. The growth conditions are listed in the Table 27.

Table 27 Comparison of the growth conditions and PL properties of samples 391MQW and 421MQW.

Parameter		391MQW	421MQW
Growth temperature	barriers	850°C	850°C
	wells	700°C	850°C
TMIn/(TMIn+TMGa) input ratio	barriers	0.137	0
	wells	0.3	0.8
Growth rate of InGaN		~2.5–3 Å/min	~5-7 Å/min
PL peak position, centre		442 nm	436 nm
PL intensity, centre		1.1 a.u.	5.9 a.u.

The quality of MQW structures was assessed by room temperature photoluminescence. As one can see from Table 27, the samples have close emission wavelength, however the PL intensity of the sample 421MQW is 5-6 times stronger.

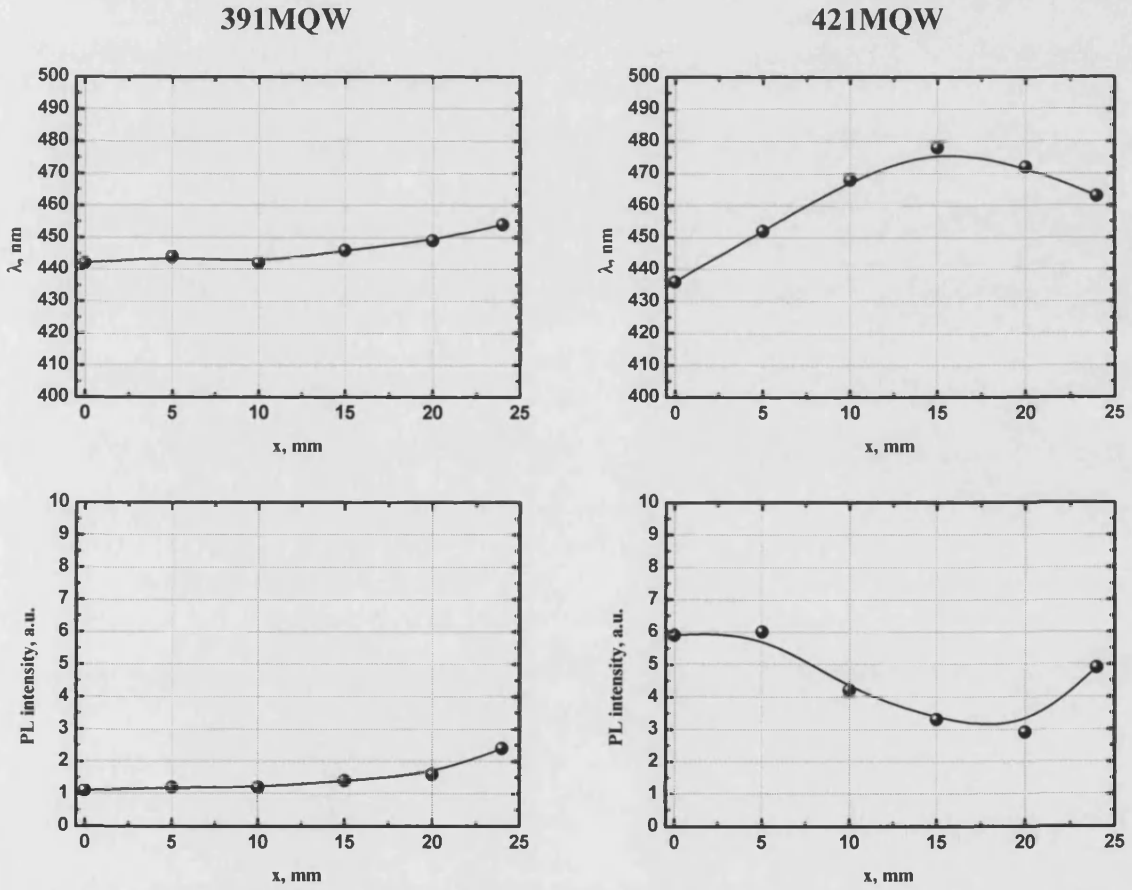

Figure 11.2. Distribution of emission wavelength and PL intensity along the radius of the wafer. Distance is measured from the centre of the wafer to the edge.

Figure 11.8 shows the dependence of the PL properties on the position along the radius of the wafer. As one can see, sample 391MQW has much better uniformity of PL peak position and PL intensity. However, sample 421MQW has more intense PL signal.

Such type of behaviour is understandable. As we discussed in Chapter 7, indium incorporation at high temperatures is very non-linear. Small fluctuations of the gas composition and substrate temperature may lead to significant change of In composition in the solid. Thus it is more difficult to control InGaN composition under high-temperature growth conditions. On the other hand, high-temperature growth results in less defect material and more efficient radiative recombination.

11.4. Decomposition of InGaN.

Low thermal stability of InGaN makes the growth of InGaN epilayers quite challenging. At high temperature InGaN can decompose either into phases with different In content, or, in most severe cases, into indium, gallium and nitrogen. The decomposition of InGaN reveals itself in grey-brown colouring of the wafer, red shift of emission wavelength and reduced efficiency of photoluminescence.

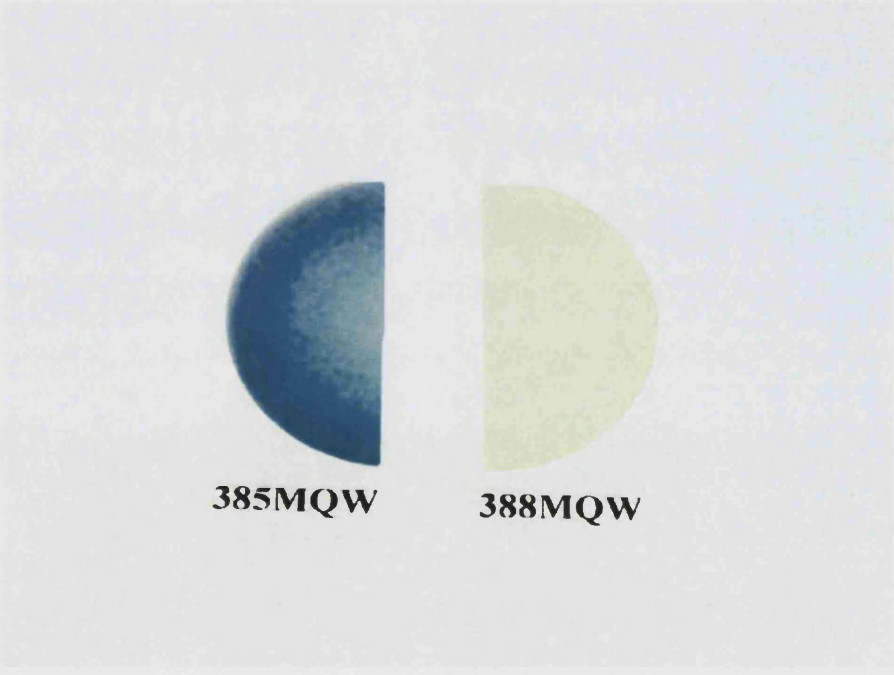

Figure 11.3. Photographs of two MQW structures with capping layer grown at 1070°C (385MQW, left) and 950°C (388MQW, right).

The decomposition process is governed by a number of factors, among them the most important are the temperature, the strain, the gas ambient and the material of the

capping layer. In practical LED and LD device structures InGaN MQW is sandwiched between GaN layers. Though the growth temperature of MQW can be reduced to increase In incorporation and prevent decomposition of InGaN, but afterwards it has to be increased again for the growth of subsequent GaN or AlGaN layers. Therefore, the problem of InGaN decomposition has to be treated more skilfully, bearing in mind not only the growth conditions of the InGaN quantum well, but also the growth of subsequent layers above the quantum well.

The following example illustrates the influence of the growth conditions of subsequent layers on the decomposition of the MQW. Samples 385MQW and 388MQW have identical structure with the exception of growth temperature of the capping layer. The temperature was 950°C for the sample 380MQW and 1070°C for the sample 388MQW. As one can see in Figure 11.3 the sample with GaN capping layer grown at 950 is transparent, while the sample with the capping layer grown at 1070°C displays evident signs of decomposition. The x-ray diffraction curves from the two samples are presented in Figure 11.4. The sample with low temperature capping layer exhibits sharper satellite peaks, which indicates superior quality of the interfaces.

Figure 11.5 presents the room temperature PL spectra from samples 385MQW and 388MQW. Both samples give comparable PL signal in terms of peak width and intensity; however, sample 388MQW exhibits stronger defect related yellow luminescence, which originates from the low temperature cap layer.

To conclude, a low temperature capping layer prevents decomposition of InGaN in MQW, but at the cost of increased defect density in the capping layer.

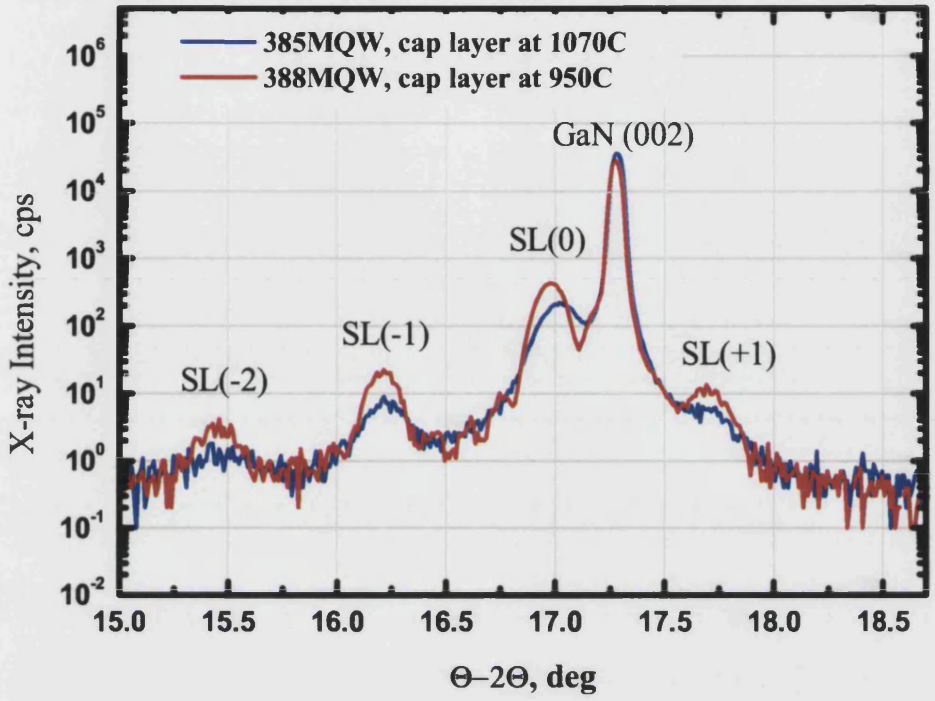

Figure 11.4. X-ray diffraction curves from two MQW structures with capping layer grown at 1070°C (385MQW) and at 950°C (388MQW). Structure with low temperature capping layer exhibits sharper satellite peaks, which indicates superior quality of interfaces.

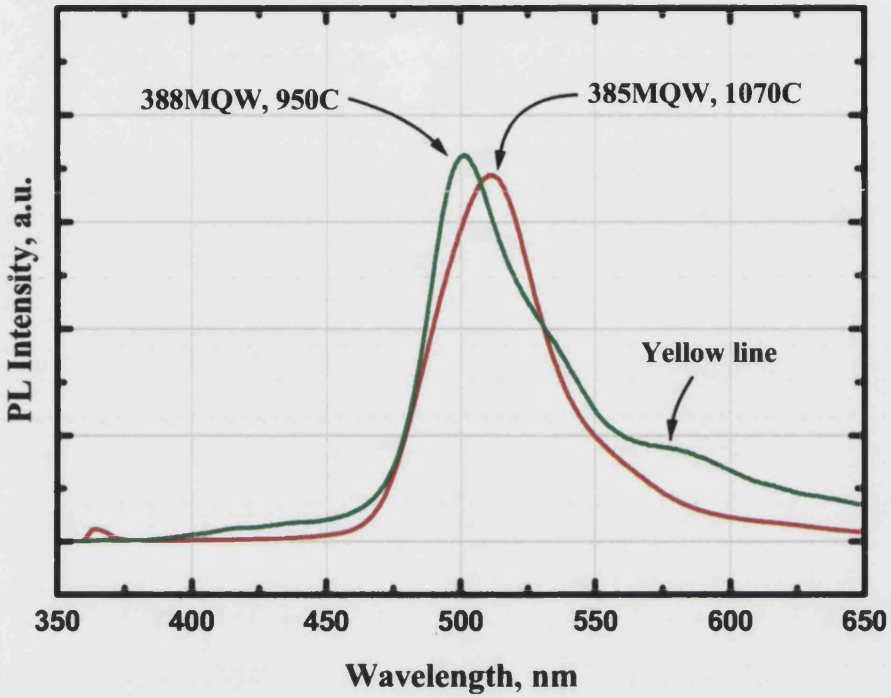

Figure 11.5 PL spectra from two MQW structures with capping layer grown at 1070°C (385MQW) and at 950°C (388MQW). Structure with low temperature capping layer exhibits increased yellow luminescence.

Obviously, a high defect density is not desirable in device applications; therefore, it is difficult to implement this low temperature approach for the growth of real device structures. An additional potential problem arises from the difficulties to grow p-type GaN at reduced temperature.

Another interesting observation is that thicker wells are more easily decomposed. Samples 380MQW and 383MQW have the same nominal In composition in the QWs and in both cases the GaN capping layer growth at 1070°C. The only difference between two samples is the thickness of QWs, which is 15 Å for sample 380MQW and 27 Å for sample 383MQW. As one can see in Figure 11.6 the sample with thicker wells is much darker than the sample with narrow wells, indicating decreased thermal stability for wider wells.

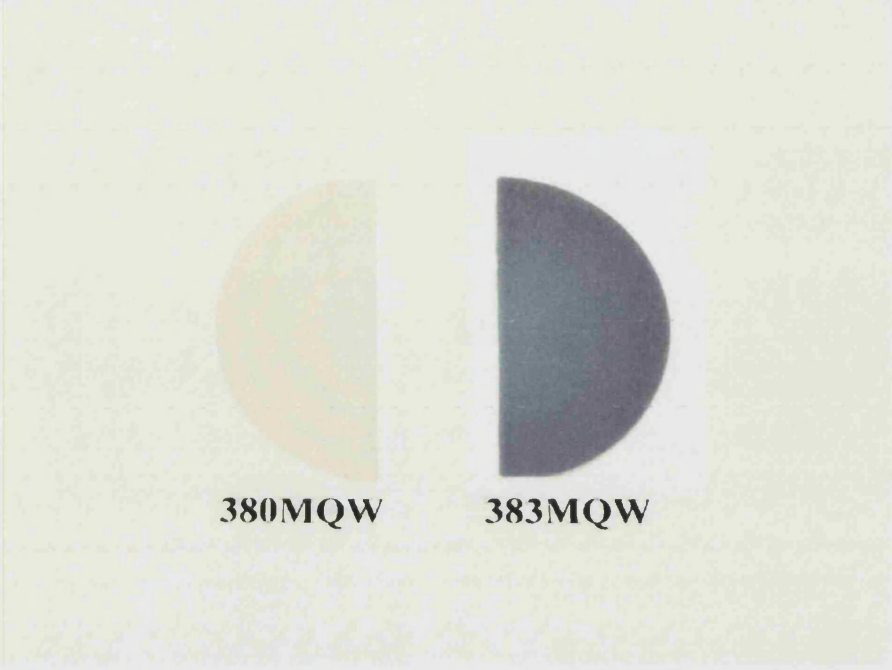

Figure 11.6. Photographs of two MQW structures with capping layer grown at 1070°C. Sample 380MQW has thinner QWs (~15Å) than sample 383MQW (27Å).

A thin AlGaN capping layer above the MQW region is known to prevent decomposition of InGaN [1]. We studied the influence of ~200Å thick AlGaN on stability of MQW experimentally. Samples 418MQW and 420MQW have similar structure, with the exception of the capping layer above MQW. In the case of sample 418MQW, a GaN capping grown at 950°C; sample 420MQW has $Al_xGa_{1-x}N$ capping layer ($x \approx 0.10–0.15$) grown at 950°C. Both samples were transparent and do not show any visual signs of InGaN decompositions. Nevertheless, the luminescence properties of the two samples are very different. Figure 11.7 presents PL spectra from two MQW samples measured under the same conditions. The sample with GaN capping layer exhibits luminescence peak from InGaN/GaN MQW at 454 nm and a broad defect-related yellow luminescence at 500-600 nm. For the sample with AlGaN capping layer the MQW-related PL peak is ~2 times higher and the intensity of yellow emission is significantly reduced. It is interesting to note that despite identical InGaN composition and well widths, the position of MQW-related peak in the sample with AlGaN capping layer is shifted to 470 nm. We explain the longer

wavelength of light emission from the sample with AlGaN capping layer by the reduced decomposition of InGaN.

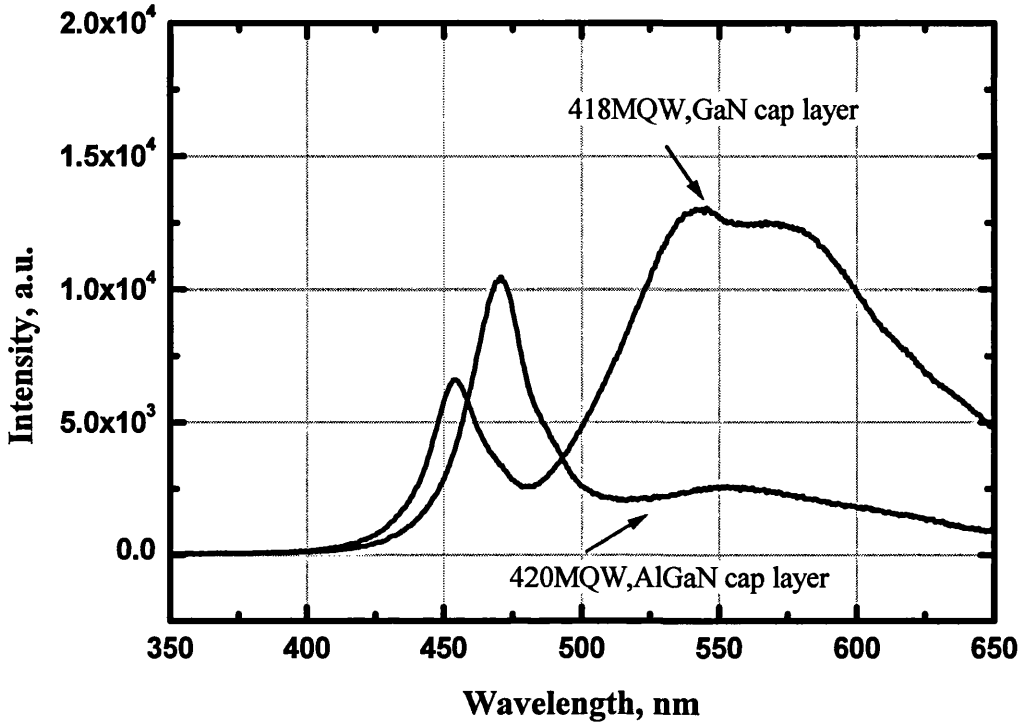

Figure 11.7. PL spectra from two MQW structures with GaN capping layer grown at 950°C (418MQW) and AlGaN capping layer grown at 950°C (420MQW). Structure with AlGaN capping layer exhibits brighter PL from MQW and weaker yellow luminescence.

11.5. Built-in electric fields in InGaN/GaN MQW structures

Many of the unusual optical properties of III-nitride based heterostructures can be consistently explained by considering effects of built-in electric fields. These fields modify the band structure and reduce the effective band gap. Consequently, this red shifts the emission wavelength (quantum confined Stark effect) and the absorption edge (Franz-Keldish effect). Because electron and hole wavefunctions are spatially separated in the electric field, the optical transition probability is reduced and carrier lifetime is increased.

III-nitrides of wurtzite structure have intrinsic spontaneous polarisation, and in addition to that, any strain in the (0001) plane results in piezoelectric polarisation. III-nitrides exhibit unusual properties in respect of polarisation fields. The spontaneous

polarisation (polarisation at zero strain) is very large in III-nitrides. The piezoelectric constants are up to ten times larger in III-nitrides, compared to conventional III-V semiconductors. For these reasons built-in electric fields have a much larger influence on optical properties of III-nitride heterostructures than in other III-V compounds.

In the following we will derive an analytical expression for the electric field in InGaN/GaN quantum well structure. We consider polarizations along the (0001) axis, because this is the direction along which standard epitaxial films and heterostructures are grown. The polarisation field has two components: a strain-independent (spontaneous) built-in polarisation field [2] and a strain induced (piezoelectric) field [3]. They add algebraically and the total polarisation field in the InGaN QW with In content x is given by equation (11.1).

$$P(x) = P^{SP}(x) + P^{PZ}(x) \tag{11.1}$$

The spontaneous polarisation of InGaN can be described by a linear approximation between spontaneous polarisations of GaN and InN.

$$P^{SP}_{InGaN}(x) = -0.032x - 0.029(1-x) \tag{11.2}$$

The piezoelectric component of polarisation is calculated from strain using the piezoelectric coefficients e_{33} and e_{13} as

$$P^{PZ} = e_{33}\varepsilon_z + e_{31}(\varepsilon_x + \varepsilon_y) \tag{11.3}$$

where ε_z is the strain along c-axis ε_x and ε_y are in-plane strain components. Usually InGaN/GaN MQW structures are grown on thick GaN buffer. In this case we can assume that the GaN barriers are unstrained and InGaN wells are pseudomorphically biaxially strained to the GaN barriers.

Table 28. Spontaneous polarization, piezoelectric coefficients, elastic constants, lattice parameters and dielectric constants for InN and GaN

	InN	GaN
Spontaneous polarization P^{SP}, [C/m^2] [4]	-3.2×10^{-2}	-2.9×10^{-2}
Piezoelectric coefficients [5,]:		
e_{33}, [C/m^2]	0.97	0.73
e_{31}, [C/m^2]	-0.57	-0.49
e_{15}, [C/m^2]		-0.3
Elastic constants [6]:		
C_{13}, [GPa]	121	106
C_{33},[GPa]	182	398
Lattice parameters: [7,8]		
a_0,[Å]	3.54	3.189
c_0,[Å]	5.705	5.185
Dielectric constants [9,10]		
ε_{11}	13.1	9.5
ε_{33}	14.4	10.4

In the case of isotropic biaxial stress the following relation between the tensile and lateral strain holds:

$$\varepsilon_z = -2\frac{C_{13}}{C_{33}}\varepsilon_x \tag{11.4}$$

Where C_{13} and C_{33} are the elastic constants of InGaN.

The strain components are given by:

$$\varepsilon_z = (c - c_0)/c_0, \qquad \varepsilon_x = \varepsilon_y = (a - a_0)/a_0 \tag{11.5}$$

Using equations (11.3), (11.4) and (11.5) the amount of piezoelectric polarization in the direction of the c-axis can be determined by

$$P_{InGaN}^{PZ} = 2\frac{a - a_0}{a_0}\left(e_{31} - e_{33}\frac{C_{13}}{C_{33}}\right) \tag{11.6}$$

The a_0 lattice constant of relaxed InGaN follows the Vegard's law (linear approximation between InN and GaN)

$$a_0 = a_0^{(GaN)} \cdot (1 - x) + a_0^{(InN)} \cdot x \tag{11.7}$$

Assuming that the quantum well is pseudomorphically strained to GaN barriers, the a lattice constant of strained InGaN is equal to that of unstrained GaN. Combining everything together we obtain the following expression for the piezoelectric polarisation in the InGaN quantum well.

$$P_{InGaN}^{PZ}(x) = 2\frac{(a_0^{(GaN)} - a_0^{(InN)})x}{a_0^{(GaN)} - (a_0^{(GaN)} - a_0^{(InN)})x}\left(e_{31} - e_{33}\frac{C_{13}}{C_{33}}\right) \tag{11.8}$$

Due to a lack of experimental data on piezoelectric elastic properties of InGaN, we adopt the following set of liner approximations between InN and GaN [4]:

Elastic constants:

$$C_{13}(x) = 121x + 106(1-x), \text{(GPa)} \tag{11.9}$$

$$C_{33}(x) = 182x + 398(1-x), \text{(GPa)} \tag{11.10}$$

Piezoelectric constants:

$$e_{31}(x) = -0.57x - 0.49(1-x), \text{(C/m}^2\text{)} \tag{11.11}$$

$$e_{33}(x) = 0.97x + 0.73(1-x), \text{(C/m}^2\text{)} \tag{11.12}$$

The total polarisation is found as a sum of the spontaneous and piezoelectric components

$$P_{InGaN}(x) = P^{SP}(x) + P^{PZ}(x) \tag{11.13}$$

The electric field in the InGaN quantum well is given by

$$E_{InGaN}(x) = -\frac{P_{InGaN}(x)}{\varepsilon_{InGaN}(x)\varepsilon_0} \tag{11.14}$$

The dependence of electric field in InGaN/GaN QW structure on indium composition of the well is presented in Figure 11.8. Because strain-independent and strain-induced components of the field have opposite signs, the electric field $In_xGa_{1-x}N$ is positive[a] for

[a] By "positive" we mean pointed along [0001] direction. In MOCVD grown structures it is direction from the substrate to the surface.

x<0.17 and negative for x>0.17. For In composition x≈0.17 the two components of the electric field cancel each other.

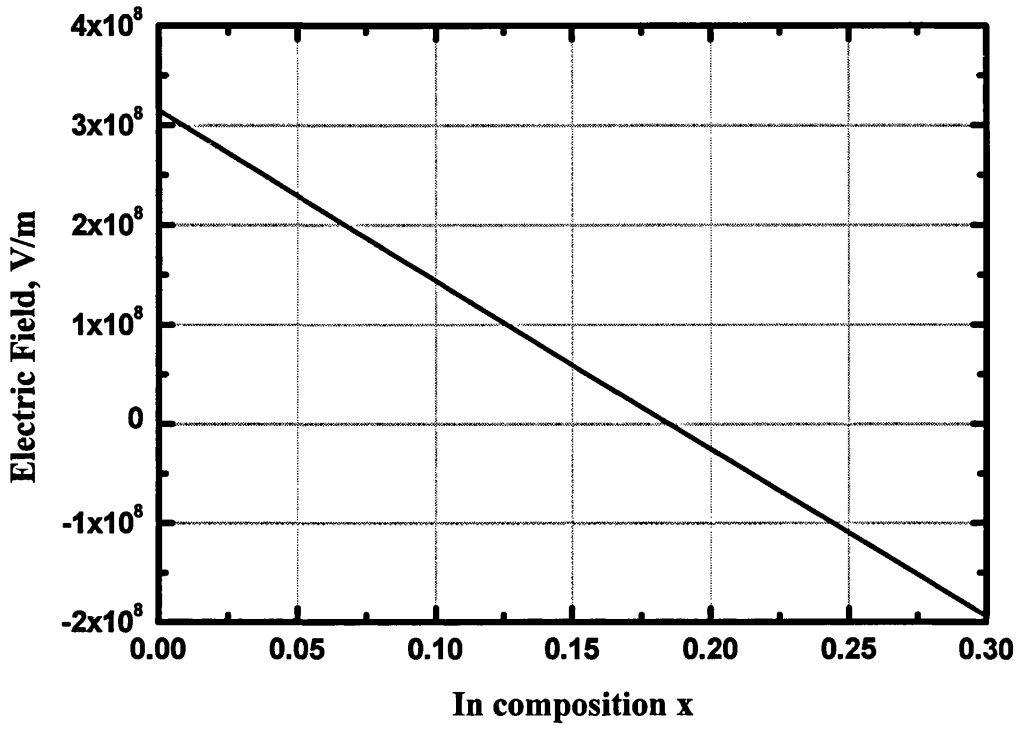

Figure 11.8. Calculated dependence of the built-in electric field in InGaN/GaN QW on indium composition.

11.6. Quantum confined Stark effect and blue shift of PL emission

Among the most significant effects of the piezoelectric field is the alteration of quantum well transition energy due to band bending in the presence of such a strong field. The most striking manifestation band bending in InGaN MQW structures is the quantum confined Stark effect. In the presence of electric field the conduction and valence bands are tilted as shown in Figure 11.9. This, in turn, reduces the effective bandgap of InGaN resulting in redshift of photoluminescence out of InGaN quantum wells.

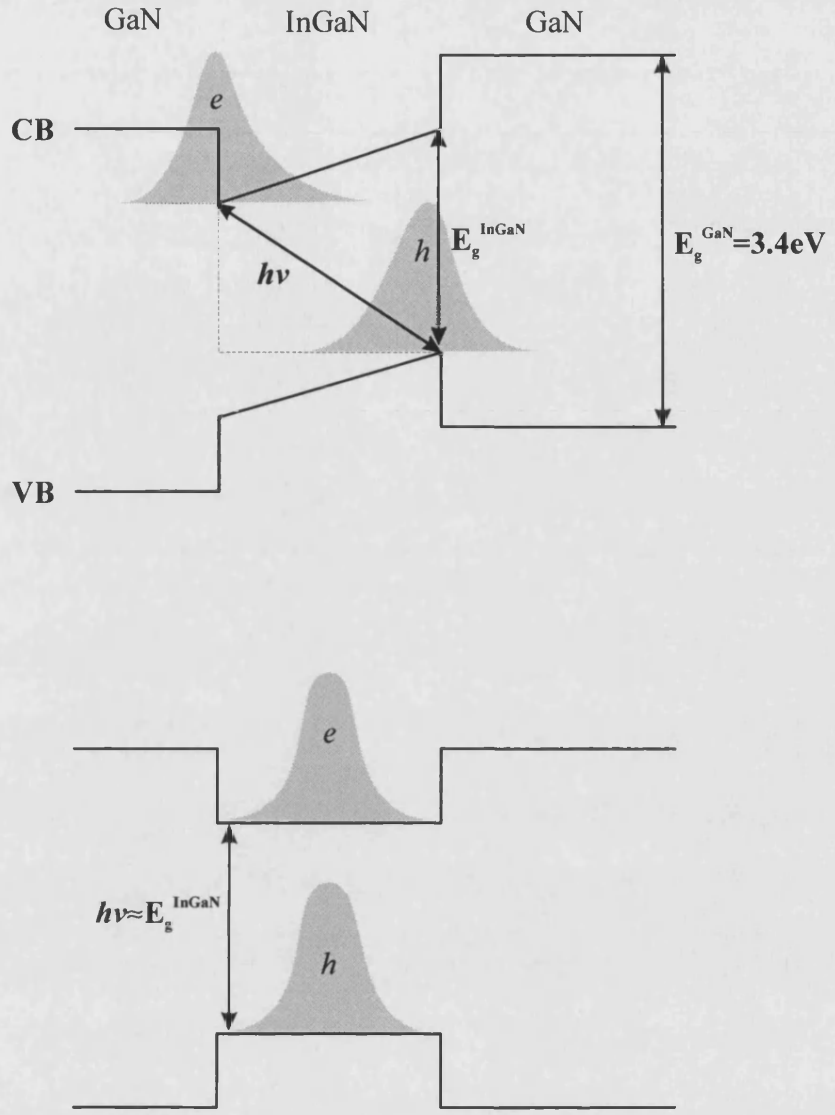

Figure 11.9 Conduction and valence band edges of InGaN/GaN quantum well structure. At low excitation (top) the radiative recombination of an electron and a hole is red-shifted in comparison to the bandgap energy due to the Stark. At high excitation (bottom) the build in electric field is screened by photo generated carriers and the PL peak exhibits a blue shift towards the bandgap energy.

The redshift depends on the width of the QW and the intensity of the electric field. At high excitation densities, the non-equilibrium carriers can reduce the polarization-induced electric fields due to screening effect. Thus, the density of photo-exited or injected electron-hole pairs has to be considered in a detailed analysis of polarization-related effects. In the first order approximation, the screening of the electric field can be expressed by

$$E(n) \approx E_0 - \frac{ned}{\varepsilon\varepsilon_0} \tag{11.15}$$

Where n is the free carrier density, E_0 is the maximum field strength given by equation (11.14), ε is the dielectric constant and d is the width of the quantum well.

Now we analyse the influence of non-equilibrium carriers on the energy of optical transitions in InGaN QW using a triangular well model. For an idealised case, neglecting thermal distribution in the bands, the emitted quantum energy hv for band-to-band recombination in a quantum well in the presence of non-equilibrium electron–hole pair density n can be expressed as [11]

$$hv = E_g(n) - edE(n) + E_e(n) + E_h(n) \tag{11.16}$$

Here, $E_g(n)$ is the carrier-density-dependent forbidden gap, which can be expressed as

$$E_g(n) = E_g(0) - \beta n^{\frac{1}{3}} \tag{11.17}$$

With β=2×10^{-8} eV/cm. E_e and E_h are positions of the lowest-energy levels in the triangular quantum well for electrons and holes, respectively, and can be calculated from

$$E_{e,h}(n) = \left(\frac{\hbar^2}{2m_{e,h}}\right)^{\frac{1}{3}} \left(\frac{9\pi eE(n)}{8}\right)^{\frac{2}{3}} \tag{11.18}$$

Assuming the square-law recombination, the density of photo-excited carrier can be described as a function of the pumping density

$$n = \sqrt{\frac{P\alpha}{hv\gamma}} \tag{11.19}$$

where P is the excitation power density, hv is the energy of the excitation light, α is the absorption coefficient for the excitation wavelength and has been taken as 1.5×10^5 cm^{-1}, and γ is the square-law recombination coefficient and has been taken as 4.8×10^{-11} cm^{3}s^{-1}.

Now, using equations (11.15), (11.16), (11.17), (11.18), (11.19) we can calculate the dependence of the PL line position on the excitation density (see Figure 11.10). For these calculations we assume $In_{0.1}Ga_{0.9}N/GaN$ QW structure with unstrained barriers and QW pseudomorphically strained to GaN. In this case the built-in electric field in the QW is given by equation (11.14) (see Figure 11.10)

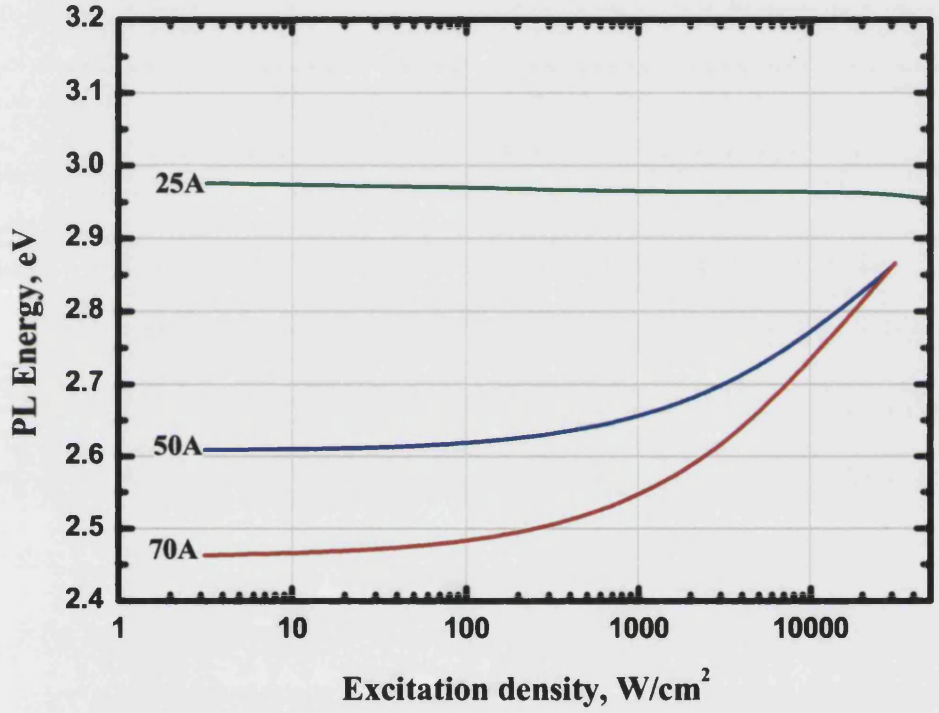

Figure 11.10 Calculated PL energy shift for $In_{0.1}Ga_{0.9}N/GaN$ in the quantum wells of different widths.

The most interesting observation here is that the shift the PL peak positions strongly depends on the width of the quantum well. For narrow wells (below 25 Å) the Stark shift is negligible, whilst for wider wells (50 Å and 70 Å) the Stark shift is quite large.

This phenomenon can be used for the express control of the quantum well thickness. Measuring two PL spectra at low and high excitation densities and comparing the positions of PL peaks one can immediately draw qualitative conclusions on quantum well thickness.

According to empirical observations, the wavelength shift smaller than 10 nm implies quantum well thickness less than 25 Å. If the position of the PL peak shifts considerably with increasing excitation power density, the quantum well must be thick (>50 Å).

For example, we compare PL spectra from two MQW samples measured at low (unfocused He-Cd laser) and high (focused He-Cd laser) excitation densities. The excitation power density was <10W/cm^2 and >1kW/cm^2, respectively. Both samples have the same nominal indium composition; however PL emission from the sample 433MQW has longer wavelength than that of the sample 425MQW. The dependence of PL on excitations density for two samples is also quite different. Sample 425MQW exhibits significant shift (~18nm) of the PL peak position, suggesting wide quantum well. On the contrary, the shift for sample 433MQW is much smaller (~5 nm), indicating reasonably narrow quantum well. These results are in good agreement with the quantum well width measured by XRD and estimated from the growth rate, which give well thickness of 25 Å for sample 433MQW and 50 Å for sample 425MQW.

More accurate analysis of the dependence of the PL peak position on excitation power density allows us to get more quantitative information on quantum well thickness, composition and the strength of internal electric field. Figure 11.12 depicts PL spectra from InGaN/GaN quantum well measured at excitation density varying from 3 W/cm^2 to 3.3MW/cm^2. The PL emission exhibits a very strong blue shift with increasing excitation power density.

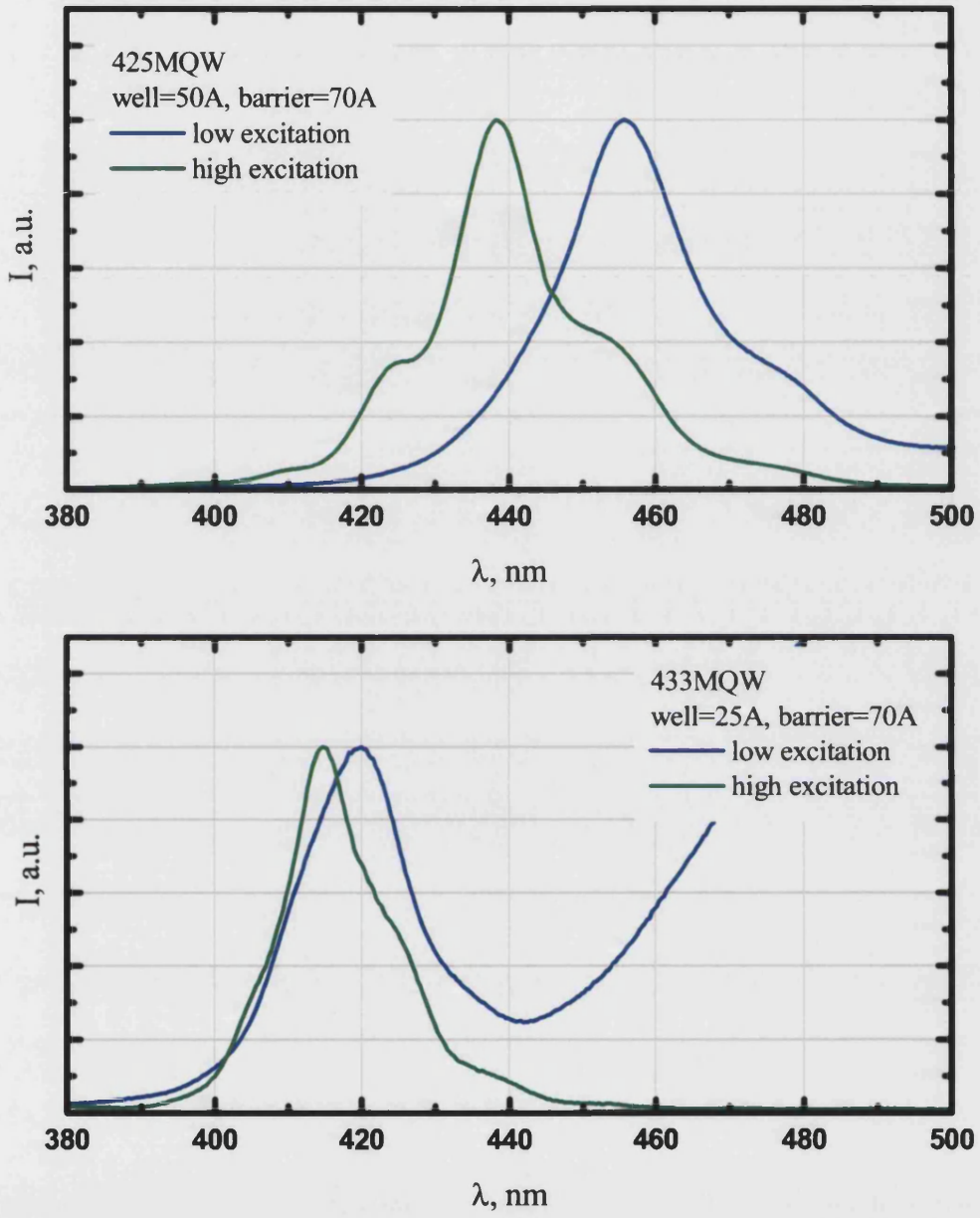

Figure 11.11. PL spectra at low (<10W/cm^2) and high (>1kW/cm^2) excitation densities. The PL emission for the sample with wider quantum wells is red-shifted due to quantum confined Stark effect. Also, the sample with wider quantum wells exhibit larger shift of the PL peak position with increasing excitation density.

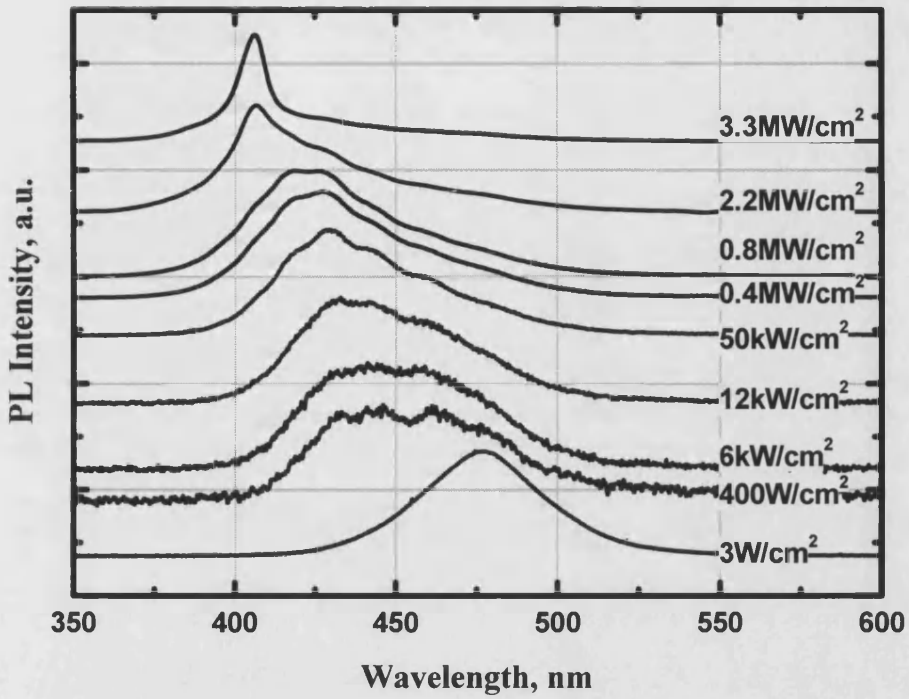

Figure 11.12. PL spectra from InGaN/GaN MQW at different excitation densities.

The positions of the PL peak versus excitation power density are presented in Figure 11.13. The continuous line represents the best fit of the Eq (11.16) to the experimental data. The fitting parameters were the well width d, the strength of the built-in electric field E_0, and the bandgap energy of InGaN $E_g(0)$. The following combination of the parameters gives the best conformity between experimental points and theoretical model:

$$d = 50 \text{ Å}$$

$$E_0 = 1.5 \times 10^8 \text{ V/m}$$

$$E_g(0) = 2.8 \text{ eV}$$

These values are in good agreement with results of the x-ray diffraction analysis.

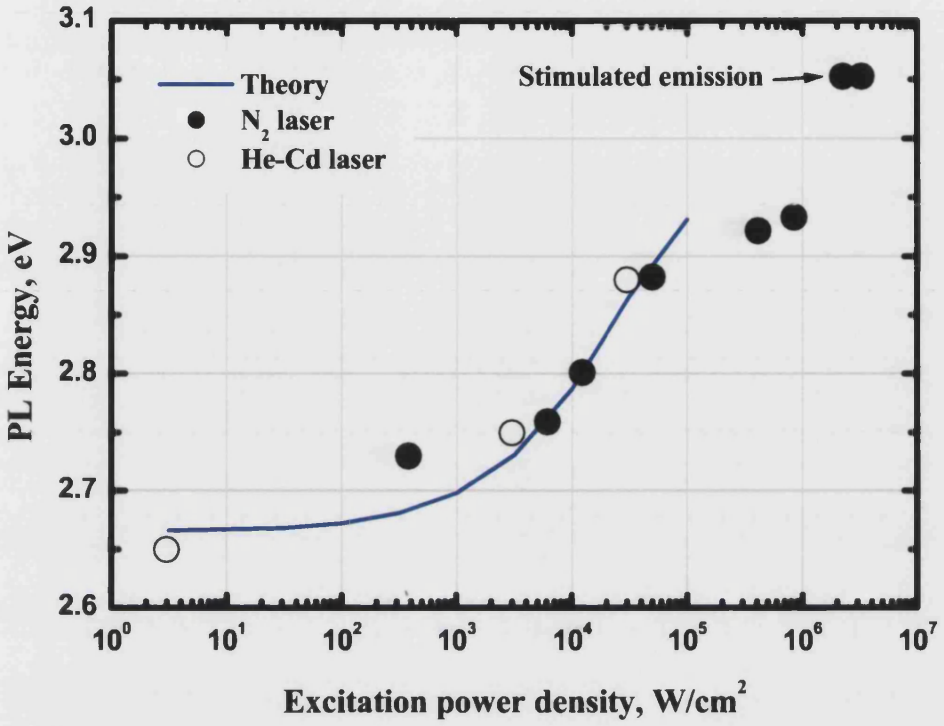

Figure 11.13 Photoluminescence peak position dependences on excitation power density in InGaN/GaN MQW. Open circles correspond to He–Cd laser excitation, and the filled ones correspond to N_2 laser pulsed excitation. The continuous line demonstrates the theoretical dependence of the emission on excitation power density.

11.7. Summary

In summary, we have successfully grown InGaN/GaN MQW structures. Different growth regimes were compared. According to our experimental results, high-temperature growth results in superior quality of MQW structures. However, the high-temperature growth regime is more difficult to control, which leads to larger variation of PL emission wavelength and PL intensity. The influence of growth conditions and various capping layers on the stability of the MQW structures has been studied. The best results were achieved when using a thin AlGaN capping layer on top of MQW structure. Also we analysed the effect of built-in electric fields on the PL properties of the MQW structures. Experimental results are in good agreement with the theoretical model. In addition we have

demonstrated that the dependence of PL peak position on excitation power density can be used for express characterisation of MQW structures.

11.8. References

1. S. Nakamura and G. Fasol, The Blue Laser Diode, Springer, Berlin, (1997)
2. F. Bernardini and V. Fiorentini, Phys. Rev. B, 56 10024
3. A. Bykhovski, B. Gelmont, and M.S. Shur, J.Appl. Phys. 74, 6734
4. O Ambacher, J. Phys. D: Appl. Phys. 31 (1998) 2653–2710.
5. Bernardini, F., Fiorentini V., Vanderbilt D.,. Phys. Rev. B 56 (1997), R10024-R10027.
6. Wright, A.F., J. Appl. Phys. 82 (1997), 2833-2839.
7. Pichugin, I.G., Tiachala, M. Izv. Akad. Nauk SSSR, Neorg. Mater. 14 (1978) 175
8. Zubrilov A. in Properties of Advanced SemiconductorMaterials GaN, AlN, InN, BN, SiC, SiGe . Eds. Levinshtein M.E., Rumyantsev S.L., Shur M.S., John Wiley & Sons, Inc., New York, 2001, 49-66
9. Davydov, V.Yu., Emtsev V.V., Goncharuk A.N., Smirnov A.N., Petrikov V.D., Mamutin V.V., Vekshin V.A., Ivanov S.V., Smirnov M.B. and Inushima T., Appl. Phys. Lett 75 (1999), 3297-3299
10. Barker, A.S., Ilegems, M., , Phys. Rev. B 7 (1973) 743
11. E. Kuokstis, J. W. Yang, G. Simin, M. Asif Khan, R. Gaska, M. S. Shur, Appl. Phys. Lett.,. 80, 977 (2002)

12. InGaN light emitting diodes

12.1. Introduction

Blue and green GaN light emitting devices (LED) have been commercially available now for some years. GaN-based *pn* homojunction LEDs have been demonstrated by many authors [1,2,3]. The emitting wavelength of pn-structures having GaN as the active region as determined by doping and ranged from 369 to 460 nm. The emission spectra is rather broad (FWHM=70 nm).

In double heterostructure light emitting diodes (DHLEDs), the active region is made of material with narrower band gap than that of the cladding layers. The two major benefits of heterostructure LEDs are the increased minority carrier injection efficiency and the ability to use wide-gap material for cladding layers. The wide-bandgap layers are transparent to the emitted light and, therefore, do not contribute to the photon re-absorption. The energy gap differences also minimise the effect of the doping level on the injection efficiency, which dominated the homojunction LED efficiency. The emission wavelength can be easily tuned by changing the bandgap of the active region.

First InGaN/GaN DH LEDs have been fabricated by Nakamura [4]. The peak wavelength was 420 nm and the FWHM of the peak emission was 25 nm. The output power of DH LEDs was 90 μW at 20 mA. In order to improve the output power and quantum efficiency, Zn- and Si-co-doping of the active region has been employed [5]. High brightness blue InGaN/AlGaN LEDs with output power of 3 mW at 20 mA have been produced. The peak wavelength and the FWHM of the EL of blue LEDs were 450 nm and 70 nm, respectively. The first candela-class blue LEDs were fabricated by Mukai [6] using a double-heterostructure structure with Zn-doped InGaN active layer. Because a higher In content in the InGaN layer causes a decrease of the luminescence intensity,

InGaN with a relatively low In content was used. To obtain blue emission, Zn doped InGaN layers were used as the active layer.

The longest peak wavelength of the electroluminescence of DHLEDs achieved is 500 nm. The crystal quality of the InGaN active layer of DHLEDs becomes poor with further increase of the indium mole fraction. When the InGaN active layer becomes thin, the elastic strain is not relieved by the formation of misfit dislocations and the crystal quality of the InGaN active layer improves. Although, double-heterostructure LEDs produce a high-power light output in the blue and blue-green regions, they have a broad emission spectrum. This broad spectrum, which results from the intentional introduction of the impurity levels into the active region of the device to produce a deep-level emission, makes the output appear whitish-blue. More narrow emission is desired for applications such as full-colour LED displays

The quantum well (QW) LED is a special class of heterojunction LED in which the thickness of the active region is less than the deBroglie wavelength and discrete energy levels for holes and electrons arise due to the wave-particle nature of the electron and hole. High power InGaN single QW LEDs have been fabricated by Nakamura [7,8]. The output power was 3 mW for green (520 nm) LEDs and 5.6 mW for blue (450 nm) LEDs. The number of QWs in the active region can be increased to 3-10 to improve the quantum efficiency. Nowadays, high brightness MQW LEDs with light output exceeding 15 mW are available commercially.

12.2. Growth procedure

LED structures were grown by low-pressure MOCVD on sapphire substrates. Typical LED structure comprises the following layers: low-temperature nucleation layer, undoped GaN buffer (2–4 μm), n-type Si-doped GaN layer (1.5-2 μm), InGaN/GaN MQW active region (25 Å/100 Å, 1-5 pairs), optional AlGaN:Mg capping layer (~200 Å), p-type

Mg-doped GaN (0.1–0.5 μm). The electron and hole concentration in the GaN:Si and GaN:Mg layers were about 3×10^{18} cm^{-3} and 4×10^{17} cm^{-3}, respectively. The structure layout is presented in Figure 12.1

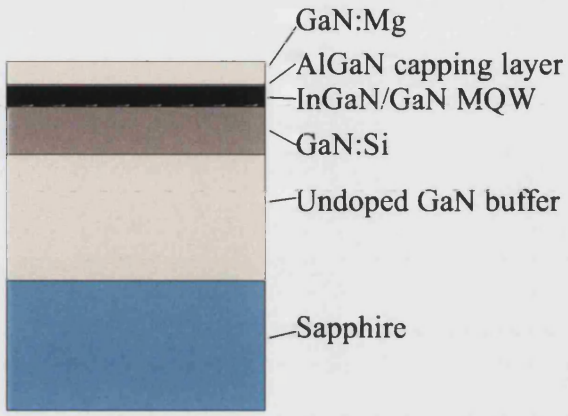

Figure 12.1. Layout of a typical LED structure

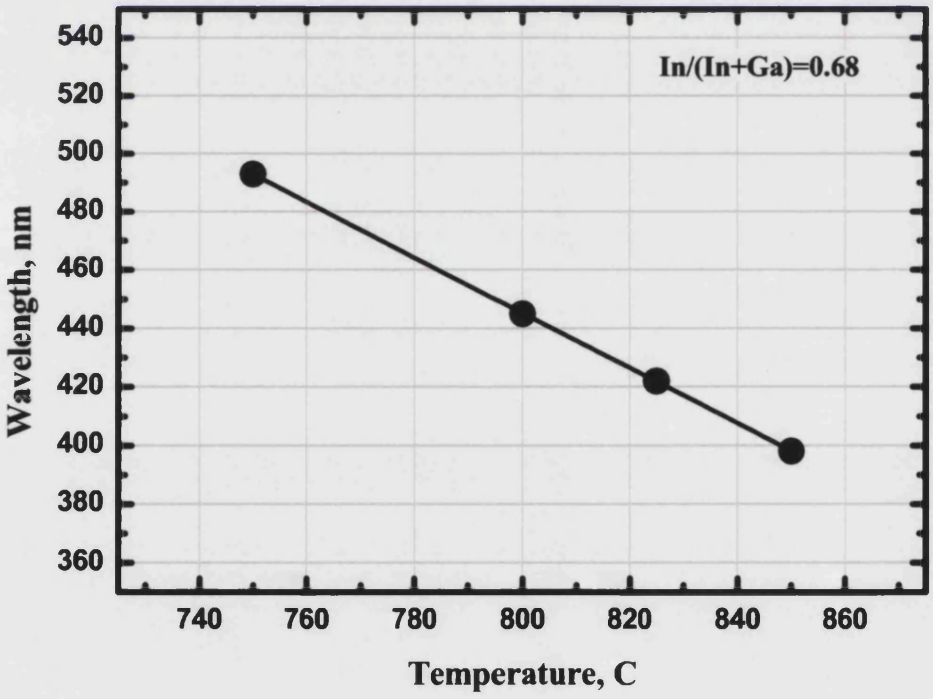

Figure 12.2. Electroluminescence emission wavelength versus growth temperature.

The active region was grown under nitrogen using high input concentration of TMIn (In/(In+Ga)=0.68) The emission wavelength was adjusted from 390nm to 500nm by variation of the growth temperature (see Figure 12.2).

12.3. Decomposition of the active region

As we have mentioned earlier, InGaN layers can spontaneously decompose during the growth of subsequent layers at high temperature. Therefore it is not surprising that the emission wavelength of LED structures depends not only on the growth conditions of the MQW region, but also on the growth conditions of the layers above quantum well. Structures 154ELT and 155ELT were grown under the same conditions with only difference in the growth temperature of the p-type barrier. In 155ELT it was reduced from 1070°C to 1000°C. The emission wavelengths of the two structures are 470 nm and 530 nm, respectively. We explain this effect by InGaN decomposition during the growth of the p-type layer.

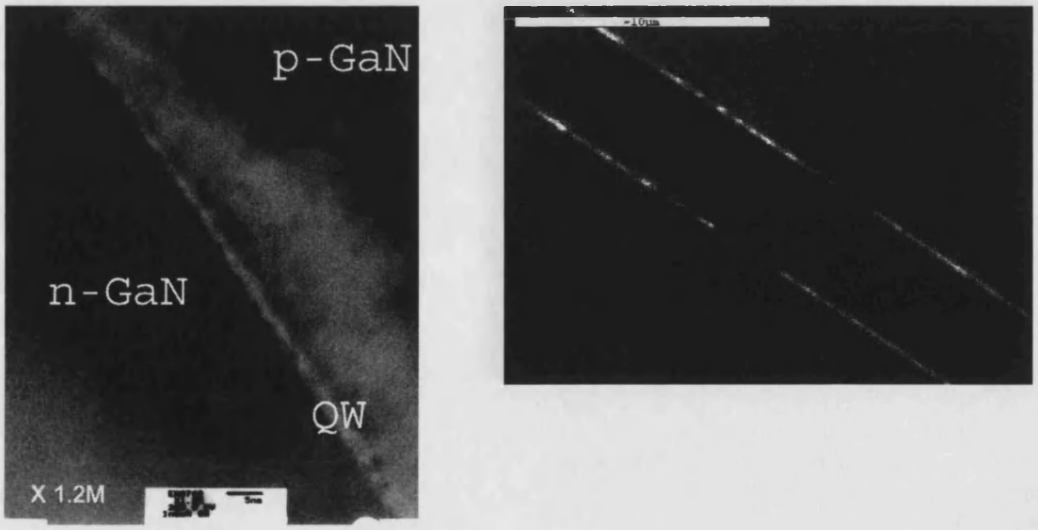

Figure 12.3. TEM micrograph of SQW LED structure (left); Microcathodoluminescence image of the active region (right)

The TEM measurements of SQW LED structures (Figure 12.3, left) revealed that the interfaces of the QW were different. The n-type interface was abrupt, while p-type interface was smeared. Microcathodoluminescence of the SQW structure is presented in

Figure 12.3, right. About 50% of the QW is dark, this indicates high level of defects causing non-radiative recombination and, possibly, partial decomposition of the InGaN layer.

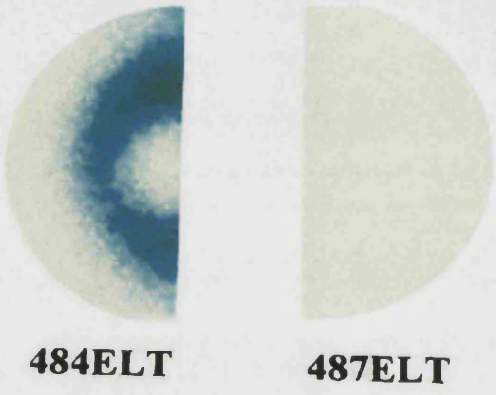

Figure 12.4 Photograph of two LED structures grown with (487ELT, right) and without (484ELT, left) AlGaN protective layer.

As we already discussed in Chapter 11, thin AlGaN capping layer above MQW region prevents decomposition of InGaN. We have used the same approach for LED structures. Some of the LED structures were grown with a thin (30–300 Å) AlGaN layer above the active region. The layer was doped with Mg and the hole density estimated from the calibration runs was in the beginning of 10^{17} cm^{-3} range. The Al composition in the AlGaN capping layer was varied from 0 to 35%. Figure 12.4 present the photograph of two LED wafers grown with and without AlGaN capping layer. Structure without AlGaN layer has dark colour, indicating partial decomposition of InGaN. In contrast, structure with AlGaN layer is transparent and exhibits brighter electroluminescence.

It should be mentioned, that in LED structures AlGaN layer also plays another important role. It acts as a blocking layer preventing electron overflow to the p-contact. Therefore, the efficiency of electron injection into quantum wells is improved.

We have studied the influence of composition and thickness of AlGaN capping layer on the efficiency of electroluminescence.

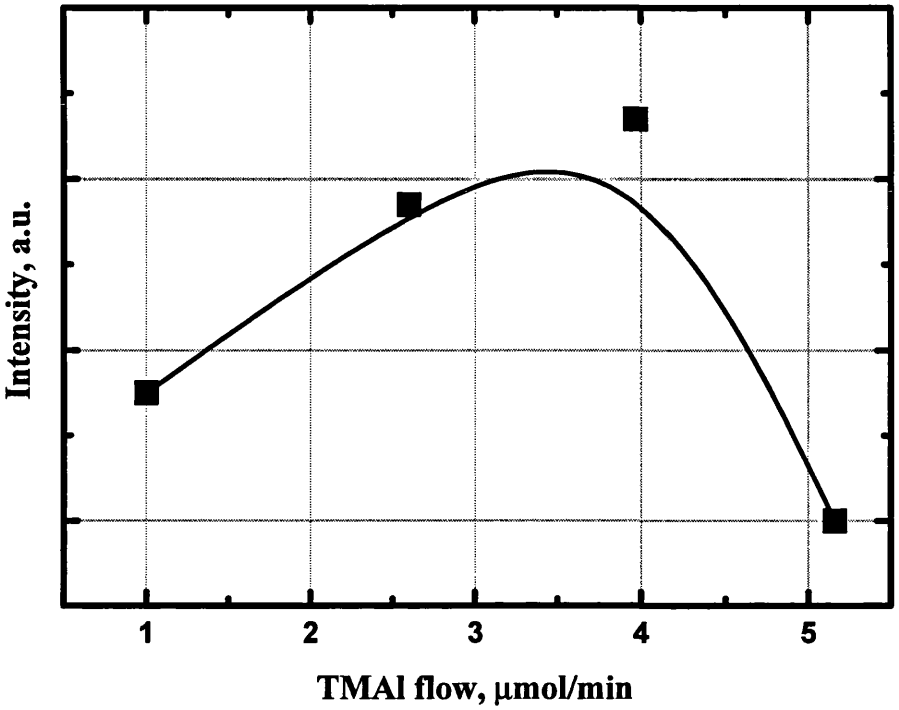

Figure 12.5. Intensity of electroluminescence versus TMAl flow during growth of AlGaN capping layer

Figure 12.5 presents the dependence of the EL intensity on the flow of TMAl during the growth of AlGaN capping layer with the TMGa flow being kept constant. The thickness of AlGaN layer was about 200 Å. As one can see, the EL intensity is increasing up to TMAl flow of 4 μmol/min and after that decays dramatically. Optimum concentration of Al measured by high resolution x-ray diffraction is about 20–25%.

Figure 12.6 shows the dependence of EL intensity on thickness of AlGaN capping layer. Again, brightness is increasing up to optimum thickness of 160 Å and decays rapidly with further increase of AlGaN thickness.

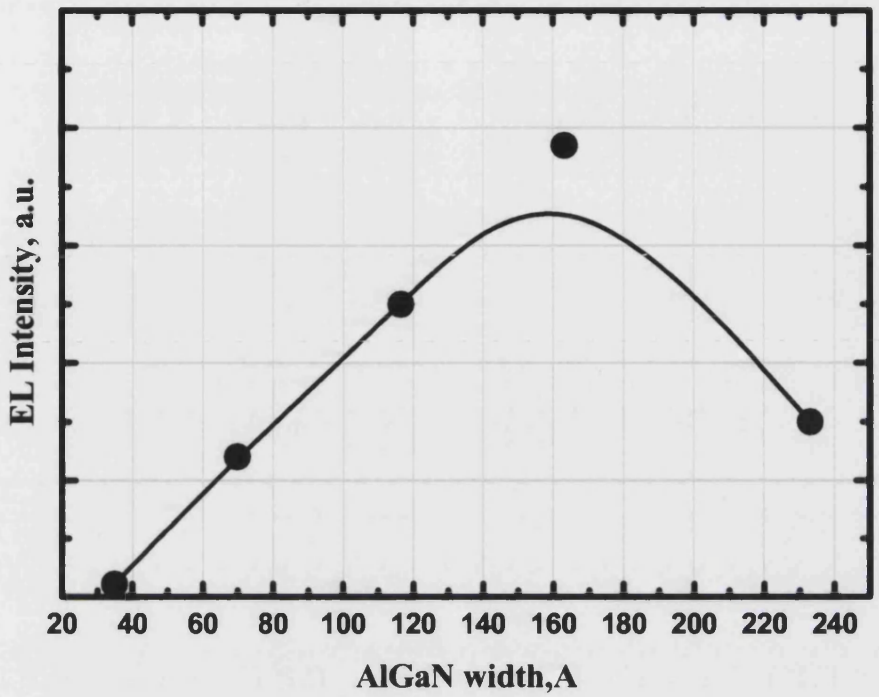

Figure 12.6. Intensity of electroluminescence versus thickness of AlGaN capping layer. Aluminium composition for all samples is about 25%.

Such behaviour can be explained by the relaxation of AlGaN with thickness or composition exceeding a certain critical value.

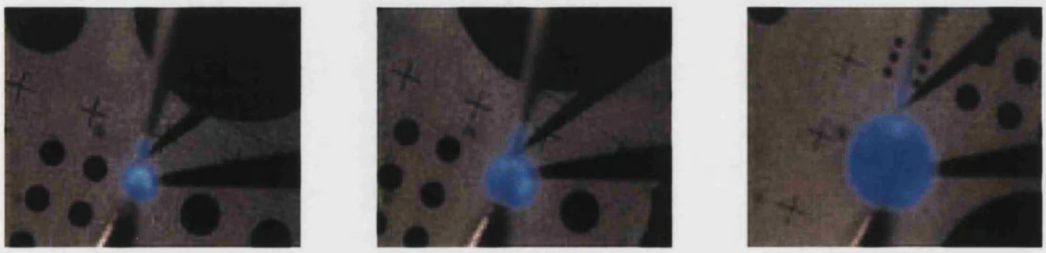

∅300 μm ∅500 μm ∅1000 μm

Figure 12.7 Blue light emission from circular mesa structures formed on LED wafer by plasma etching

Figure 12.8 Blue light emission from LED chip at driving currents of 1 mA (left), 5 mA (middle) and 20 mA (right). Chip dimensions are 300×300 μm.

Figure 12.7 shows test LED structures fabricated for the LED wafer grown in our laboratory. Circular mesas of different diameter were formed by the Reactive Ion Etching, after that p- and n-contacts were deposited by e-beam sputtering. The diameters of the mesas were varied from 30 μm to 3000 μm. This allows electrical characterisation of LEDs over a wide range of current densities.

Figure 12.8 show an industrial type of LED chip. The dimensions of the chip are 330×330 μm^2. The output optical power measured by Si photodetector was in excess of 5 mW at driving current if 20 mA (see Figure 12.9). The saturation of the optical power at high driving currents is likely to be caused by inefficient heat dissipation and overheating of the device.

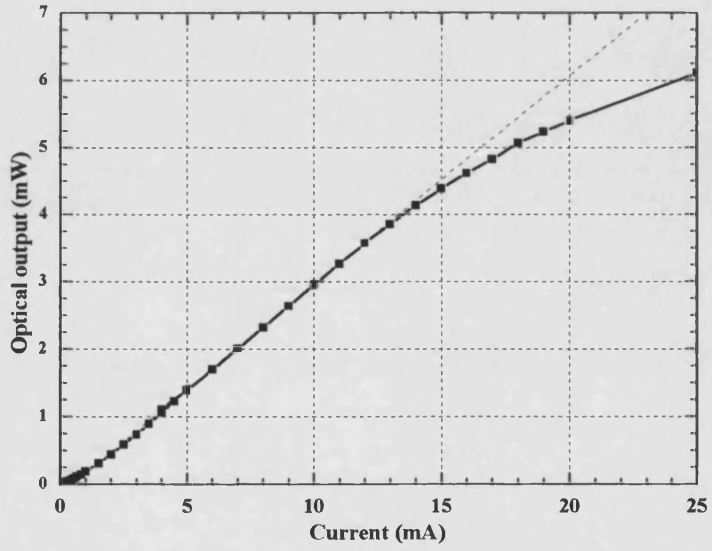

Figure 12.9 Output optical power of the InGaN LED versus driving current

Current-voltage characteristics of fabricated InGaN LEDs are shown in Figure 12.10

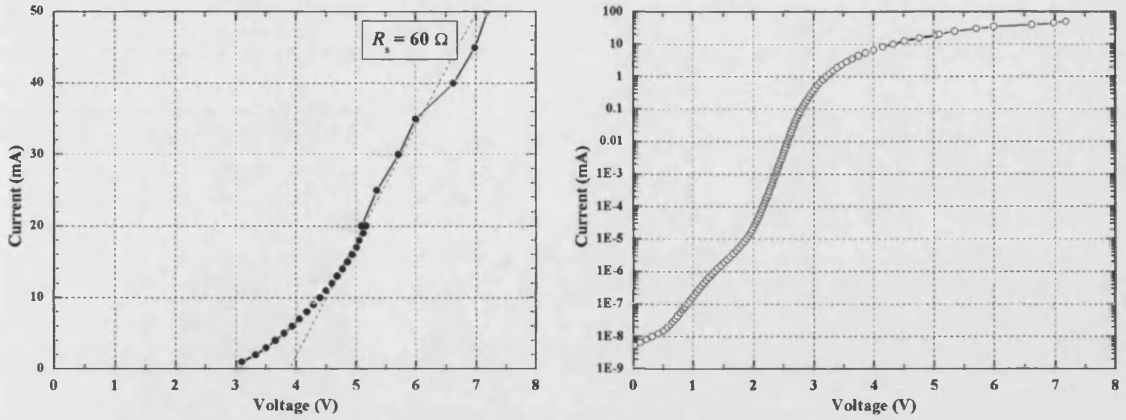

Figure 12.10 Forward current voltage characteristics of the LED chip.

12.4. Big chip[a]

III-nitride based light emitting diodes have wide applications in solid-state lighting technology. The idea is to replace conventional incandescent or fluorescent lamps by more reliable and compact semiconductor light sources – LED lamps.

The main problem of conventional LED-lamp problem is the very low light power of a single LED (about 10 mW of output light) as compared to fluorescent lamps (about 10 W of output light) at comparable efficiencies (about 10%). Therefore, there is 1000 times difference in the output light from these sources.

Maximal current through single LED is limited by quantum efficiency which is decreasing at high current densities (see Figure 12.11). Ideally, the optimum current density should be increased to about 100 A/cm^2. However this is a long term task, which requires a major breakthrough in the growth technology. Therefore, we propose to increase light output using a larger area chip design.

In the case of big chips with $S = 0.1$ cm^2, it is difficult to provide satisfactory current spreading by fabricating device with monolithically deposited p-contact and n-contact fabricated laterally of the light-emitting area. Therefore, we used a so-called interdigitated

[a] Postgrowth operations performed at the Ioffe Institute, St.Petersburg, Russia

contact pattern consisting of a number of connected stripes (fingers). The layout of the contact net is presented in Figure 12.12 (left) and Figure 12.13.

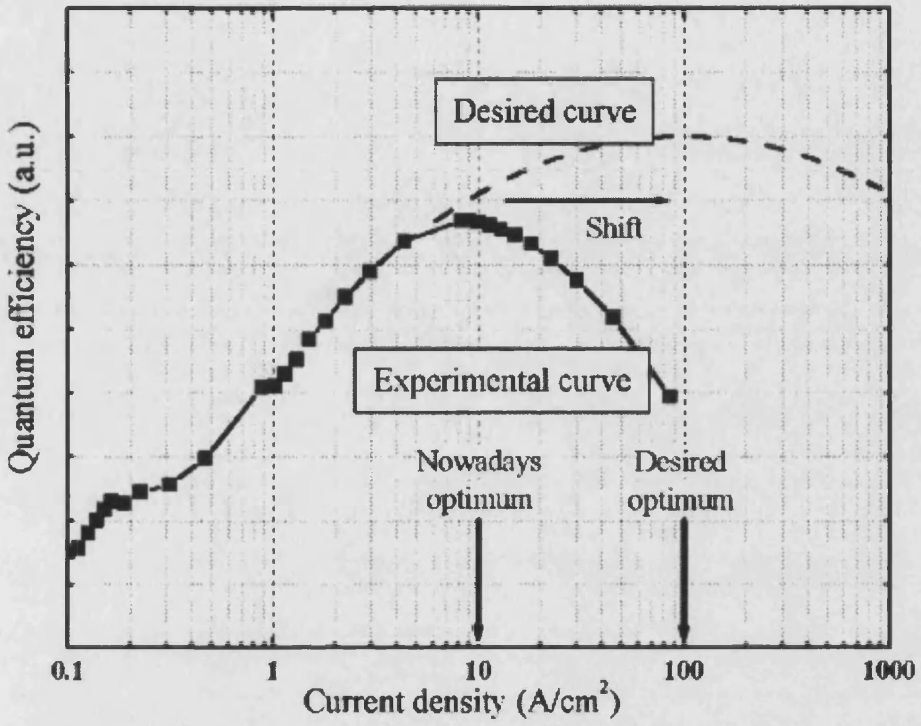

Figure 12.11. LED quantum efficiency versus current density[a]

Several big chips were fabricated on two LED wafers with MQW active region. The wafers light-emission wavelength was about 410 nm (violet light). A mesa structure was defined by reactive ion etching. The p-type contact was formed by deposition of semitransparent Ni/Au (30 nm/30 nm) film on the top of the mesa. Afterwards the p-type contact was strengthened by deposition of Ni (0.1 μm). The n-type contact was formed by deposition of Al (0.1 μm) and strengthened by deposition of Cr (0.1 μm). The sidewalls of the mesa were passivated by SiO_2.

[a] Measured at the Ioffe Institute, St.Petersburg, Russia by Dr V.Bougrov

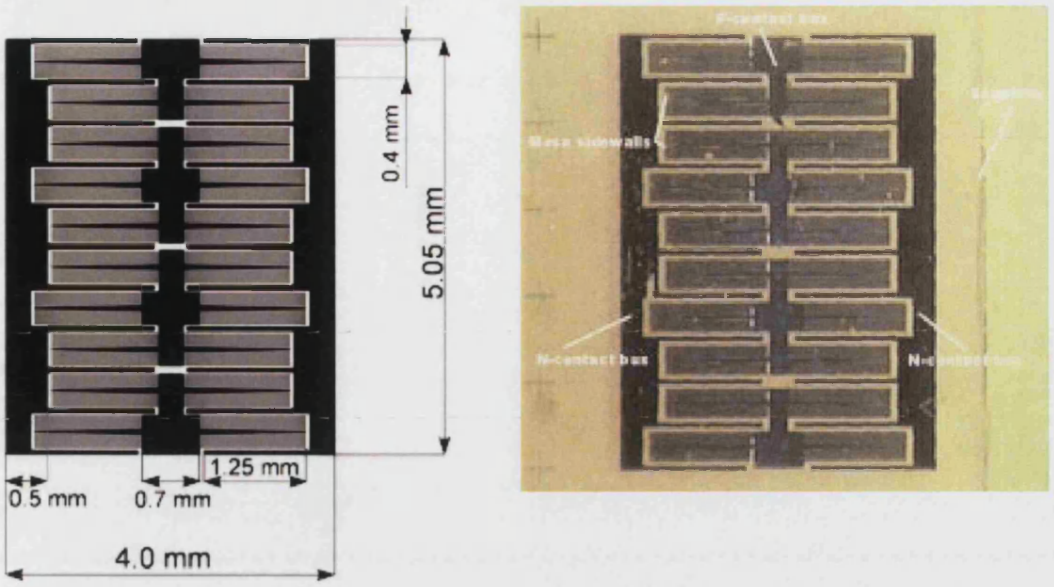

Figure 12.12. Drawing (left) and photograph (right) of a big chip.

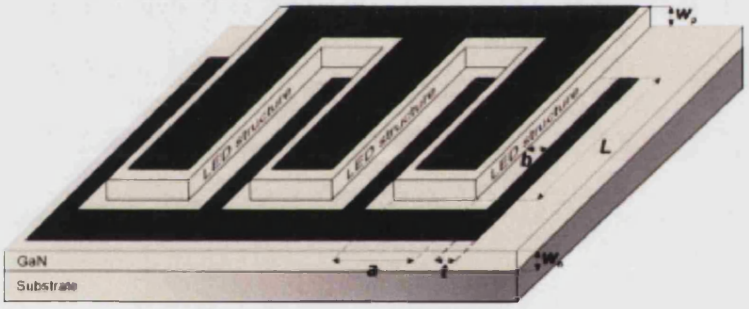

Figure 12.13 Interdigitated contact pattern.

Figure 12.14 demonstrates successful operation of a big chip at current of 2 A. The IV curve for a big chip is presented in Figure 12.15.

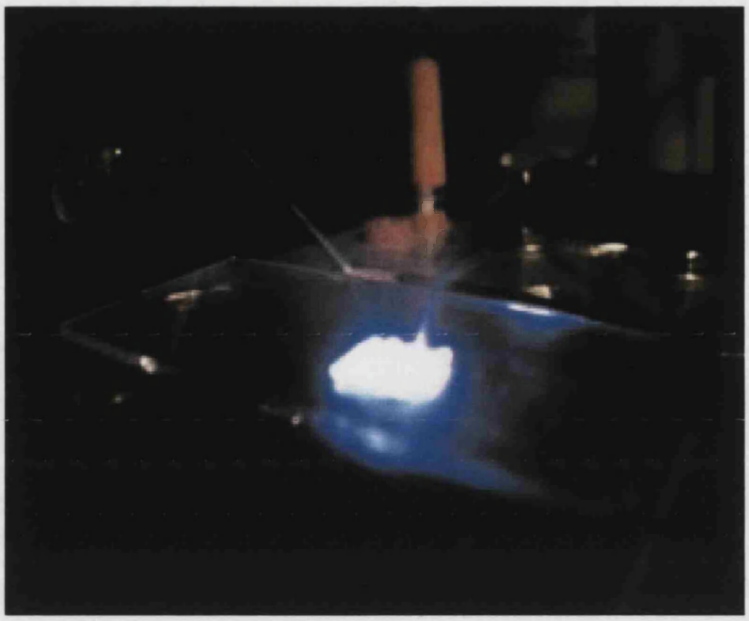

Figure 12.14. Operation of the big chips at current of 2 A

As one can see, the differential resistance of measured at the linear part of the IV curve is about 1.5 Ω.

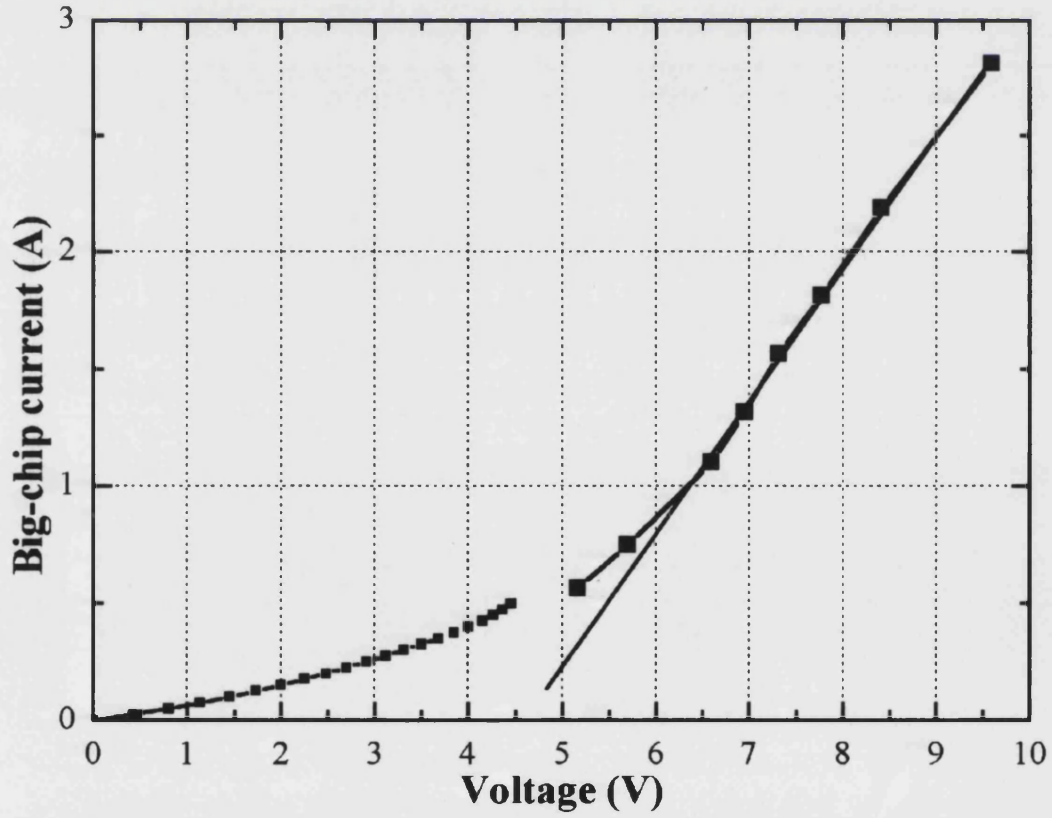

Figure 12.15. I-V characteristic of a big chip

12.5. Summary

We demonstrated successful growth of III-nitride based LED structures emitting in the range 390-500nm. The problem of thermal decomposition of InGaN in the active region has been studied. It was shown, that thin AlGaN capping layer above active region effectively prevents decomposition of the MQWs and improves efficiency of the devices. According to our experiments the optimum thickness of AlGaN layer is about 150-200 Å and Al content is about 20-25%. Finally, we have fabricated large area light emitting diodes with operational current of 2 A.

12.6. References

1. H. Amano, M. Kito, K. Hiramatsu, and I. Akasaki, Jpn. J. Appl. Phys. 28, L2112 (1989).
2. S. Nakamura, T. Mukai, and M. Senoh, Jpn. J. Appl. Phys. 30, L1998 (1991).
3. B. Goldenberg, J. D. Zook, and R. J. Ulmer, Appl. Phys. Lett. 62, 381 (1993)
4. S. Nakamura, M. Senoh, T. Mukai, Appl. Phys. Lett. 62, 2390 (1993)
5. S. Nakamura, M. Senoh, T. Mukai, Appl. Phys. Lett. 64, 1687 (1994)
6. T Mukai, S Nagahama, N Iwasa, M Senoh , T Yamada, J. Phys.: Condens. Matter 13, 7089, (2001)
7. S. Nakamura, M. Senoh, N. Iwasa, S. Nagahama, T. Yamada, T. Mukai, Jpn. J. Appl. Phys., 34, L1332 (1995).
8. S. Nakamura, M. Senoh, N. Iwasa, S. Nagahama, Jpn. J. Appl. Phys., 34, L797 (1995).

13. Laser structures for optical pumping

13.1. Introduction

During last decade, the main focus of III-V nitride research was the realization of a reliable and cheap LD, which would be the shortest-wavelength semiconductor laser ever demonstrated [1]. Optically pumped III-nitride laser structures have been demonstrated by Schmidt *et al* [2]

In this chapter, we report on successful optical pumping of MQW InGaN/GaN/AlGaN laser structures.

13.2. Experiment

Laser wafers were grown by the low-pressure MOCVD on sapphire substrates. The growth sequence included the deposition of GaN buffer layer, AlGaN cladding layer, GaN bottom waveguide layer, MQW region, AlGaN capping clayer and GaN top waveguide layer (see Figure 13.1). The structure parameters of the samples under study are presented in Table 29.

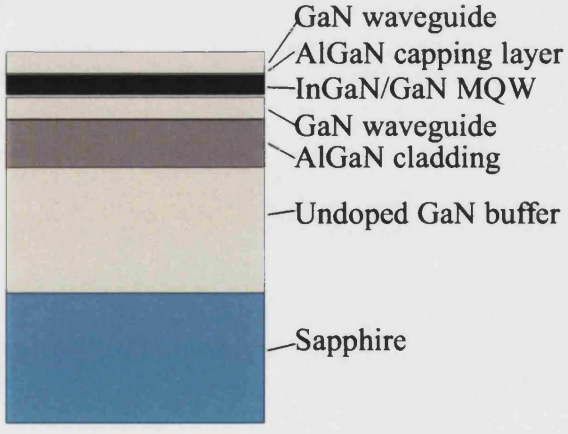

Figure 13.1 InGaN/GaN MQW laser structure

Table 29. Structural parameters of the samples 532, 533, 534.

Layer #	Layer Material	Layer Thickness, nm
Sample 532		
1	GaN: undoped	110
2	$Al_{0.24}Ga_{0.76}N$	18
3	$In_{0.04}Ga_{0.96}N$ / GaN MQW	2 / 12 (5 pairs)
4	GaN: undoped	140
5	$Al_{0.19}Ga_{0.81}N$	425
6	GaN: undoped	2000-2500
Sample 533		
1	GaN: undoped	115
2	$Al_{0.21}Ga_{0.79}N$	27
3	$In_{0.06}Ga_{0.94}N$ / GaN MQW	2.1 / 23 (5 pairs)
4	GaN: undoped	120
5	$Al_{0.16}Ga_{0.84}N$	600
6	GaN: undoped	2000-2500
Sample 534		
1	GaN: undoped	146
2	$Al_{0.23}Ga_{0.77}N$	22
3	$In_{0.09}Ga_{0.91}N$ / GaN MQW	3.5 / 11.6 (5 pairs)
4	GaN: undoped	130
5	$Al_{0.157}Ga_{0.843}N$	580
6	GaN: undoped	2000-2500

Differently shaped (stripes, discs, triangles etc) and sized mesas were etched using plasmochemical ICP etching (see Table 29). The cavities of the same shape and dimensions were arranged in 1000 x 1000 μm^2 arrays. The idea was to average over a large number of the same shaped and sized mesas by exciting the whole array simultaneously.

Table 1. Shape and size of cavities employed in optical pumping experiments.

Cavity Field #	Cavity Type	Size	Spacing
1	Circles	∅5 μm	10 μm
2	Circles	∅10 μm	20 μm
3	Circles	∅20 μm	40 μm
4	Circles	∅50 μm	100 μm
5	Circles	∅100 μm	200 μm
6	Stripes	20 μm×1000 μm 20 μm×500 μm 20 μm×300 μm	20 μm 20 μm 20 μm
7	Stripes	20 μm×150 μm 20 μm×100 μm 20 μm×60 μm	20 μm 20 μm 20 μm
8	Rings	40 μm inner diameter 5 μm width	100 μm
9	Triangles	5 μm side	10 μm
10	Triangles	10 μm side	20 μm
11	Triangles	20 μm side	40 μm
12	Triangles	50 μm side	100 μm
13	Triangles	100 μm side	200 μm
14	Stripes	5 μm×1000 μm 5 μm×500 μm 5 μm×300 μm	10 μm 10 μm 10 μm
15	Stripes	5 μm×150 μm 5 μm×100 μm 5 μm×60 μm	10 μm 10 μm 10 μm
16	Rings	10 μm inner diameter 5 μm width	40 μm

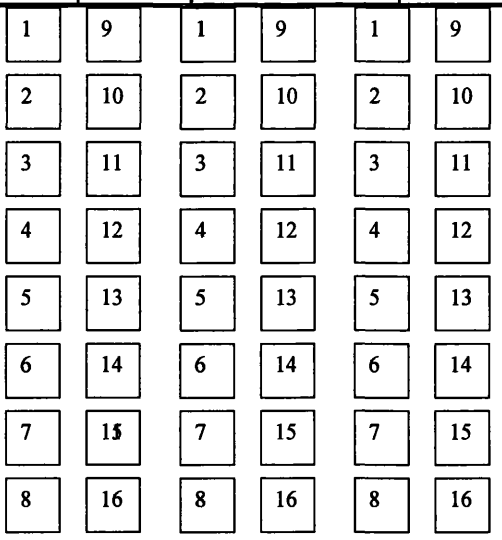

Figure 13.2. Location of cavity fields denoted as 1, 2, 3...16 on sample face. Each cavity field has dimension of 1000×1000 μm^2

13.3. Optical pumping experiments[a]

The photo pumping was performed at room temperature using a nitrogen gas pulsed laser with a peak wavelength of 337.1 nm and having a peak power of ~1kW. The pulse duration was about 10 ns and a repetition rate was 100 Hz. The laser beam was focused on the sample surface fixed at a XY-stage by a quartz lens yielding an excitation power density estimated up to ~15 MW/cm^2. The excitation power density was reduced and adjusted by a number of UV filters. The angle of excitation on the sample face was ~60 deg. Emission spectra from the sample were analysed with a monochromator (Ocean Optics PC2000 with a CCD-detector) in direction perpendicular to the exciting beam (so called, edge emission mode) and corrected for instrumental response.

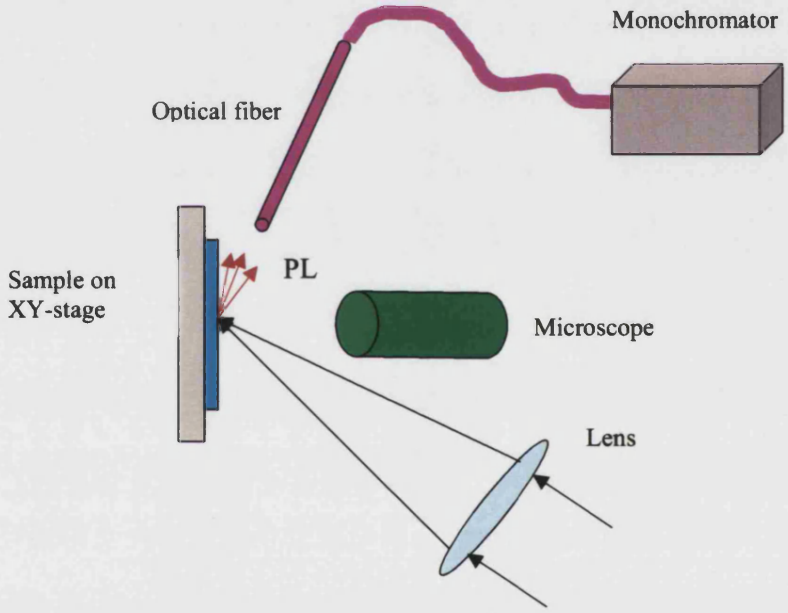

Figure 13.3 A scheme of optical pumping experiments.

13.4. Results and discussion

At low power densities, below the stimulated emission threshold, spectra of a relatively wide spontaneous photoluminescence (PL) band (with peak wavelength of ~412-

[a] Experiments performed at Ioffe Institute, St.Petersburg, Russia by Dr A. Zubrilov

417 nm (sample #532, #533), ~430-435 nm (sample #534), and FWHM of 20-30 nm) dominated by electron-hole recombination in the InGaN MQW active layer were observed.

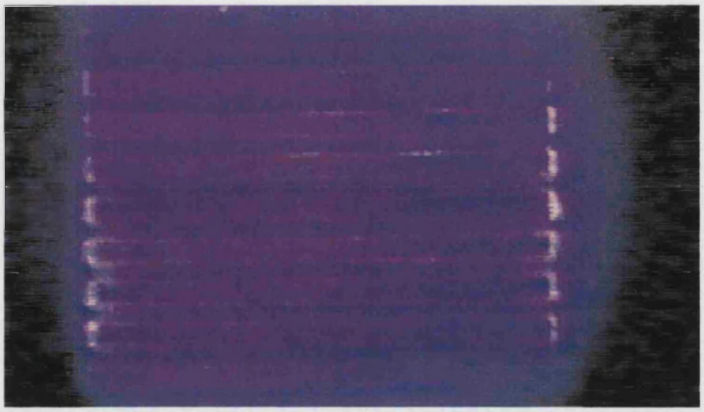

Figure 13.4. Micro-photo of a set of 20μm x 500μm stripe cavities under optical pumping above threshold.

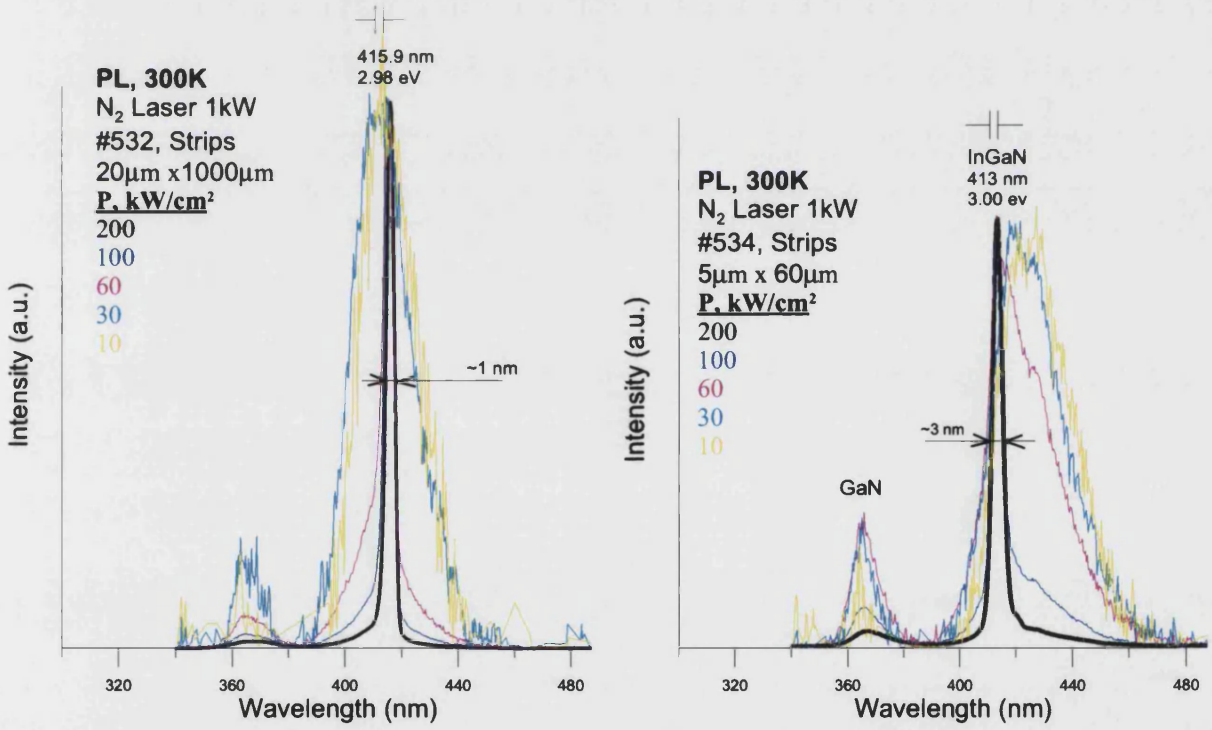

Figure 13.5 Spontaneous and stimulated emission spectra of laser structures. Left: sample #532, stripe cavity of 20 μm×1000 μm; right: sample #534, stripe cavity of 5 μm×60 μm.

Also, the known exciton-related (or, at higher pumping, electron-hole plasma related) peak from GaN undoped layers was seen in the spectra at ~365-375 nm wavelength (Figure 13.5). Below, we will discuss luminescence features of the InGaN MQW active layer (no stimulated emission from GaN layers was detected).

At high power densities (Figure 13.4), when the power density was above the threshold, the PL output peak rose nonlinearly with increasing laser excitation density. Also, a narrowing of the peak was observed. The minimum of the full width at half maximum (FWHM) of the peak at room temperature was only ~1 nm[a] for longest stripe cavities as seen in Figure 13.5 (area #6, #14). That type of PL dependence on excitation power density proves the realization of stimulated emission at room temperature.

Photo pumping experiments were performed at different areas of the samples. For cavities longer than 100 μm the threshold pump power was rather low for all studied samples and estimated to be at a level of 0.05 to 0.4 MW/cm^2 depending on the type of cavity as seen in Figure 13.6. For short cavities (L<500 μm), threshold is decreasing with increasing L following $1/L$ law. For cavities above 500 μm, some saturation of threshold was observed. Within experimental error, no considerable dependence of the threshold on the cavity shape (stripes, discs, triangles) was observed. Three studied samples exhibited almost the same minimum threshold of 0.05 MW/cm^2 for the longest stripe cavities. These facts were attributed to the very good quality of InGaN MQW's and well optical confinement in the active layer as well as low reflectivity of the cavity facets. As a result, a one-pass mode emission was realized in the cavities.

[a] We could not observe separate cavity Fabry-Perot resonances by our spectrometer, because for such long cavities the mode spacing $\Delta\lambda$ is only about a half of angstrom (in accordance with equation: $\Delta\lambda=\lambda^2/[2L(n-\lambda dn/d\lambda)]$) that is much lower than the spectrometer resolution.

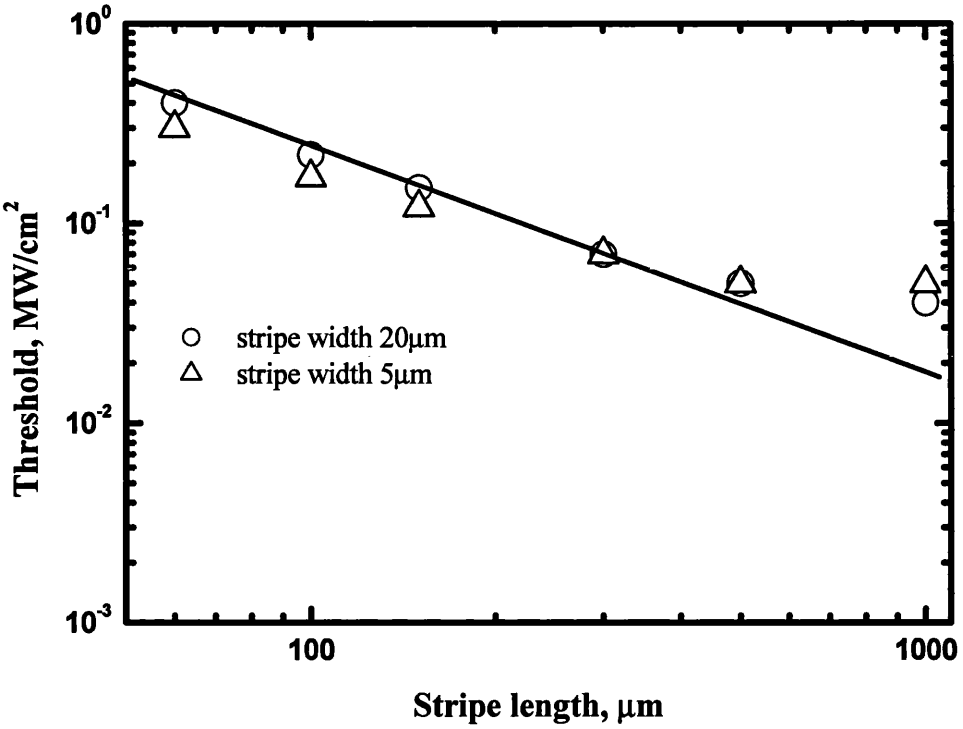

Figure 13.6. Threshold of stimulated emission versus cavity stripe length.

Saturation effects seen in Figure 13.6 and Figure 13.7 were attributed to strong effect of internal optical loss (α_i) inside the stripe cavities including scattering of light by dislocations in the longest stripes (L>500 μm). The peak wavelength of stimulated emission and its FWHM as a function of the length of the stripe cavities are shown for sample #532 in Figure 13.8. A similar effect was found in sample #534 with higher InN composition in the active layer (a shift of stimulated emission peak wavelength from 427 nm to 413 nm for the stripe cavity length reduced from 1000 to 60 μm). The redshift of the emission wavelength with increasing stripe length can be explained by larger influence of loses due to GaN absorption tails in long cavities.

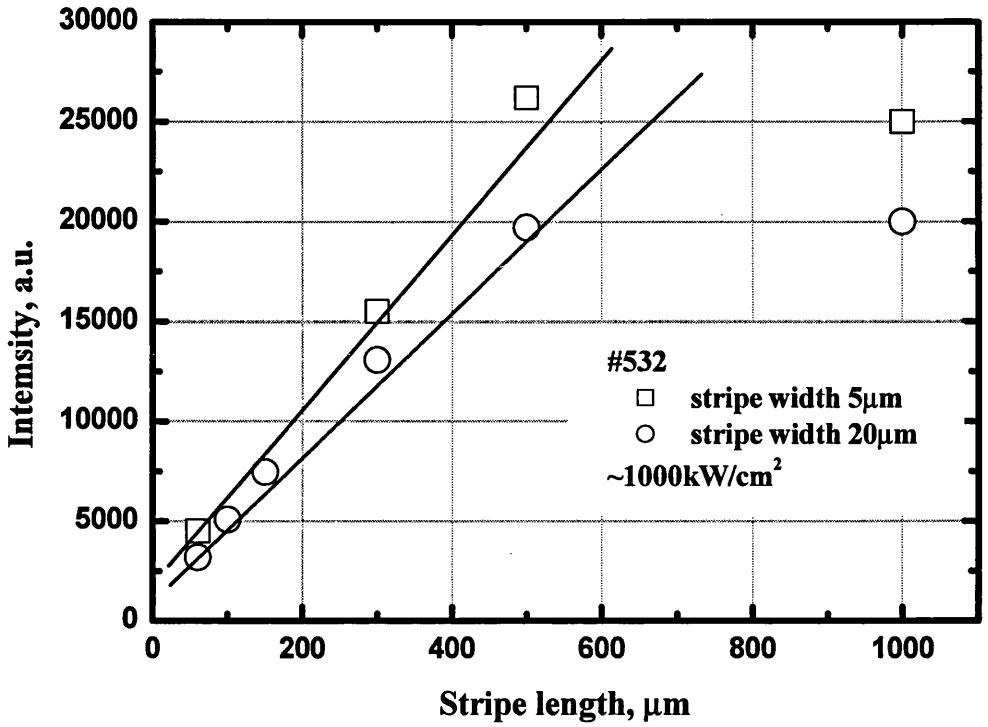

Figure 13.7. Integral intensity of stimulated emission versus the length of the stripe cavities at the pumping power density of ~1000 kW/cm^2

13.4.1. Variable excitation length measurements

We used the Variable Excitation Length (VEL) method to measure the gain in our stripe cavities. In this method, laser light is focused through a lens on a stripe with the constant excitation width. The excitation length l is varied from zero to the stripe length by a screen. The laser beam is focused on a constant area, so that optical pumping power density is kept constant for different excitation lengths. If the pumping power density is high enough, spontaneous emission is amplified as it passes through the excited volume to the stripe edge resulting in stimulated emission. A short excitation length yields only weak spontaneous emission.

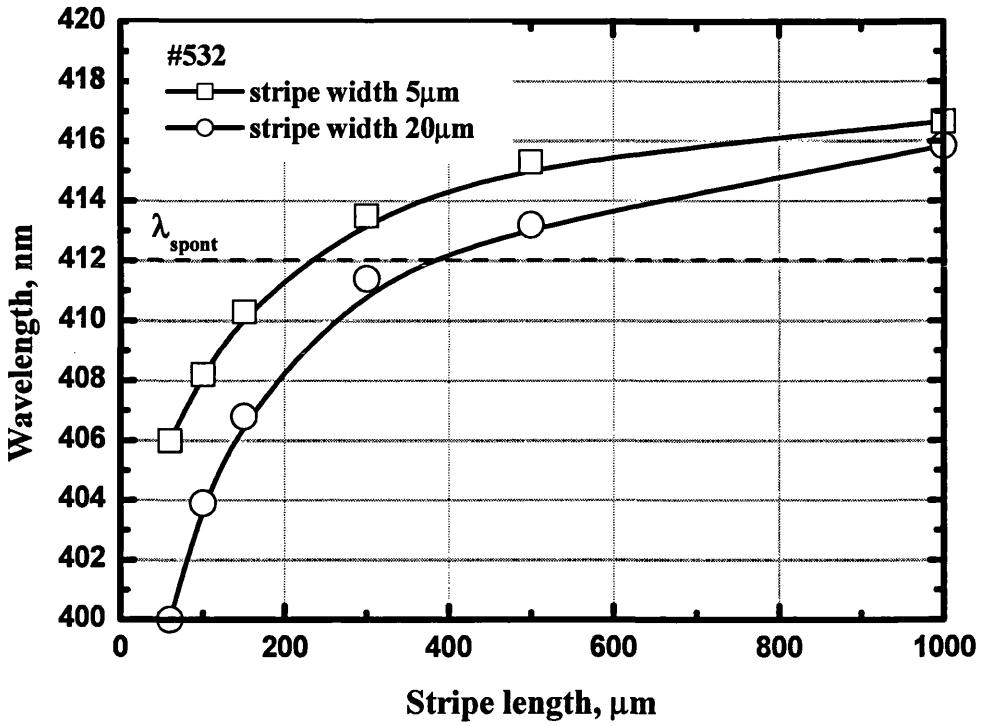

Figure 13.8. Wavelength of stimulated emission versus the length of the stripe cavities at the pumping power density of ~600 kW/cm^2. Spontaneous emission is centered at ~412 nm

With increasing excitation length, emission increases, and stimulated emission appears. An aperture is used to ensure that none of the light, which has passed out of the excited volume before reaching the edge of the crystal, is detected. A straightforward calculation shows that the detected emission intensity I is expressed as

$$I = I_l \frac{1}{g'}[\exp(g'l) - 1] \tag{13.1}$$

where I_l the spontaneous emission rate per unit length, which is proportional to pumping power density; g' is the net optical modal gain, which is the difference between modal gain and internal loss; l is the excitation length. The formula works well up to the excitation length where the saturation effect is observed. The measured emission intensity is plotted as a function of the excitation length (see Figure 13.9), and the net gain is found from the fitting the data by equation (13.1). The measured gain depends on the pumping

intensity. Following the procedure above, we have obtained the net gain of ~40 cm^{-1} at 65 kW/cm^2 for a 1000-mm length stripe (sample #532).

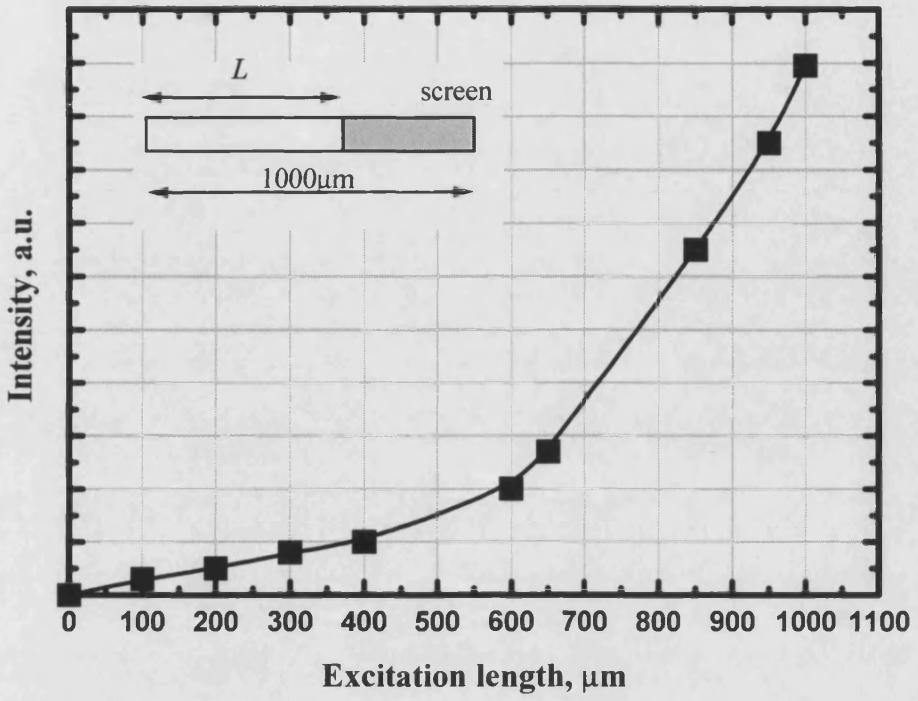

Figure 13.9. The use of Variable Excitation Length method to measure the gain in stripe cavity

To estimate mirror loss in our samples the following experiment was performed. The threshold pumping level for a 5×150 μm stripe was found to be 120 kW/cm^2. VEL measurements performed on a 5×300 μm stripes at the same pumping level give net gain $g' \approx 200$ cm^{-1}. We have assumed that the internal losses are the same for the 150 and 300 μm stripes. Thus, the threshold value of the net gain for the 5×150 μm stripe is $g'_{th} \approx 200$ cm^{-1}. From the threshold condition for lasing

$$g'_{th} = \langle g_{th} \rangle - \langle \alpha_i \rangle = \Gamma g_{th} - (1-\Gamma)\alpha_i = \alpha_m = \frac{1}{L} \ln \frac{1}{R} \tag{13.2}$$

one can obtain that the net threshold gain must be equal to the mirror loss for this stripe length. Here $\langle\ \rangle$ denotes averaging over mode profile, Γ is the optical confinement factor, and α_m is the mirror loss.

Thus, the mirror reflectivity is

$$R = \frac{1}{\exp(g'_{th}L)} = \frac{1}{\exp(200cm^{-1} \cdot 0.015cm)} = 0.049 \tag{13.3}$$

This value is low for a good laser cavity, so special care should be taken to improve the quality of the mirrors.

13.4.2. Differential Quantum Efficiency Measurement

In the case of optical pumping the differential quantum efficiency is given by the ratio between input P^{in} and output P^{out} power $\eta_d = \frac{P^{out}}{P^{in} - P^{in}_{th}}$. To determine differential quantum efficiency η_d, which, one should calibrate arbitrary units of the spectrometer signal to be able to measure output power of the lasing.

Below threshold rate equation for the carrier density N created by the optical pumping with power P^{in} has the form

$$\frac{dN}{dt} = \frac{P^{in}\eta_i}{V_a \hbar\omega_{exc}} - \frac{N}{\tau} \tag{13.4}$$

where V_a is the active region volume, $\hbar\omega_{exc}$=3.68 eV is the excitation energy, η_i is the pumping efficiency equal to the part of the light, which is not reflected by the sample-air interface, absorbed in the structure and contributes to the carrier density in the active region, τ is the carrier lifetime. We have assumed here, that all the carriers generated by the absorbed light are captured to the active region and decay radiatively. Quasi-steady state near threshold carrier density can be obtained from the equation (13.4)

$$N_{th} = \frac{P^{in}_{th}}{V_a \hbar\omega_{exc}} \eta_i \tau \tag{13.5}$$

Above threshold rate equation is

$$\frac{dN}{dt} = \frac{(P^{in} - P^{in}_{th})\eta_i}{V_a \hbar\omega_{exc}} - g_{th} v_g N_{ph} \tag{13.6}$$

where N_{ph} is the photon density in the cavity, g_{th} is the threshold material gain, v_g is the light group velocity in the material. Here we have used the fact that the above-threshold carrier density and gain clamp at their threshold values. In quasi-steady state one can obtain the above-threshold photon density

$$N_{ph} = \frac{P^{in} - P_{th}^{in}}{g_{th} v_g V_a \hbar\omega_{exc}} \eta_i \tag{13.7}$$

Output power is expressed via the photon density as

$$P^{out} = N_{ph} \hbar\omega v \, \alpha_m V \tag{13.8}$$

where V is the optical cavity volume and $\hbar\omega$ is the energy of the emission quantum. Substituting (13.7) into (13.8) and using the threshold condition (13.2) for the g_{th}, we obtain P^{out}

$$P^{out} = \eta_i \frac{\hbar\omega}{\hbar\omega_{exc}} \frac{\alpha_m}{\alpha_m + \langle\alpha_i\rangle} \left(P^{in} - P_{th}^{in}\right) = \eta_d \left(P^{in} - P_{th}^{in}\right) \tag{13.9}$$

Here the definition of the optical confinement factor $\Gamma = V_a / V$ has been used.

Thus, experimental determination of the differential efficiency gives possibility to calculate internal loss, provided that the mirror loss and pumping efficiency η_i are known.

$$\langle\alpha_i\rangle = \left(\frac{\eta_i}{\eta_d} \frac{\hbar\omega}{\hbar\omega_{exc}} - 1\right) \alpha_m \tag{13.10}$$

Then the threshold material gain can be calculated using equation (13.2)

$$g_{th} = \frac{\langle a_i \rangle + \alpha_m}{\Gamma} \tag{13.11}$$

The pumping efficiency can be roughly estimated as

$$\eta_i = (1 - R_i)(1 - \exp(-d_{abs} \alpha_{abs})) \tag{13.12}$$

$$R_i = \frac{(n_{GaN} - 1)^2}{(n_{GaN} + 1)^2}$$

where R_i is the reflection coefficient at the sample-air interface, d_{abs} is the thickness of the structure layers which absorb the excitation light and supply carriers in the active region, α_{abs} is the absorption coefficient at the excitation wavelength. The refractive index of GaN is equal to n_{GaN}=2.7 giving reflection coefficient $R_i = 0.2$. The absorbing length of the structure is about 0.3 μm. It includes the 0.2 μm width of the GaN/InGaN optical guiding layers and 0.1 μm width of the cap GaN layer. The absorption coefficient α_{abs} is about 10^5 cm^{-1}. Then, the pumping efficiency $\eta_i = 0.68$ was obtained from the equation (13.12). The differential quantum efficiency for the 20 × 300 μm stripe (sample #532) was found to be $\eta_d = 0.3$. The energy of the emission quantum is $\hbar\omega = 2.98$ eV, and the mirror loss for the stripe is $\alpha_m = 200$ cm^{-1}. It gives for the modal internal loss (see equation (13.10))

$$\langle \alpha_i \rangle = (1-\Gamma)\alpha_i = 206 \text{ cm}^{-1} \tag{13.13}$$

The optical confinement factor for this structure was calculated as $\Gamma = 0.04$. In result, we obtain the following internal loss for the structures in the sample #532 $\alpha_i = 215$ cm^{-1}. Then, the threshold material gain for this type of structures can be calculated from equation (13.11) as $g_{th} \approx 10000$ cm^{-1}. These parameters are similar to those reported for the InGaN/GaN laser structures where lasing under pulsed electrical pumping was observed.

We should mention here, that we have obtained an overestimated value of the internal loss. The first reason is that we have used the expression for the sample-air reflection coefficient, which assumes normal incidence of light at the sample, whereas the incidence angle was about 60 degrees. The second reason is that not all the carriers created in the cap GaN layer can reach the active region and contribute to the gain. Thus, the pumping efficiency should be less than the obtained one resulting in smaller value of the internal loss.

13.5. Summary

To summarise we can make the following conclusions

1. Stimulated emission from stripes has been reached at thresholds as low as ~50 kW/cm^2 and for stripe length up to 1000 μm indicating very good quality of the samples material and good optical confinement. This value roughly corresponds to 13 kA/cm^2 threshold current for electrical pumping. The best world results are 2-4 kA/cm^2.Thus, quality of the structures is enough to realise electrically pumped GaN/InGaN MQW laser.
2. Successful optical pumping of very long stripe cavities (up to 1000 μm length) at low thresholds indicates to very good quality of InGaN MQWs as well as good optical confinement inside the stripes. No considerable difference in threshold characteristics has been observed for the laser structures with different cavity shapes indicating poor optical reflectivity of cavity facets, which is confirmed by our measurements. Thus, mirror quality should be significantly improved to realise continuous-wave (CW) electrically pumped GaN/InGaN MQW laser.
3. The following typical structure parameters were obtained:
   a) Mirror reflection coefficient R = **5-7%**
   b) Optical confinement factor Γ = **0.04**
   c) Differential quantum efficiency η_d = **0.3** for stripe length L = 300 μm
   d) Internal loss $\alpha_i \approx$ **215 cm^{-1}**
   e) Material threshold gain $g_{th} \approx$ **10000 cm^{-1}**

These values correspond to the level of currently reported parameters for InGaN/GaN laser structures, where lasing under pulsed electrical pumping was observed.

13.6. References

1. S. Nakamura and G.Fasol. *The blue laser diode: GaN based light emitters and lasers. Spinger-Verlag Berlin Heidelberg NY,* 1997
2. T. J. Schmidt, X. H. Yang, W. Shan, J. J. Song, A. Salvador, W. Kim, Ö. Aktas, A. Botchkarev, H. Morkoc. Appl. Phys. Lett. 68, 1820 (1996)

Conclusions

We have studied the MOCVD growth of III-nitride epitaxial layers and device structures. A number of important issues have been discussed, including the nucleation of GaN on sapphire substrates, the doping process, the growth of AlGaN and InGaN alloys. Heterostructures such as AlGaN/GaN superlattices, InGaN/GaN multiple quantum wells, were successfully fabricated. We have studied the influence of built-in piezoelectric fields on the mobility and density of the carriers in p- and n-type doped AlGaN/GaN superlattices. The operation of a III-nitride based light emitting diode has been demonstrated. The output power was in excess of 5 mW at driving current of 20 mA. Room temperature lasing under optical pumping of separate confinement InGaN/GaN/AlGaN heterostructures has been attained. The pumping power threshold for stimulated emission was found to be about 50 kW/cm^2.

The properties of III-Nitride epilayers and structures were attained using various characterisation methods including photoluminescence, electroluminescence, Hall effect measurements, high-resolution x-ray diffraction, current-voltage measurements and other techniques. A new method for extracting structural parameters of the epilayers from x-ray scans has been developed.

Although the present work emphasises an empirical approach, the due attention is paid to underlying physical mechanisms. In most cases, we attempted to develop a first-principle theoretical model, explaining the experimental observations.

As it was proved by the optical pumping experiments, the quality of the device structures is sufficient for realisation of III-nitride lasers operating in the pulsed mode. Therefore, our immediate plans include a demonstration electrically driven III-nitride laser.

Another problem to be solved is the low internal quantum efficiency of III-nitride optoelectronic devices. The highest internal quantum efficiency is about 30%, while typical values are about 10–15%. The internal quantum efficiency drops dramatically with increasing current density. Nowadays, the optimal current density corresponding to the highest efficiency is about 10 A/cm^2. However, for high-brightness LEDs the current density should be increased at least by one order of magnitude.

Still a lot has to be done in the growth technology of III-Nitrides. Although significant progress has been made over the last few years, III-nitride technology still does not have a level of matureness that we see in conventional semiconductor materials. Many fundamental problems remain to be solved in the areas of defect density reduction, efficient p-type doping, growth of AlGaInN quaternary alloys etc.

List of relevant publications and presentations

Publications

1. *Luminescence properties of gallium nitride layers grown on silicon carbide substrates by gas-phase pitaxy in a chloride system*, A.S. Zubrilov, Yu.V. Mel'nik, D.V. Tsvetkov, V.E. Bugrov, A.E. Nikolaev, S.I. Stepanov, V.A. Dmitriev, Semiconductors **31** (5), p. 523-526 (1997).
2. *Apparatus for growing GaN films on large-area substrates by the method of chlorine vapor-phase epitaxy*, S.I. Stepanov, D.V Tsvetkov, A.E Cherenkov, Technical Physics Letters **24** (10), p. 813-815.
3. *The initiation of GaN growth by molecular beam epitaxy on GaN composite substrates*, T.S. Cheng, S.V. Novikov, V.B. Lebedev, R.P. Campion, N.J. Jeffs, Yu.V. Melnik, D.V. Tsvetkov, S.I. Stepanov, A.E. Cherenkov, V.A. Dmitriev, D. Korakakis, O.H. Hughes, C.T. Foxon, J. Crystal Growth **197** (1-2) p. 12-18.
4. *Strain relaxation in GaN layers grown on porous GaN sublayers*, M. Mynbaeva, A. Titkov, A. Kryzhanovski, I. Kotousova, A.S. Zubrilov, V.V. Ratnikov, V.Yu. Davydov, N.I. Kuznetsov, K. Mynbaev, D.V Tsvetkov, S. Stepanov, A. Cherenkov, V.A. Dmitriev,MRS Internet Journal of Nitride Semiconductor research, **4**, article 14 (1999).
5. *Deep Centers and Persistent Photoconductivity Studies in Variously Grown GaN Films*, A.Y. Polyakov, N.B. Smirnov, A.V. Govorkov, A.S. Usikov, N.M. Shmidt, B.V. Pushnij, D. Tsvetkov, S.I. Stepanov, V.A. Dmitriev, M.G. Milvidskij, V.F. Pavlov, MRS Internet Journal of Nitride Semiconductor research, v 5S1, article W11.81 (2000).
6. *Scanning electron microscope studies of GaN films grown by hydride vapor phase epitaxy*, A.Y. Polyakov, A.V. Govorkov, N.B. Smirnov,, M.G. Mil'vidskii, D.V. Tsvetkov,, S.I. Stepanov,, A.E. Nikolaev, V.A. Dmitriev, Solid-State Electronics **43** p. 1937-1943, (1999)
7. *Light Emitting Diode with Charge Asymmetric Resonance Tunneling*, Y.T. Rebane, Y.G. Shreter, B.S. Yavich, V.E. Bougrov, S.I. Stepanov, W.N. Wang,Phys. Stat. Sol (A), **180**, 121, (2000).
8. *High quality GaN layers grown by hydride vapor phase epitaxy – a high resolution X-ray diffractometry and synchrotron X-ray topography study*, J. Chaudhuri, C. Ignatiev, S. Stepanov, D. Tsvetkov, A. Cherenkov,V. Dmitriev, Z. Rek, Materials Science and Engineering **B78,** p.22–27, (2000)
8. *Influence of Poisson's ratio uncertainty on calculations of the bowing parameter for strained InGaN layers,* S. Stepanov, W.N. Wang, B.S. Yavich, V. Bougrov,

Y.T. Rebane and Y.G. Shreter, MRS Internet J. Nitride Semicond. Res. **6**, article 6 (2001).

9. *Optically detected magnetic resonance of paired defects in as-grown magnesium-doped GaN,* J. John Davies, G.N. Aliev, S.J. Bingham, D. Wolverson, S. Stepanov, B.Yavich, W.N. Wang, Phys. Rev. B **67** (2003)

Presentations

1. *The growth of III-nitrides by HVPE method,* S.I. Stepanov,Yu.V. Melnik, A.E. Nikolaev, I.P. Nikitina, 1st Russian Workshop "GaN, InN, AlN: Structures and Devices", St. Petersburg, Russia, June 1, 1997
2. *Properties of GaN homoepitaxial layers grown on GaN epitaxial wafers,* V. Dmitriev, A. Nikolaev, A. Cherenkov, D. Tsvetkov, S. Stepanov, I. Nikitina, A. Kovarsky, M. Yagovkina, V. Davidov, MRS. Proc., **512** 451-456 (1998)
3. *AlN/GaN and AlGaN/GaN Heterostructures Grown by HVPE on SiC Substrates,* Yu.V. Melnik, A.E. Nikolaev, S.I. Stepanov, A.S. Zubrilov, I.P. Nikitina, K.V. Vassilevski, D.V. Tsvetkov, A.I. Babanin, Yu.G. Musihin, V.V. Tretyakov and V.A. Dmitriev, MRS. Symp. Proc. **482**, p.245-249, (1998).
4. *HVPE GaN and AlGaN "substrates" for homoepitaxy,* Yu.V. Melnik, A.E Nikolaev, S. Stepanov, I.P. Nikitina, K. Vassilevski, A. Ankudinov, Yu. Musikhin and V.A. Dmitriev, Materials Science Forum, **264-268**, p. 1121 -1124, (1998).
5. *AlN epitaxial layers grown by HVPE method on SiC substrates,* S.I. Stepanov, Yu.V. Melnik, A.E. Nikolaev, I.P. Nikitina, A.I. Babanin, N.I. Kuznetsov, V.A. Dmitriev, in Proc.: 2nd Russian Workshop "GaN, InN, AlN: Structures and Devices" St. Petersburg, Russia, June, 1998 (in Russian) p. 14 (NG01)
6. *GaN Layers Grown by HVPE on p-type 6H-SiC Substrates,* S.I. Stepanov, Yu.V. Melnik, A.E. Nikolaev, V.A. Dmitriev,1st Russian Workshop "GaN, InN, AlN: Structures and Devices", St. Petersburg, Russia, June, 1997
7. *HVPE growth of AlGaN alloys,* Yu. Melnik, A. Nikolaev, S. Stepanov, A. Zubrilov, I. Nikitina, and V. Dmitriev, Book of Abstract of the E-MRS Spring Meeting p. L22 (1997),
8. *HVPE GaN and AlGaN "substrates" for homoepitaxy,* Yu. Melnik, A. Nikolaev, S. Stepanov, I. Nikitina, K. Vassilevski, A. Ankudinov, Yu. Musikhin and V. Dmitriev, Abstracts of International Conference on Silicon Carbide, III-nitride and Related Materials, August 31 -September, 1997 Stockholm, Sweden, p. 268.
9. *AlN/GaN and AlGaN/GaN heterostructures grown by HVPE on SiC substrates,* Yu. Melnik, A. Nikolaev, S. Stepanov, I. Nikitina, K. Vassilevski, A. Babanin, V. Davydov and V. Dmitriev, Book of Abstracts MRS Fall Meeting, December, 1997, Boston, p. 138 (1997)

10. *GaN and AlN layers Grown by Nano-Epitaxial Lateral Overgrowth Technique on porous Substrates*, M. Mynbaeva, A. Titkov, A. Kryzhanovski, A. Zubrilov, V. Ratnikov, V. Davydov, N. Kuznetsov, K. Mynbaev, S. Stepanov, A. Cherenkov, I. Kotousova, D.V Tsvetkov, V. Dmitriev, MRS Fall 1999 meeting, (1999).

11. *Light emitting diode with charge asymmetric resonance tunneling*, Y.T. Rebane, Y.G. Shreter, B.S. Yavich, V.E. Bougrov, S. Stepanov and W.N. Wang, Third International Symposium on Blue Laser and Light Emitting Diodes, Berlin, Germany (2000)

12. *Charge asymmetric resonance tunneling LED*, Y.T. Rebane, Y.G. Shreter, B.S. Yavich, V.E. Bougrov, S. Stepanov and W.N. Wang, 4th European GaN Workshop, Nottingham , UK (2000)

13. *Differential quantum efficiency measurements of III-nitride LEDs*, Y.G. Shreter , V.E. Bougrov, Y.T. Rebane, D.V. Tarkhin, B.S. Yavich, S.I. Stepanov and W.N. Wang, 4th European GaN Workshop, Nottingham , UK (2000)

14. *Light emitting diode with charge asymmetric resonance tunneling*, Y.T. Rebane, Y.G. Shreter, B.S. Yavich, V.E. Bougrov, S.I. Stepanov and W.N. Wang, International Workshop On Nitride Semiconductors, Nagoya, Japan (2000)

15. *III-nitride LED modulation measurements: differential quantum efficiency, I-V characteristic, and overheating*, Y.G. Shreter, V.E. Bougrov, Y.T. Rebane, D.V. Tarkhin, B.S. Yavich, S.I. Stepanov and W.N. Wang International Workshop On Nitride Semiconductors, Nagoya, Japan (2000)

16. *XRD and PL measurements of MOCVD grown InGaN epilayers and determination of the bowing parameter*, S. Stepanov, W.N. Wang, B.S. Yavich, V. Bougrov, Y.T. Rebane and Y.G. Shreter UK Nitride Consortium Workshop, Bath (2001)

17. *III-nitride efficient LEDs*, P.J. Wang, V.E Bougrov, Y.T Rebane, Y.G. Shreter, S.I. Stepanov, C.L. Tseng, B.S. Yavich, W.N. Wang, Proceedeings SPIE, vol 4445, p.99-110 (2001)